



# Contribution to the design of soft hybrid generators : combination of electroactive materials

Clara Lagomarsini

## ► To cite this version:

Clara Lagomarsini. Contribution to the design of soft hybrid generators : combination of electroactive materials. Automatic. Université Grenoble Alpes, 2018. English. NNT: 2018GREAT001 . tel-01827397

**HAL Id: tel-01827397**

**<https://theses.hal.science/tel-01827397>**

Submitted on 2 Jul 2018

**HAL** is a multi-disciplinary open access archive for the deposit and dissemination of scientific research documents, whether they are published or not. The documents may come from teaching and research institutions in France or abroad, or from public or private research centers.

L'archive ouverte pluridisciplinaire **HAL**, est destinée au dépôt et à la diffusion de documents scientifiques de niveau recherche, publiés ou non, émanant des établissements d'enseignement et de recherche français ou étrangers, des laboratoires publics ou privés.

## THÈSE

Pour obtenir le grade de

**DOCTEUR DE LA COMMUNAUTE UNIVERSITE  
GRENOBLE ALPES**

Spécialité : **Génie Electrique**

Arrêté ministériel : 25 mai 2016

Présentée par

**Clara LAGOMARSINI**

Thèse dirigée par **Alain SYLVESTRE**, Professeur, Université  
**Grenoble Alpes**, et  
codirigée par **Claire JEAN-MISTRAL**, Maître de conférences,  
**INSA Lyon**

préparée au sein du **Laboratoire de Génie Electrique de  
Grenoble (G2eLab)**  
dans l'**École Doctorale d'Electronique, Electrotechnique,  
Automatique & Traitement du Signal (EEATS)**

## **Contribution à la conception de générateurs hybrides souples: association de matériaux électro-actifs**

Thèse soutenue publiquement le **11 Janvier 2018**,  
devant le jury composé de :

**M. Skandar BASROUR**

Professeur, TIMA, Grenoble, Président

**M. Lucian DASCALESCU**

Professeur, PPRIME, Poitiers, Rapporteur

**M. Elie LEFEUVRE**

Professeur, Université Paris-Sud, Paris, Rapporteur

**M. Davide FABIANI**

Maître de conférences, Université de Bologne, Italie, Examinateur

**M. Stéphane MONFRAY**

Ingénieur de recherche, ST Microelectronics, Crolles, Invité

**Mme. Claire JEAN-MISTRAL**

Maître de conférences, INSA Lyon, Lyon, Co-directrice

**M. Alain SYLVESTRE**

Professeur, Université Grenoble-Alpes, Directeur de thèse





*Ai miei genitori,*

*che mi hanno sempre sostenuto in ogni mia scelta*





## Acknowledgements

This work would not have been possible without the help of the people around me, that I want to thank for the sustain along these three years.

First of all, I would like to express my gratitude to my two supervisors, Alain Sylvestre and Claire Jean-Mistral, for giving me the possibility to carry out this work. It was a pleasure to work with them both for their scientific expertise and their human contact. Thank you for your time, for sharing with me your ideas and for the constant patience and advices you gave me along my thesis!

Special thanks go to Stephan Monfray from STMicroelectronics for having followed always with interesting ideas and reflection points the evolution of the work.

I am also grateful to the members of InnoEney: Isabelle Schuster, Fabien Gauthier and Christine Dominjon for the possibility to participate to this exceptional program and for continuously organize fulfilling and interesting formations, who allowed me to professionally grow and to meet exceptional PhDs from all Europe!

I also wish to thank all the members of the jury for their participation, their expertise and their helpful comments and questions: special thanks to Skandar Basrour, that I had the pleasure to know during my thesis and that I hugely appreciate for his scientific competence and brilliance. Thank a lot for your precious suggestions and for having accepted the presidency of the jury. Thanks also to Lucian Dascalescu and Elie Lefevre for having accepted to review my manuscript and to Davide Fabiani, for coming from Italy to assist to my defense and for the collaboration we carried out with Giulia in the last part of my work.

It was a great pleasure to work in G2eLab and I really want to thank all the people that I met there. Thanks to the director James Roudet, to all the administration (Catherine Valentin, Elise Riado, Geneviève Teissedre, Nadine Michel...) and to all the technicians that made my life easier in the lab. Some special thanks go to Jean-Paul Baroux and Christophe Pollet, that were precious technical addition to my work, to Jean-Luc Palenzuela, Sebastien Flury, Julien Bamberger and to all the technical team.

Thanks to all the members of MDE: first of all to Rachelle and Tariq, for being awesome friends and for their constant support along these three years. Grenoble would not have been the same without you! Special thanks also to Nelly Bonifaci, Olivier Lesaint, Jean-Luc Reboud, Pascal Rain and Olivier Gallot-Lavallee for all the interesting discussion we had. Thanks to all the PhD that made the ambience in the lab. The ones in MDE: Florian, Laure, Priscilla, Joko, Raphael, Nathan, Vikas, Saber, Achraf... and the ones in the other teams: Anthony, Ahmed, Andres, Baoling, Geoffrey, Thomas... I wish you all a successful future!

All the devices fabrication realized during this thesis would not have been possible without the help of the staff working in the FabLab in Grenoble. I warmly thank Jérôme Maisonnasse for his technical competences and for always leaving me the possibility to use the FabLab facilities despite the huge number of users.

I am also grateful to the people of Néel Institute, especially to Jean-Luc Garden and Emmanuel Andre, for their expertise in Parylene deposition, their helpfulness and for the good times spent together around a coffee!

I also want to thank with all my heart all the exceptional friends that I met in Grenoble along these three years, we spent great moments together and they allowed me to enjoy the time out of the lab. Thanks especially to my Italians (Cinzia, Jesus, Silvia, Loreto, Adrica, Alberto, Elena...) and international friends (Ahmed, Remy, Gabriel...).

Some special thanks go also to all the special people in Italy, for their support despite the distance: Imma, Cristina, Francesca, Mattia, Eleonora, Teddy, Paolo and to Marghe, Gemma, Silvia, Giulia. Thank you for the positive energy you give me every time I come back.

Last but not least, I would like to thank my parents, my brother and all my family for always encouraging me in all the moments of my life. Thank you for your unconditional love that push me to do my best!



## Summary

Over the last years, embedded sensors have gained in accuracy and precision, while following the demands of miniaturization and lower power consumption. Scavenging human kinetic energy to produce electricity is an attractive alternative for the power supply of these low-power-consumption devices. E-textiles for health-monitoring or biomedical implants are some of the possible applications that could benefit from a self-powering system.

In this context, in 2013, a first prototype of soft energy scavenger was developed by our research group through the collaboration between LaMCoS and G2Elab laboratories. This electrostatic generator was based on the dielectric elastomers generators (DEGs) technology, which relies on the mechanical deformation of a thin layer of dielectric material (acrylic or silicone) sandwiched between two compliant electrodes and an electret material, namely an insulator developing a surface potential. The main advantages of these hybrid scavengers are their low-cost, compliance, light-weight and adaptability to complex shapes. In addition, they can work on a large scale of temperatures and frequencies ( $<100\text{Hz}$ ), which make them attractive to harvest and convert human kinetic energy.

The objectives of this PhD work were focused on the first prototype optimization to realize a second-generation device with higher energy output, better suitability for wearable applications and longer lifetime. New alternatives hybrid scavengers based on different operating principles but also various association of materials were designed.

To these aims, the first stage of the study consisted in the investigation of new conformant electret materials representing the charges reservoir for electrostatic generator polarization in the scavenger structure. Different variants of poly(p-xylylene) polymers, better known with the commercial name of Parylene, were tested as new potential electret materials, mainly due to their highly conformability and possibility of CVD-deposition on complex shapes. The surface potential decays (SPDs)

on electrets charged by corona discharge method were monitored over time for different Parylene types, samples thicknesses and charging voltages. These characterizations were aimed to evaluate the performance of Parylene electrets and to monitor the charge dynamic under mechanical conditions close to the final applications but also under harsher environmental temperatures. As a result of these tests, fluorinated Parylenes (AF-4 and VT-4) showed excellent long-term charge retention performance (over 1.5 years) both for positive and negative charges.

The second part of the work was related to the design of optimized soft generators realizing the electromechanical coupling and hybridizing two different electroactive materials. Two different working modes for the scavengers were developed: the first one is based on electret mode while the second one employs an electroactive material (electret or piezoelectric materials) as polarization source of a classic DEG. Through numerical simulations, optimizations were performed with the aim of maximizing the power output and increasing the lifetime of the devices. Finally, centimeter scale prototypes were realized as new promising solution for autonomous wearable generators and characterized with the final objective to exploit the mechanical deformation given by human body at knee level while walking.



## Table of Contents

<b>CHAPTER 1. CONTEXT AND OBJECTIVES .....</b>	<b>1</b>
1.1 General context.....	3
1.2 Energy harvesting process and technologies.....	5
1.3 Applications to human body.....	7
1.3.1 Energy harvesting strategies for wearable devices .....	10
1.3.1.1 Electromagnetic scavengers .....	10
1.3.1.2 Piezoelectric scavengers .....	11
1.3.1.3 Electrostatic scavengers .....	11
1.3.1.4 Technologies comparison .....	12
1.4 Location and technology choice .....	14
1.5 Objectives and organization of the work .....	16
<b>CHAPTER 2. STATE-OF-THE-ART: PIEZOELECTRIC AND ELECTROSTATIC TECHNOLOGIES .....</b>	<b>20</b>
2.1 Piezoelectric technology.....	22
2.1.1 Basic principles and equations .....	23
2.1.2 Working modes .....	25
2.1.3 Piezoelectric materials .....	27
2.1.4 Possible configurations.....	29
2.1.5 Existing wearable devices .....	31
2.2 Electrostatic technology .....	35
2.2.1 Vibrating Energy Harvesters (VEH) .....	38
2.2.1.1 State-of-the-art on wearable devices.....	39
2.2.2 Dielectric elastomers generators (DEGs) .....	43
2.2.2.1 Basic principles .....	44
2.2.2.2 Materials .....	45
2.2.2.3 Mechanical excitation .....	51



## Table of contents

2.2.2.4 Existing devices for wearable applications .....	53
2.2.3 Electrets as polarization source .....	56
<b>Conclusion .....</b>	<b>59</b>
<b>CHAPTER 3. ELECTRET MATERIALS.....</b>	<b>62</b>
3.1 Physical principles and experimental techniques .....	64
3.1.1 General definitions .....	64
3.1.2 Energy traps .....	65
3.1.3 Charges stability over time .....	66
3.1.4 Electret surface potential.....	68
3.1.5 Charges injection by corona discharge method.....	69
3.1.6 Surface potential decay (SPD) measurements .....	70
3.1.7 Energy distribution of trapped charges.....	73
3.1.8 Electrets in energy harvesting applications: state-of-the-art.....	75
3.2 Electrets fabrication and tests .....	78
3.2.1 Materials characteristics and fabrication .....	78
3.2.2 Electrets charging and SPD monitoring.....	81
3.2.3 Thermally stimulated discharge (TSD) measurements.....	90
3.2.4 Environmental charges stability .....	92
<b>Conclusion .....</b>	<b>95</b>
<b>CHAPTER 4. ELECTRET-BASED ENERGY HARVESTING DEVICES .....</b>	<b>98</b>
4.1 Device working principle .....	100
4.2 Proof of concept .....	103
4.3 Scavenger design optimization.....	111
4.3.1 Experimental tests .....	115
4.3.2 Device performance .....	118
4.3.3 Ideal macroscopic scavenger prototype .....	122
4.3.4 Towards an embedded scavenger .....	124
4.4 Power management unit .....	128

<b>Conclusion .....</b>	<b>135</b>
<b>CHAPTER 5. DEG-BASED ENERGY HARVESTING DEVICES .....</b>	<b>138</b>
5.1 Electret polarization .....	141
5.1.1 Device structure and working principle .....	141
5.1.2 Materials selection .....	144
5.1.3 DE capacitance variation .....	146
5.1.4 Electret polarization voltage .....	149
5.1.5 Scavenging phase .....	154
5.2 Piezoelectric polarization .....	156
5.2.1 Working principle .....	157
5.2.2 Materials selection .....	160
5.2.3 Devices structures .....	161
5.2.4 Mechanical excitation .....	165
5.2.5 DE capacitance variation .....	166
5.2.6 Experimental setup .....	168
5.2.7 Devices performance .....	169
5.2.8 Performance optimization .....	172
<b>Conclusion .....</b>	<b>175</b>
<b>Conclusions and perspectives .....</b>	<b>178</b>
<b>Résumé .....</b>	<b>184</b>
<b>REFERENCES .....</b>	<b>196</b>
<b>APPENDIX A. CHEMICAL VAPOR DEPOSITION (CVD) .....</b>	<b>207</b>
<b>APPENDIX B. SPD CURVES FITTING .....</b>	<b>211</b>



## LIST OF SYMBOLS

CNT	Carbon Nanotube
DE	Dielectric Elastomer
DEG	Dielectric Elastomer Generator
FEP	Fluorinated Ethylene Propylene
HV	High voltage
MFC	Macro Fiber Composite
MEMS	Micro Electro Mechanical System
PE	PolyEthylene
PEEK	PolyEther Ether Ketone
PP	PolyPropylene
PTFE	PolyTetraFluoroEthylene
PVDF	PolyVinyliDene Fluoride
PZT	Lead Zirconate Titanate
RSPD	Relative Surface Potential Decay
SECE	Synchronous electric charge extraction
SSHI	Synchronized Switch Harvesting on Inductor
SPD	Surface Potential Decay

## List of symbols

$\nu$	Attempt-to-escape frequency
$\eta$	Efficiency
$\beta$	Heat rate
$\epsilon_r$	Relative permittivity
$\lambda$	Stretching ratio
$\sigma$	Surface charge density
$\tau$	Time constant
$\epsilon_0$	Vacuum permittivity
$P_{\text{avg}}$	Average power
$C$	Capacitance
$Q$	Electric charge
$i$	Electric current
$V_s$	Electret surface potential
$R$	Resistance



# **CHAPTER 1.**

## **CONTEXT AND OBJECTIVES**





## **Chapter 1. CONTEXT AND OBJECTIVES**

In the last years, the willing of increasing life quality resulted in the integration of sensors and intelligent devices in our everyday life. These devices are evolving into an interconnected network also named Internet of Things (IoT), which is estimated to involve around 30 billion of objects by 2020 [1.1]. The increase in the number of these electronic devices has faced the challenge of powering systems through new sustainable ways of electrical energy generation. In our environment, energy is present in a number of different forms, such as light, heat, sound and motion. These sources can be employed for electrical energy generation through the “energy harvesting process”. This introductory chapter aims at giving an overview of the principle and the main technologies for ambient energy scavenging and the motivations for the technologies chosen in the present work with the perspective of harvesting human kinetic energy while walking.

### **1.1 General context**

The term “energy harvesting” refers to the process consisting in the conversion of the lost ambient environmental energy into electrical energy for low power levels ( $<1\text{W}$ ). For higher level of electrical power, the term “energy production” is generally referred to well-known structures such as wind or hydro turbines. In the last year, small-scale energy harvesters have been developed to supply low-power consumption embedded electronic devices, with the willing to replace batteries in sensor nodes (*i.e.* a node including sensors, microcontrollers and wireless transceivers). Thanks to the ultra-low-power electronic developments, the power consumption and size of electronic devices and components have significantly decreased. Small-scale devices power consumptions levels typically stand between few microwatts for MicroElectroMechanical Systems (MEMS) sensors and actuators, to few hundreds of

milliwatts for Global Positioning System (GPS) and MP3 players. Most of the embedded or wearable devices normally remain in sleep mode for the higher percentage of time (close to 99% of operation time) and wake up for operation (sensing) only few milliseconds [1.2]. The average power consumption of such embedded sensor node can thus be reduced below 100  $\mu$ W. Figure 1. 1 shows the typical power consumption of some of the most employed small-scale electronic devices extracted from [1.2].

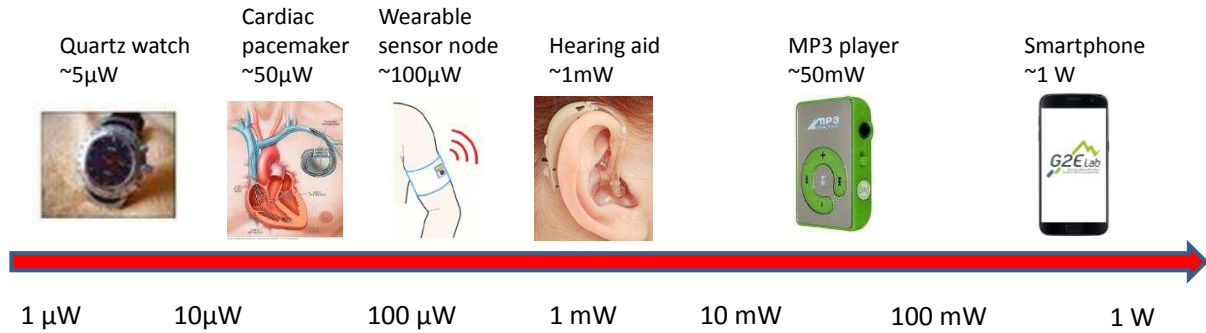


Figure 1. 1: Power requirements of selected battery-operated systems

Figure 1. 2 presents the power density available from different ambient sources (mechanical, thermal and radiant) and their applicability to power supply low-power-consumption devices, underlying a good match between systems requirement and available energy for low-consumption applications. For example, energy harvesting density from vibration mechanical sources is around 10-500  $\mu\text{W.cm}^{-3}$  which is quite enough to supply a vibration sensor (10 nW) or a calculator (1  $\mu$ W). Replacing batteries by an energy harvester is thus possible and various embedded applications with mean power consumption lower than 100 $\mu$ W can be designed and developed.

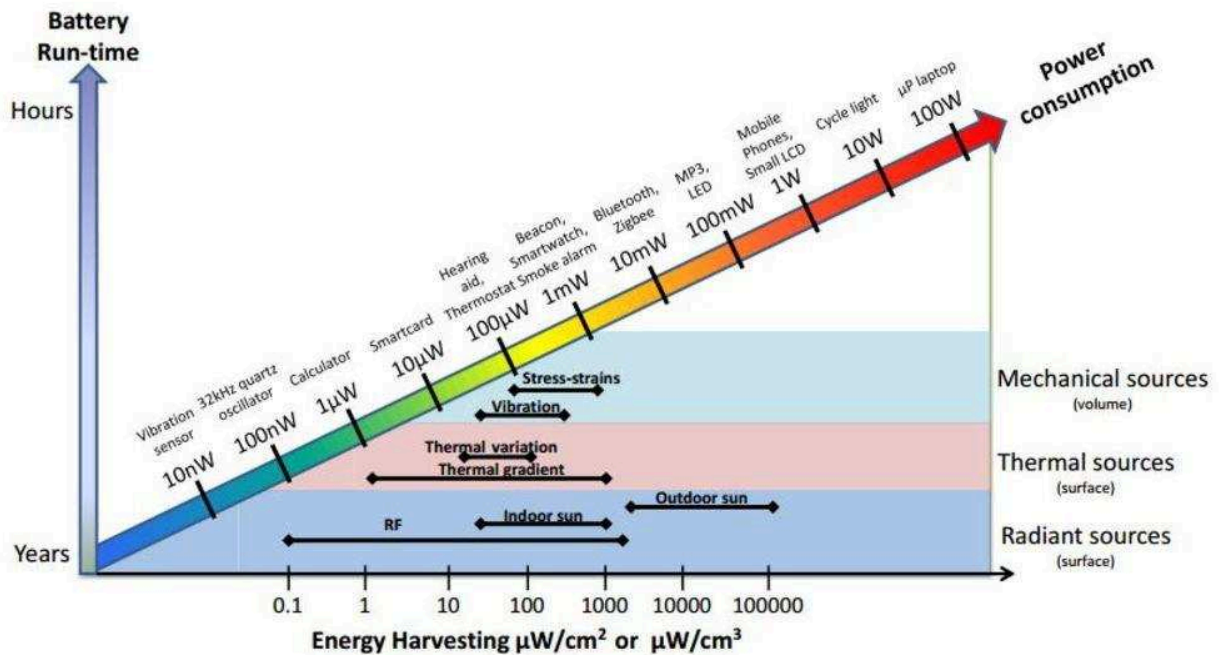


Figure 1. 2: Power densities overview of different ambient energy sources versus average power consumption of some electronic devices [1.3]

In case energy scavengers are replacing conventional batteries, the benefits are both from an environmental and from a practical point of view. Indeed, eliminating the need of batteries recharging reduces drastically the maintenance and operation cost of embedded devices, but also allows them to be operational in harsh environments where batteries cannot sustain the conditions (temperature, humidity...). When the power supplied by the energy harvesting device is not sufficient to substitute the normal battery, energy scavengers can instead be employed as assistance energy sources to increase the lifetime of conventional batteries.

## 1.2 Energy harvesting process and technologies

The complete energy harvesting process can be resumed with the schematic blocks shown in Figure 1. 3:

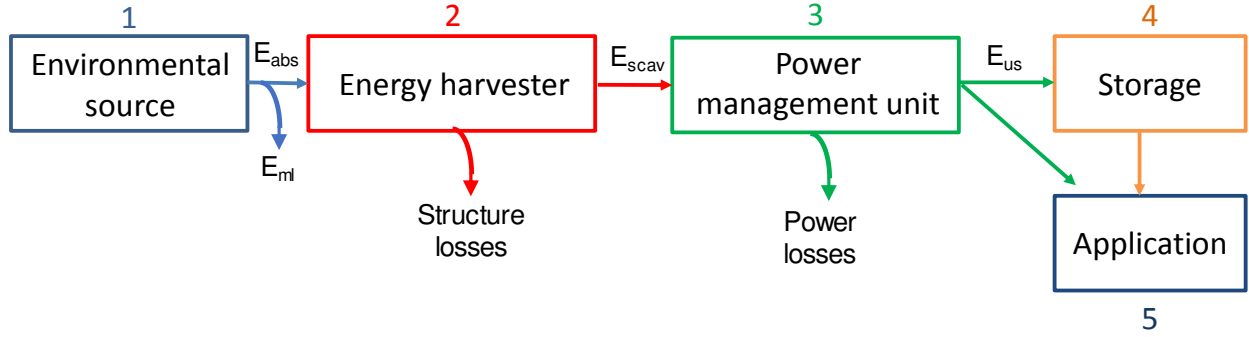


Figure 1. 3: Complete energy harvesting cycle schematic blocks

- **Environmental source** (block 1): energy can be captured from the environment ( $E_{abs}$ ) in a wide range of forms (light, heat or vibrations) and represents the input energy of the harvesting system, to be converted into electrical energy. Only a part of the available environmental energy is captured, depending on mechanical coupling between the structure and the environment.
- **Energy harvester** (block 2): it represents the core block of the system. This transducer, which can be realized through different technologies (see 1.3.1), allows energy conversion to the electric domain ( $E_{scav}$ ). Depending on the nature of the input source and to the characteristics of the scavenger, its output power can vary in terms of amplitude, frequency and phase.
- **Power management unit** (block 3): it is used to treat the output electrical signal of the scavenger to meet the requirement of the final application (see 4.4).
- The final useful energy ( $E_{us}$ ) can be either stored into a **storage** capacitor (block 4), either be used to directly supply the **final application** (block 5). This latter can be, for example, one of the devices presented in Figure 1. 1. Losses are present at each level of this energy conversion cycle, leading to global efficiency of the scavengers from few percentages to tens of percentage, depending on the technology used.

One of the most mature and developed technology employed for energy transduction (block 2) consists in the photovoltaic cells, which convert ambient light into electrical

energy. Thermal generators are instead employed to produce electricity from a temperature gradient by exploiting the Seebeck effect. Nevertheless, when no light or temperature gradients are present in the environment, other energy sources need to be envisaged. Among them, mechanical energy sources represent one of the most promising sources, especially in the small-scale domain, due their ubiquity, high energy density and versatility. Various mechanical energy sources (vibration, pressure or strain) can be found in everyday environment, such as natural phenomena (wind, waves, seismic motion...), industrial machines and equipment, household appliances (fans, fridge...) and vehicles (cars, planes, trains...). In addition, human movements can be employed as high-amplitude/low-frequency kinetic energy harvesting source. The following chapter focuses on energy scavenging applications related to human motions, namely the application field of the devices proposed in this work.

### 1.3 Applications to human body

Harvesting energy from human body movements could be useful and necessary in wearable and embedded applications for the power supply of sensors measuring vital parameters such as heart rate, temperature or oxygen flow in the blood. These low-power consumption sensors are generally small-size and can be fixed on cloths, watches or bands. In [1.4], the author reports that a total power level of  $1\text{ }\mu\text{W}$  is a realistic value for body sensors nodes (*i.e.* temperature, blood oxygen or blood pressure monitoring systems) power supply, as these devices present data rates lower than  $32\text{ bits.min}^{-1}$ . A pulse oximeter with an average power consumption of  $62\text{ }\mu\text{W}$  was instead reported in [1.5], when measurements were performed every 15 seconds.

To produce an output level acceptable to replace or integrate batteries, the design of the energy scavengers needs to be realized with the aim of efficiently coupling the transduction system to the body movements, *i.e.* maximizing the energy extraction from its environment. Two possible solutions to extract energy may be employed: active and passive coupling [1.6]. In the first case, the user needs to do a specific task to obtain

the generator movement, while in case of passive powering of electronic devices, energy dissipated during natural movements is exploited for electrical energy generation (i.e. walking, breathing or heart-beats). These lost ambient energy sources on human body are characterized by low to medium amplitudes and by low frequencies (few Hz), while the acceleration values significantly vary according to the different locations. Indeed, while walking at 5 km.h<sup>-1</sup>, peak acceleration levels of 100 m.s<sup>-2</sup> can be reached at ankle level with a frequency of 1.2 Hz, while the acceleration in the vertical direction is equal to 20 m.s<sup>-2</sup>. When considering other location on the body, the frequency remains constant but the acceleration levels on the vertical axis are close to 7 m.s<sup>-2</sup> [1.7].

The major **body motions** during walking were analyzed in [1.8], in order to evaluate the force and the torque generated through the relative displacement of human segments. Results are shown in Table 1. 1.

	Work [J]	Power [W]	Max torque [Nm]	Negative work	
				[%]	[J]
<b>Heel strike</b>	1-10	2-20	-	50	1-5
<b>Ankle</b>	33.4	66.8	180	28.3	19
<b>Knee</b>	18.2	36.4	40	92	33.5
<b>Hip</b>	18.96	38	40-80	19	7.2
<b>Elbow</b>	1.07	2.1	1-2	37	0.8
<b>Shoulder</b>	1.1	2.2	1-2	61	1.3

Table 1. 1: Summary of total work (with negative work percentage) and maximal torque done by the muscles at each joint or body segment during each step of the walking cycle and power exerted by three male subjects of average weight 82 kg and average height 1.80 m walking at a natural speed of 1 Hz (i.e. two steps) [1.8], [1.9]

The designed passive energy harvesting device should obviously be able to withstand the above reported maximal torques. The mechanical energy necessary to induce the scavenger movement (namely the absorbed energy) should be lower than the work produced by normal tasks (reported as “work” in Table 1.1), in order not to require additional effort by the user. From the above reported study, the higher mechanical

work generated while walking is at ankle (33.4 J), hip (18.96 J) and knee levels (18.2 J).

**Human breath** can instead be employed in an energy harvesting system either by exploiting the air flow emitted during breathing [1.10], either by employing the chest movement (using a tight band around the chest) [1.11], [1.12]. In this last case, considering a respiration rate of 10 breaths/minute and an overestimated force applied of 100 N over a maximal 0.05 m distance, the total mechanical power that can be exerted is equal to 0.83 W [1.13].

Finally, **blood pressure** can also be considered as a potential source for harvesting energy for wearable devices [1.14], [1.15]. In this case, the maximal mechanical power available is equals to 0.93 W when considering a resting heart rate of 60 beats per minute, and a heart stroke volume of 70 ml passing through the aorta per beat [1.13]. One can note that, among the three highlighted solutions, movements induced by walking seem to be the most attractive source for energy harvesting applications as it presents the highest input mechanical energy and as passive solutions can be designed (Figure 1. 4). Scavenging a mean power of 100  $\mu$ W to supply an embedded device from ankle, knee or tip movements (available energy >35 W) appears a reasonable and achievable goal.

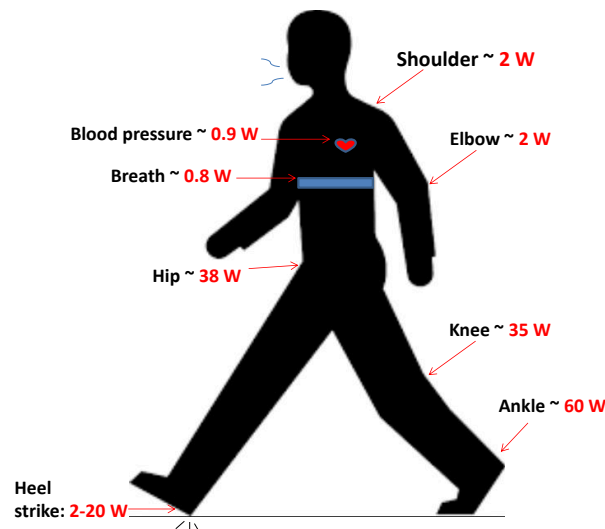


Figure 1. 4: Total available power from human-body everyday activities

### 1.3.1 Energy harvesting strategies for wearable devices

In human kinetic energy harvesting, a dedicated mechanical extraction mechanism is necessary to efficiently harvest the irregular and occasional movements made by the user, as underlined in the previous section. The second stage of a harvesting device is then composed by the transduction mechanism that must convert the input extracted mechanical energy into electricity. Among the different available technologies, electromagnetic, piezoelectric and electrostatic are the most employed technologies to convert mechanical energy from motion. A brief description and comparison of the different technologies will be provided in the following paragraphs.

#### 1.3.1.1 Electromagnetic scavengers

Electromagnetic converters are based on the electromagnetic induction phenomenon, namely the generation of a voltage (electromagnetic force) across a conductive material when it is exposed to a variable magnetic field. The technique is usually realized, according to Faraday's law, through the relative motion between a coil and a permanent magnet. The schematic of a simple architecture of a vibration-based electromagnetic system is shown in Figure 1. 5.

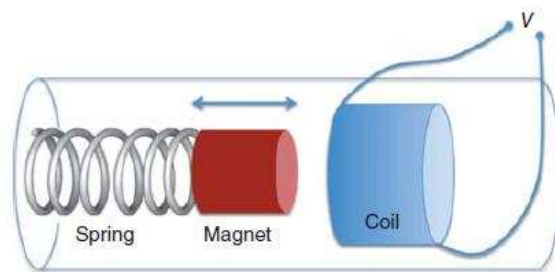


Figure 1. 5: Basic architecture of a vibration-based electromagnetic energy harvester [1.16]

These systems are usually employed for low frequencies (2-20 Hz), low impedance and medium size devices [1.16].



### 1.3.1.2 Piezoelectric scavengers

The direct piezoelectric effect was discovered in 1880 by Jacques and Pierre Curie and denotes the capability of a material of generating electric charge in response to an applied mechanical stress. Piezoelectricity appears from the internal crystalline structure level: the mechanical stress induces in fact an internal dipole moment in the material, which in turn produces electrical charge across its surfaces. Piezoelectric materials include single crystal (e.g. quartz), piezoceramic (e.g. lead zirconate titanate PZT), polymeric materials (e.g. polyvinylidene fluoride PVDF) and composite materials (e.g. macro fiber composite MFC). Various structures can be designed to exploit piezoelectric effect including beam, cantilever, stack or more complicated one. Piezoelectric devices are high impedance, high voltage, and compact size devices and can present high power density level.

### 1.3.1.3 Electrostatic scavengers

Electrostatic converters are based on the principle of variable capacitance coupled with a supply source.

Based on the classification proposed by Gilbert *et al.* in [1.17], we propose a division of these converters into two main categories: those involving vibrations (vibration energy harvesting: VEH) and those aiming harvesting intermittent movements (i.e. walking movements). In the first category, the capacitance variation is usually obtained by attaching one electrode of a capacitor to an oscillating mass, the second one remaining fixed. The capacitance change can be obtained either by varying the distance between the two capacitor plates, either by changing the overlap between the two plates.

Among the scavengers harvesting intermittent and slow movements, dielectric elastomers generators (DEGs) can be considered one of the most promising technologies. These converters are made of a thin elastomeric dielectric film sandwiched between two compliant electrodes, whose capacitance variation is obtained by the mechanical stretch of the membrane.

The most relevant drawback of the electrostatic harvester is represented by the necessity for an external voltage source for capacitance charging. This problem can be addressed by using electrets materials, i.e. dielectrics with a permanent electric charge or dipole polarization, to provide the bias voltage.

### 1.3.1.4 Technologies comparison

A comprehensive comparison between the harvested energy densities of the different technologies is desirable but difficult to achieve, due to the different possible operation modes of the scavengers (vibration based, strain based...). General characteristics of scavenged energy density can therefore be underlined. The principal advantages and drawbacks of the different technologies are reported in Table 1. 2.

Energy harvesting technology	Advantages	Drawbacks	Scavenged energy density trends
<b>Electromagnetic</b>	<ul style="list-style-type: none"> <li>-No need of external polarization</li> <li>-High currents output</li> <li>-Robust design</li> </ul>	<ul style="list-style-type: none"> <li>-Low output voltages</li> <li>-Difficult to integrate with MEMS fabrication processes</li> <li>-Poor performance in micro-scale</li> </ul>	<ul style="list-style-type: none"> <li>-High on a microscopic level</li> <li>-Decreases with volume [1.18]</li> </ul>
<b>Piezoelectric</b>	<ul style="list-style-type: none"> <li>-Simple structure</li> <li>-No need of external polarization</li> <li>-MEMS compatibility</li> <li>-High output voltages</li> </ul>	<ul style="list-style-type: none"> <li>-High output impedance</li> <li>-Brittleness in PZT</li> <li>-Poor coupling in PVDF</li> <li>-Low output currents</li> </ul>	<ul style="list-style-type: none"> <li>-High at macroscopic level</li> <li>-Decreases at microscopic level [1.18]</li> </ul>
<b>Electrostatics</b>	<ul style="list-style-type: none"> <li>-High output voltages</li> <li>-Easy to integrate with MEMS (VEH)</li> <li>-High power densities (DEGs)</li> <li>-High strains (DEGs)</li> </ul>	<ul style="list-style-type: none"> <li>-Need of an external polarization source for electret-free converters</li> <li>-Low output currents</li> <li>-High output impedance</li> </ul>	<p>VEH: -Low at macroscopic level</p> <p>-Increases as volume decreases</p> <p>DEG: -High energy densities for small and large-scale devices</p>

Table 1. 2: Schematic comparison between the main energy harvesting technologies

Electromagnetic and piezoelectric technologies offer the advantage over the other principles of not requiring an external voltage for energy conversion and present a high harvested energy (up to  $100 \text{ mJ.cm}^{-3}$ ). Electromagnetic scavengers show complementary behavior in terms of output signal, impedance matching and optimal load in relation to piezoelectric techniques. On the other hand, the integration of electromagnetic harvesters into MEMS or wearable applications results more difficult due to the use of coil elements.

The main advantages of piezoelectric materials in energy harvesting are their large power densities and ease of application. Piezoelectric systems are good candidates for small-scale vibration harvesters; although, they present low coupling strength at micrometric scale and they require large load impedances to reach the optimal working point [1.2].

Electrostatic VEHs present instead the highest potential for integration with microelectronics and their energy density increases with size reduction.

For low-frequency applications, such as those related to wearable sensors, polymer-based devices (i.e. DEGs) constitute a valid alternative because of their high energy density (up to  $1 \text{ J.cm}^{-3}$ ), inexpensiveness, compliance and high strains (up to 400%) [1.19].

The technology choice should thus be done based on the desired location of the scavenger and the input mechanical available source. When relative displacement induced by vibrations, impact or force is the mechanical source, either electromagnetic or electrostatic transduction can be used. Velocity is more typically associated with electromagnetic transduction as a magnetic flux variation is needed. The strain or stress, resulting in a deformation within the mechanical system, typically employs active materials (i.e. piezoelectric or dielectric materials). A comparison between these last two categories was performed in [1.20], where one of most widely employed piezoelectric polymer PVDF and classic dielectric elastomers materials (silicone and acrylics) were reviewed. Their results are summarized in Table 1. 3.

	Piezopolymers	Dielectric elastomers (DE)	
	PVDF	Silicone	Acrylic
<b>Density [g.cm<sup>-3</sup>]</b>	1.7 - 2.1	1	1
<b>Young's modulus [GPa]</b>	2.5 - 3.2	1×10 <sup>-3</sup>	2×10 <sup>-3</sup>
<b>Maximum stress [MPa]</b>	5	3	7.2
<b>Maximum strain [%]</b>	0.1	100	400
<b>Maximum energy scavenging density [J.cm<sup>-3</sup>]</b>	0.06	1.63	4.1

Table 1. 3: Comparison between the main technologies for strain energy harvesting

As shown in Table 1. 3, acrylic DE results in the better performance in term of maximum scavenged energy density, obtained under high deformation conditions.

## 1.4 Location and technology choice

The goal of this PhD work is to develop energy harvesting devices to extract the human kinetic energy while walking and convert it into electricity to supply low-power consumption systems. A mean output power of 100  $\mu$ W is the target as it is classically required for embedded sensor node (paragraph 1.1). Regarding the mechanical input source available on human body (paragraph 1.3), our system will be integrated at knee level to exploit the relative movement between the upper and lower part of the limb, namely a variation of angle. Indeed, the mechanical energy available at knee level is high enough to design a passive structure able to harvest a small amount of energy without requiring additional efforts from the user. Moreover, as most of the embedded sensor are located in the upper part of the human body (chest...), this location is closer to the final application than ankle location avoiding the need of long wires between the scavenger and the sensor node. Hip could also be a logical location to scavenge human kinetic energy. Nevertheless, the scavenger should exploit low frequency vibrations and thus using classic rigid technologies such as electromagnetic one, leading to high encumbrance and possibility to disturb the user during normal activities. For these reasons, knee level was selected. As reported in [1.21], the angle variation at kneecap

level is between  $5^\circ$  and  $60^\circ$  while walking ( $\theta_w$ ) and between  $5^\circ$  and  $120^\circ$  while running ( $\theta_r$ ), as shown in Figure 1. 6.

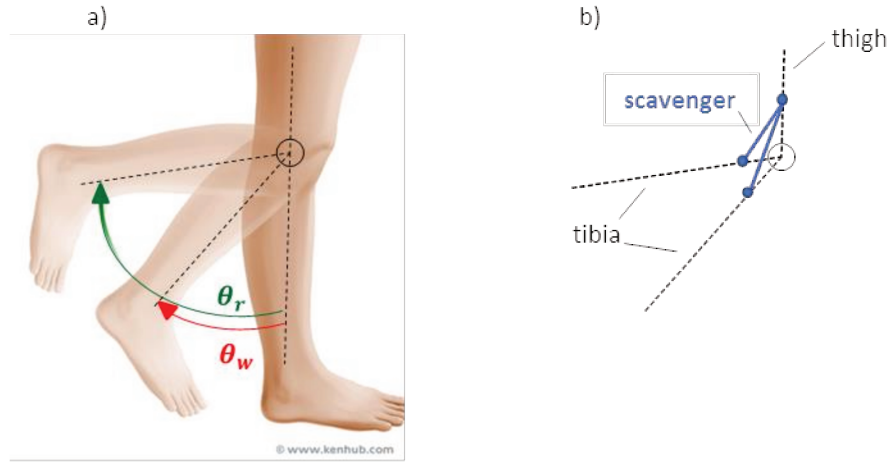


Figure 1. 6: Relative movement imposed by knee displacement while walking/running (a) and possible insertion point of the scavenger behind the knee

A harvester can easily be integrated behind the knee straddling the two segments of the leg (Figure 1.6b). As it, the variation of the angle can be converted in a strain whose value depends on the two insertion points of the scavenger on the limb and on the scavenger length. Based on the results obtained on [1.21] and in order to avoid any excessive additional mechanical work for the user, the scavenger device will be subjected to a maximal uni-axial deformation of 50% of its initial length.

Considering the resulting strain induced by the leg movement, the normal walking/running frequencies (1-3 Hz) and the maximal encumbrance of the system ( $10 \times 5 \text{ cm}^2$  surface area, low thickness), electrostatic converters based on DEs were selected as energy harvesting technology in this work. Indeed, compared to piezoelectric material, DEs can sustain high level of deformations, develop a high energy density (paragraph 1.3.1.4) and are very soft materials, which are advantageous for embedded scavengers (lower additional mass, perfectly compliant, no disturbance for the user).

## 1.5 Objectives and organization of the work

The main objective of this work is to design soft electrostatic generators based on dielectric elastomers to supply wearable devices. As the main drawback of DEs technology consists in the external voltage supply, hybrid structures guaranteeing the replacement of external voltage need to be conceived. To do so, two different hybrid solutions will be proposed:

- In the first one (whose basic schematic is represented in Figure 1. 7), dielectric elastomers are coupled with electret materials to improve the performance of an electret-based electrostatic generator. This work, based on the technology developed by our research group [1.22] in 2013, aims designing an optimized prototype in term of output energy, decreasing the encumbrance and increasing the lifetime of the device.

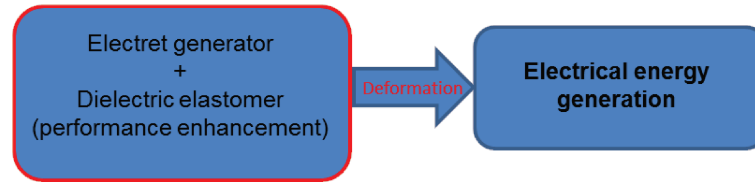


Figure 1. 7: Blocks schematic of the electret-based working mode of the electrostatic device

- In the second working mode, the dielectric elastomer membrane plays the active role of an electrostatic transducer (DEG transducer) and is coupled with different active materials (electret or piezoelectric material) with the aim of eliminating the need of an external voltage source. The basic blocks schematic of this operating principle is shown in Figure 1. 8.

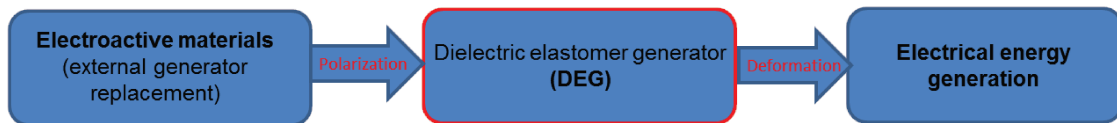


Figure 1. 8: DEG-based schematic of the working principle

Focusing on our objectives, the following challenges have been faced:

- Investigation studies on electrets materials employed as polarization sources for electrostatic energy harvesting devices. In order to find a conformant electret material with high stability, experimental studies on polymeric electret materials were performed. Specifically, poly(p-xylylene) polymers (known with the generic name of Parylene), were studied as electret materials for our applications and compared to results obtained from conventional electrets. As we aim developing wearable scavengers, used in different temperature and relative humidity environmental conditions, these parameters were also considered to evaluate their influence on the electret material performance.
- Concerning the first working mode (Figure 1. 7), the main goal consisted in the optimization of the devices (shape, size, material used...) to maximize the energy extraction and energy conversion. Based on the analytical modelling of the system and the results of Finite Element Method (FEM) simulation, a centimeter scale prototype was realized and tested. Possible solutions for the power management circuit were also investigated in order to consider the full energy harvesting cycle.
- Concerning the second working mode based on DEG devices (Figure 1. 8), possible polarization solutions based on active materials were investigated. As explained in paragraph 1.4, these types of generators were selected as energy harvesting technologies due to their high scavenged energy density. In order to eliminate the external polarization source, these DEGs were coupled with two active materials: electrets and piezoelectric. For this latter, two different devices were designed: one based on PZT ceramics and one based on a piezoelectric polymers (PVDF).

In the second chapter, the state-of-the art on piezoelectric and electrostatic scavengers will be presented. This chapter will describe the working principle, the equations governing these technologies, the performance and working conditions generally

employed for these systems. Examples from the literature will be developed with applications focusing on human body energy scavenging. From this overview, the technology choice made in this work will be underlined.

The third chapter is dedicated to the characterization of different Parylene variants as electret materials for energy harvesting applications. We will present the physical principle of electret materials and the experimental techniques employed in this work for electret characterization. Then, results obtained on the suitability of different Parylene species for our applications will be presented for various testing and environmental conditions.

In the fourth chapter, the first scavenger design (Figure 1.7) will be presented, mainly focusing on issues about design optimization, materials influence on device performance and size reduction. Results obtained on the experimental realization of an operational prototype will be presented and issues about the power management circuit will be considered.

The last chapter will present the second scavenger working mode (Figure 1.8), employing dielectric elastomers as active transducers for energy generation. The two polarization solutions coupling dielectric elastomers generators with active materials (electret and piezoelectric) will be presented, focusing on the device experimental realization and performance. The results obtained on three operational prototypes will be presented, and possible improvements on their performance will be discussed at the end of the chapter, opening new perspectives for future works.

A global balance will finally close this thesis, where the most relevant points of this project will be summarized. Outlooks for future development works will be proposed, aiming to better develop the new technology based on hybrid devices and to realize a final complete structure embeddable on human body





**CHAPTER 2.**

**STATE-OF-THE-ART:  
PIEZOELECTRIC AND  
ELECTROSTATIC  
TECHNOLOGIES**



## **Chapter 2. STATE-OF-THE-ART: PIEZOELECTRIC AND ELECTROSTATIC TECHNOLOGIES**

The objective of this chapter is to review the two technologies employed in this work for energy harvesting devices conception and development, namely the piezoelectric and the electrostatic ones. First, the basic principles of the two techniques will be described together with the equations helping the reader to understand the working mode of these technologies. The materials employed for devices fabrication will be reviewed, together with their principal characteristics. Then, the state-of-the-art relative to wearable devices will be presented, to give an overview on the maximum amount of energy that can be harvested by these devices in different configurations. In the last paragraph, the employment of electret materials as polarization source will be introduced.

### **2.1 Piezoelectric technology**

Piezoelectricity originates in materials presenting high asymmetry in the dielectric crystal, which leads to a non-coincidence between the positive and negative charges barycenter. At rest, the system is at the electrical equilibrium but, when a mechanical solicitation is applied, the charges barycenter is shifted. As a consequence, an electrical dipole is formed in the unit cell of the crystal. The summation of the individual dipoles results in a polarization which induces an electric potential across opposite electrode faces (direct piezoelectric effect). Conversely, the application of an electric field through the material induces a modification in the mechanical structure due to a change between the charges barycenter (converse piezoelectric effect). The piezoelectric effect is represented in Figure 2. 1.

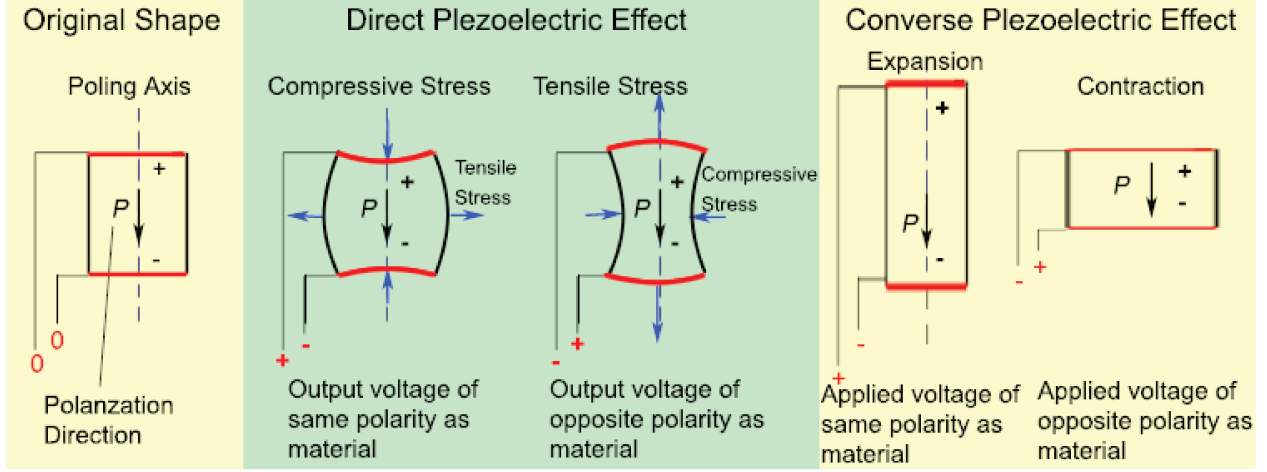


Figure 2. 1: Direct and converse piezoelectric effects representation [2.1]

For practical applications, the direct piezoelectric effect can be exploited to realize sensors or energy scavenging devices, while the converse piezoelectric effect is employed for the realization of actuators.

### 2.1.1 Basic principles and equations

The constitutive equations for a piezoelectric material are given by [2.2]:

$$\begin{cases} \underline{D} = \underline{d} \cdot \underline{T} + \underline{\varepsilon}^T \cdot \underline{E} \\ \underline{S} = \underline{s}^E \cdot \underline{T} + \underline{d}^t \cdot \underline{E} \end{cases} \quad (2.1)$$

where  $\underline{S}$ ,  $\underline{T}$  and  $\underline{D}$  respectively represent the mechanical strain, the mechanical stress and the electrical displacement (charge density).  $\underline{E}$  indicates the electric field, while  $\underline{s}^E$  and  $\underline{\varepsilon}^T$  respectively stand as the compliance under zero or constant electrical field (namely the index E) and the dielectric permittivity under zero or constant stress (specified by the superscript T).  $\underline{d}$  describes the piezoelectric constant, where the superscript t means the transposed matrix. The first equation provides a linear relation between the generated electrical charges and the applied mechanical stress (direct piezoelectric effect), while the second describes the linear relation between the applied electric field and the resulting mechanical strain (converse piezoelectric effect).

Piezoelectric materials are anisotropic, which means that their behavior depends on the direction of the strain and on the polarization orientation. It is thus necessary to define tensors to describe the piezoelectric material properties (i.e. compliance and permittivity matrix). These quantities are defined through a crystal coordinate system, denoted through 123 axes (Figure 2. 2).

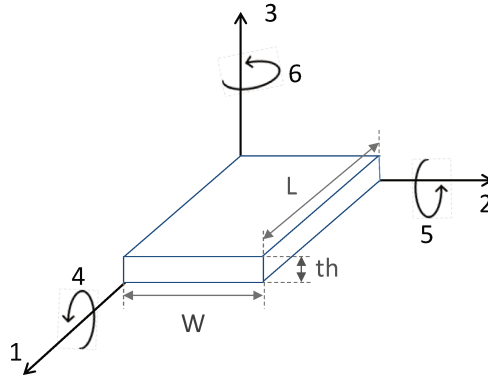


Figure 2. 2: Piezoelectric material mechanical axis position

The axis 1, 2 and 3 are used for translations, while 4, 5 and 6 are referred to rotations. The quantities introduced in the system of equations (2.1) can be expressed as following:  $\underline{E}$  and  $\underline{D}$  through a 3-components vector,  $\underline{T}$  and  $\underline{S}$  through 6-components tensors. The piezoelectric coefficients  $\underline{d}$  are expressed through a 6x3 tensor, the dielectric permittivity  $\underline{\epsilon}$  through a 3x3 tensor and the compliance matrix through a 6x6 tensor.

As explained, the absence of a center of symmetry is a necessary condition for the material to exhibit a piezoelectric effect. Although the symmetry does not directly define the value of the piezoelectric coefficients, considerations about symmetry are important to define the number of piezoelectric coefficients. The piezoelectric tensor, in fact, has a maximum number of 18 independent components. This number, although, can be drastically reduced if certain symmetries exist in the crystal structure or microstructure [2.3]. For the PZT ceramic, as example, due to the hexagonal crystal symmetry, the compliance matrix, the piezoelectric coefficient and the permittivity matrix can be respectively written as [2.2]:

$$\underline{s}^E = \begin{bmatrix} s_{11}^E & s_{12}^E & s_{13}^E & 0 & 0 & 0 \\ s_{12}^E & s_{11}^E & s_{13}^E & 0 & 0 & 0 \\ s_{13}^E & s_{13}^E & s_{33}^E & 0 & 0 & 0 \\ 0 & 0 & 0 & s_{44}^E & 0 & 0 \\ 0 & 0 & 0 & 0 & s_{44}^E & 0 \\ 0 & 0 & 0 & 0 & 0 & 2(s_{11}^E - s_{12}^E) \end{bmatrix} \quad (2.2)$$

$$\underline{d} = \begin{bmatrix} 0 & 0 & 0 & 0 & d_{15} & 0 \\ 0 & 0 & 0 & d_{15} & 0 & 0 \\ d_{31} & d_{31} & d_{33} & 0 & 0 & 0 \end{bmatrix} \quad (2.3)$$

$$\underline{\varepsilon}^T = \begin{bmatrix} \varepsilon_{11}^T & 0 & 0 \\ 0 & \varepsilon_{11}^T & 0 \\ 0 & 0 & \varepsilon_{33}^T \end{bmatrix} \quad (2.4)$$

It can be noticed that only three independent elements are present within the piezoelectric tensor  $\underline{d}$ . Following the reference system of Figure 2. 2, one can note that the coefficient  $d_{15}$  is related to shear stress. As this latter is not practical for energy harvesting applications, in the next paragraph the two working modes generally employed for energy scavengers will be described, namely the longitudinal (33) and translational (31) modes.

### 2.1.2 Working modes

The two working modes employed for piezoelectric energy harvesters are normally the 33 and the 31 modes. For both modes, the voltage is generated along the 3-direction, while the applied stress is respectively along the 3-direction and 1-direction, as shown in Figure 2. 3 [2.4].

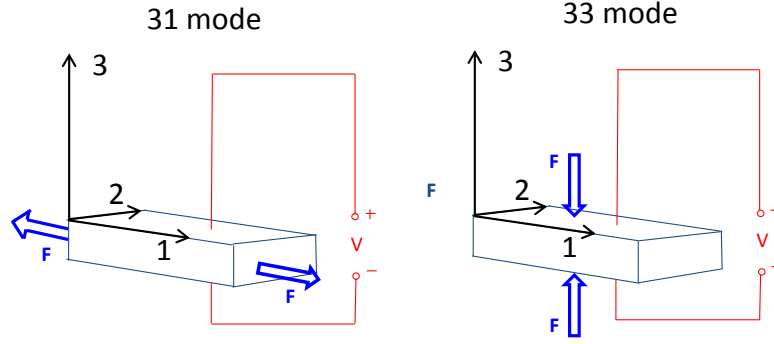


Figure 2. 3: Piezoelectric generators working modes: 31 mode and 33 mode

When the piezoelectric material is operated in 31 mode, the constitutive equation describing the direct piezoelectric effect can be simplified to:

$$\underline{D}_3 = \underline{d}_{31} \cdot \underline{T}_1 + \underline{\varepsilon}_{33}^T \cdot \underline{E}_3 \quad (2.5)$$

Instead, for the 33 mode, the stress acts in the same direction as the voltage appears and the above equation becomes:

$$\underline{D}_3 = \underline{d}_{33} \cdot \underline{T}_3 + \underline{\varepsilon}_{33}^T \cdot \underline{E}_3 \quad (2.6)$$

For each solicitation mode, the energy converted from the mechanical to the electrical domain can be derived through an electromechanical coupling coefficient  $k_{ij}$ , defined through the following equation [2.4] :

$$k^2 = \frac{\text{electric energy output}}{\text{mechanical energy input}} \quad (2.7)$$

This coefficient relates the converted energy to the total available energy to evaluate the electromechanical efficiency of the system.

Referring to the two previously described working mode, this coefficient respectively becomes:



$$k_{31} = \frac{d_{31}}{\sqrt{\varepsilon_{33}^T s_{11}^E}} \quad (2.8)$$

$$k_{33} = \frac{d_{33}}{\sqrt{\varepsilon_{33}^T s_{33}^E}} \quad (2.9)$$

The higher the coupling coefficient  $k$ , the more mechanical energy is scavenged. When operating in 33 mode, the coupling coefficient is generally higher. Nevertheless, obtaining high deformation is easier for 31 configurations compared to the 33 ones [2.5].

### 2.1.3 Piezoelectric materials

Piezoelectric materials can be divided into natural and synthetics [2.6]. Quartz ( $\text{SiO}_2$ ) is the most employed natural single crystal piezoelectric material. Due to the high precision of its oscillation frequencies, this material is often employed as resonator in digital watches. Among the man-made piezoelectric materials, it can be included ceramics, polymeric materials and composites. Most of ceramics presents a crystal structure as perovskite, which basic structure is shown in Figure 2. 4.

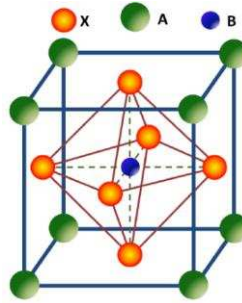


Figure 2. 4: Schematic of a perovskite crystal [2.7]

A perovskite consists in a face-centered cubic structure with cations in the corners of the cube and anions in its center. Among them, the most well-known ceramics are Barium titanate ( $\text{BaTiO}_3$ ) and Lead zirconate titanate ( $\text{Pb}[\text{Zr}(\text{x})\text{Ti}(1-\text{x})]\text{O}_3$ ), most

commonly known as PZT. Among the polymeric materials, the most performant is polyvinylidene fluoride (PVDF), which piezoelectricity was discovered by Kawai [2.8]. This polymer presents the largest piezoelectric coefficient compared to other bulk polymers [2.9], and can thus be found in the majority of soft applications. Table 2. 1 compares the performance of these two materials:

	<b>PZT</b>	<b>PVDF</b>
<b>Strain coefficient <math>d_{31}</math> [<math>10^{-12}</math> m/v]</b>	320	20
<b>Strain coefficient <math>d_{33}</math> [<math>10^{-12}</math> m/v]</b>	650	30
<b>Coupling coefficient <math>k_{31}</math> [CV/Nm]</b>	0.44	0.11
<b>Coupling coefficient <math>k_{33}</math> [CV/Nm]</b>	0.75	0.16
<b>Dielectric constant <math>\epsilon_r</math></b>	3800	12
<b>Elastic modulus [<math>10^9</math> N/m<sup>2</sup>]</b>	50	3
<b>Tensile strength [<math>10^7</math> N/m<sup>2</sup>]</b>	2	5.2

Table 2. 1: Comparison of two piezoelectric materials used in this work [2.10]

As shown in Table 2. 1, ceramic materials strain coefficients and electromechanical coefficients are significantly higher than PVDF, resulting in higher output voltages. Nevertheless, due to their high stiffness and brittles, PVDF materials are preferred for compliant and low mechanical impedance applications.

Piezocomposite materials can be considered an update of the existing piezoceramic. As described in [2.11], they can be divided in two categories: piezo-polymer with the piezoelectric material immersed in an electrically passive matrix (i.e. PZT in epoxy matrix) and piezo-composites, namely composite materials constituted by two different ceramics (i.e. BaTiO<sub>3</sub> fibers reinforcing a PZT matrix). These two categories can be a compromise between the piezoelectric properties of PZT and mechanical properties of polymers, but their cost is higher. In this work, PZT and PVDF piezoelectric materials

will thus be employed as polarization source for our hybrid structure working in DEG mode.

### 2.1.4 Possible configurations

A thin-layer geometry shape is often employed in most of piezoelectric energy harvesters both for reducing the total encumbrance of the structure and for obtaining a fast response to mechanical solicitations. The most common piezoelectric structures, as reported in [2.12], are:

#### - Cantilever beams:

Piezoelectric cantilever beams adopt the direct piezoelectric effect of 31-mode to convert mechanical energy into electrical energy.

The simplest design consists in the ‘unimorph configuration’ (Figure 2. 5a), namely a clamped-free beam which is made of one piezoelectric layer bonded with a non-active material (usually a metallic surface to conduce the generated charges). When the external mechanical excitation frequency equals the self-frequency of the piezoelectric cantilever beam (first flexural mode), the structure resonates, and the maximal output voltage is reached. The main advantage of this configuration consists in the generation of high mechanical strains within the piezoelectric material near the clamped end. To further improve the device output, alternative configurations may be adopted, i.e. the ‘bimorph’ structure (Figure 2. 5b), which consists of two piezoelectric layers bonded to a central metallic one. Finally, to reduce the structure resonance frequency of the structure, proofs mass may be added at the free side of the cantilever, as shown in Figure 2. 5c.

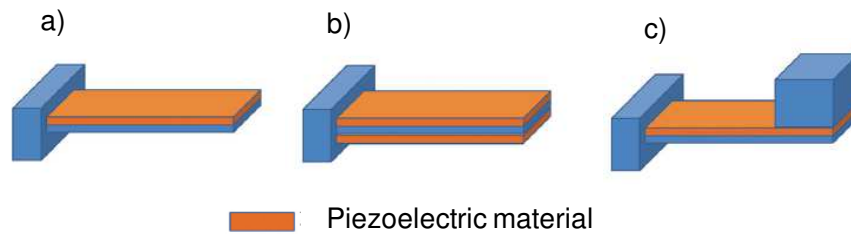


Figure 2. 5: Different configurations for piezoelectric cantilevers structures: unimorph (a), bimorph (b) and unimorph with proof mass at the free end (c) [2.12]

### -Cymbal:

Cymbal transducers are normally employed for applications with high impact forces. The structure is made of a piezoelectric ceramic disc and two end caps at each sides of the structure, as shown in Figure 2. 6.

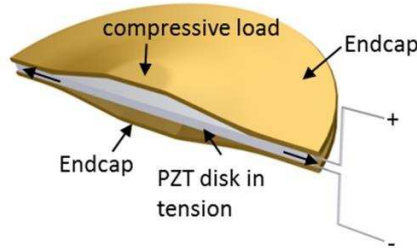


Figure 2. 6: Cymbal structure representation [2.13]

When an axial stress is applied to the cymbal transducer, the steel end caps convert and amplify the axial stress to radial stress in the PZT disc, resulting in a combination of both the  $d_{33}$  and the  $d_{31}$  piezoelectric coefficients. This transducer allows scavenging higher energy outputs compared to the cantilevers: the cymbal structure in fact guarantees the solicitation of a larger amount of piezoelectric material compared to the cantilevers, where the stress is concentrated near the clamp end and decreases at locations close to the free end. Anyway, these structures are not suitable for low magnitude vibrations (i.e. human body and ambient environmental vibrations) and are more adapted for high amplitude stresses, necessary to produce a significant deformation on the PZT.

### -Circular diaphragms

This configuration, similarly to the cantilevers, works under 31 operation mode. The structure includes a circular piezoelectric ceramic disc bonded to a metal layer (Figure 2. 7). The higher output power is achieved under clamped boundary conditions [2.14]. Further improvement on the low-frequencies device performance may be obtained by inducing a pre-stress in the piezoelectric material, which can be done either in the fabrication stage of the piezoelectric-metal composite, either by adding proof masses to the structure.

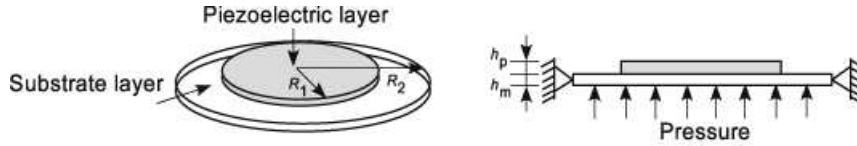


Figure 2. 7: Circular diaphragm configuration [2.15]

### -Other configurations

Depending on the input source harvested by the device, different configurations have been designed to increase the electromechanical coupling. Figure 2. 8a shows a flag design proposed in [2.16] and employed with flexible piezoelectric material to harvest flow motions. In Figure 2. 8b a ring-MEMS (RMEMS) structure is shown [2.17], aiming to achieve low resonance frequencies in a small encumbering structure.

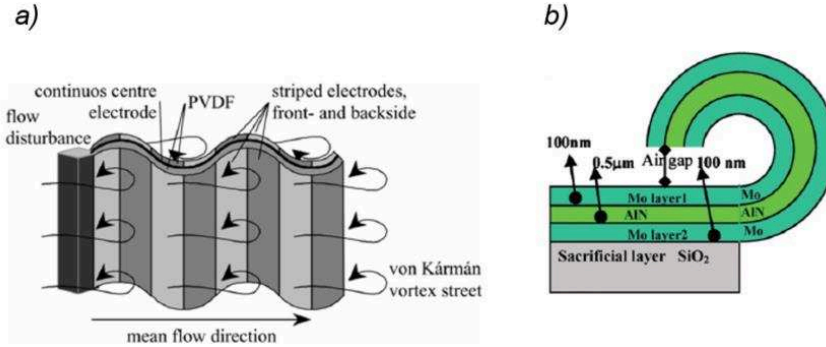


Figure 2. 8: Other configuration employed in the literature for piezoelectric energy harvesters [2.12]

Other solutions may be adopted to improve the performance of the energy harvester, i.e. stack structures, frequency-tuning techniques (spring-mass systems, stoppers or auxiliary beams) or modification of the piezoelectric materials properties and electrodes configuration.

In the next paragraph, configurations mostly employed for wearable applications will be described through practical examples found in the literature.

## 2.1.5 Existing wearable devices

Several examples can be found in the literature for piezoelectric energy harvester integrated in the shoe: one of the earliest examples was proposed in [2.18], where a

cylindrical PZT stack was integrated with a hydraulic system to amplify the force on the piezoelectric material. The device was made of two cylindrical tubes in the insole, housing a PZT stack. Although the prototype was heavy and bulky, it could scavenge an average power between 250 and 700 mW (depending on the user's gait and weight). One of the first energy harvesting device from human walking made of PVDF was developed by Massachusetts Institute of Technology (MIT) researchers [2.19] to harvest the bending movement of the sole while walking using the  $d_{31}$  mode. The device (Figure 2. 9a) is made of a bimorph structure with two 8-layers stacks of 28- $\mu\text{m}$ -thick PVDF sheets. At a bending frequency of 0.9 Hz, an average output power of 1.3 mW was obtained on a resistive load of 250 k $\Omega$ .

The same researchers developed a PZT bimorph structure using two curved-shaped 5 cm  $\times$  5 cm  $\times$  15  $\mu\text{m}$  PZT strips (TH6R piezoelectric transducers) bounded to a steel strip [2.20]. The device, shown in Figure 2. 9b, was installed at the heel of a Navy work boot to harvest the parasitic energy of heel strike, harvesting up to 8.4 mW when connected to a resistive load of 500 k $\Omega$ .

More recently, a shoe-mounted piezoelectric vibration energy harvester (PVEHs) was presented in [2.21]. The device is made of a 2.5  $\mu\text{m}$ -thick PZT thin film with total dimensions of 11.75 mm  $\times$  15 mm and deposited on a 40  $\mu\text{m}$ -thick stainless steel. The cantilever device presents a seismic mass of 0.93 gr at the free end and can harvest a maximum output power of 20  $\mu\text{W}$ , on an optimal load resistance of 33.9 k $\Omega$ .

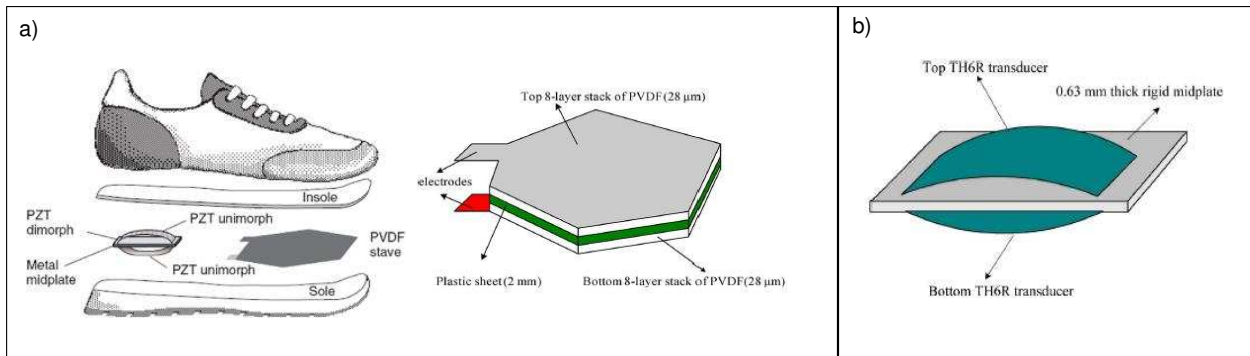


Figure 2. 9: Examples from the literature of shoe energy harvesting piezoelectric transducers [2.22]

Several examples of piezoelectric energy scavenging from human limbs can also be found in the literature. In [2.23], a flexible energy harvesting device to harvest energy from human motion was presented, through of a shell structure made of PVDF material (Figure 2. 10a). This device was tested by integrating ten shell structures in a band for wearing on the elbow joint and with four shell structures for wearing on the finger to harvest the bending motion given by human body. A maximal power output of 210  $\mu\text{W}$  was obtained on a resistive load of 90  $\text{k}\Omega$  for the structure integrated in the elbow, with a bending velocity of 0.8 Hz.

Other examples involving human kinetic energy scavenging include the linear impact-based generator proposed by Renaud *et al.* [2.24]. The device (shown in Figure 2. 10b) includes a 750-gr impact mass and two piezoelectric cantilevers at the two ends of the groove to harvest the impact energy. The device was predicted to harvest up to 40  $\mu\text{W}$  when positioned on a wrist of a walking person, with excitation of 1 Hz frequency and 0.1  $\text{m.s}^{-2}$  acceleration.

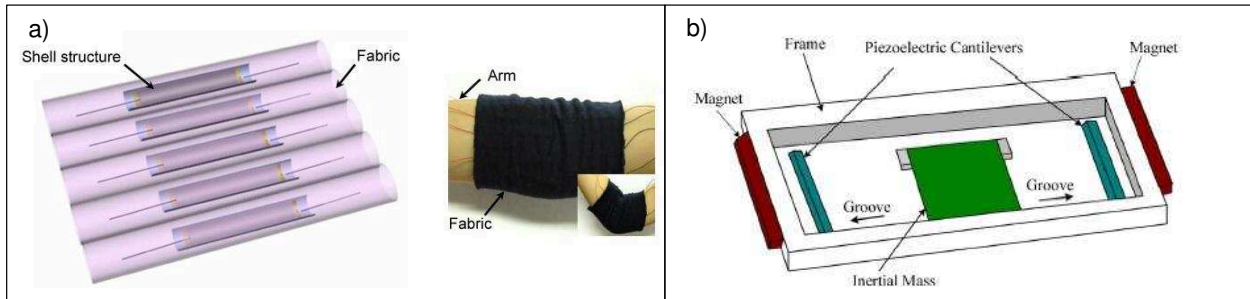


Figure 2. 10: Examples of piezoelectric human-limbs energy scavengers [2.22], [2.23]

Rotational devices were also employed to harvest human kinetic energy at knee level. Among these latter, the one proposed in [2.25] consists of a piezoelectric bimorph, whose solicitation is imposed by a plectrum standing in the inner part of the circular frame (Figure 2. 11a). When a rotation is imposed to the structure (between 0.1 and 1  $\text{rev.s}^{-1}$ ), the plectrum exerts a deflection movement on the piezoelectric material, allowing scavenging an energy output between 160 and 490  $\mu\text{J}$ , depending on the rotational speed. Further improvement of this design consisted in the substitution of

the mechanical plucking system with a magnetic one, allowing scavenging up to 0.7 mW per piezoelectric, when actuated by knee-joint motion at 0.9 Hz [2.26]. Size reduction challenge resulted in a of 5 cm<sup>3</sup> rotational device presented in [2.27], based on the frequency-up conversion strategy and made of a piezoelectric beam plucking through magnetic coupling with a rotating proof mass (Figure 2. 11b). Power outputs in the range of ten  $\mu$ W were obtained with frequencies between 0.5 and 4 Hz and with acceleration values between 1 to 20 m.s<sup>-2</sup>. A peak power of 43  $\mu$ W was obtained at 2 Hz and 20 m.s<sup>-2</sup> working conditions with the rotor going into continuous rotation.

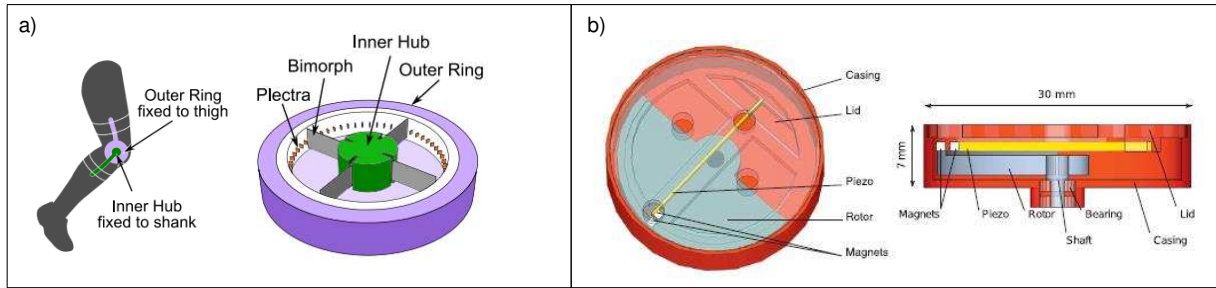


Figure 2. 11: Wearable rotational piezoelectric scavengers [2.25], [2.27]

Other devices were tested for energy harvesting from a backpack [2.28], from mouse-clicking [2.29] or heart beats [2.30].

On Table 2. 2 some of the previously described devices used for human kinetic energy harvesting are summarized.



Ref.	Location	Material	Piezo dimensions	Testing conditions	Scavenged power
[2.19]	Shoe	PVDF	37.5 cm <sup>3</sup>	0.9 Hz	1.3 mW @ 250 kΩ
[2.20]	Shoe	PZT	25 cm <sup>3</sup> (×2)	0.9 Hz	8.4 mW @ 500 kΩ
[2.21]	Shoe	PZT	1.4 cm <sup>3</sup>	24 Hz, 0.3 m.s <sup>-2</sup>	20 μW @ 33.9 kΩ
[2.23]	Elbow	PVDF	1.8 cm <sup>3</sup> (×10)	0.8 Hz	0.21 mW @ 90 kΩ
[2.24]	Wrist	PZT cantilever	2.5 cm <sup>3</sup>	1 Hz, 0.1 m.s <sup>-2</sup>	40 μW @ 300 kΩ
[2.26]	Knee	PZT bimorphs	0.18 cm <sup>3</sup> (×8)	0.9 Hz	5.8 mW @ 18 kΩ
[2.27]	Knee	PZT	0.012 cm <sup>3</sup>	2 Hz, 20m.s <sup>-2</sup>	43 μW @ 150 kΩ
[2.28]	Backpack	PZT	-	5 Hz	0.4 mW
[2.29]	Finger	PVDF	6 mm <sup>3</sup>	~2.5Hz	~2.5–25 nW
[2.30]	Heart	PZT	0.3 cm <sup>3</sup>	15 Hz	10 μW

Table 2. 2: Piezoelectric wearable scavengers' comparison

## 2.2 Electrostatic technology

Electrostatic scavengers are based on variable electrical capacitors, whose value is changed by the application of an external mechanical displacement. A simple design of parallel plate capacitor is shown in Figure 2. 12 and is made of two parallel conductive plates (the electrodes) separated by a certain gap. The capacitance value is determined by the area ( $A$ ) and distance between the electrodes ( $d$ ) and the dielectric permittivity ( $\epsilon_r$ ) of the material separating them, namely:

$$C = \epsilon_0 \epsilon_r \frac{A}{d} \quad (2.10)$$

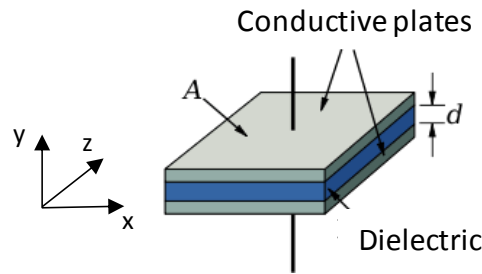


Figure 2. 12: Parallel-plates capacitor representation

where  $\varepsilon_0$  represents the vacuum permittivity.

While few electrostatic devices based on dielectric permittivity variation can be found in the literature [2.31], the majority of examples act on the variation of the capacitance geometrical parameters ( $A$  and  $d$ ).

When the capacitance ( $C$ ) is charged, a certain amount of charge is stored in the two plates ( $Q$ ), resulting in a voltage through the electrodes ( $V$ ). These quantities are related by the following relationship:

$$Q = CV \quad (2.11)$$

By considering the charges concentrated on the plates surfaces, the electrical stored energy can be written as [2.32]:

$$W = \frac{1}{2} \iint_{\text{plate surface}} V(s)\sigma(s)ds = \frac{1}{2} CV^2 \quad (2.12)$$

As previously described, electrostatic generators are based on a capacitance variation through an external mechanical force. As the two plates of the capacitor are oppositely charged, an electrostatic force acting on the plates will be present (Maxwell force). By considering an isolated capacitor, this electrostatic force along the  $y$  direction (Figure 2. 12) can be derived by equation (2.12):

$$F_e = -\frac{dW}{dy} = \frac{1}{2} V^2 \frac{dC}{dy} \quad (2.13)$$

During capacitance change, the energy transferred from the mechanical to the electrical domains is represented by the work of the electrostatic force. By supposing a linear variation of the capacitance [ $C_1$ - $C_2$ ] with time [ $t_1$ - $t_2$ ], the work produced by the force  $F_e$  on the transducer can be expressed as [2.32]:

$$W(t) = \int_{t_1}^{t_2} F_e v dt = \int_{t_1}^{t_2} \frac{1}{2} V^2 \frac{dC}{dy} \frac{dy}{dt} dt = \int_{C_1}^{C_2} \frac{1}{2} V^2 dC \quad (2.14)$$

where  $v$  represents the capacitance change velocity.

One can note from equation (2.14), that the work is positive for increasing capacitance values, while it is negative when the capacitance decreases. When the work is positive, the energy in the mechanical domain is increased with consequently decrease of the electrical energy. A negative work indicates instead an energy transfer from the mechanical to the electrical domain

Among the various possible operating modes, two main working modes are generally used for the device energetic cycle, namely charge-constrained or voltage-constrained.

The charge-constrained cycle employs a constant charge on the capacitance plates and is based on the voltage variation with changing capacitance. The capacitance plates are charged (up to  $V_{start}$ , named bias or polarization voltage) when the variable capacitance reaches its maximal value  $C_{max}$ . The application of an external mechanical force, acting against the electrostatic force between the electrodes, induces capacitance variation until its minimal value  $C_{min}$ . During this stage, the amount of charge in the system is kept constant, which consequently induces voltage increase across the capacitor plates (till the maximal value  $V_{max}$ ). The initial charge can either derive from a reservoir controlled by an electronic circuit, to which the initial charge flows back at the end of the cycle, either be given by a fixed charge source (i.e. electret materials), as better explained in paragraph 2.2.3. The energy gain ( $E$ ) in this working mode can be expressed as:

$$E = \frac{1}{2} (C_{max} - C_{min}) V_{max} V_{start} \quad (2.15)$$

The voltage-constrained cycle instead consists in the application of a constant voltage to the capacitance plates and in the consequent variation of the charge stored in the capacitance induced by capacitance variation. The energetic cycle begins when the equivalent capacitance is at its maximal value ( $C_{max}$ ). At this stage, the capacitor plates are charged through a reservoir up to a polarization voltage  $V_{max}$ . When, the capacitance decreases to its minimal value ( $C_{min}$ ) due to external mechanical excitation, the voltage is kept constant. Consequently, the excess charge on the

capacitor will flow back to the reservoir during the capacitance decrease phase, resulting in a net energy gain ( $E$ ) given by:

$$E = \frac{1}{2} (C_{max} - C_{min}) V_{max}^2 \quad (2.16)$$

The different phases of these two working modes can be represented through the Q-V diagrams, which outline a surface area representing the electrical energy generated during the process (Figure 2. 13).

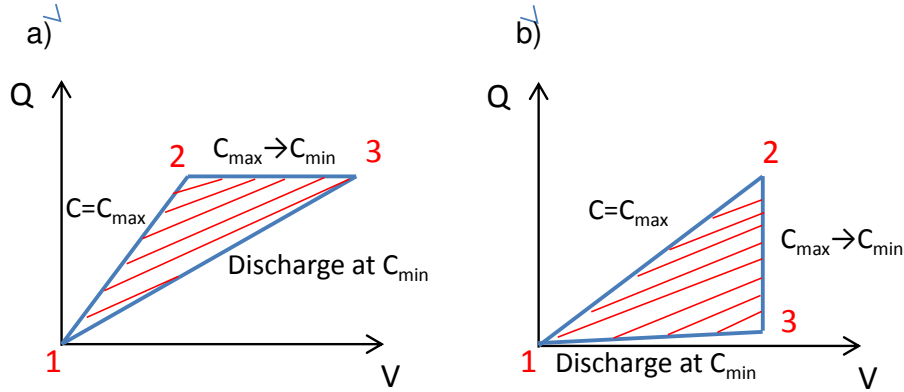


Figure 2. 13: Q-V diagrams for charge-constrained (a) and voltage-constrained (b) cycles in electrostatic scavengers

Capacitance variation can be achieved through electrostatic transducers designs either through vibration energy harvesters (VEH) either by the use of soft deformable dielectric materials (Dielectric Elastomers Generators: DEG), as described in the next paragraphs.

### 2.2.1 Vibrating Energy Harvesters (VEH)

These devices are normally made of two electrically isolated plates, whose position is changed by vibration excitations acting on the device.

Two kinds of displacement are normally imposed to the electrode: either in the principal direction of their plane (Figure 2. 14a), either in the normal direction (Figure

2. 14b). In the perpendicular motion of the electrodes (*out-of-plane gap closing configuration*), the distance between the two electrodes is varied, while the overlapping area is kept constant during the energy cycle. In the second case, also called *in-plane gap varying configuration*, the parameter which determines the capacitance variation is the overlap area between the two electrodes.

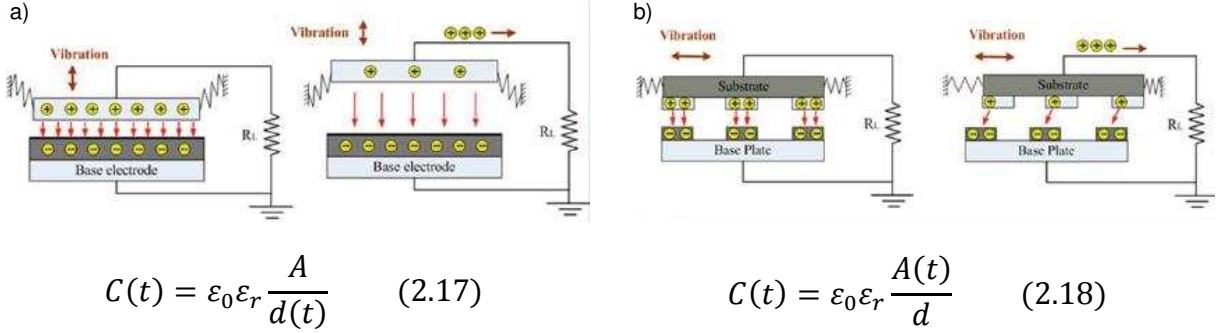


Figure 2. 14: VEH working modes: out-of-plane gap closing (a) and in-plane overlap varying (b) [2.33]

Most of the electrostatic VEH devices developed in the literature are in the centimeter scale and work under resonant frequencies ranging between 2 Hz to 2 kHz, when external acceleration between 0.25 g and 14.2 g are applied to the systems [2.33]. In the next paragraph, significant examples found in the literature for low-frequencies energy harvesting devices suitable for wearable applications will be presented.

### 2.2.1.1 State-of-the-art on wearable devices

In [2.35], an innovative multilayer out-of-plane electrostatic energy harvesting device for heart blood pressure scavenging was reported. The system presents a cylindrical structure with a diameter of 6 mm and a multiplayer configuration (Figure 2. 15) allows scavenging up to 20  $\mu\text{J}$  per beat under 75 V polarization voltage.

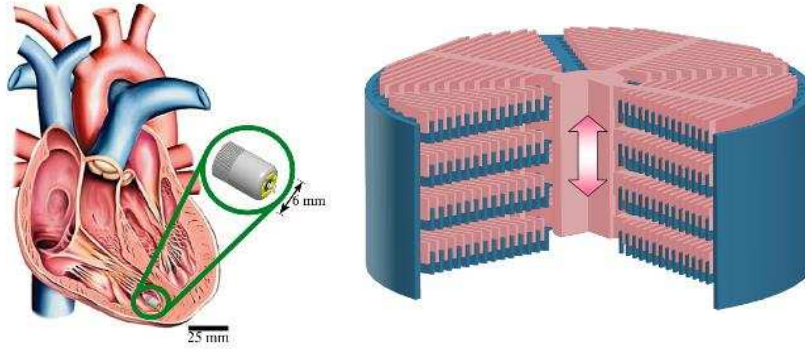


Figure 2. 15: Electrostatic device for blood pressure energy scavenging [2.35]

Among the low-frequency devices, Miao *et al.* [2.36] developed an out-of-plane “meso-scale” device made of a 4.3 g gold proof mass, suspended through a highly flexible polyimide membrane between a silicon plate and a basic plate made of quartz (Figure 2. 16). The equivalent capacitance of the device can vary from a minimal value of 1 pF to a maximal value of 100 pF under external mechanical vibrations. Experimental tests were performed through a polarization voltage source of 26 V and resulted in an output voltage of 2.3 kV and a maximal power output power of 24  $\mu$ W at 10 Hz, namely the resonant frequency of the system. The same research group presented a MEMS electrostatic generator suitable for low-frequency wearable applications [2.37], with a non-resonant operating mode. The device operates in constant-charge mode and, when pre-charged under 30 V, it can deliver an output voltage of 250 V and output energy of 0.2  $\mu$ J per cycle, at a frequency of 1 Hz, corresponding to the excitation frequency of the lower human limb.

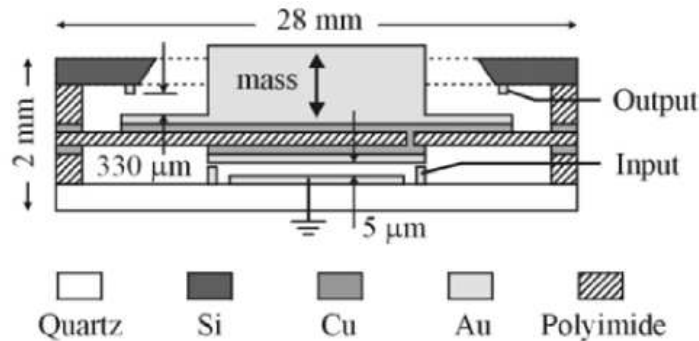


Figure 2. 16: Examples of low-frequencies VEHs found in the literature [2.36]

In the following, other examples of low working frequency electrostatic devices will be presented. These systems, even if they are not specifically conceived for wearable applications, present dimensions and working frequencies that could be adapted for human kinetic energy scavenging.

Among these, an innovative design of VEH rotary comb was presented in [2.38] and shown in Figure 2. 17a. The reported harvester consisted of 12 sets of fixed combs, a grid-like proof mass integrated with movable combs, six ladder springs, and stoppers to avoid a pull-in phenomenon between the movable and fixed combs of the harvester. When an acceleration is exerted on the rotary system, the movable mass rotates with a rotary comb and thus the total capacitance of the system (made of the overlap and air gap capacitance) changes (Figure 2. 17b). A maximum power of  $0.39 \mu\text{W}$  can be delivered on an optimum load of  $80 \text{ M}\Omega$  when the VEH is subjected to a vibration level of  $0.25 \text{ g}$  at a frequency of  $63 \text{ Hz}$ .

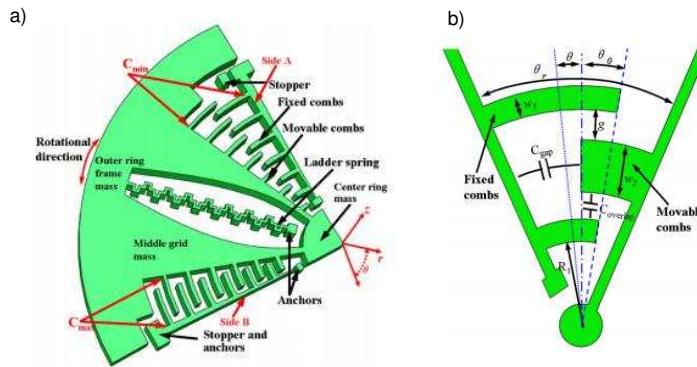


Figure 2. 17: Rotational VEH device schematic [2.38]

More recently, Cottone *et al.* [2.39] presented a MEMS electrostatic silicon gap-closing comb vibration energy harvester based on frequency amplification. This is obtained through multiple-mass impacts to the wall of a central cavity in combination with elastic stoppers (Figure 2. 18). By shaking the device with frequency in the range between  $10$  and  $60 \text{ Hz}$ , the ball impacting within the oscillating proof mass allows the transfer of the kinetic energy to the gap-closing comb structure, which consequently

resonates at its natural frequency of 92 Hz. Output power between 0.25 and 0.45  $\mu\text{W}$  were achieved at 0.3 g amplitude with 15 V bias voltage.

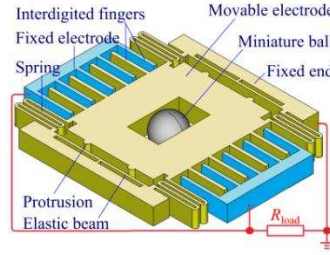


Figure 2. 18: Gap-closing comb low-frequency VEH obtained through frequency amplification [2.39]

Another innovative electrostatic VEH device scavenging multi-axial low-frequency motion was presented in [2.40] and shown in Figure 2. 19. The device structure consists of a variable gap electrostatic architecture and employs a spherical proof mass magnetically coupled to the transducer through a magnetic fluid for upper electrode actuation. The proof mass is free to move on the plane and is used to magnetize the ferrofluid. Because of magnetization, the ferrofluid applies a uniform magnetic pressure to the top surface of the variable capacitor, thus changing the gap between the two electrodes. Energy densities as high as  $9 \text{ mJ} \cdot \text{mm}^{-2}$  were obtained with a 100 V bias voltage, under low frequency vibration inducing ball movement with velocities in the range between 2 and  $18 \text{ mm} \cdot \text{s}^{-1}$ .

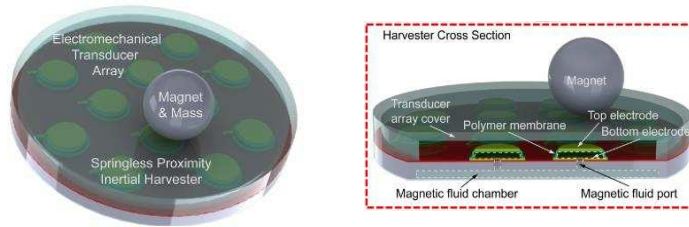


Figure 2. 19: Innovative hybrid design for out-of-plane gap closing device [2.40]

The performance of low-frequencies electrostatic VEH devices are summarized in Table 2. 3.



Ref.	Dimensions	Polarization	Testing conditions	Scavenged power
[2.35]	0.11 cm <sup>3</sup>	75 V	1-2 Hz	~20μW
[2.36]	18 mm <sup>3</sup>	26 V	10 Hz	24 μW @ 50 MΩ
[2.37]	200 mm <sup>2</sup>	30V	1 Hz	0.2 μW @ 50 MΩ
[2.38]	40 mm <sup>3</sup>	15 V	63 Hz, 0.25 g	0.39 μW @ 80 MΩ
[2.39]	100 mm <sup>2</sup>	15 V	10-6 Hz, 0.3 g	0.25 - 0.45 μW
[2.40]	3.14 mm <sup>2</sup> (×12)	100 V	2 -18 mm.s <sup>-1</sup>	0.9 μW
[2.41]	10 mm <sup>2</sup>	30 V	10 Hz	0.5 μW

Table 2. 3: Summary table of VEH reviewed from the literature

Electrostatic VEH are normally made of rigid materials and present quite high resonant frequencies. For these reasons, when working with wearable low-frequencies applications, scavengers made of soft deformable polymers are normally preferred, as described in the next paragraph.

### 2.2.2 Dielectric elastomers generators (DEGs)

Dielectric elastomers generators are soft electrostatic devices made of a deformable elastomeric membrane sandwiched between two compliant electrodes. The main advantages of these systems consist in their low-cost, easiness of fabrication, resistance to high strains (excessing 100% the initial length), capability of working in a large frequency range and generating high energy density. The maximal energy density of a dielectric elastomer generator varies between 4.1 J.g<sup>-1</sup> and 6.3 J.g<sup>-1</sup> under biaxial stretching [2.42]. More reasonable value around 0.84 J.g<sup>-1</sup> was underlined in recent study taking into account losses and parameter variations [2.43]. The low-weight and biocompatibility of these materials are particularly suitable for wearable applications. Their main drawback, as for the VEH systems, consists in the necessity of an external polarization source to perform the energetic cycle.

### 2.2.2.1 Basic principles

The typical configuration is shown in Figure 2. 20, presenting a thin elastomeric film whose sides are coated through compliant electrodes.

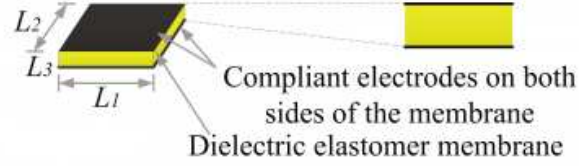


Figure 2. 20: Schematic of dielectric elastomer device: basic configuration

By applying an electric field ( $E$ ) across the electrodes, electrostatic attraction will occur between the opposite charges on the two electrodes, while homo-charge repulsion will occur at each electrode. As a consequence, electrostatic pressure across the electrodes (Maxwell stress) will cause the film to contract in thickness and, due to film incompressibility, a concomitant area expansion will occur.

The Maxwell stress ( $p_m$ ) is expressed as:

$$p_m = \epsilon_0 \epsilon_r E^2 \quad (2.19)$$

When employed in generator mode instead, the reverse process will occur. When the film is in stretched state (up to the maximal capacitance condition), electric charges are placed on the two sides of the film. When the film contracts, the elastic stresses in the film will act against the electrostatic field pressure, resulting in an increase in the stored electrical energy. From a microscopic level (Figure 2. 21a), film release causes opposite charges to be pushed farther apart and charges with same polarity to be compressed together due to film thickness decrease. The energy cycle is represented in Figure 2. 21b.

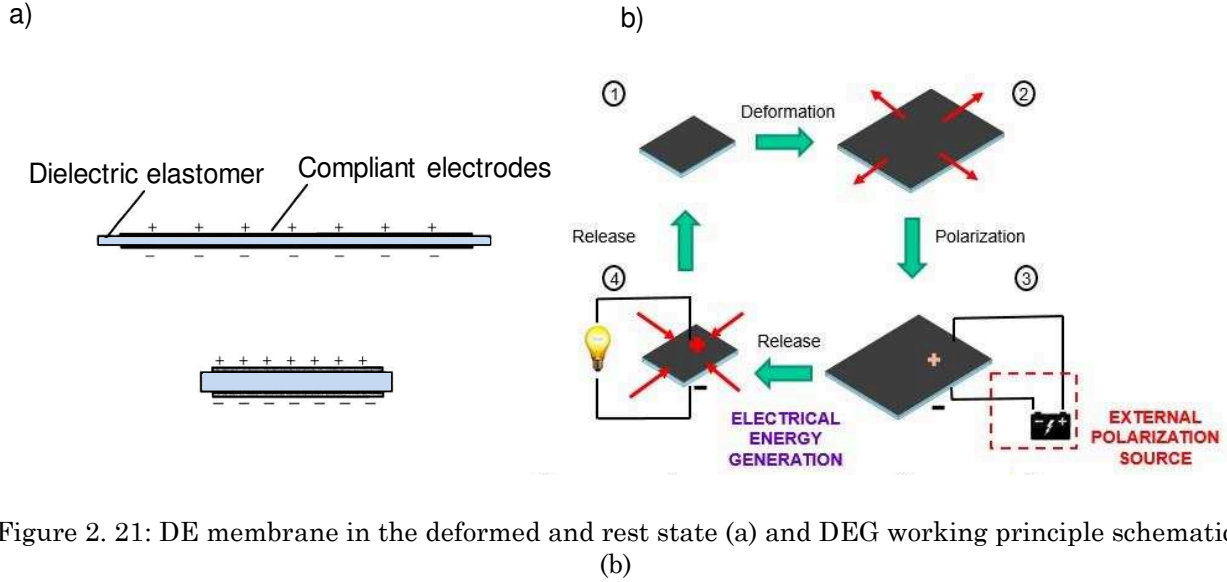


Figure 2. 21: DE membrane in the deformed and rest state (a) and DEG working principle schematic (b)

The energy cycle for DEGs is characterized by four main phases: stretch, charge, active phase and discharge. During the stretch phase, an external force, acting in one (uni-axial) or two directions (bi-axial) is applied to the film. As a consequence, the film area ( $A$ ) will increase, while its thickness ( $d$ ) decreases, resulting in a total increase of the device equivalent capacitance. When the device is at its maximal deformation state (namely maximal capacitance), a polarization voltage is applied at the two sides of the polymer, which will store an input electrical energy (charge phase). The structure is therefore released till reaching a point of equilibrium between elastic and electric stresses. This is the active phase of the cycle: the input electric energy is thus amplified thanks to the mechanical strain movement. Finally, during the discharge phase, all charges are removed from the structure and the material returns to its initial dimensions.

### 2.2.2.2 Materials

DIELECTRIC MATERIAL: The performance of the material used as dielectric elastomers is evaluated on the basis of its mechanical and electric properties. These latter should include high electrical breakdown field, high dielectric permittivity, low

losses (dielectric and resistive) while from a mechanical point of view the material should be able to sustain large stretch ratios and minimize the viscoelastic losses (i.e. creep and stress relaxation effects) [2.44]. The most widely used elastomeric materials are based on commercial formulations of acrylic materials and silicones.

The most employed acrylic material is 3M VHB 4910, which is a commercial material presenting high dielectric constant and high electrical breakdown strength. Various commercial silicones are available from major companies (Wacker, Parker, DowCorning, Nusil...) and an in-depth comparison of their performances is out of the scope of this PhD work. Based on the knowledge and expertise of our research group on DEG, as well as on relevant publications comparing silicone polymers [2.45]–[2.47], promising silicone materials have been selected such as DowCorning Sylgard 186 or ELASTOSIL® silicone film by Wacker. As their mechanical and electrical properties are similar, we will refer to this category of material as silicone in the rest of this chapter. Thus, silicone elastomers are widely employed in DE designs, due to their lower viscoelasticity compared to acrylics (resulting in higher operating frequencies) and operability over a large temperature range. A comparison between some of the most relevant properties for generator mode of these two categories of materials is shown in Table 2. 4.

	<b>Acrylics</b>	<b>Silicones</b>
<b>Maximum electric field [MV/m]</b>	440	350
<b>Dielectric constant</b>	4.5-4.8	2.5-3.0
<b>Maximal energy scavenged density [J.cm<sup>-3</sup>]</b>	4.1	1.63
<b>Maximum stress [MPa]</b>	7	3
<b>Equivalent Young's modulus [MPa]</b>	2	1
<b>Strain at failure [%]</b>	400	100
<b>Viscoelastic losses [%]</b>	20	5-20 [2.48]

Table 2. 4: Principal characteristics of DE materials [2.48]–[2.51]

One can note that acrylics materials present more suitable electrical properties to be employed for generator mode devices, with scavenged energy density up to  $4.1 \text{ J.cm}^{-3}$  [2.51]. Their main drawback consists in their high viscoelastic losses, which in fact drastically reduce their output power and limit their working frequency range to 50 Hz [2.52].

Other materials employed in the literature for energy harvesting devices include polyurethane-based polymers (presenting the highest dielectric constant -around 7.5- over the other presented DE) and natural rubber (namely a green material). Koh *et al.* [2.42] presented a nonlinear model showing that natural rubber can outperform VHB elastomers under specific operating conditions and for strains lower than 15%. In [2.53], two different commercial natural rubbers (ZruElast A1040 and Oppo Band 8003™) were characterized as low-cost dielectrics for wave energy harvesting applications. These materials present lower dielectric permittivity (3.4 and 2.8) and higher stiffness compared to VHB4910, but they exhibit higher dielectric strength and lower hysteresis losses than acrylics. Energy densities equal to  $369 \text{ mJ.g}^{-1}$  were obtained from the authors from high pressure membrane inflation tests.

New elastomers formulations are being commercially developed and many researches are focusing on the development of new materials to improve the performance of dielectric elastomers. Most of them focuses on the increase of the dielectric constant of the material, through the addition of fillers to the elastomeric matrix [2.47]. These latter may consists of: high dielectric constant ceramic particles (i.e. titanium dioxide  $\text{TiO}_2$  [2.54], barium titanate  $\text{BaTiO}_3$  (BT) [2.55], lead magnesium niobate–lead titanate  $\text{Pb}(\text{Mg}_{1/3}\text{Nb}_{2/3})\text{O}_3$ – $\text{PbTiO}_3$  (PMN-PT) [2.56]), conductive particles (i.e. carbon black (CB), multi-walled carbon nanotubes (MWCNT) [2.57], and graphite (GP) [2.58]), or highly polarizable conjugated polymers, i.e. undoped poly(3-hexylthiophene), polyaniline, or polythiophene incorporated by blending [2.59]

Nevertheless, the relevant dielectric constant increase determined by these techniques may also leads to some side effects, such as increase in the Young modulus of the dielectric or decrease of its breakdown field. In others cases, the embedded conductive

particle could form agglomerates with consequently presence of highly conductive groups in the elastomer matrix. This results in high losses and risk of short-circuits in the polymer. Encapsulation strategies were thus employed to limit these phenomena, as presented in [2.60], [2.61].

Regarding this state of art on the performance of dielectric membrane, silicone material will be chosen for our application as they are commercially available, low cost and develop a good compromise between electric and mechanical properties. Among all the available silicones, Polypower from Danfoss and Sylgar186 from Dowcorning will be used in our hybrid structure.

Dielectric elastomers materials modelling: Hyperelastic models are often employed in the literature to describe the DE large strains. A brief reminder (strain energy, principal stress) is detailed to underline their non-linear stress-strain behavior. The strain energy function  $W$  is normally derived from Mooney-Rivlin, Yeoh and Ogden forms.

The strain energy density derived from the Moonley-Rivlin model is described, under the hypothesis of material incompressibility and isotropy under un-deformed condition, by the following equation:

$$W = C_{10}(I_1 - 3) + C_{01}(I_2 - 3) \quad (2.20)$$

Where  $C_{10}$  and  $C_{01}$  are materials parameters and  $W$  is dependent on  $I_1$  and  $I_2$ , representing the first and second invariants of the left Cauchy-Green deformation tensor. These latter can be derived from the eigenvalues of the deformation gradient tensor as following:

$$I_1 = \lambda_1^2 + \lambda_2^2 + \lambda_3^2 \quad (2.21)$$

$$I_2 = \lambda_1^{-2} + \lambda_2^{-2} + \lambda_3^{-2} \quad (2.22)$$

Where  $\lambda_1$ ,  $\lambda_2$  and  $\lambda_3$  represent the principal stretch ratios.

The Yeoh strain-energy function is instead expressed by the following relationship:

$$W = C_{10}(I_1 - 3) + C_{20}(I_1 - 3)^2 + C_{30}(I_1 - 3)^3 \quad (2.23)$$

Where  $C_{10}$ ,  $C_{20}$  and  $C_{30}$  are materials parameters and  $W$  depends only on  $I_1$ .

Ogden model assumes that the stretch ratios are always positives and thus the powers of the stretch ratio are allowed to assume any value. The Ogden strain-energy function is expressed as:

$$W = \sum_{i=1}^N \frac{\mu_i}{\alpha_i} (\lambda_1^{\alpha_i} + \lambda_2^{\alpha_i} + \lambda_3^{\alpha_i} - 3) \quad (2.24)$$

Where  $\mu_i$  and  $\alpha_i$  are materials parameters and  $N$  is the number of terms.

For materials used in this work, mechanical material parameters were found through classic hyperelastic tensile tests realized in the LaMCoS laboratory, as deeply described in [2.43], or taken from the literature. In both cases, the material was subjected to a medium strain rate in accordance with the frequency operation of the final application (1-2Hz) and parameters were extracted from steady-state (to avoid Mullin's effect). Moreover, as hysteresis is very low, viscous losses are neglected in a first approximation on this work. Figure 2.22 shows the mechanical behavior for a medium solicitation speed for acrylics and silicones materials.

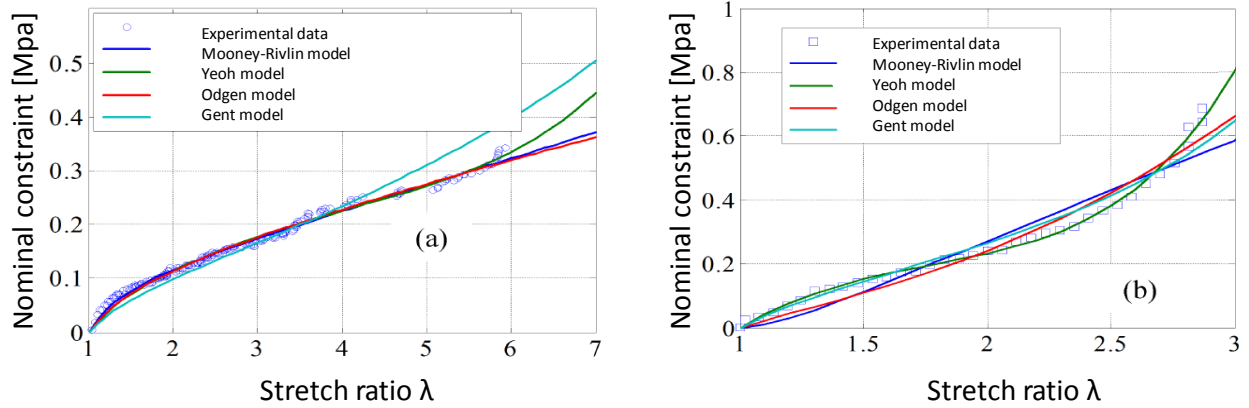


Figure 2. 22: Mechanical behaviors models for acrylic VHB (a) and silicone Polypower (b) (modified from [2.43])

Thus, for incompressible materials, the principal Cauchy stresses  $t_i$  (force per unit of area in the deformed configuration) can be calculated from the derivative of the strain potential energy with respect to the stretch ratio  $\lambda_i$ , as following:

$$t_i = \lambda_i \frac{dW}{d\lambda_i} - p \quad (2.25)$$

Where  $p$  represents the hydrostatic pressure and it depends upon kinetic boundary conditions [2.62].

This mechanical law will be used in all our analytic modelling and numerical simulation developed in chapter 4 and 5 on our hybrid structures.

**ELECTRODES:** Besides the choice of the active dielectric layer, also electrodes represent a crucial component for the device performance. These latter need to be compliant and be electrically conductive under high applied strains. Carbon grease electrodes are one of the most widely employed solution for fast proof-of-concepts, as they provide good conductivity at high strains. They are low-cost and easy to apply. Graphite and carbon powder are other easy-use and fabrication methods, providing high adherence to the polymer surface. These dry electrodes are often employed for multilayer devices to avoid the slippage effect between the layers observed with carbon grease. Their main drawback consists in conductivity losses at high strains, because the individual particles are pulled apart and lose contact [2.63].

Carbon grease electrodes are normally applied by simple smearing or spray coating on the DE surface. For precise or patterned electrode, several deposition techniques have been tested, i.e. shadow masking, stamping or printing techniques (see [2.64] for details).

Metals electrodes are less employed for DE, mainly due to their high Young modulus (limiting the film stretchability) and low elasticity (which can cause cracks on the metal surface and thus the presence of non-conducting areas on the electrode). Different solutions have been developed in the literature with the aim of overcome these limitations, i.e. patterned electrodes designs [2.65] employment of corrugated membranes [2.66] or implantation of metallic nano-clusters forming a conductive network below the elastomer surface [2.65], [2.67]. These solutions may be adopted especially in actuation mode, for low DE deformation strains.



Silver nanowires (AgNw) [2.68], graphene [2.69] and single-walled carbon nanotube (SWCNT) [2.58] are other additives frequently employed in the literature to create electrodes. These latter are highly stretchable electrodes, promising for future applications. Nevertheless, the higher cost of these materials and the brittleness of their surfaces make their applicability difficult for large surface areas [2.58].

Finally, composites polymer namely conductive particles mixed into an insulating matrix especially silicone one, is a class of electrodes largely employed in actuators and generators. They are easy to process and offer correct performance in term of conductivity. Nevertheless, their conductivity tends to drastically decrease with the increase of strain, leading to huge research on this class of electrodes.

Based on the in-depth comparison made by Rosset *et al.* [2.64] and the previous descriptions, carbon grease will be employed as fast and cheap solution to create electrodes for our devices proof-of-concepts.

### **2.2.2.3 Mechanical excitation**

The variation of the equivalent electrical capacitance between the rest and deformed state in the energetic cycle (described in Figure 2.21) is strictly dependent on the mechanical excitation applied on the elastomeric membrane. The possible deformation modes of an elastomeric membrane are shown in Table 2.5 with the respective capacitance variations and scavenged energy as a function of the mechanical stretch  $\lambda$ .

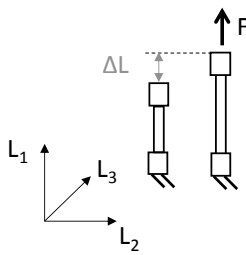
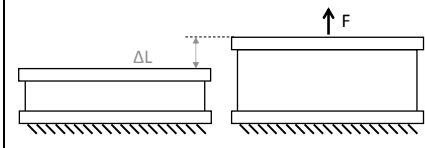
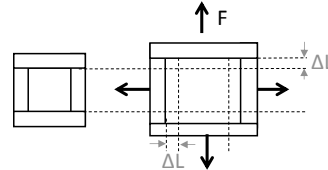
UNI-AXIAL DEFORMATION	PURE-SHEAR DEFORMATION	BIAXIAL DEFORMATION
		
$\lambda_2 = \lambda_3 = \frac{1}{\lambda_1}$	$\lambda_2 = 1 \quad \lambda_3 = \frac{1}{\lambda_1}$	$\lambda_2 = \lambda_1 \quad \lambda_3 = \frac{1}{\lambda_1^2}$
$\frac{C_{max}}{C_{min}} = \lambda_1$	$\frac{C_{max}}{C_{min}} = \lambda_1^2$	$\frac{C_{max}}{C_{min}} = \lambda_1^4$
$E_s = E_{def\_max}(\lambda_1 - 1)$	$E_s = E_{def\_max}(\lambda_1^2 - 1)$	$E_s = E_{def\_max}(\lambda_1^4 - 1)$

Table 2. 5: Possible elastomeric membrane deformation mode and correspondent characteristic components

These values are derived by the hypothesis of film incompressibility and by assuming a resulting uniform deformation on the film surface.

One can note that, when considering the same dimension of the DE membrane, the biaxial deformation mode allows scavenging the higher electrical energy. Figure 2.23 shows the evolution of the energetic gain (namely the ratio between the scavenged energy:  $E_s$  and the energy stored in the maximal deformation state:  $E_{def\_max}$ ) as a function of the membrane stretch ratio  $\lambda$ .

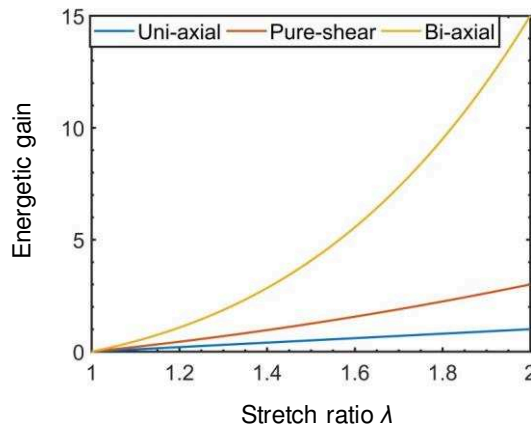


Figure 2. 23: Evolution of the energetic gain as a function of the extension ratio for different deformation modes

### 2.2.2.4 Existing devices for wearable applications

One of the first example of wearable DEG was developed in [2.44] and located on a boot heel to scavenge the mechanical pressure of the foot during walking. The device, shown in Figure 2.24, was made of 20 stacked layers of pre-strained VHB 4910 dielectric elastomer films and was able to scavenge an electrical energy output of 0.8 J per step. The structure presents a coupling medium (made of gel or fluid) to transfer the compression of the heel into the deflection of the diaphragm and to increase the comfort of the user while walking.

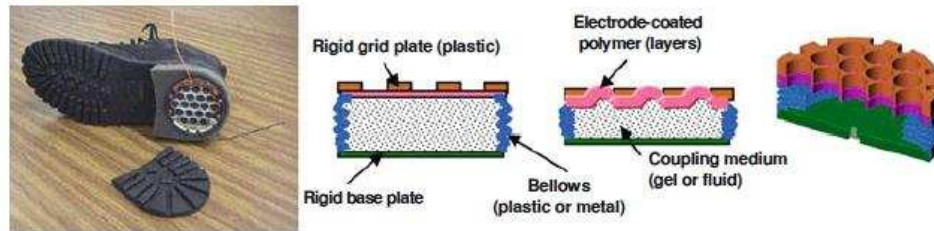


Figure 2.24: DEG-based energy harvesting device for foot strike energy scavenging [2.44]

To scavenge energy from foot pressure through DEGs, a “energy harvesting kit” (Figure 2.25a) commercialized by StretchSense [2.70] is available for purchasing. This kit includes an encapsulated DEG (Figure 2.25b) working under 1.1 kV operating voltage and a priming managing system, which manage charge on the generator. The kit also provides a 9 V battery to impose the initial kick start to the system, which is then polarized through the self-priming circuit.

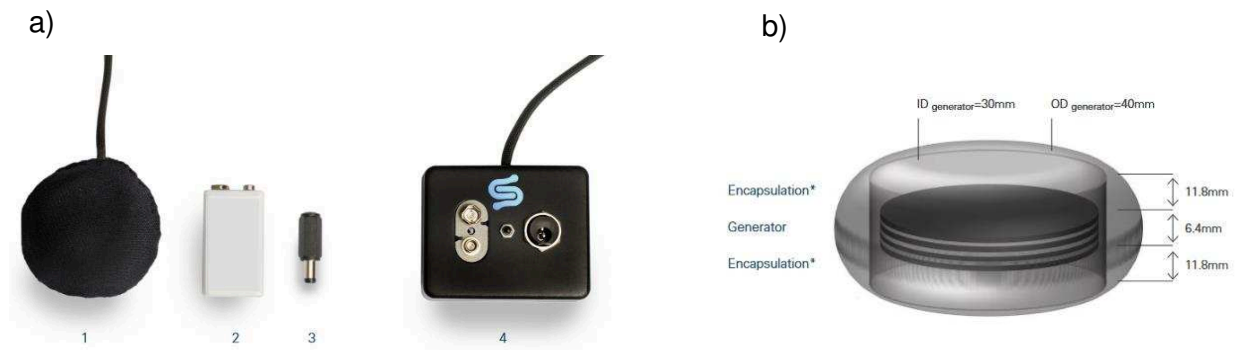


Figure 2. 25: DEG-energy-harvesting kit from StretchSense (a) and dimensions of the DEG device (b) [2.70]

Another small-scale device working under pressure deformations was presented in [2.71] (Figure 2.26). The device is made of 8-cm circular frame and has a mass of 1 gr. When pushing its central part with a finger by 4-5 cm once a second, an output power of approximately 0.12 W can be generated.

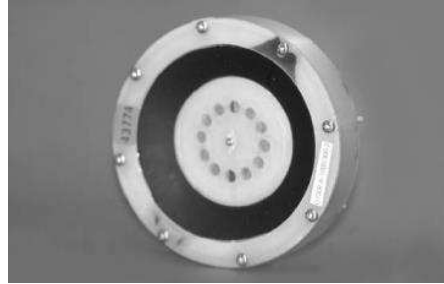


Figure 2.26: Small-scale DEG device working under pressure deformations [2.72]

An energy harvesting system based on the integration of an EAP roll on a modified commercially available knee brace (Figure 2.27a) was proposed in [2.73]. Under a bias voltage of 500 V the device was able to produce an average output power of 3.13  $\mu\text{W}$  over 15 seconds by bending the user knee of approximately 66 degrees through flexions and extensions cycles of approximately one second.

In [2.74], a DEG device to be integrated at human knee level was presented, made of an acrylic patch with a total surface area of  $3 \times 5 \text{ cm}^2$  (Figure 2.27b). Under a polarization voltage of 170 V, the device can scavenge a final total energy of 100  $\mu\text{J}$  when a 50% stretch ratio is applied to the structure at 1 Hz frequency.

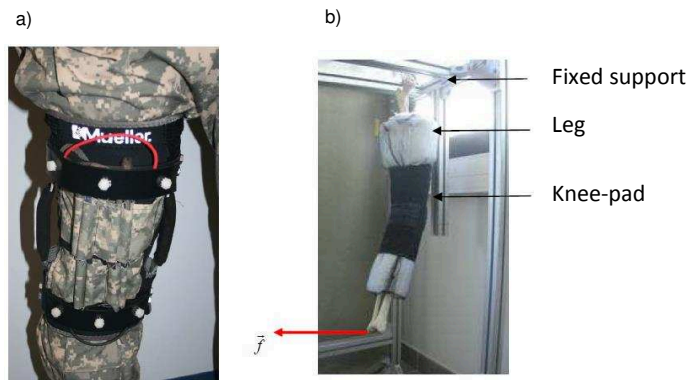


Figure 2. 27: DEG-based energy harvesters for human knee movements harvesting [2.73], [2.74]

Other devices presented in the literature, although not tested on human body, present dimension and working conditions suitable for human kinetic energy scavenging. Among these, Mc Kay *et al.* [2.75] proposed an integrated, self-priming dielectric elastomer generator made of two acrylic-based DEGs pairs: a portion of the generated energy of a first DEG is used as extra charge for the energetic cycle of a second DEG (Figure 2.28). This principle introduces in the circuit few additional electronic components (diodes or dielectric elastomer switches) and partially overcome the need of an external HV source. Only a first initial polarization voltage of 10 V is needed in the system, making it interesting for wearable applications. The device, tested under low amplitude (20 mm) and frequency (3 Hz) conditions, can scavenge a maximal energy output of 4.4 mJ, namely an energy density of  $12.6 \text{ mJ.g}^{-1}$ .

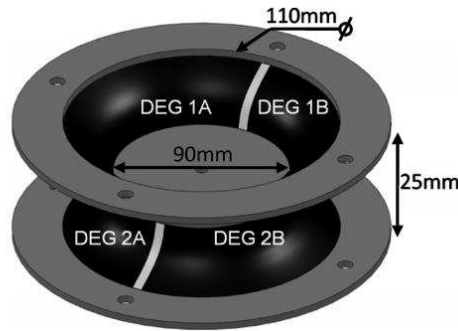


Figure 2.28: Integrated self-priming circuit schematic [2.75]

A stacked DEG configuration with a total volume lower than  $1 \text{ cm}^3$  was reported in [2.76]. The device is made of four sub-stacks of 12 active silicone membranes and can scavenge an output power of 1.8 mW (namely  $2.1 \text{ mW.cm}^{-3}$  power density) under 1.6 Hz cyclical compression.

On Table 2. 6, DEG devices suitable for human movements energy harvesting are summarized.

Ref.	Location	Dimension	Polarization	Testing conditions	Scavenged power
[2.44]	Shoe	-	1 kV	1 Hz	0.8 W
[2.73]	Knee	-	500 V	1 Hz	3.13 $\mu$ W
[2.74]	Knee	15 cm <sup>2</sup>	170 V	1 Hz	100 $\mu$ W
[2.75]	-	0.31 cm <sup>3</sup>	10 V	3 Hz	13mW
[2.76]	-	0.86 cm <sup>3</sup>	70 V. $\mu$ m <sup>-1</sup>	1.6 Hz	1.8mW
[2.77]	Arm	125 cm <sup>2</sup>	-	~1 Hz	20 mW

Table 2. 6: DEGs for wearable applications summary

### 2.2.3 Electrets as polarization source

The main drawback of electrostatic devices is the need of a polarization source to perform the energetic cycle. To overcome this limitation, different devices have been proposed in the literature introducing a layer of dielectric material with embedded electrical charges, called *electret* material. This material can ensure, in a small volume, the permanent electric polarization of the variable capacitor, eliminating the need of an external voltage source. By considering a parallel-plates capacitor design (Figure 2.29a), in the hypothesis of system neutrality, the sum of the total charge of the system (namely the electret charge  $Q_{el}$ , the charge on the counter-electrode  $Q_2$  and the charge on the upper electrode  $Q_1$ ) is equal to 0. Mechanical solicitations will induce capacitance variation leading to charge transfer between the two electrodes in order to re-equilibrate them, thus resulting in a current circulating in the system.

The equivalent electrical circuit (Figure 2.29b) is made of an electrical capacitance  $C_{el}$  with a series voltage generator  $V_s$ , standing as electret internal capacitance and polarization voltage, and a variable capacitor (controlled by external solicitation)  $c_v(t)$ . A parasitic capacitance is also introduced in the circuit, mainly associated to the system geometry and to connection wires.

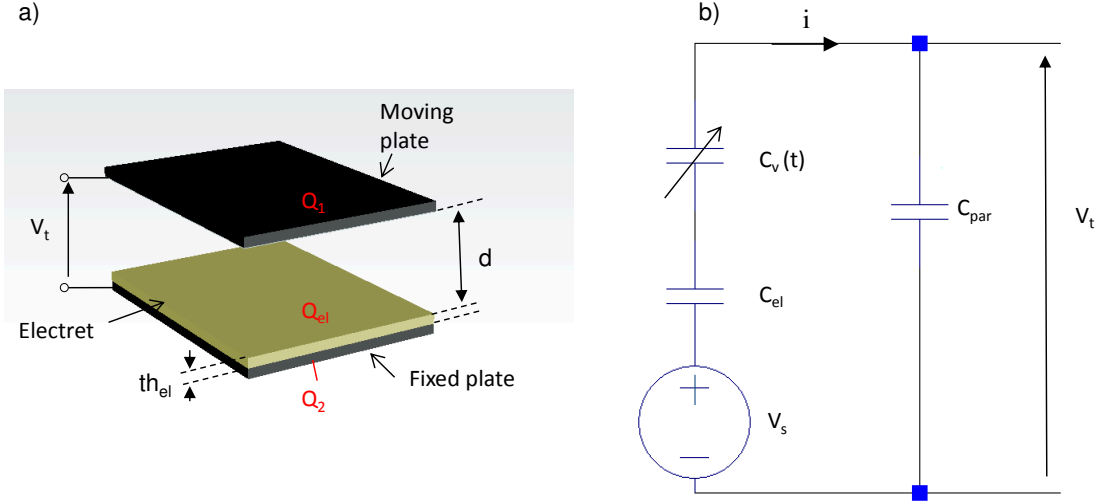


Figure 2.29: Schematic (a) and equivalent circuit model (b) of electret-based electrostatic scavengers

One can derive that the current circulating in the system  $i(t)$  is:

$$i(t) = \frac{dQ_1}{dt} = \frac{d}{dt} [(V_t + V_s)C_t] \quad (2.26)$$

Where  $V_t$  and  $V_s$  respectively represent the total voltage through the capacitor and the surface potential of the electret and  $C_t$  represents the total capacitance of the system, made by the combination of  $C_{el}$  and  $c_v(t)$ .

Several electret-based electrostatic devices have been developed in the literature for autonomous system design, through continuous or texturized electret surfaces.

Among the low working frequency devices, the one presented in [2.78] was able to scavenge  $38 \mu\text{W}$  under 20 Hz vibrations, using an electret layer charged at 1100 V. The device is made of patterned electret with a total area of  $2 \text{ cm}^2$  and work under in-plane overlap varying solicitation mode obtained through Parylene lateral springs (Figure 2.30a). In [2.79], a device with texturized electret materials charged at  $-400 \text{ V}$  and working under in-plane gap varying mode was presented. Micro-balls are integrated in the system as movable bearings for low-frequency ambient vibration energy harvesting (Figure 2.30b). Under external 20-Hz-oscillation at  $0.7 \text{ g}$  acceleration, the device can scavenge an output power of  $6 \mu\text{W}$  in a low volume ( $3 \text{ cm}^3$ ).

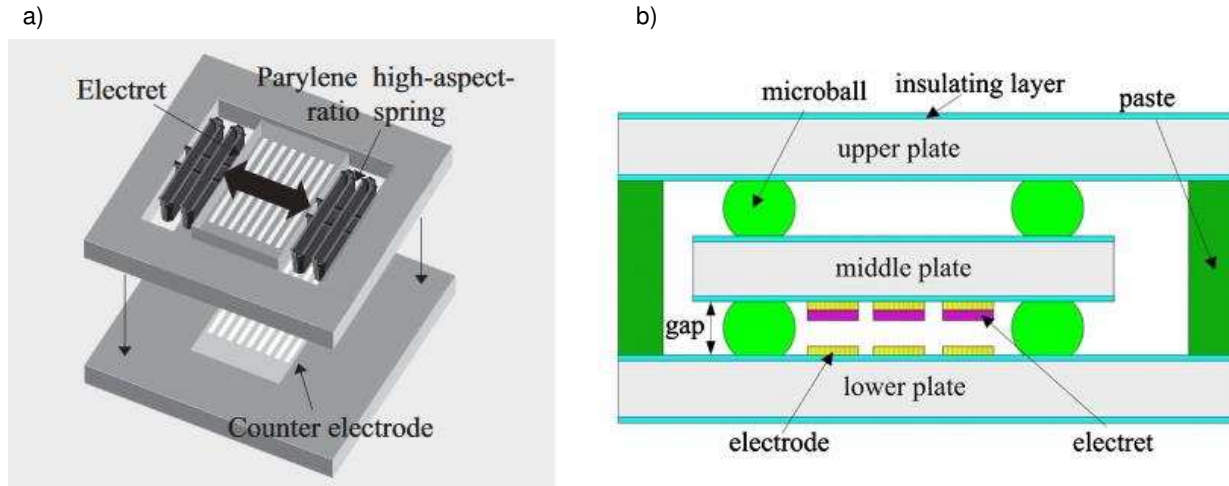


Figure 2. 30: Electret-based electrostatic micro-scale devices working under in-plane overlap (a) and out-of-plane gap varying (b) modes

A broadband energy harvesting device made of two cantilever-mass subsystems with dual resonant structure was presented in [2.80] (Figure 2.31). A continuous output power between  $6.2 \mu\text{W}$  and  $9.8 \mu\text{W}$  was obtained under vibration excitation of  $9.3\text{m.s}^{-2}$  amplitude in the frequency range from 36.3 Hz to 48.3 Hz, namely a bandwidth equal to 30% the resonant frequency.

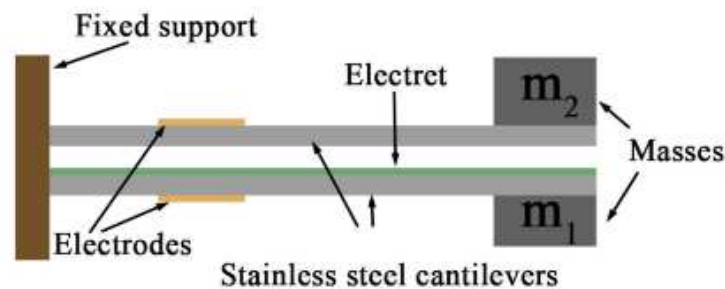


Figure 2. 31: Example of electret-based low-frequencies electrostatic device [2.80]



Our research group first worked on a hybrid generator coupling DE with electret materials [2.81], scavenging  $33\mu\text{W}$  at  $1\text{Hz}$  and allowing fabricating hybrid devices suitable for human movements energy scavenging. The device design and working principle will be detailed in Chapter 4.

Table 2. 7 summarizes the properties and performance of the most relevant low-frequencies electret-based devices found in the literature.

Ref.	Dimensions	Electret Vs	Testing conditions	Scavenged power
[2.78]	$2\text{ cm}^2$	$1100\text{ V}$	$1.2\text{ mm}_{\text{pp}} @ 20\text{ Hz}$	$28\text{ }\mu\text{W}$
[2.79]	$3\text{ cm}^2$	$400\text{ V}$	$0.7\text{ g} @ 20\text{ Hz}$	$5.9\text{ }\mu\text{W}$
[2.80]	$7.5\text{ cm}^2$	$950\text{ V}$	$9.3\text{ m.s}^{-2} @ 36.3\text{-}48.3\text{ Hz}$	$6.2\text{-}9.8\text{ }\mu\text{W}$
[2.82]	$9\text{ cm}^2$	-	$50\text{ mm}_{\text{pp}} @ 2\text{ Hz}$	$40\text{ }\mu\text{W}$
[2.83]	$3\text{ cm}^2$	$600\text{ V}$	$0.5\text{ mm}_{\text{pp}} @ 21\text{ Hz}$	$12\text{ }\mu\text{W}$
[2.84]	$4\text{ cm}^2$	$640\text{ V}$	$1.2\text{ mm}_{\text{pp}} @ 20\text{ Hz}$	$700\text{ }\mu\text{W}$
[2.81]	$25\text{ cm}^2$	$1000\text{ V}$	$1\text{ Hz}$	$33\text{ }\mu\text{W}$

Table 2. 7: Review of most relevant low-frequency electret-based devices found in the literature

Details about electret physical principle and the characteristics of electret materials mostly employed for energy harvesting applications will be given in the next chapter.

## Conclusion

This chapter has allowed us to make a state-of-the-art of the two technologies employed in this work: what emerges from this bibliographic study is that DEG devices offer the higher energy density compared to the other technologies and can work under low frequencies ranges, typical of human body movements (Table 2.8).

Technology	Theoretical maximal energy density	Frequency range	Advantages and drawbacks
Piezoelectric (PZT based)	$56 \times 10^{-3} \text{ J.cm}^{-3}$	-	✓No need of an external polarization ✗Frequency increase with miniaturization
Piezoelectric (PVDF-based)	$60 \times 10^{-6} \text{ J.cm}^{-3}$	<100 kHz	✓No need of an external polarization ✗Low coupling
Electrostatic (VEH)	$44 \times 10^{-3} \text{ J.cm}^{-3}$	1 Hz -2 kHz	✓MEMS design ✗Lower energy density ✗Need of a polarization source
Electrostatic (DEGS)	$4.1 \text{ J.cm}^{-3}$	0.5 - 100 Hz	✓High energy densities ✓Low working frequency ✗Need of a polarization source

Table 2. 8: Characteristics of electrostatic and piezoelectric energy harvesting technologies [2.49], [2.85]

It is important to underline that these values of energy density are strictly dependent on the application and on the transduction mechanism employed in the device.

The main disadvantage of DEGs consists in the high polarization voltage needed to perform the energetic cycle. This issue may be overcome by employing (i) electret materials as polarization sources which allow obtaining high surface potentials in low volumes or (ii) piezoelectric materials which allow obtaining high voltage outputs with simple design systems. Hybrid devices coupling these principles (electret or piezoelectric with dielectric materials) will be designed to obtain soft scavengers with high energy output. The proposed hybrid devices working principles and designs will be described in chapters 4 and 5.



# **CHAPTER 3.**

## **ELECTRET MATERIALS**



## **Chapter 3. Electret materials**

This chapter focuses on the results obtained from the fabrication and tests of three variants of polymeric electrets materials in the family of Parylenes, namely Parylene C, AF-4 and VT-4. Firstly, we aim to provide an overview on the main definitions and physical principles of electret materials, to help the reader better understanding the presented results. Then, the fabrication techniques and characterization tests employed in this work will be described. Lastly, the fabrication, measurements and performances on the materials analyzed in this work will be presented and specifically the isothermal surface potential decay, environmental influence on electrets charge retention and energetic characterization of charge trapping.

### **3.1 Physical principles and experimental techniques**

#### **3.1.1 General definitions**

Electrets can be defined as dielectric materials with a quasi-permanent electric charge or dipole polarization. These materials can be considered as the electrostatic equivalent of permanent magnets and can generate a quasi-permanent internal and external electric field. Electrical charges stored in the dielectric material may consist of monocharges (also referred to as “real charges”) and dipolar charges. These latter are aligned dipoles that can be induced in dipolar materials containing dipolar molecules or in ferroelectric materials. “Real charges” can be spatially distributed on the surface of the material (surface charges) or within the bulk, forming the so-called space charges. The different types of charges are shown in Figure 3.1.

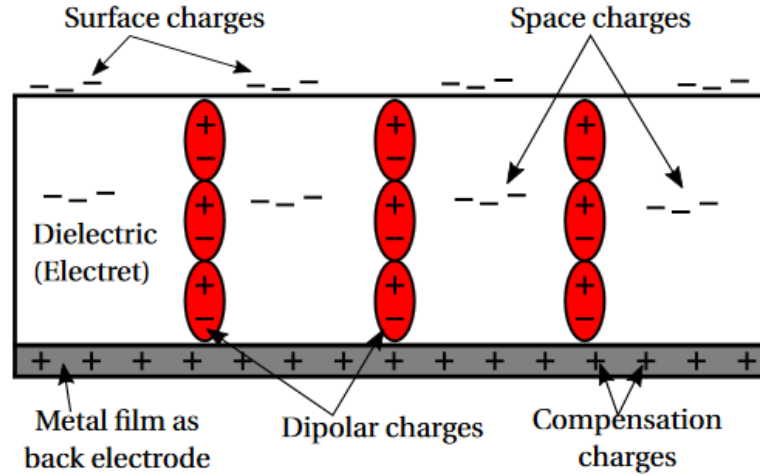


Figure 3.1: Types of charges in an electret material [3.1]

Electrets can be realized with different dielectrics in terms of structures and properties. First electrets were made of thick plates of carnauba wax and other similar substances, while, starting from early fifties, thin electrets from inorganic dielectrics and polymers have attracted a high attention [3.2]. In our work, polymeric materials for energy harvesting applications were tested, as better described in 3.1.8.

### 3.1.2 Energy traps

The phenomenon of charges trapping supposes the existence of localized states inside the material. The energy-band theory is generally used to explain charge transport within polymers, which are characterized by a gap, separating conduction and valence band, higher than 4 eV. This ideal energy-band theory is modified due to high defects density in polymer materials. According to the different nature of these defects (chemical and physical), different energy of localized states can exist in the mid of the energy gap [3.3].

Two types of traps can thus be distinguished, namely shallow and deep traps. Shallow traps are present in the tail of the valence and conduction band and correspond to low

energy charge carriers localization. Deep traps are present in the gap of the polymer and are characterized by higher energetic depth, as can be seen in Figure 3.2.

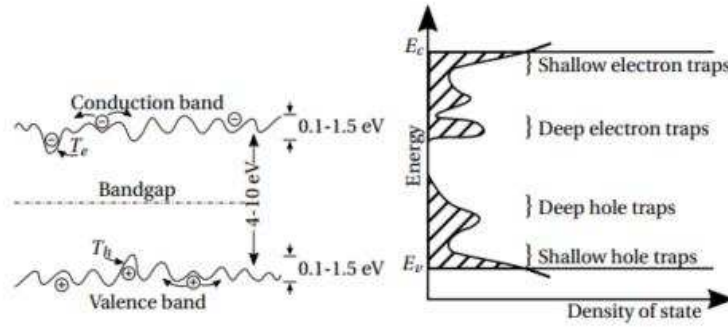


Figure 3. 2: Energy diagram in a polymer electret (a) and possible distribution of the density of the localized states (b) [3.4]

According to traps density and energetic level, these localized states can either enhance or reduce charge mobility. Several physical mechanisms were widely discussed in literature [3.3] to describe charge transport in materials submitted to different external energies.

De-trapping toward the transport states (conduction and valence bands) and recombination between charges of opposite polarity are the main mechanisms responsible for reducing trapped charges density. Oppositely, de-trapping can randomly occur towards deeper localized states, commonly named re-trapping.

### 3.1.3 Charges stability over time

The term “quasi-permanent”, used to describe the polarization of electret materials, is because the amount of charges implanted in the electret does not remain constant over time, but decay with a certain speed. The charge decay over time can be due to internal mechanisms, such as bulk neutralization or surface conduction or to external environment, i.e. neutralization by gas air ions.



This latter can occur from recombination between surface charges present on the electret materials and free ions present in a surrounding gaseous environment (i.e. air).

Surface displacement of charges may occur due to carriers hopping through different traps or may be of ohmic nature. This mechanism can be quantified through surface conductivity of the material, which is also influenced by external environmental condition, such as air relative humidity [3.5].

Bulk neutralization consists in charge decay through the bulk of the material and is mainly caused from charge injection or internal polarization processes.

Charge injection may result from charges migration in the bulk of the material. These charges can be present in the interface between air and electret or between electret and metal electrode.

Internal polarization may be due to volume conduction (namely charge transport through the bulk of the material) and to the dipolar response (in case of presence of intrinsic dipole in the material).

All the phenomena are shown in Figure 3.3.

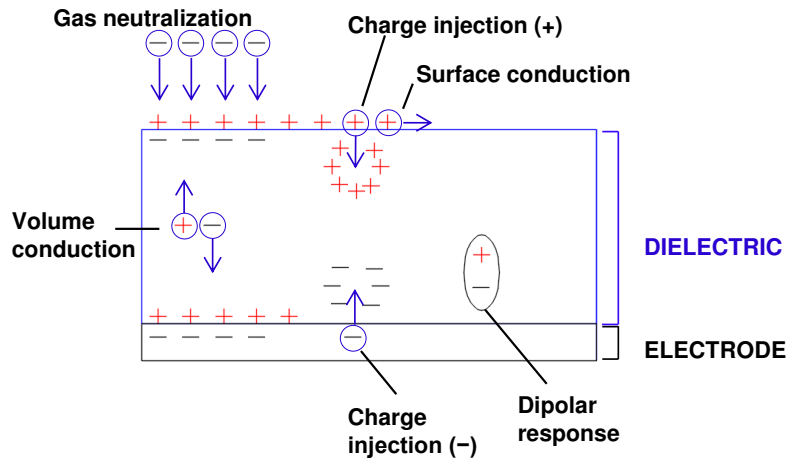


Figure 3. 3: Mechanisms responsible for electret charges decay over time [3.6]

Several models have been developed in the literature based on kinetic equations taking in consideration different charge mobility phenomena (i.e. capture and release from traps, creation of carriers pairs, recombination, stochastic hopping...) [3.3]. As a deepen study of charge transport in the materials from a microscopic point of view goes beyond the objective of this work, the reader is referred to the literature [3.3], [3.7] for deeper information about the physical mechanisms of charge decay in polymeric electrets.

### 3.1.4 Electret surface potential

The surface potential of an electret is determined by the net charge density of the electret in a certain instant of time. The information extracted from surface potential measurements only concerns the total amount of charges retained in an electret material and not their energetic or spatial distribution.

Assuming a thin space-charge dielectric layer with a uniform distribution of charges in the lateral dimension (schematic in Figure 3.4), the surface charges density  $\sigma$  can be derived from the surface potential  $V_s$  through the equation 3.1:

$$\sigma = \frac{\varepsilon_0 \varepsilon_r V_s}{d} \quad (3.1)$$

where  $\varepsilon_0$  represents the vacuum permittivity,  $\varepsilon_r$  the dielectric material relative permittivity and  $d$  the thickness of the electret material.

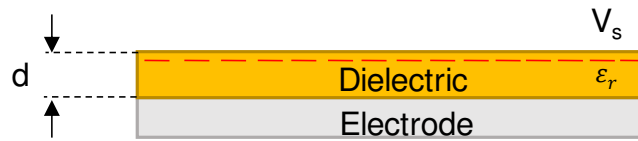


Figure 3. 4: Electret material configuration

Equation 3.1 can also be used to determine the theoretical maximal charges density ( $\sigma_{max}$ ) an electret can retain. This value can be expressed by equation 3.2:

$$\sigma_{max} = \varepsilon_0 \varepsilon_r E_{max} \quad (3.2)$$

where  $E_{max}$  represents the maximal electric field strength the material can withstand. It is important to highlight that this theoretical limit is calculated under the assumption that all the charges stand on the surface of the material. Beneath, other parameters determine the maximal charge retention in the electret, i.e. trap sites availability and charging conditions.

### 3.1.5 Charges injection by corona discharge method

Depending on the physical principle employed for electret production, different types of electret materials can be distinguished (i.e. thermo-, mechano-, electro-electrets...). Electro-electrets are produced by application of a strong electric field across the dielectric material sandwiched between two metal electrodes, causing polarization, injection of charge carriers or both [3.8]. Electrets formed by carrier injections can also be achieved either by electron beam implantation or corona discharge method. This latter is the technique chosen in this work due to its short duration, its simple use and implanted charges surface homogeneity and stability over time. The schematic and experimental setup employed in this work is shown in Figure 3.5.

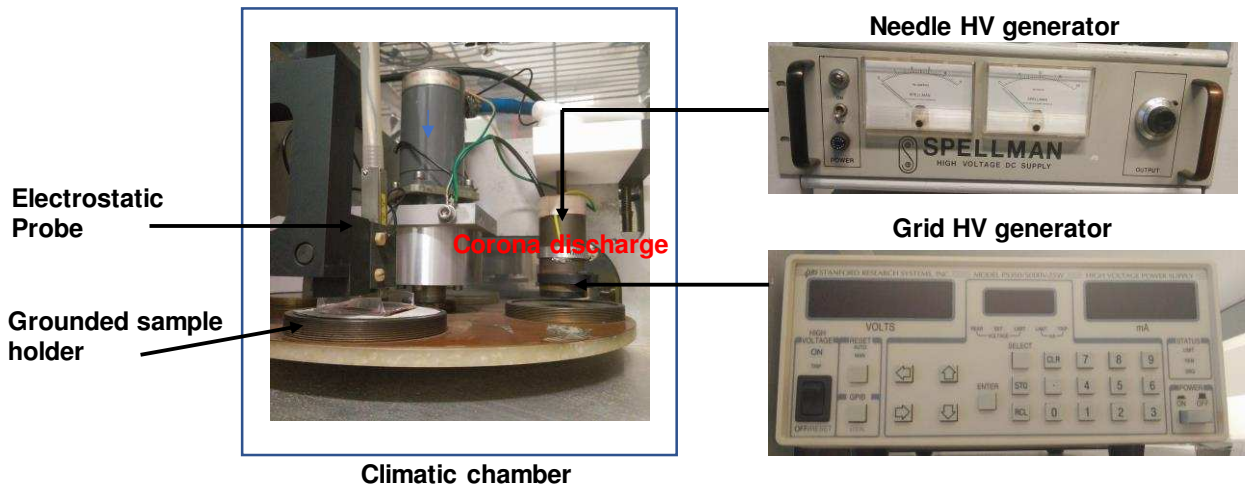


Figure 3. 5: Schematic and experimental setup of corona discharge method employed in this work for electret fabrication.

Corona discharge of air is the mechanism exploited for electret fabrication in this technique. When a conductive needle is electrically charged (normally with a voltage ranging between 5 to 10 kV), the surrounding air is ionized by electrical discharge. The produced ions are then accelerated by potential difference toward the sample, whose lower face stands to the mass. A control grid is placed between the needle and the sample to guarantee a homogeneous charge distribution on the electret surface and to control its maximal charging potential. When the surface potential of the sample equals the one of the grid in fact, no more potential difference pulls ions towards the electret surface and no more charges implantation occurs. Depending on the corona polarity, either positive or negative ions can be produced. Negative air corona discharge mainly generates  $CO_3^-$  ions, while  $(H_2O)_nH^+$  ions predominate in case of positive corona discharge [3.9].

In the setup employed in this project, two double polarity high voltage (HV) generators (SPELLMAN and SRS PS350) are respectively connected to the needle and to the control grid, which stands at 3 cm from the needle end. The possibility to control the HV generators polarity allowed us to produce both negatively and positively charged electrets materials. The metallic plate connected to the mass for sample positioning stands at a fixed distance of 2 mm from the grid. The sample plate spatial position is controlled by a rotation motor: once the charging process is completed the sample is shifted to the measurement stage to register the surface potential decay (SPD) over time.

### 3.1.6 Surface potential decay (SPD) measurements

Surface potential decay (SPD) measurements were performed using an electrostatic voltmeter with the experimental setup shown in Figure 3. 6:

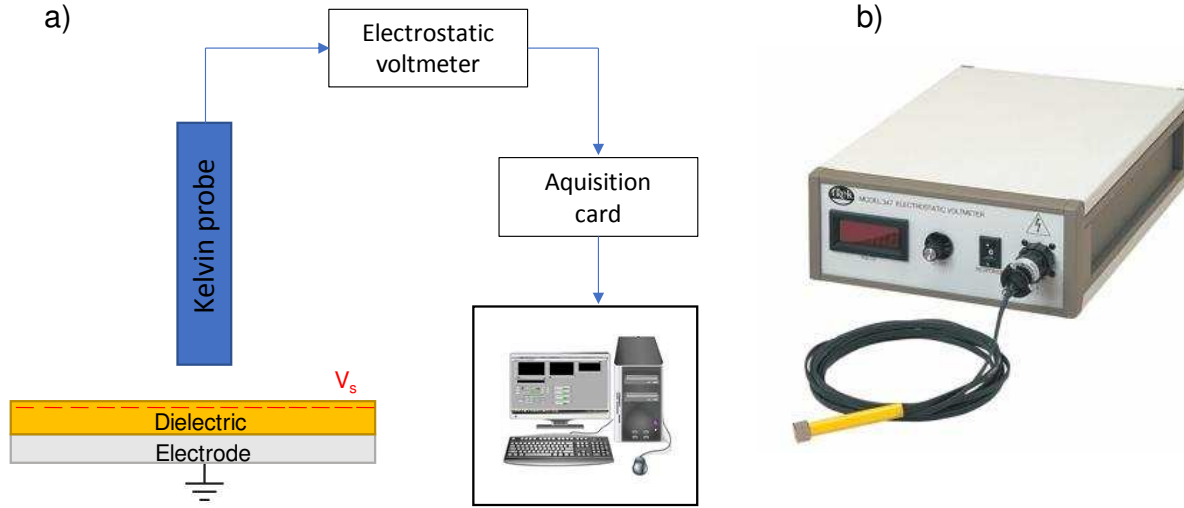


Figure 3. 6: Schematic of experimental setup of surface potential measurement (a) and electrostatic voltmeter employed in this work (b)

In this work, an electrostatic voltmeter TREK 347 and a Kelvin probe were employed. This instrument consists of a vibrating sensor which determines the surface potential of the electret by detecting the electric field generated by the charges above the surface of the material. By placing the probe over the material surface, a parallel-plate capacitor  $C$  is formed between the probe surface and the charged surface of the material. This configuration induces in the vibrating sensor element a current, proportional to the electric field present on the surface under test:

$$I = U \frac{dC}{dt} \quad (3. 3)$$

where  $U$  represents the potential difference between the tested surface and the vibrating probe. This current value is treated by a detection circuit to produce a tension  $V$  in the probe allowing the compensation of the current  $I$ . This value is thus equal to the surface potential  $V_s$  of the material under test. As already discussed in 2.2.3, this is one of the most important parameter determining the performance of electret-based electrostatic generators. The electrostatic voltmeter employed in this work presents measurement accuracy higher than 0.05% and a resolution of 1 V [3.10].

By monitoring  $V_s$  over time, the SPD of the electret can be evaluated. As an example, the SPD of 25 $\mu\text{m}$ -thick Teflon FEP is shown in Figure 3.7 for positively and negatively charged samples.

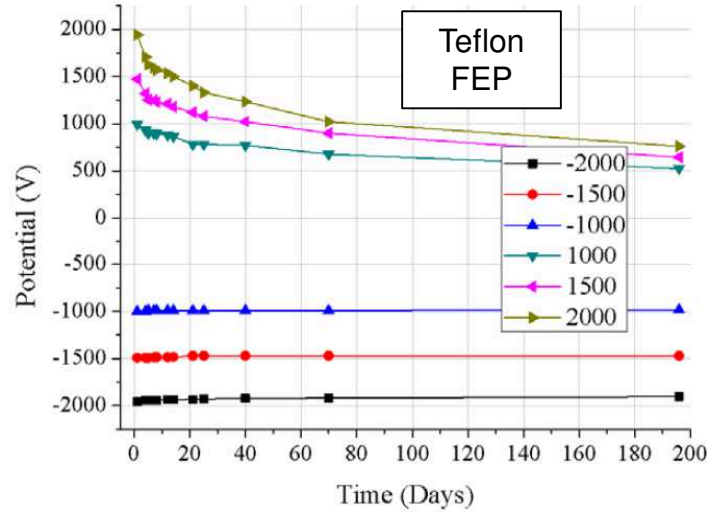


Figure 3. 7: SPD of 25- $\mu\text{m}$ -thick Teflon FEP [3.11]

A qualitative diagnosis on the conduction process in the electret material can be derived from the SPD curves.

- In case surface conduction prevails, the SPD is independent from the initial charging voltage, depends on the materials thickness and has a non-uniform distribution over the sample surface.
- In case of dominant bulk conduction in the dielectric, the SPD follows a power law decrease over time and its trend is dependent from the initial charging voltage. In addition, the cross-over phenomenon may occur. This effect, which was observed in different literature works [3.12], [3.13] manifests when  $V_s(t)$  curves obtained at higher values of initial charging potentials ( $V_0$ ) cross the ones obtained for samples with lower  $V_0$ .
- Gas neutralization may be evaluated by comparing SPD curves of electrets fabricated under the same charging conditions but kept in different gaseous environments.

As it was shown in [3.14], surface conduction becomes important only in highly humid environments, while gas neutralization plays an important role especially in highly insulating dielectrics and in particular environments [3.15]. When SPD at ambient environmental conditions are monitored, several theories [3.16] instead consider bulk transport process the main responsible for surface potential decay over time.

### 3.1.7 Energy distribution of trapped charges

In this work, Thermally Stimulated Discharge (TSD) method was employed to characterize the electret charge trapping from an energetic point of view. This technique consists in heating up the charged electret material and measuring the surface potential over time upon thermal stimulation.

As described in paragraph 3.1.2, ions are trapped in localized states in the material. The trapped carriers during the heating process will gain enough energy to be de-trapped and to jump to the conduction or valence bands or in other neighbor traps sites (re-trapping process). Through thermal stimulation, the energetic characterization of material traps can thus be derived.

Beneath, by using this technique, surface potential thermal stability of electrets materials for our applications can be evaluated.

In this experiment, the electret sample was put on a grounded plate and heated up using a temperature controller (LINKAM TMS 94). During thermal stimulation, the corresponding surface potential of the electret over time was measured each second using the electrostatic voltmeter (TREK 347), by using the experimental setup shown in Figure 3.6. By differentiating the electret surface potential  $V_s(T)$  as a function of temperature, the thermally stimulated current was derived as described in [3.1]. This was done by assuming that no re-trapping occurs and, once a carrier is de-trapped, it directly moves to the valence or conduction band, no more contributing to the electret electric field. Equation 3.4 describes the derived released thermally-stimulated current:

$$I(T) = \frac{\varepsilon_0 \varepsilon_r}{d} \beta \frac{dV_s(T)}{dT} \quad (3.4)$$

where  $\varepsilon_0$  and  $\varepsilon_r$  respectively represent the vacuum permittivity and the relative permittivity of the material.  $d$  represents the thickness of the material, while  $\beta$  and  $T$  are respectively the heat rate and the absolute temperature in Kelvin. Starting from  $I(T)$ , the energy activation of the traps can be derived. In fact, this current represents the charges released from the electret over the time and can be expressed by equation 3.5:

$$I(T) = -\frac{dn}{dt} = n \nu \exp\left(\frac{-E_a}{k_b T}\right) \quad (3.5)$$

where  $n$  is the total number of carriers contained in the traps, which have activation energy equal to  $E_a$ .  $\nu \exp(-E_a/k_b T)$  is the probability per unit of time that a carrier escapes from the trap, where  $k_b$  is the Boltzmann constant and  $\nu$  represents the attempt-to-escape frequency which typically stands between  $10^{12} \text{ s}^{-1}$  and  $10^{14} \text{ s}^{-1}$  in polymer electrets [3.4]. When assuming the temperature linearly increasing with time, the release current in equation 3.5 becomes:

$$I(T) = -\frac{dn}{dt} = n \exp\left(-\frac{\nu}{\beta} \int_0^T \exp\left(\frac{-E_a}{k_b T'}\right) dT'\right) * \nu \exp\left(\frac{-E_a}{k_b T}\right) \quad (3.6)$$

From the solution to equation 3.6 differentiated with respect to temperature, the relationship between activation energy and peak temperature can be derived as following:

$$\frac{E_a}{k_b T_p} = \ln\left(\frac{T_p \nu}{\beta}\right) + \ln\left(\frac{T_p k_b}{E_a}\right) \quad (3.7)$$

Within the range  $10^{12} < \nu/\beta < 10^{16}$ , applicable to the majority of polymeric materials [3.1], and  $273 < T_p < 773 \text{ (°K)}$ , equation 3.7 can be simplified as:

$$\frac{E_a}{k_b T_p} \approx \ln\left(\frac{T_p \nu}{\beta}\right) - 3.52 \quad (3.8)$$



From the temperature at which the release current peak occurs ( $T_p$ ), one can thus derive an estimation of the activation energy of the traps present in the material. Different current peaks indicate the presence of different energy traps in the material, while if the carriers are trapped at a single energy level, only one peak appears in the derived TSD current. The magnitude of the TSD current and specifically its time integral gives an indication on the amount of charge released during thermal stimulation of the electret material.

### **3.1.8 Electrets in energy harvesting applications: state-of-the-art**

Among the different electret materials employed in literature works for energy harvesting applications, we may distinguish two categories: inorganic materials and polymeric materials. The most widely used inorganic materials are: silicon oxide ( $\text{SiO}_2$ ) and aluminum oxide ( $\text{Al}_2\text{O}_3$ ). These latter can provide high surface charge density and temperature stability, but their long-term charge retention at ambient conditions is usually lower compared to polymeric materials [3.17]. Besides, soft and compliant electret materials are necessary in our energy harvesting devices, in order to adhere to the complex scavenger structure and follow its mechanical deformation.

These are the reasons why polymeric materials were selected in this work as electrets for the development of energy harvesting devices. Among this category, different types of polymers can be found in literature works. Fluorinated polymers such as Fluorinated Ethylene Propylene (FEP) [3.11], PolyTetraFluoroEthylene (PTFE) [3.18], CYTOP™ [3.19] and Teflon AF [3.20] are the most widely employed due to their long-term charges stability. Table 3.1 shows their interesting parameters as electrets materials [3.21].

Electret	Dielectric strength [V. $\mu\text{m}^{-1}$ ]	$\epsilon$	Maximal surface charge density [mC.m <sup>-2</sup> ]
Teflon (FEP/PTFE)	100-140	2.1	0.1-0.25
CYTOP	110	2	1-2
Teflon AF	200	1.9	0.1-0.25

Table 3.1: Characteristics of the most well-known polymeric electrets employed in the literature for energy harvesting applications

Other examples of electrets polymers employed in the literature for energy harvesting applications are Kapton [3.22], PolyPropylene (PP) [3.23] or PolyEthylene (PE) [3.24].

More recently, Parylene materials have emerged as electrets for energy harvesting applications [3.25]–[3.27]. This class of poly(p-xylylene) polymers are produced by chemical vapor deposition (CVD) and are a promising category of electrets as they can combine the adaptability to complex shapes with high surface charge densities. Among them, the most widely known are Parylene C and AF-4 (often referred as Parylene HT). In this thesis, both have been studied as electret materials for energy harvesting devices, together with Parylene VT-4, which is another variant of fluorinated Parylene. On this latter, no literature works as electret material can be found, mainly due to its later commercialization. Parylene C is the most widely employed in energy harvesting devices and the preliminary tests made on this thesis are aimed to be compared with the results found in the literature and as reference point for the fluorinated polymers study. Figure 3.8 shows the results found in the literature on different Parylene variants stabilities as electret materials, fabricated with the parameters reported in Table 3.2.

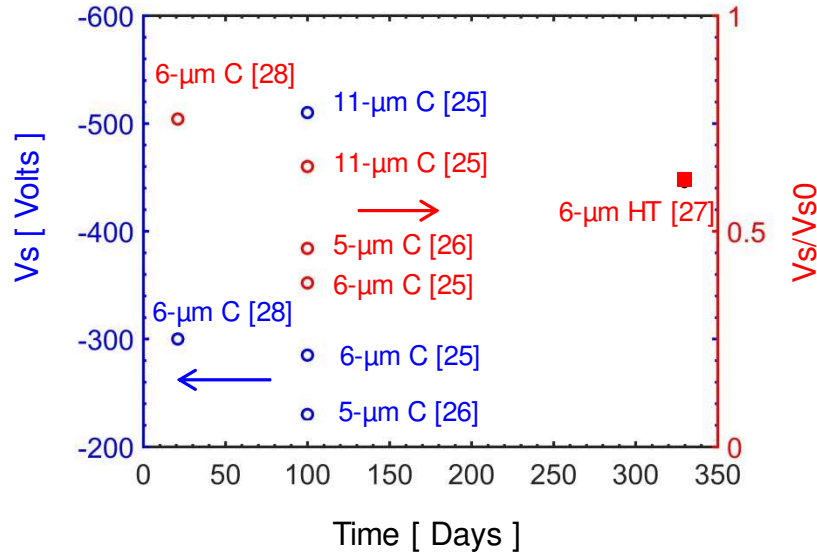


Figure 3. 8: Surface potential for different Parylene materials reported in literature works

Ref.	Material	Substrate	Corona discharge conditions
[3.27]	7.32- $\mu\text{m}$ Parylene HT	Soda lime wafers	$I_n = 0.02 \mu\text{A}$ , $I_g = 0.2 \mu\text{A}$ $T_s = 100^\circ\text{C}$ , $t_c = 180 \text{ s}$
[3.28]	6- $\mu\text{m}$ Parylene C	Copper jig	$V_n = \pm 2.7 \text{ kV}$ , $V_g = \pm 300 \text{ V}$ $T_s = \text{RT}$ , $t_c = 180 \text{ s}$
[3.26]	5- $\mu\text{m}$ Parylene C	Copper mesh embedded in PDMS	$V_n = -4 \text{ kV}$ , $V_g = -500 \text{ V}$ $T_s = 100^\circ\text{C}$
[3.25]	Parylene C: 4 $\mu\text{m}$ , 6 $\mu\text{m}$ , 8 $\mu\text{m}$ , 11 $\mu\text{m}$ , 23 $\mu\text{m}$	40 $\mu\text{m}$ Pyrex + 200 nm Cr + 300 nm Au + 40 nm Cr	$V_n = -8 \text{ kV}$ , $V_g = -1.2 \text{ kV}$ $T_s = \text{RT}$

Table 3.2: Specifications of Parylene electret materials reported in Figure 3.8.  $I_n$  and  $V_n$  stands for the needle current and voltage respectively;  $I_g$  and  $V_g$  represent the grid current and voltage;  $T_s$  stands for the charging temperature and  $t_c$  the charging process duration.

Compared to Teflon electrets, which can maintain high surface potentials over long durations (see Figure 3.7), Parylene materials have high surface charge density (close to  $2 \text{ mC}\cdot\text{m}^{-2}$ ) and display additional advantage to be highly compliant.

## 3.2 Electrets fabrication and tests

### 3.2.1 Materials characteristics and fabrication

Electret material characteristic and performance are of crucial importance in case of electret-based electrostatic generators. The electret material used in the previous energy harvesting device made by our research group [3.11] consisted in a 50 $\mu$ m-thick Teflon FEP film, which is commercialized in form of films by DuPont™. To be able to adapt the electret material to different and more complex shapes, in this work we focused our attention on Parylene electret materials, specifically on three variants: Parylene C, Parylene AF-4 and Parylene VT-4. These highly conformant poly(p-xylylene) polymers exist in fact in different variant, whose basic version is named Parylene N. Its chemical structure and the one of the materials tested in this work are shown in Figure 3.9.

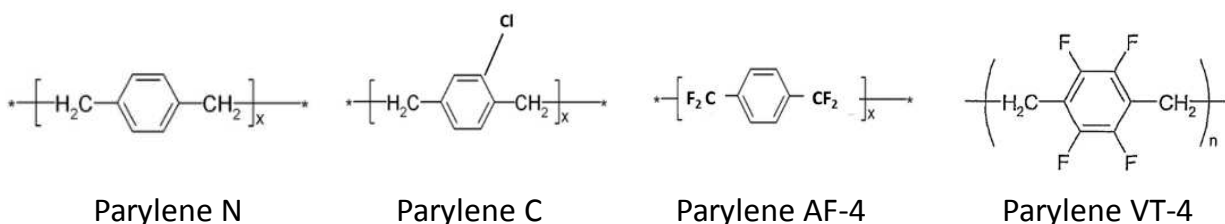


Figure 3. 9: Chemical structure of the basic variant of Parylene (N) and of the materials tested in this work.

These materials exhibit excellent chemical and dielectric properties, as reported in 3.3 for the three materials analyzed in this work.

	PARYLENE C	PARYLENE AF-4	PARYLENE VT-4
<b>Definition</b>	Poly(monochloro-para-xylylene)	Poly(tetrafluoro-para-xylylene) F-AF4: Substitution of 4 H atoms by 4 F atoms at the additional (aliphatic) groups	Poly(tetrafluoro-para-xylylene) F-VT4: Substitution of 4 H atoms by 4 F atoms at the aromatic benzene ring
<b>Density [g.cm<sup>-3</sup>]</b>	1.29	1.51	1.60
<b>Durable heat resistance [°C]</b>	100	350	140
<b>Melting point [°C]</b>	290	500	-
<b>Dielectric constant (@ 1 KHz)</b>	3.00	2.24	2.38
<b>Dissipation factor (@1 KHz)</b>	0.0395	0.0019	0.0018
<b>Dielectric strength [V.μm<sup>-1</sup>] @ 5 μm</b>	180-220	1000	280
<b>Volume resistivity (@ 23°C, 50%RH) [Ω.cm]</b>	8.8×10 <sup>16</sup>	2.0×10 <sup>17</sup>	1.1×10 <sup>17</sup>
<b>Surface resistivity (23 °C, 0 %RH) [Ω.cm]</b>	1.0×10 <sup>14</sup>	5.0×10 <sup>14</sup>	4.7×10 <sup>17</sup>

Table 3.3: Principal properties of the studied Parylene variants [3.29]–[3.32]

Parylene C presents an asymmetric polymeric chain due to the substitution of a chlorine atom in one of the aromatic hydrogens of the basic variant. The two fluorinated polymers instead are both characterized by 4 fluorine atoms, which stand in the benzene ring in case of Parylene AF-4, while they are situated in the additional group for Parylene VT-4.

The first material tested in this project was Parylene C, which was produced by Chemical Vapor Deposition (CVD) using the facilities of Néel Institute, at the CNRS of Grenoble. This laboratory has a high level of expertise on the deposition process of Parylene C using a device for low pressure CVD, shown in Figure 3.10. Details about the elaboration process of Parylene materials can be found in APPENDIX A.

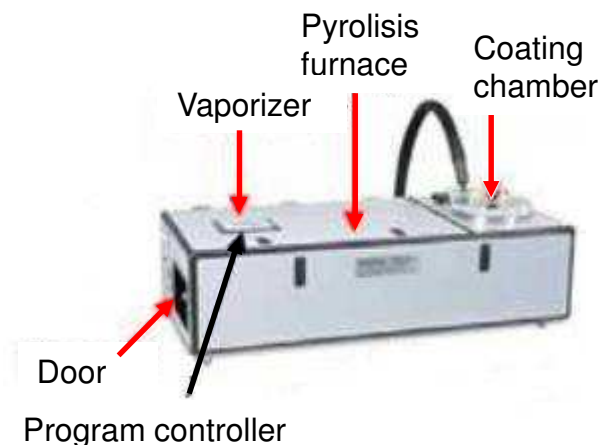


Figure 3. 10: Chemical vapor deposition (CVD) equipment [3.29]

Samples were deposited on a stack of Inox 416L and a 50-nm-thick Au substrate. The choice of a metal substrate was made to reproduce the real application of electrostatic energy scavengers, where a ground electrode is present in the lower part of the electret material and to guarantee the electrical contact with the mass during the charging process and the monitoring of the surface potential decay.

The maximal layer thickness fabrication for Parylene-C material was equal to  $6.5 \mu\text{m} \pm 0.5 \mu\text{m}$ , as the experimental CVD setup employed for the fabrication is not adapted for higher thickness values. To monitor the influence of the material thickness on the charges stability over time, a stack of two Parylene-C layers with a total thickness of  $13.5 \mu\text{m}$  was also fabricated. All the samples were deposited on substrates of total surface equal to  $9\text{cm}^2$  using A-174 silane adhesion promoter.

Fluorinated Parylene tests were made on three different samples thicknesses (3, 6 and  $9 \mu\text{m}$ ) fabricated by the company Comelec SA on  $9\text{-cm}^2$  surface-area Aluminum substrates. All the samples were pre-treated by plasma activation and adhesion promotor vaporization.

### 3.2.2 Electrets charging and SPD monitoring

Electrets were fabricated by charging with corona discharge method by using the experimental setup described in paragraph 3.15. Samples were charged for 180 seconds using a needle voltage of  $\pm 8\text{kV}$  (depending on the desired polarity of the electret material), and by setting the control grid potential according to the desired initial surface potential of the electret. Once the charging process was completed the electret Surface Potential Decay (SPD) and the Relative Surface Potential Decay (RSPD), namely the ratio between  $V_s(t)$  and  $V_s(0)$ , were registered over time.

The first preliminary series of tests were performed by charging at ambient environmental conditions Parylene-C samples. On this polymer, different studies can be found in the literature: Genter *et al.* [3.25] found RSPD values of Parylene C deposited on a stack of Cr/Au/Cr after 100 days respectively equals to 0.38 and 0.65 of the initial value for the 6- $\mu\text{m}$  and 11- $\mu\text{m}$  thick samples, corresponding to surface potentials of  $-285\text{ V}$  and  $-510\text{ V}$ . RSPD values equals to 0.76 after 21 days were reported by Wada *et al.* [3.28] for 6- $\mu\text{m}$ -thick Parylene C samples deposited on copper jig and charged at  $-2700\text{ V}$ . Yi Chiu *et al.* [3.26] presented 5- $\mu\text{m}$ -thick samples deposited on copper substrates with RSPD values after 724 days equals to 0.52.

The differences in the SPD values reported in these studies may be attributed to the different fabrication parameters, which influence the performance of the electret material, as shown in [3.3]. In this work, we chose to monitor the SPD at ambient environmental conditions of the two thicknesses of Parylene-C samples deposited on Au substrates with different charging voltages, as shown in Figure 3.11. High value of charging potentials were chosen on the basis of the characteristic required for electret materials in our energy harvesting devices [3.11]. Indeed, scavenged energy increases with the increase of the surface potential value of the electret as reported in our previous study [3.11] and detailed in chapter 4. The target for the surface potential of the electret is  $\pm 1000\text{V}$ , leading to interesting level of scavenged energy and easy comparison with the generator designed in past studies realized at our laboratory.

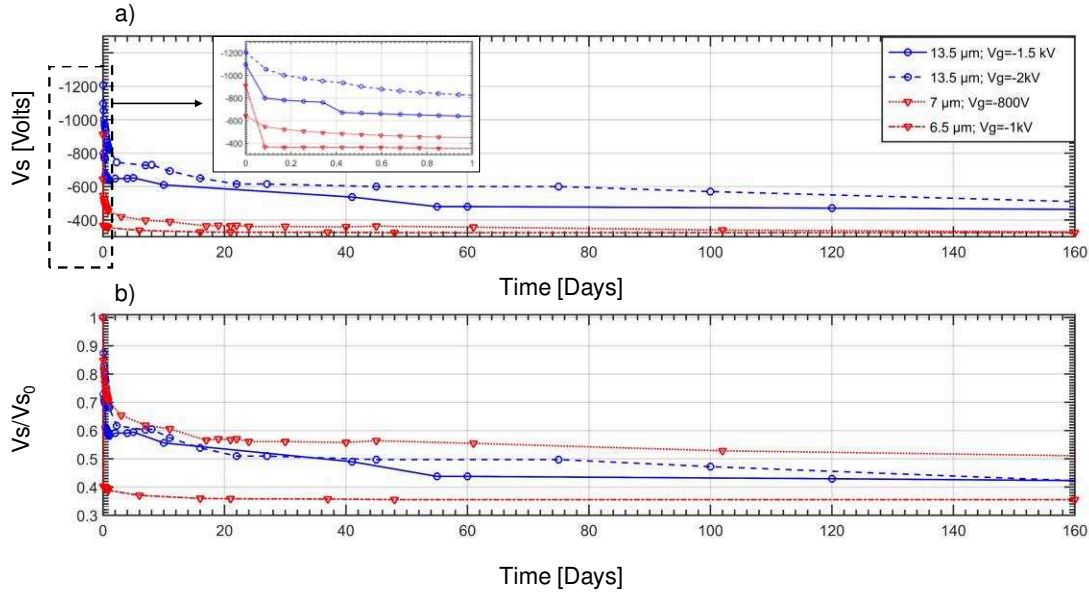


Figure 3. 11: Absolute (a) and relative (b) SPD on Parylene C samples with different charging voltages.

The surface potential trends and values obtained were consistent with the ones found by Gender *et al.* in [3.25] (where  $V_g = -1200$  V): 7- $\mu\text{m}$  sample surface potential after 100 days was equal to  $-300$  V with a charging voltage of  $-1000$  V, while the 13.5- $\mu\text{m}$  thick samples with a charging voltage of  $-2000$  V reached a final surface potential of approximately  $-500$  V. Studies on influence of pre-charging annealing temperature on Parylene-C charges stabilities were also performed in our laboratory and presented in [3.33], showing a further improvement of charge retain in the polymer.

Due to the symmetric polymer chain and the apolar nature of fluorinated Parylenes, we predicted higher charges stability in these polymers over Parylene-C. In this latter in fact, partial initial implanted charges annihilation can occur due to the  $C-Cl$  polar groups present in the lateral polymeric chain, thus reducing the total surface potential over time. Consequently, a deeper study was performed on the performance of the fluoropolymer AF-4 and VT-4 as electret materials. On this latter, no literature works can be found, while few studies were performed on Parylene AF-4 as electret material.



Specifically, Raschke *et al.* [3.34] presented the first tests on Parylene AF-4 electret material, charging an electret sample at  $-500$  V and showing its temperature stability over time. Lo *et al.* presented a micro-power generator built by depositing a  $7.32\mu\text{m}$ -thick layer of Parylene AF-4 on a PolyEtherEtherKetone (PEEK) rotor and able to harvest up to  $8.23\text{ }\mu\text{W}$  power at  $20\text{ Hz}$  [3.27]. These promising results require confirmation with further investigations on long-term charge stability. Starting from these considerations, the influence of charges polarity (Figure 3.12) and initial charging voltage (Figure 3.13) on the long-term charge stability of Parylene AF-4 was monitored in different samples thicknesses ( $3$ ,  $6$  and  $9\text{ }\mu\text{m}$ ) to evaluate its feasibility for energy harvesting applications. For all samples, three different measurements were performed to evaluate the results repeatability. Median value is represented on the figures. The corresponding initial surface charge densities  $\sigma_s$  [ $\text{mC}\cdot\text{m}^{-2}$ ] calculated from (3.1) for different charging conditions are reported in Table 3.4:

$d$ [ $\mu\text{m}$ ] $\downarrow$ $V_s$ [ $\text{V}$ ] $\rightarrow$	<b>1000</b>	<b>1500</b>	<b>2000</b>
<b>3 (AF-4)</b>	6.6	9.9	13.2
<b>6 (AF-4)</b>	3.3	5.0	6.6
<b>9 (AF-4)</b>	2.2	3.3	4.4

Table 3.4: Initial surface charge density  $\sigma_s$  [ $\text{mC}\cdot\text{m}^{-2}$ ] of Parylene AF-4 electrets with different thicknesses ( $d$ ) and charging voltages ( $V_s$ )

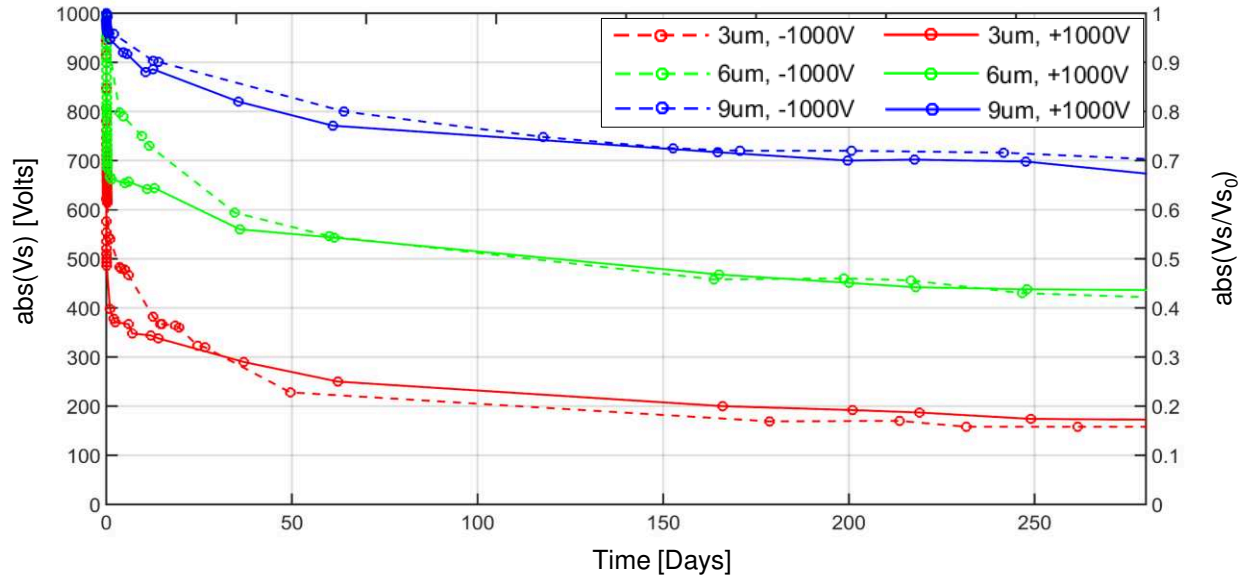


Figure 3. 12: Comparison of positive and negative charges stability for different thicknesses of Parylene AF-4 samples

For Parylene AF-4, long-term stability for positive and negative charges appears quasi-identical: the surface potentials for samples of respective thicknesses 3, 6 and 9  $\mu\text{m}$  after 280 days were equals to 170 V, 438 V and 695 V for positive polarization and to -158 V, -430 V and -716 V for negative polarization. These latter correspond respectively to surface charge densities of 1.1, 1.5 and 1.7  $\text{mC}\cdot\text{m}^{-2}$ , which are higher than the different Teflon variants reported in Table 3.1 and comparable to the values found for CYTOP.

To evaluate the influence of the initial charging voltage on the long-term SPD, we chose to monitor negative homocharges, as negative charged electrets were employed in our energy harvesting device and as long-term stability resulted close for both polarities. Figure 3.13 shows the results on different thicknesses of Parylene AF-4 for different charging potentials.

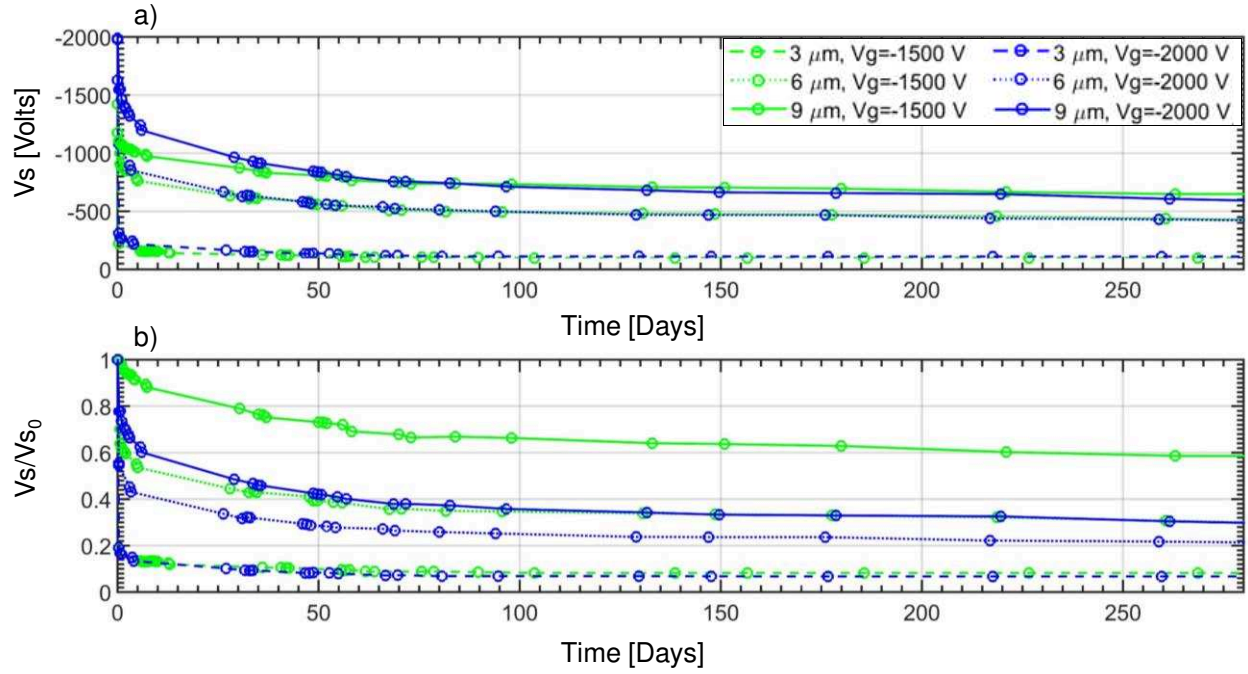


Figure 3. 13: Influence of control grid voltage on negative charges stability of different Parylene AF-4 samples thicknesses. Absolute (a) and relative (b) surface potential decay

SPD of 9 μm-thick Parylene VT-4 was also monitored over the long term for different initial charging potentials (−1000 V, −1500 V and −2000 V, respectively equals to 2.3, 3.5 and 4.7 mC.m<sup>-2</sup>), as shown in Figure 3.14.

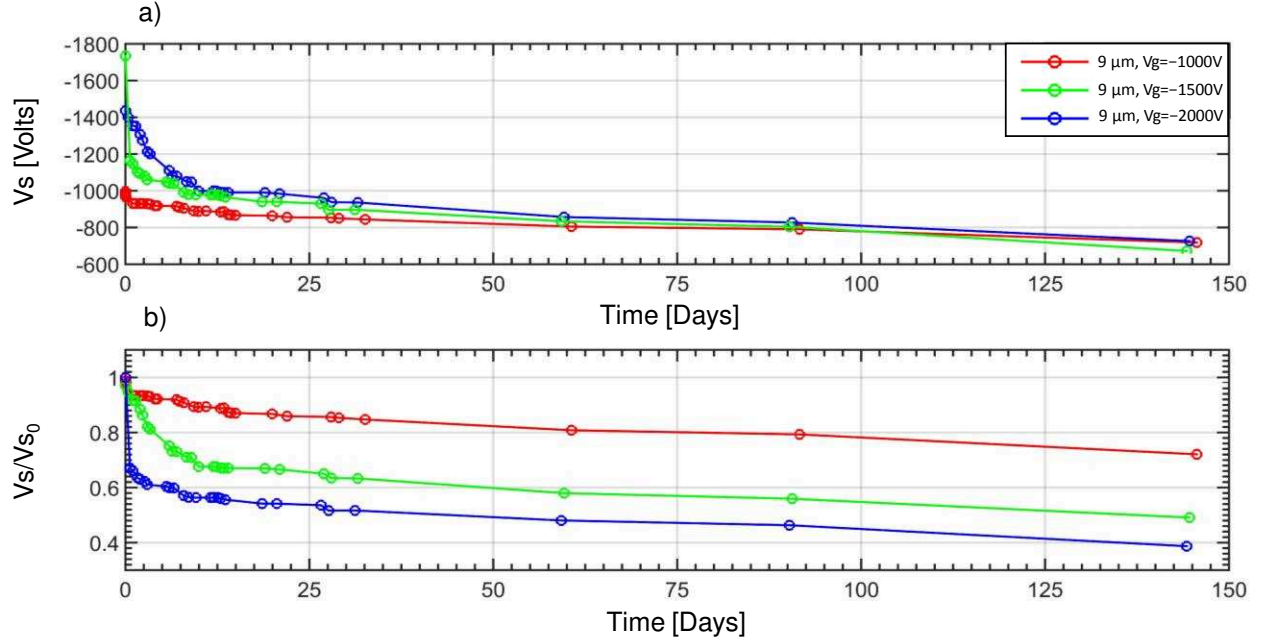


Figure 3. 14: Influence of control grid voltage on negative charges stability of 9-μm-thick Parylene VT-4 samples: absolute (a) and relative (b) surface potential decay

From the above figures, one can distinguish two different SPD zones in the analyzed samples: a first rapid exponential decrease which occurs in the first 5 days and a second slower decay in the following days. The function that better described the trend of the SPD curves, as already found by Li *et al.* [3.35] for PolyEthylene (PE), was the double exponential, with R-square values for all the samples higher than 0.90.

$$V(t) = a_1 e^{-t/\tau_1} + a_2 e^{-t/\tau_2} \quad (3.9)$$

Where  $a_1$  and  $a_2$  and  $\tau_1$  and  $\tau_2$  respectively stand for the amplitudes and the time constants of the first ( $a_1, \tau_1$ ) and second ( $a_2, \tau_2$ ) exponential components.  $\tau_1$  and  $\tau_2$  are the principal interesting values in our study for the evaluation of the device lifetimes.

Table 3.5 shows the time constants obtained from the fitting for selected samples to underline the influence of the Parylene variant, charging voltage and thickness on the

SPD. The other fitting parameters and examples of fitted curves results for the proposed sample are reported in APPENDIX B.

	6- $\mu\text{m}$ Parylene AF-4		9- $\mu\text{m}$ Parylene AF-4		9- $\mu\text{m}$ Parylene VT-4	
$V_0$ [V]	$\tau_1$ [d]	$\tau_2$ [d]	$\tau_1$ [d]	$\tau_2$ [d]	$\tau_1$ [d]	$\tau_2$ [d]
−1000	7.7	460.8	14.6	833.4	8.5	744.6
−1500	0.7	220.1	4.7	817.7	4.1	438.2
−2000	0.2	191.0	4.2	351.4	1.0	322.8

Table 3.5: Time constants of the SPD curves (until 150 days) fitted with a double exponential function

The following considerations can be extracted from the above results:

- For all the charging potentials,  $\tau_2$  (which stands for charge time constant in the second part of the SPD curve) is significantly higher than  $\tau_1$ . These dynamics are consistent with the trends commonly observed for long-term measurements in other experimental studies on polymeric electrets [3.3] and could be associated with the presence of two types of traps in the material, namely shallow and deep traps (see paragraph 3.1.2). The dynamics of the two types of traps are respectively represented by  $\tau_1$  and  $\tau_2$ . For our applications, in order to guarantee the lifetime of the device, the long-term charge stability is the most important parameter, which is associated to deep traps charge retention. Consequently, 9- $\mu\text{m}$ -thick Parylene AF-4 charged at −1000 V seems the best candidate among the different tested samples.
- For all thicknesses, it can be observed that the final surface potential of the samples reaches approximatively the same values for the different charging voltages and consequently higher initial charging voltages induce high SPD. This behavior was confirmed by charging a 3  $\mu\text{m}$ -thick Parylene AF-4 sample with an initial surface potential of −200 V. The sample surface potential after 280 days was within the same confidence interval as the ones charged at higher

initial potentials, with final  $V_s$  value equal to  $-140$  V. Relative SPD resulted equal to 0.7 instead of 0.18 obtained for samples with an initial surface potential of  $-1000$  V. The potential achieved corresponds to trap site saturation, leading to a stabilization of the surface voltage independently from the initial charging one.

- Regarding the influence of the thickness, thicker electrets present higher long-term charges stability, as commonly observed in literature for polymeric electrets [3.25]. For same charging potentials, higher thicknesses samples present higher time constants ( $\tau_1$  and  $\tau_2$ ). This can be associated, as discussed in [3.36], by the presence of a higher internal field caused by charge injection in thinner electrets, which can determine partial charge drift in the volume of the material. Charge transport by hopping between the shallow traps in the material volume can thus appear, resulting in a faster SPD for higher charging voltages and for lower material thicknesses. The desired characteristics for electrets employed in electrostatic energy harvesters are: low thicknesses (to increase the equivalent electrical capacitance value), high surface potential values and stability over time. From the above considerations, it can be concluded that thicker Parylene samples present higher stability and surface potential over time. A compromise between thickness and surface potential value needs thus to be found for our application, as it will be discussed in chapter 4.
- From Figure 3.12, one can note that the analyzed Parylene AF-4 samples present a difference between positive and negative homo-charges stability lower than 10%, making this material suitable for applications with double polarity electret materials [3.37]. For these devices, PTFE and FEP are not suitable materials, due to the lower stability of positive charges compared to the negative ones, except when applying specific treatments with titanium-tetrachloride vapor [3.38], [3.39].
- By comparing 9- $\mu\text{m}$ -thick Parylene AF-4 sample to Parylene VT-4 with same thickness, it can be concluded that the long-term charge retention of the two

fluoropolymers is similar, with SPD differences in the range of 5%. Specifically, surface potential values as high as  $-740$  V and  $-780$  V were respectively obtained after 100 days. This similarity could be associated to the similar properties of the two materials (as shown in Table 3.3) in terms of volume and surface conductivity. Both materials present good charge retention over time and can thus be considered potential candidates as electrets for electrostatic energy harvesters.

As expected, by comparing the same thickness ( $6\text{ }\mu\text{m}$ ) of Parylene-C with the fluorinated variant AF-4, this latter presents a surface potential after 100 days  $\sim 50\%$  higher, as shown in Figure 3.15.

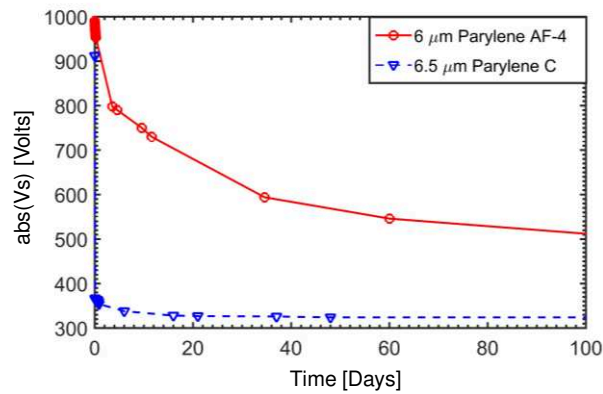


Figure 3.15: SPD comparison between  $6\text{-}\mu\text{m}$  thick Parylene C and AF-4

For these reasons, the test described in the following part will be focused on fluorinated Parylene materials. The feasibility of all the tested Parylene electret materials when integrated in the energy harvesting device will be evaluated in chapter 4.

To better reproduce our real application of energy harvesting devices, fluorinated Parylene samples charge stability was also monitored when deposited on Al-metalized surface of SemiFlex™ 3D printing material from Ninjatek. A  $100\text{-}\mu\text{m}$ -thick aluminum layer, standing as electrostatic generator ground electrode, was deposited using a metal sputter system (QUORUM Q150T). The results of Parylene AF-4 SPD showed good agreement with the one deposited directly on the metallic surface, demonstrating

good polymer adhesion also when deposited on the scavenger substrate. The schematic and the results obtained on the two different substrates are shown in Figure 3.16 for the 9- $\mu\text{m}$ -thick sample charged at  $-2000\text{ V}$ .

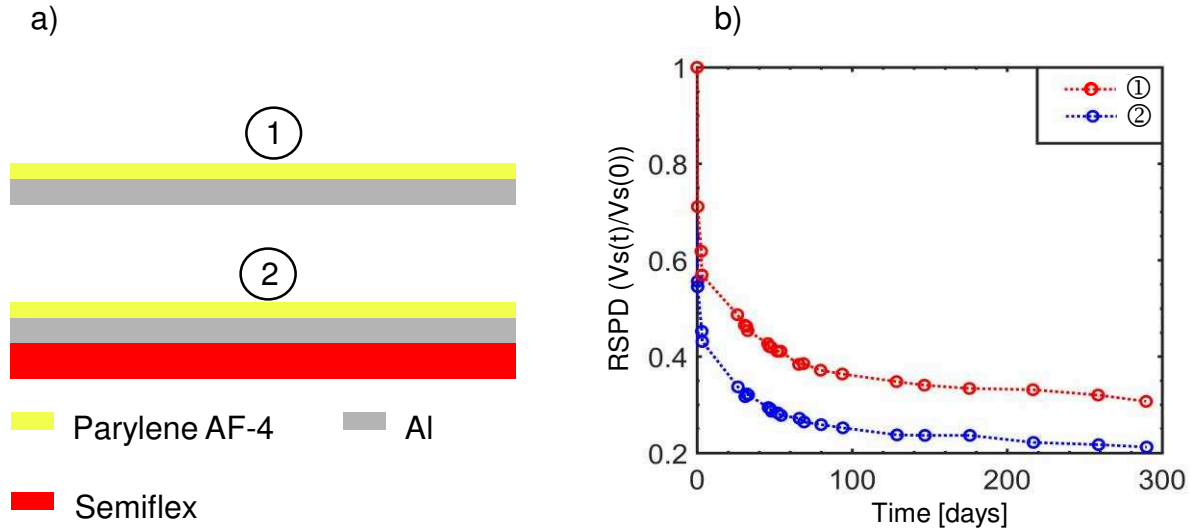


Figure 3.16: Schematic (a) and RSPD median values (b) of 9- $\mu\text{m}$  thick Parylene AF-4 deposited on different substrates with  $V_s = -2000\text{ V}$

### 3.2.3 Thermally stimulated discharge (TSD) measurements

The tests performed in the previous paragraph, only concerned the measurement of the total charge retained in the material for different charging parameters and environmental storage conditions. In this part, Thermally Stimulated Discharge (TSD) measurements results will be presented with the aim to characterize the charge retention in the polymer from an energetic point of view, as explained in paragraph 3.1.7.

Experiments were performed by linearly heating up the sample to a maximal temperature of  $250\text{ }^{\circ}\text{C}$  with a speed of  $2\text{ }^{\circ}\text{C}\cdot\text{min}^{-1}$ . RSPD measurements and derived charge release current, calculated using equation 3.5, are shown in Figure 3.17.



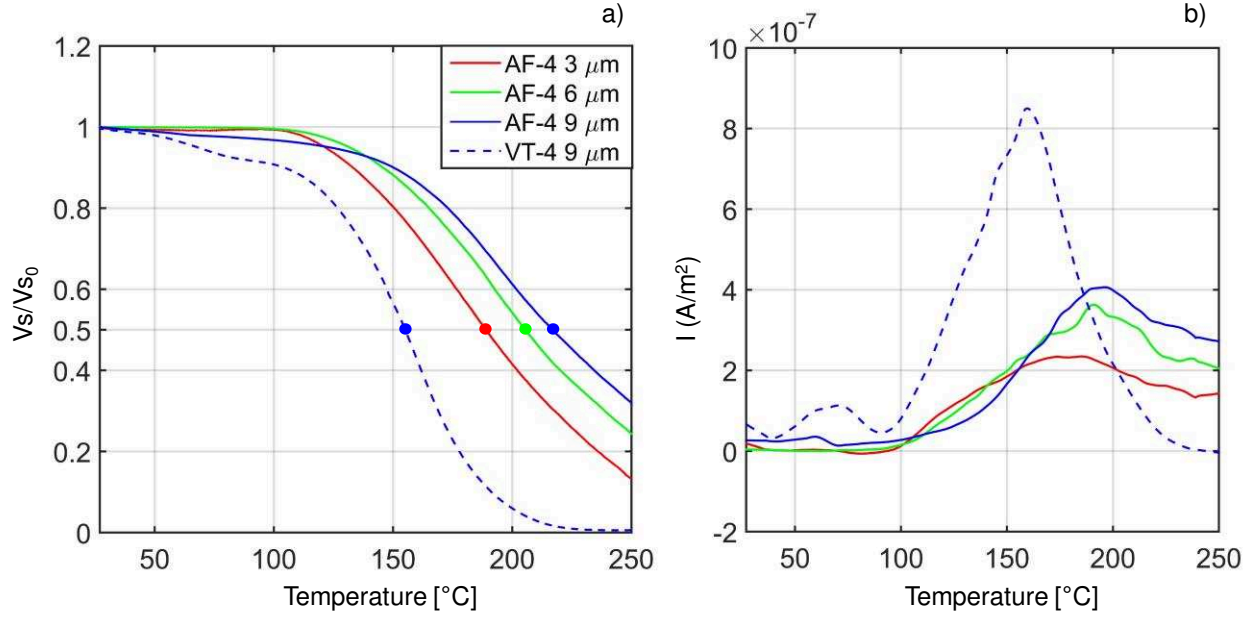


Figure 3. 17: Thermally stimulated potential decay (a) and derived charge release current  $I(T)$  (b)

TSD measurements on Parylene AF-4 confirmed the results found from isothermal potential decay measurements: while linearly heating up the electrets, higher thickness samples showed higher charge stability. Specifically, the half-value temperature  $T_{1/2}$  (i.e. the temperature at which the surface potential of the electret reaches a value equal to half the initial one) of the 9- $\mu\text{m}$ -thick sample of Parylene AF-4, is 10 °C higher compared to the 6- $\mu\text{m}$ -thick sample and 25 °C higher compared to the thinner material tested (3  $\mu\text{m}$ ). By comparing this material with Parylene VT-4, one can note that this latter presents a half-value temperature equal to 155 °C, namely 62 °C lower compared to the same thickness of the other fluorinated polymer sample. For Parylene AF-4 the temperature peaks ( $T_p$ ) of the derived release currents correspond to 185 °C, 191 °C and 196 °C for respectively increasing thicknesses, while for 9- $\mu\text{m}$ -thick Parylene VT-4  $T_p$  is equal to 160 °C. Using equation 3.8, the activation energies of 9- $\mu\text{m}$ -thick Parylene AF-4 and VT-4 samples were calculated and were found to be respectively equals to 1.23 eV and 1.16 eV. These values are consistent with the ones found in the literature for polymeric electrets [3.3] and with the value of

1.26 eV found in [3.40] for Parylene AF-4 and can be associated to space-charge polarization of the fluorine species. As shown in [3.41], C-F bonds dissociation and consequent migration and trapping of fluorine species at the interface with electrode may occur at low frequencies and high temperatures ( $>100^{\circ}\text{C}$ ). These fluorine species compensate the positive charge on the electrode, thus inducing surface potential decrease because of electrical neutrality. This hypothesis seems to be in agreement with our results and could explain the peaks shown in Figure 3.17.

From results obtained on TSD, 9- $\mu\text{m}$ -thick Parylene AF-4 presents better performance in term of stability compared to the same thickness of Parylene VT-4.

### 3.2.4 Environmental charges stability

In chapter 3.2.2, SPD results obtained when keeping the samples at normal room temperature (RT) conditions (mean temperature and RH respectively equal to  $26^{\circ}\text{C}$  and 40%) were presented. Nevertheless, when considering our wearable application, harsher environmental conditions can occur, influencing electrets charge stability over time. The evolution of electret surface potential, when exposed to different temperature and relative humidity (RH) values, was thus evaluated for the 9- $\mu\text{m}$  thick fluorinated Parylene samples. As this work aims in developing energy harvesting devices for wearable applications, it can be assumed that the maximal temperature value at which the electret materials will be exposed is equal to  $80^{\circ}\text{C}$ . The maximal RH value was calculated using the humidex index, which is an indicator used by meteorologists to describe how hot the weather perception, by combining the effect of heat and humidity [3.21]. The humidex can be calculated by the following simplified formula, based on works carried out by Masterton *et al.* [3.42]:

$$\text{Humidex} = T_{\text{air}} + 0.56 \times \left[ 6.11 \times e^{5417.75 \left( \frac{1}{273.16} - \frac{1}{T_{\text{dew}}} \right)} - 10 \right] \quad (3.10)$$

where  $T_{\text{air}}$  represents the air temperature ( $^{\circ}\text{C}$ ) and  $T_{\text{dew}}$  the dewpoint (K). Table 3.6 shows the effect on human body caused by the different humidex ranges [3.43]:

ZONE	HUMIDEX RANGE	EFFECT ON HUMAN BODY
1	Less than 29	Little or no discomfort
2	30 to 34	Noticeable discomfort
3	35 to 39	Evident discomfort
4	40 to 45	Intense discomfort
5	Above 45	Dangerous discomfort
6	Above 54	Heat stroke probable

Table 3.6: Degree of comfort or discomfort of human body for different humidex ranges

Considering an air temperature equal to 30°C, corresponding to the maximal mean temperature registered during summer in France, it can be calculated that a humidex index equal to 39 (limit of zone 3) is obtained for RH value equal to 60%. We thus set the maximal RH values used in the protocol equal to 60%.

In the first set of experiments, the influence of temperature and RH in the first days after samples charging was evaluated. Samples were charged using corona discharge method with an initial charging voltage equal to  $-1000\text{ V}$ . After 48 hours, two environmental conditions-controlled protocols were applied (Figure 3.18) using a climatic chamber (VOTSCH VC0018) and monitoring the SPD of the samples every second during the experiment duration. In the temperature-controlled protocol (Figure 3.18a), the temperature was linearly increased with a speed of  $0.25^\circ\text{C}/\text{min}$  till the maximal temperature of  $80^\circ\text{C}$ . Then, this value was maintained constant for 2 hours before linearly decreasing it until reaching the environmental one. During all the protocol duration, the RH value was maintained fixed at 35%. In the RH-controlled protocol instead (Figure 3.18b), the relative humidity was varied between 30% and 60% by maintaining each RH value constant for 1 hour to let the sample absorb water and then increased to the following step with a speed of  $5\%.\text{min}^{-1}$ . The temperature was maintained fixed for all the protocol duration at  $30^\circ\text{C}$ .

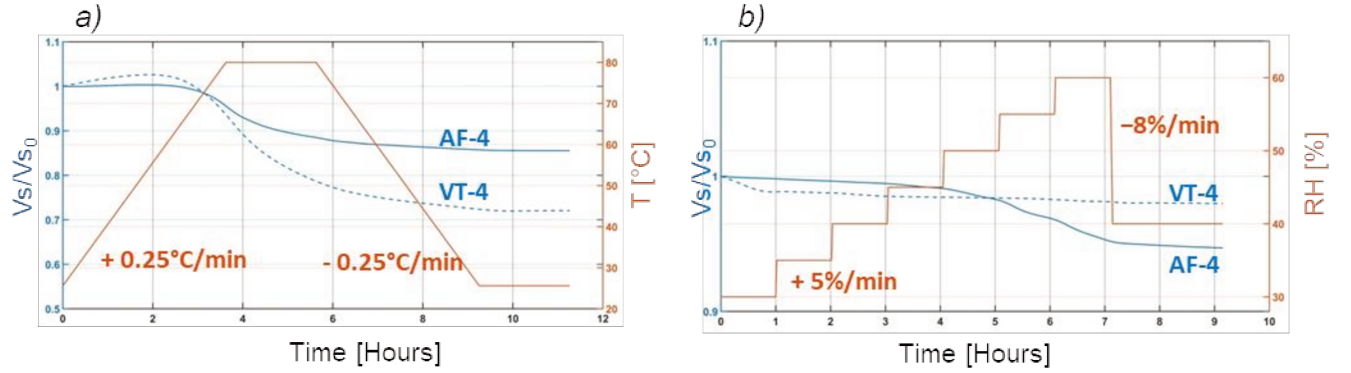


Figure 3. 18: Results obtained from the temperature (a) and RH (b) protocols applied on 9-μm thick fluorinated Parylene samples after 48 hours from charging

When the first protocol was applied, 9-μm-thick Parylene AF-4 and VT-4 samples RSPD at the end of the measures were respectively equal to 0.86 and 0.74, with values higher than 0.95 for temperatures lower than 72°C. The RH protocol induced RSPD values respectively equal to 0.95 and 0.98 for AF-4 and VT-4.

It is important to highlight that in this phase (48 hours after charging) the surface potential of the samples is not yet stabilized to a constant value, and the SPD measured in these experiments stands in the same confidence interval calculated for samples maintained at RT conditions (Figure 3.14). For these reasons, we were not able to quantitatively define how the environmental conditions influenced the SPD of the samples.

To better understand this point, the same protocols were applied on a stabilized 9μm-thick fluorinated Parylene charged at  $-1000\text{ V}$ , namely all the measurements described in Figure 3.18 were done 200 days after the electret charging was done (these samples are named “long-term sample” in the rest of this chapter). In this case, when applying the two environmental protocols, the surface potentials of the samples remained quasi-constant for all the experiments durations, with RSPD values higher than 0.95 (Figure 3.19a).

We thus tested the performance of long-term samples when extended solicitations were applied, by maintaining them at the extreme environmental conditions of the two protocols for 24 hours in the climatic chamber. These conditions correspond to 80 °C and 35% RH for the temperature protocol and to 60% RH and 30 °C for the relative humidity one. The results obtained on 9µm-thick Parylene AF-4 and VT-4 are shown in Figure 3.19b:

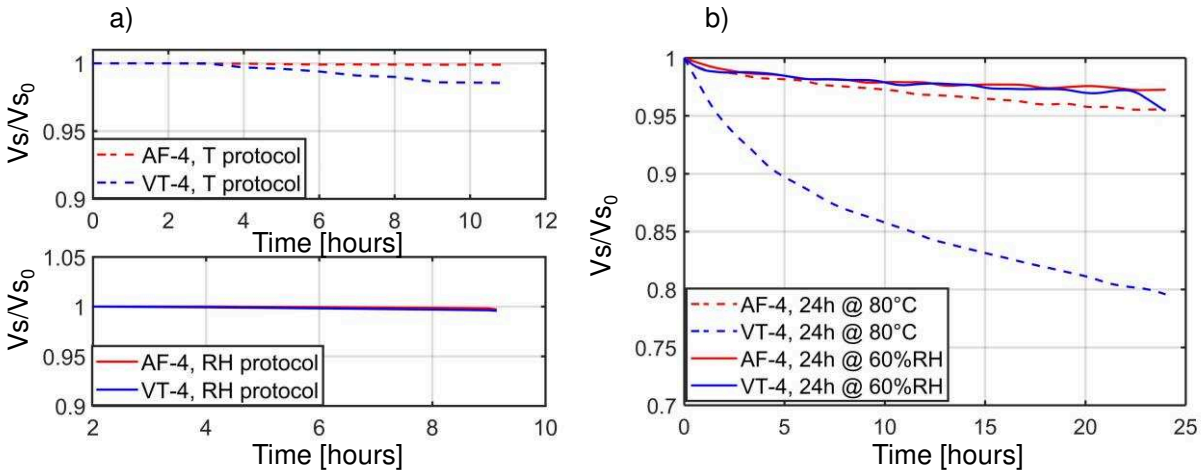


Figure 3. 19: SPD values of long-term samples during the application of two environmental protocols (a) and maintained for 24 hours at extreme environmental conditions (b)

One can note that AF-4 and VT-4 showed good stability (RSPD close to 1) when maintained for 24 hours at 60% RH. In addition, Parylene AF-4 was found to be an excellent electret also for harsh environments applications, showing RSPD value equal to 0.95 when 24-hours thermal solicitation at 80 °C was applied. Parylene VT-4, although presenting lower thermal stability over time compared to the other fluorinated variant, showed a high RSPD value equal to 0.80.

## Conclusion

In this chapter, three poly-p-xylylene polymers variants, namely Parylene C and the fluoropolymers Parylene AF-4 and VT-4 were tested as electret materials for energy

harvesting applications. We demonstrated that the fluorinated variants present surface potential over long-term more than 50% higher than Parylene C, probably because of their apolar nature and symmetric chemical structures. These fluoropolymers showed after 100 days surface potential values as high as  $-740$  V for 9- $\mu\text{m}$ -thick Parylene AF-4, and equal to  $-780$  V for the same thickness of Parylene VT-4 samples, independently from the initial charging voltage. From isothermal potential decay measurements differences lower than 10% were observed between the positively and negatively charged Parylene AF-4 electrets, indicating its applicability also for devices with double polarity electrets materials. Faster potential decays were measured in samples with lower thickness due to higher charge injection from the surface to the bulk. Thermally Stimulated Discharge (TSD) measurements confirmed the results obtained for isothermal SPD, specifically the higher stability of 9- $\mu\text{m}$ -thick Parylene AF-4 sample over the thinner ones. TSD peaks were shown at temperatures (respectively equals to  $185$  °C,  $191$  °C and  $196$  °C for thicknesses of 3, 6 and 9  $\mu\text{m}$  for Parylene AF-4) comparable to Teflon AF with same thickness, namely  $50$ °C higher than CYTOP [3.44]. Moreover, Parylene AF-4 showed temperature stability up to  $100$  °C for all the thicknesses tested and higher charge retention than Parylene VT-4 when maintained for 24 hours at  $80$ °C. Both materials presented good stability when maintained for 24 hours in high RH environments.

In conclusion, 9- $\mu\text{m}$ -Parylene AF-4 resulted the most suitable electret between the polymers tested for the development of energy harvesting devices.

In the next chapter, the application of these three conformant electrets polymers on energy harvesting devices (with particular focus on 9- $\mu\text{m}$ -Parylene AF-4) will be presented and discussed.



# **CHAPTER 4.**

## **ELECTRET-BASED ENERGY HARVESTING DEVICES**





## **Chapter 4. Electret-based energy harvesting devices**

As discussed in Chapter 1, the aim of this work is to fabricate an energy scavenger to be integrated at human limb level to exploit the relative movement between the upper and lower part of the limb, namely a variation of the angle. The design of the device needs thus to be properly chosen to fit the location and the characteristics of human movement. This means that the scavenger needs to work under low working frequencies (1 to 2 Hz when considering walking or running) and low deformation forces (of the order of few Newton). In addition, the device needs to be made of soft materials and to be compliant in order not to disturb human movements. To accomplish these requirements and to obtain an energy level useful for low-power consumption devices supply (see paragraph 1.1), a hybrid structure coupling electret material with dielectric elastomers is chosen. In this chapter, the first hybrid energy harvesting device previously developed by our team will be presented. A description of the working principle and the constitutive equations will be first introduced. Then, both the influence of the electret material performance studied in chapter 3 and the scavenger shapes will be discussed aiming to increase the power output of the device and reduce the total encumbrance of the structure. Lastly, the results on the experimental realization of an energy harvesting prototype will be presented and different solutions for the power management unit will be discussed.

### **4.1 Device working principle**

The schematic and working principle of the device are shown in Figure 4. 1.

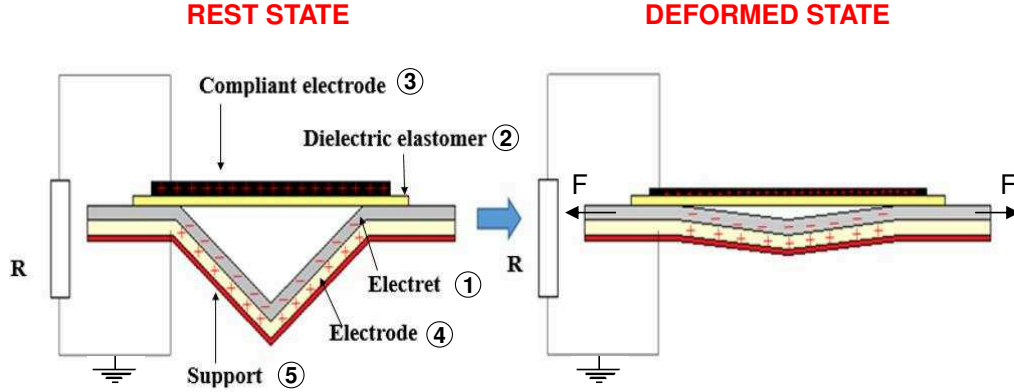


Figure 4. 1: Schematic and working principle of the energy harvesting device

The main structure is constituted by a texturized support (⑤ in Figure 4. 1) on which a ground electrode (④) and an electret material (①) are deposited. This latter is charged by corona discharge method up to surface potential  $V_s$ , given by implanted charges (see paragraph 4.3.1 for details). On the upper part stands the elastomeric membrane (②) on which a compliant deformable electrode (③) is applied. The elastomeric membrane is used as dielectric layer between the upper electrode and the electret material. Beneath guarantying the applicability of a stretch to the device, it also avoids the contact between these two elements, which could compromise the stability of the electret material over time. The total equivalent electrical capacitance ( $C_{tot}$ ) of the device in the rest state is given by the contribution of the series of the three elements:

$$\frac{1}{C_{tot}} = \frac{1}{C_{DE}} + \frac{1}{C_{air}} + \frac{1}{C_{el}} \quad (4.1)$$

Namely  $C_{DE}$ ,  $C_{air}$  and  $C_{el}$  represent respectively the equivalent capacitances of the dielectric elastomer, of the air and of the electret material. When uni-axial mechanical deformation is applied to the structure, the dielectric elastomer (②) stretches and the two lateral sides of the texturized support (⑤) undergo a vertical movement: the electret material (①) thus moves toward the upper part of the device, thus reducing the air gap between the electret and the dielectric elastomer. The texturized support on which lays the electret material was necessary to couple the two electroactive elements (electret and dielectric): in fact, while the hyperelastic nature of the

elastomeric material allows it supporting high deformation strains, high solicitations on the electret material could lead to mechanical fracture and electrical discharge. Ideally, when the structure is at its maximal deformation state, no residual air gap is present between the two electroactive elements. In this state, the device presents the maximal equivalent capacitance. The charges induced on the two electrodes (③ and ④) by the electret material (①) will thus reorganize following the device capacitance variation. Consequently, a flux of charges between the two electrodes will occur resulting in an electrical current circulating through an external electrical load  $R$ . Then, the device will go back to its initial position. When the electret gets away from the upper electrode, the electrical current will flow back through the load  $R$ . As the mechanical force acting on the device is quite sinusoidal, the output current and voltage are alternatives.

The equivalent electrical circuit describing the working principle is shown in Figure 4.2.

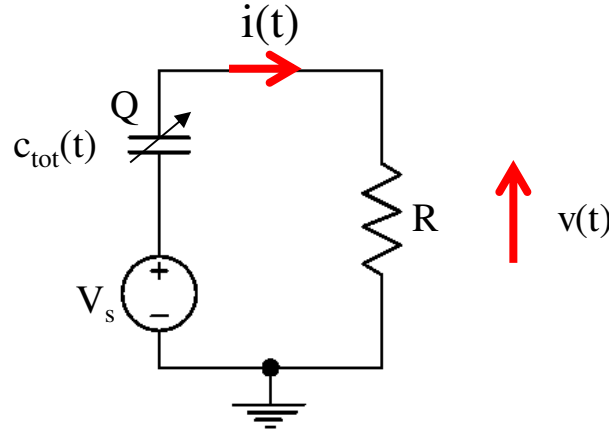


Figure 4. 2: Equivalent electrical circuit of the energy harvesting device

As explained in paragraph 2.2.3, the device is represented as a variable capacitor  $C_{tot}$ , namely the series of the three constitutive elements and a constant voltage generator, whose value ( $V_s$ ) is equal to the electret surface potential. The constitutive equations of this device can be expressed as:

$$\begin{cases} i = \frac{\partial Q}{\partial t} = \frac{V_s}{R} - \frac{Q}{RC_{tot}} \\ P_{avg} = \frac{1}{t_2 - t_1} \int_{t_1}^{t_2} R \left( \frac{\partial Q}{\partial t} \right)^2 dt \end{cases} \quad (4.2)$$

where  $i$  stands as the electric current,  $Q$  represents the electric charge on  $C_{tot}$  at the instant  $t$ ,  $R$  the resistive load and  $P_{avg}$  the average power output calculated between the instants  $t_1$  and  $t_2$ .

## 4.2 Proof of concept

The first hybrid structure developed in 2012 by our team with this principle was constituted by a texturized triangular support made of three patterns, as shown in Figure 4.3 [4.1].

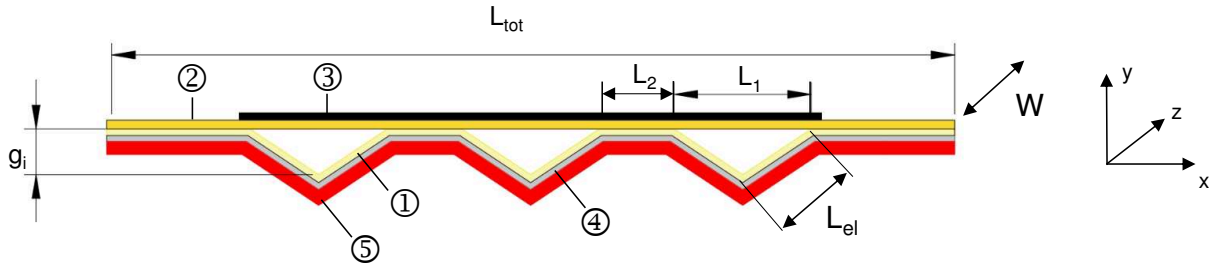


Figure 4. 3: First device schematic

Based on the desired location (behind the knee), the scavenger handles an active deformation of 50% at 1 Hz in a pure-shear mode (the width  $W$  is supposed to remain constant during deformation). It is composed of active parts ( $L_1$ ) and passive parts ( $L_2$ ) which amplify the output deformation to reach the desired deformation level in the active part.

The optimal dimensions of the scavenger at rest were:  $L_{tot}=10$  cm,  $g_i=1.2$  cm,  $L_1=2$  cm,  $W=3$ cm,  $L_{el}=1.5$  cm. The electret material (① in Figure 4.3) chosen in the first device consisted of a commercial 50- $\mu$ m-thick Teflon FEP. Its optimal surface potential was

found to be equal to  $-1000$  V. The elastomeric membrane chosen in this application consisted of a silicone membrane (Danfoss Polypower®) with a rest thickness of  $40\text{ }\mu\text{m}$  and a dielectric constant equal to 3, and an upper electrode made in carbon grease (846 MG Chemical). This first proof of concept scavenges up to  $33\text{ }\mu\text{W}$ , on an optimal load of  $99\text{ M}\Omega$ . The corresponding scavenged energy density, was about  $0.55\text{ mJ.g}^{-1}$  and can increase up to  $1.42\text{ mJ.g}^{-1}$  in ideal case (with no residual air gap).

Optimizations are necessary to reach the required level of  $100\text{ }\mu\text{W}$  enough to supply a low-consumption device. The scavenger shape must be adjusted in order to reduce the residual air gap leading to increase of the output performances. Before that, one can be interested in the influence of the dielectric material but also of the electret surface potential value on the output power.

To evaluate the influence of the dielectric elastomer on the device performance, we compare the device parameters in case of presence and absence of this elastomeric membrane (DE). In this last case, the dielectric layer separating the two elements is simply replaced by air (dielectric constant of 1) with the same thickness. Simulations of the three-patterns triangular shape (Figure 4.3), in the ideal case with no residual airgap, were first performed by implementation of equations 4.1 and 4.2 on Matlab Simulink. Capacitance calculation through equation 4.1 consists of a simple analytical equation detailed in [4.1], calculated for all the deformation states through geometrical considerations on the resulting deformed configuration. Ideal pure-shear case is considered with no edge effect and no mechanical losses.

Simulation results obtained on the device performance with two different dielectric materials (DE and air) are shown in Figure 4.4.

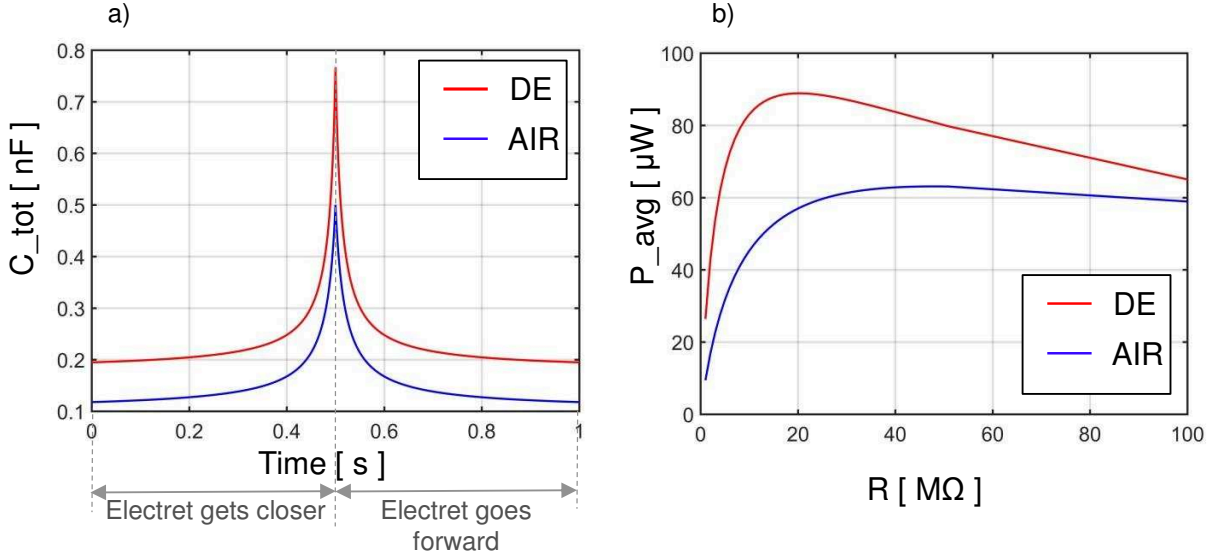


Figure 4. 4: Influence of the dielectric elastomer membrane on the device performance: evolution of the total electrical capacitance as a function of time (a) and average scavenged power for different loads.

One can note that, when considering the same device encumbrance, the presence of the DE membrane increases the total capacitance of the device and the energy harvested: while in case of presence of the DE an ideal power of 85  $\mu\text{W}$  can be scavenged on an optimal load of 20  $\text{M}\Omega$ , the maximal power scavenged with a layer of air is equal to 62  $\mu\text{W}$  on an optimal load of 40  $\text{M}\Omega$ , namely 27 % lower. The dielectric elastomer membrane contributes to enhance the performance of the device. Indeed, the dielectric constant of the DE is higher and its breakdown field is more than 10 times larger compared to the one of air (whose breakdown field is equal to 3  $\text{kV}\cdot\text{mm}^{-1}$ ). More the permittivity of the dielectric elastomer increases, more energy is scavenged. Regarding materials available (see chapter 2), acrylic and silicone could fit our requirements of high dielectric constant but acrylic elastomers develop too high electric and mechanical losses thus reducing the potential scavenged energy. Thus, silicone will be used in our improved prototype (specifically Sylgard 186 from Dow Corning). Moreover, more the elastomeric membrane is thin, more energy is scavenged. The simulations have shown a diminution of at least 18% in the theoretical output power between the case of minimum elastomeric thickness (40  $\mu\text{m}$ ) and maximum one (350  $\mu\text{m}$ ) [4.2].

On another end, as underlined in [4.1], electret surface potential has a huge impact on the output performances of the scavenger. For the first proof of concept detailed in Figure 4.3, 33  $\mu\text{W}$  was scavenged with a Teflon FEP electret developing a surface potential of  $-1000\text{ V}$ , but 150  $\mu\text{W}$  is expected with the same structure with  $-2000\text{ V}$  surface potential of the electret.

Electret thickness could also be influent. Figure 4.5 shows the performance of the triangular shaped prototype (Figure 4.3) when Parylene AF-4 electret (one of the most promising electret material, as seen in chapter 3) is employed, as a function of its thickness and surface potential. The dielectric elastomer is classic silicone membrane with a thickness of  $40\text{ }\mu\text{m}$  and a dielectric constant of 3.

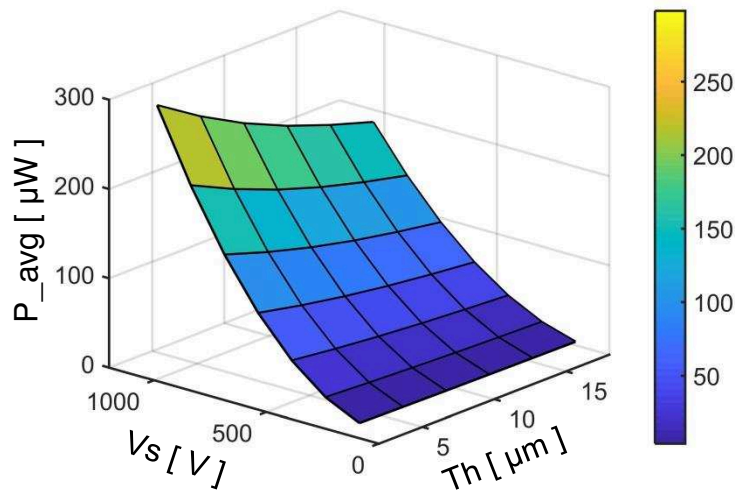


Figure 4. 5: Performance of the triangular shaped device with Parylene AF-4 as electret material: influence of the thickness ( $Th$ ) and of the surface potential ( $V_s$ )

As derived from equations (4.2), lower electret material thickness and higher surface potential  $V_s$  result in a higher power scavenged by the device. As an example, 6- $\mu\text{m}$  and 9- $\mu\text{m}$ -thick Parylene AF-4 could scavenge a theoretical output power of respectively 240  $\mu\text{W}$  and 210  $\mu\text{W}$  when  $V_s = -1000\text{ V}$ . Nevertheless, the results obtained in chapter 3 revealed higher charge retention for higher thickness electret materials, leading to higher device lifetime and performance.



Figure 4.6 shows the results obtained when integrating the charge stability results given by the various Parylene materials after 100 days in the analytical modelling previously presented (derived from equations 4.1 and 4.2). Parameters (Parylene type, thickness, measured dielectric constant, measured surface potential after 100 days) and the theoretical performances (output power on optimal load) for a three-patterns triangular support are summarized in Table 4.1. No residual air gap is considered in the deformed state.

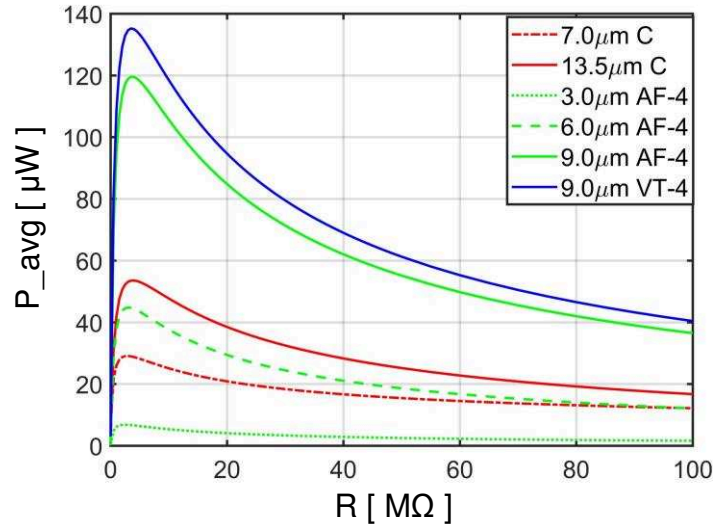


Figure 4. 6: Performance of the device with different electret Parylenes

Name	Parylene type	$\epsilon_r$	Thickness [μm]	$V_s$ [V]	$P_{avg}$ [μW]	$R_{opt}$ [MΩ]
C1	C	3.15	7.0	-300	29.1	3.0
C2	C	3.15	13.5	-500	53.5	4.0
A1	AF-4	2.24	3.0	-158	6.8	2.5
A2	AF-4	2.24	6.0	-430	44.8	3.0
A3	AF-4	2.24	9.0	-740	119.5	3.5
V1	VT-4	2.38	9.0	-780	135.2	3.5
Teflon FEP [4.1]		2.10	50.0	-1000	85.0	20

Table 4. 1: Characteristics of the Parylene electret material and corresponding scavenger performance

Simulation results revealed that output power higher than 100  $\mu\text{W}$  can be obtained when employing 9- $\mu\text{m}$ -thick fluorinated Parylene materials. Specifically, a theoretical average output power of 120  $\mu\text{W}$  and 135  $\mu\text{W}$  can be respectively obtained with Parylene AF-4 and VT-4. These values are higher than the one obtained with the first prototype (85  $\mu\text{W}$  in theory). This is due to the high charge density present in the two polymers (respectively equals to 1.7  $\text{mC}\cdot\text{m}^{-2}$  and 1.8  $\text{mC}\cdot\text{m}^{-2}$  for AF-4 and VT-4) which guarantees a high electret surface potential in a lower material thickness, lower thickness resulting in a higher equivalent capacitance.

Figure 4.7 shows the capacitance variation over time (equation 4.1) and the voltage output (equation 4.2) of the device made of 9- $\mu\text{m}$ -thick Parylene AF-4 electret material, which resulted from chapter 3 as the most suitable among the tested polymers in terms of charge retention and environmental stability. This device described in Figure 4.3 (triangular shape), is subjected to a deformation of 50% at 1 Hz.

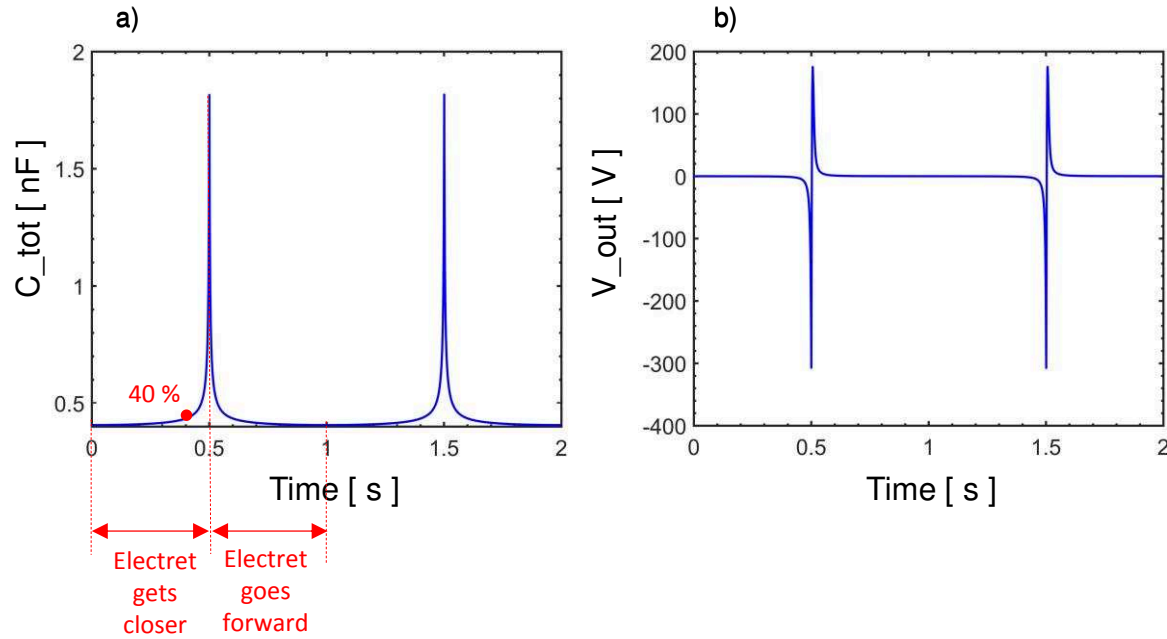


Figure 4. 7: Electrical parameters of the device with 9- $\mu\text{m}$ -thick Parylene AF-4 (sample A3 in Table 4. 1): capacitance variation (a) and output voltage through the optimal load (b)

The electrical capacitance (Figure 4.7a) first linearly increases and then reaches its maximal value (no residual airgap,  $g_f=0$ ) with an exponential trend. The higher

capacitance variation occurs for deformation values higher than 40% (point reported in Figure 4.7a), namely an air gap between the two elements lower than 0.6 mm.

Figure 4.7b shows the output voltage trend through the 3.5 M $\Omega$  optimal load. One can note that the output voltage presents an alternative trend as a function of the deformation state on the device, due to charge recombination between the two electrodes. This trend is classic for electret-based electrostatic devices [4.1],[4.6]. The maximum power transfer to the external load ( $R$ ) occurs when this latter is close to the harvester internal impedance. A power management unit will then be necessary to adapt the voltage output to the final storage or application unit, as it will be discussed in paragraph 4.5.

The results obtained with silicone dielectric elastomer and Parylene AF-4 electret are promising (120  $\mu$ W) but remains theoretical. Further improvements (on the prototype shape) are necessary to guarantee its performance and lifetime (millions of cycles without performance deterioration). Indeed, the triangular shape guarantees a simple solution as coupling element between the DE and the electret material, but it also creates a stress concentration area on the electret in the tip of the triangle structure. The Comsol structural mechanical module was employed for Finite Element Method (FEM) simulations of the triangular shape, using the parameters described in Table 4.2.

	<b>Material</b>	<b>Young modulus [MPa]</b>	<b>Poisson ratio</b>
ELECTRET	50- $\mu$ m-thick Teflon FEP	480	0.48
DE	40- $\mu$ m-thick Danfoss Polypower	1.1	0.47
GROUND ELECTRODE	130- $\mu$ m-thick electrically conductive tape	300	0.49
FRAME	400- $\mu$ m-thick plastic acetate	1600	0.4

Table 4. 2: Parameters employed for structural mechanics FEM simulations

Figure 4.8b shows the von Mises stresses developed on the triangular device by the application of an external mechanical force in the maximal deformation state, shown in Figure 4.8a:

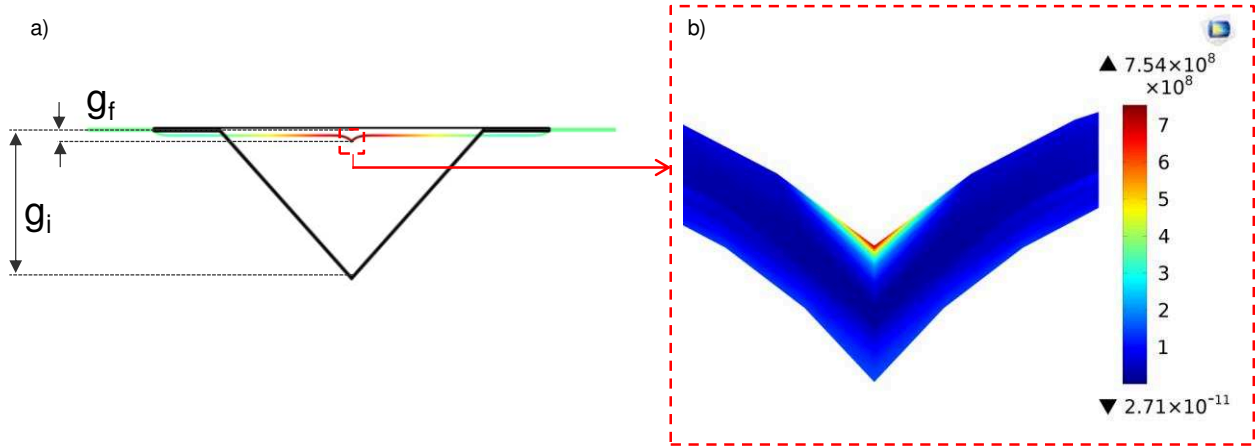


Figure 4. 8: Device schematic in the rest and deformed state (a) and simulations results on the Von Mises stresses [Pa] acting on the structure in the maximal deformation state (b).

Simulated von Misses stresses are high (750 MPa), underlying an important deformation for the electret material that can cause mechanical breakdown or accelerate the fatigue process (creation and propagation of cracks). Beneath the high mechanical stresses developed in the electret material, the tight apex angle results in a higher residual final air gap between the two electroactive elements in the central part of the structure, as shown in Figure 4.8a. The ideal condition of  $g_f=0$  cannot be reached in experiments with this shape, resulting in a lower variation of the electrical capacitance of the device and in the decrease of the total energy harvested by the device. Numerical simulations confirm the experiments done in [4.1] and revealed a residual final air gap ( $g_f$ ) between the upper and lower part of the structure equal to 500  $\mu\text{m}$  in the maximal deformation condition, which is a huge value. Decreasing the residual air gap is necessary to achieve the needed output electrical power of 100  $\mu\text{W}$  that could supply low-consumption sensors. To overcome these limitations (output power, stresses), new **design structures** are conceived, with the aim of ameliorating the performance and lifetime of the devices.

### 4.3 Scavenger design optimization

Starting from the first realized prototype, shape optimization was performed over the 3-frames triangular shape with the aim of increasing the power output. We propose to degrade the triangular shape up to a ‘bol’ shape to reduce the sharp profiles. Two control geometrical parameters were employed to this aim: the curvature radius of the apex ( $R_a$ ) and the one of the basis of the triangular shape ( $R_b$ ), see Figure 4.9.  $R_b$  was varied between 0.2 and 2 mm, while  $R_a$  values between 0.5 and 10 mm were tested. The objectives are the minimization of von Mises stresses on the prototype and maximization of the capacitance variation of the device between the rest and the deformed state (50%). On Table 4. 3, the different material parameters and properties employed in the FEM simulations are reported.

	Material	$\epsilon_r$	Young modulus [Mpa]
ELECTRET	50- $\mu$ m thick Teflon FEP	2.0	480
DE	40- $\mu$ m thick Sylgard 186 (Hyperelastic Moonley Rivlin model with $C10=0.105$ MPa and $C01=0.08$ MPa [4.3])	2.70	0.85 [4.4]
UPPER ELECTRODE	846 Carbon conductive grease (MG Chemical)	-	$\sim 0.1$
LOWER ELECTRODE	100-nm thick Au electrode	-	$79 \times 10^3$
SUPPORT FRAME	0.8mm-thick 3D-printed Filaflex (Ninjatek)	-	3.62

Table 4. 3: Parameters employed for FEM simulations

One can note that the electret used here is the same as the one in the proof of concept as we want to underline only the benefit of the design optimization and not the materials and shape benefits. The dielectric elastomer is the Sylgard186 which has quite the same characteristics of the Danfoss Polypower elastomer and which will be used in the experimental part. The first optimization showed that the structure reaching the higher capacitance variation was the one with  $R_b = 0.2$  mm and  $R_a = 10$  mm, namely the ‘bol’ structure. Nevertheless, high von Mises stresses were present at lower electrode level, which can induce electrode cracks or fractures. Indeed, when  $R_a$

is higher than 2 mm, the length of the electret material is too small and the structure cannot handle high strains without high stresses at lower electrode and electret level. For this reason, a ‘serpentine’ shaped support was conceived with a variable number  $N$  of basic patterns. Shapes with  $N$  varying between 10 and 30 were tested, this upper limit being fixed by the spatial resolution of the 3D printing fabrication. The optimal number of serpentes to insure high deformation on the structure (50%) is equal to 25. In the following, this prototype will be named ‘serpentine’ shape. The last shape chosen from the preliminary optimization was the one presenting  $R_b = 0.2$  mm  $R_a = 2$  mm, named ‘rounded’ prototype, due to low von Mises stresses and the low air gap reachable in the maximal deformation state. The three shapes schematics and parameters of a single pattern are shown in Figure 4.9.

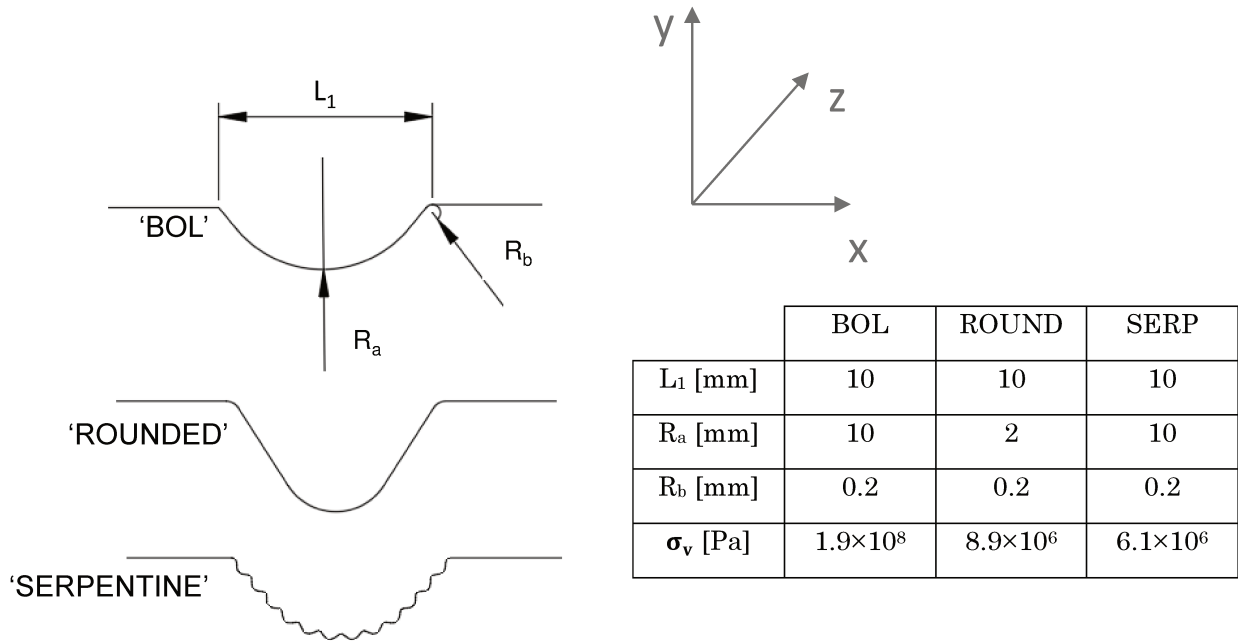


Figure 4. 9: Schematics and dimensions of the shapes chosen from the optimization study

One can note that, from a mechanical point of view, the lower stresses applied to the lower electrode and to the electret material are obtained for the serpentine-shaped support (6.1 MPa). The ‘bol’ shape presents instead the higher values and thus this shape will be studied only for comparison with the other structures. The ‘rounded’ structure and the von Mises stresses results obtained on the electret from FEM

simulations (mechanical module of Comsol Multiphysics) in the maximal deformation state are respectively shown in Figure 4.10 a and b.

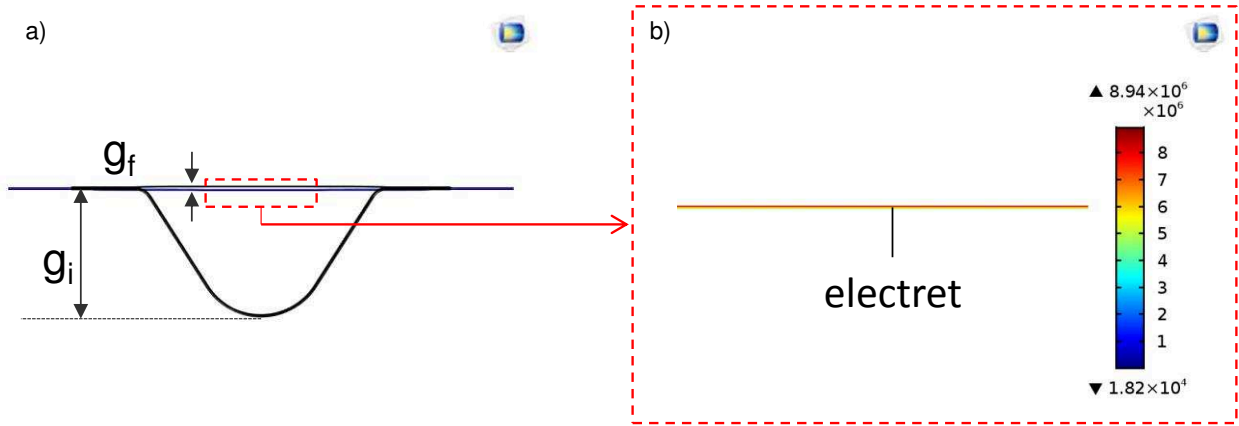


Figure 4.10: Resulting deformed structure on the ‘rounded’ device (a) and von Mises stresses [Pa] distribution on the electret material (b)

One can note that lower final air gap values (equal to  $100 \mu\text{m}$ ) (Figure 4.10 a) can be obtained in the deformed configuration, with no stress concentration areas in the geometry (Figure 4.10 b). Stresses distribution on the electret material are more uniform and 2 orders of magnitude lower than the simple triangle shape.

For the three chosen prototypes, the electromechanical module of Comsol Multiphysics was employed to calculate their capacitance variation following the 1-Hz cyclic mechanical deformation representative of human motion. Indeed, analytic expression of the capacitance variation assumes a more complex form in these shapes and cannot be calculated through simple geometrical considerations as in the simple triangular case. Beneath, analytical method does not account for edge electrostatic effects that can decrease the global capacitance value. Perfect pure-shear deformation mode was implemented for DE deformation, with constant membrane width in the different phases (see paragraph 2.2.2.3 for details) and material parameters listed in Table 4.3.

The energies scavenged by the devices were calculated with Matlab Simulink equations implementations. Simulations results obtained for the average scavenged power and for the voltage output on the optimal resistive load are shown in Figure

4.11, while Table 4. 4 summarizes the principal electrical parameters calculated in case of no residual air gap ( $g_f$ ) in the final deformation state.

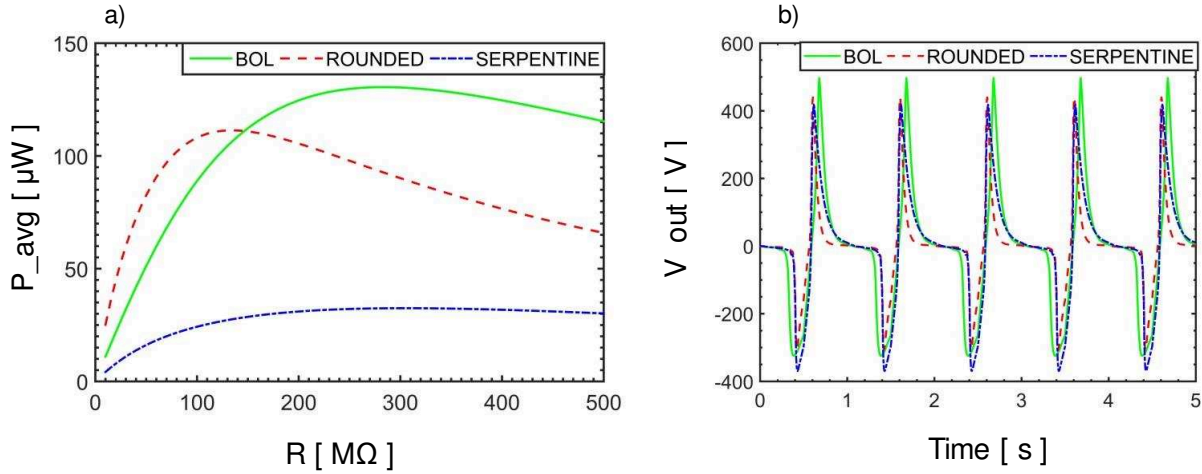


Figure 4.11: Performance of the devices: average output power as a function of the resistive load  $R$  (a) and output voltage through the optimal  $R$  (b)

	$C_{max}$ [F]	$C_{min}$ [F]	$C_{max} / C_{min}$	$P_{avg}$ [ $\mu W$ ]
<b>BOL</b>	$6.28 \times 10^{-10}$	$2.7 \times 10^{-10}$	2.36	130
<b>ROUND</b>	$5.6 \times 10^{-10}$	$2.71 \times 10^{-10}$	2.07	112
<b>SERP</b>	$5.0 \times 10^{-10}$	$2.69 \times 10^{-10}$	1.85	33

Table 4. 4: Summary table on the different devices performance

As underlined in Figure 4.11 b, the three structures develop quite similar output voltage trends, typical of electrostatic structures. Only the maximal value and the response time differ. The ‘bol’ exhibits the maximal output voltage while the ‘rounded’ structure shows the quickest response time (sharp increase and decrease when electret gets close and away from the dielectric). Regarding the performances, the ‘serpentine’ shape can scavenge only 33  $\mu W$  for a wide range of resistances probably due to a low capacitance ratio. A ratio of 2 is generally the minimal value for a scavenger to be efficient. The ‘bol’ structure scavenges the highest output power (130  $\mu W$ ) on a huge



optimal load of 280 M $\Omega$ . The ‘rounded’ prototype presents the best compromise between scavenged output power and mechanical stresses on the structure: a theoretical output power of 112  $\mu$ W can be obtained on an optimal resistive load of 130 M $\Omega$ . This prototype was thus chosen for the experimental realization and tests, as described in the following paragraphs.

### 4.3.1 Experimental tests

Experimental realization of the ‘rounded’ prototype was performed using materials listed in Table 4. 3 (Sylgard186 as dielectric and Teflon FEP as electret), in order to validate the optimization of the shape design. The support frame was realized using the 3D printing facilities of FABLAB in Grenoble. The 3D printer employed for the prototypes frame realization was Ultimaker 2 Extended+ model, whose printing parameters were adapted through experimental tests for flexible materials printing. SemiFlex™ by Ninjatek, whose principal characteristics are reported in Table 4. 5, was the material selected for the prototype realization.

<b>SemiFlex™ 3D Printing Filament mechanical properties</b>	
Tensile Strength, Yield [MPa]	9
Tensile Strength, Ultimate[MPa]	43
Tensile Modulus [MPa]	25
Elongation at Yield [%]	49
Elongation at Break [%]	600

Table 4. 5: Principal mechanical properties of the 3D printing material: SemiFlex™ by Ninjatek

Due to the semi-flexible nature of the material and to its low tensile modulus (25 MPa), the resulting frame is suitable for wearable applications as low stretching force is required to deform it (see performance paragraph 4.3.2). On the 3D-printed frame, 100-nm thick Au electrode was deposited through metal sputtering (QUORUM Q150T). A good adhesion of the gold electrode to the frame is noted with a very low electrode

surface resistance. A 50- $\mu\text{m}$ -thick commercial sheet of Teflon FEP was then glued on the ground electrode with Loctite 401 glue. The electret was subsequently charged with a surface potential of  $-1000\text{ V}$  through corona discharge method. Charging process was performed through the experimental setup described in paragraph 3.1.5 on different points of the electret in the deformed state, with the aim of obtaining a uniform charge distribution on the electret surface. The surface potential of the electret was checked thanks to an electrostatic probe (TREK 347). Then the Sylgard 186 elastomeric membrane (home-made material obtained by mixing two parts A and B and deposited with spin-coating process) is glued on the passive part of the frame and the upper electrode is deposited onto the membrane. This compliant electrode is a hand-brushed carbon grease electrode from MG Chemical. Finally, the electric contacts are realized: a wire is soldering on the lower ground electrode and a wire is fixed onto the upper electrode.

Figure 4.12 shows the experimental realization of the prototype, while on Figure 4.13 the mechanical test bench (a) and the experimental setup for prototype testing (b) are represented.

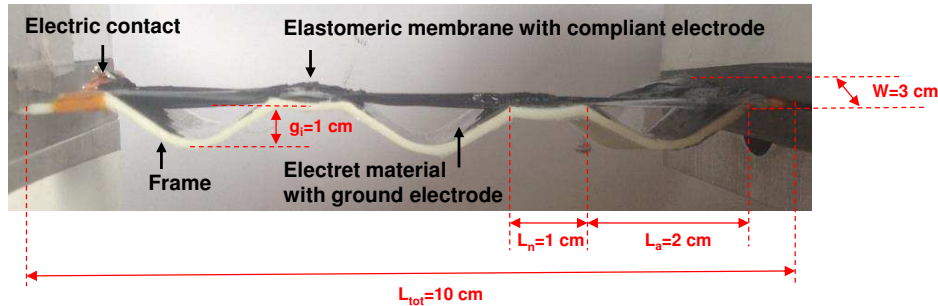


Figure 4.12: Prototype experimental realization

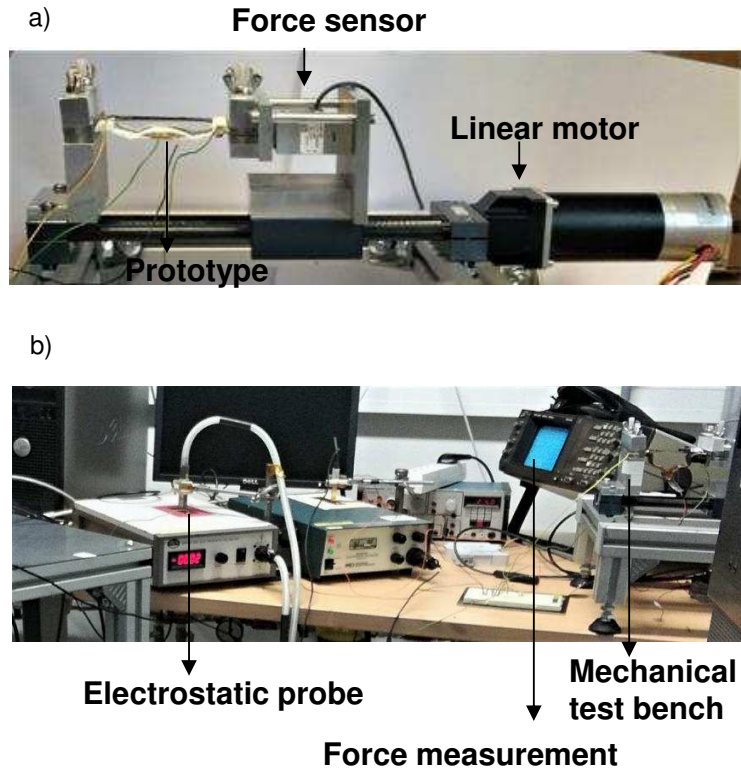


Figure 4.13: Mechanical test bench (a) and experimental setup for prototype testing (b)

The structure is clamped on one side on the test bench and can move on the other. The mechanical deformation was imposed to the device using a linear table from Igus, piloted by a linear DC motor (SM56.3 from STOGRA) controlled through a Labview interface, allowing imposing a linear movement in both directions with a determined speed (up to  $20 \text{ cm.s}^{-1}$ ) and acceleration (up to  $0.4 \text{ m.s}^{-2}$ ). Deformation cycles of 1 Hz and 50% were applied to the device, simulating the relative movement imposed by human limbs. The test bench also presents a force sensor (S2M from HBM) to measure the external force imposed to the device. To avoid electrical disturbance, a dielectric layer (Teflon) encapsulate the prototype in the two metallic jaws. The voltage output from the prototype is registered using an electrostatic probe (TREK 347) on a delocalized point, to avoid additional input resistive components classically present with recorders (i.e.

oscilloscope probes). Measurements were performed through different resistive loads ( $R$ ) to find the optimal value.

### 4.3.2 Device performance

The experimental testing results on the ‘rounded’ prototype were correlated with numerical simulations results. The minimal value experimentally reachable for the final air gap ( $g_f$ ) with our prototype was equal to  $100\text{ }\mu\text{m}$  (measurement done with a thickness sensor from Mitituyo in the experimental set-up described in Figure 4.13). In fact, as our prototypes are hand-made, lower final air gaps are not reachable: the different elements are not perfectly aligned and contact points between the electret material and the DE appear for lower air gaps.  $100\text{ }\mu\text{m}$  is thus the safety value found for  $g_f$ . This condition was thus set as final deformation state of the device in the FEM simulations to compute the scavenged power. Results obtained from the adjusted numerical simulations and from the experimental measurements are shown in Figure 4.14.

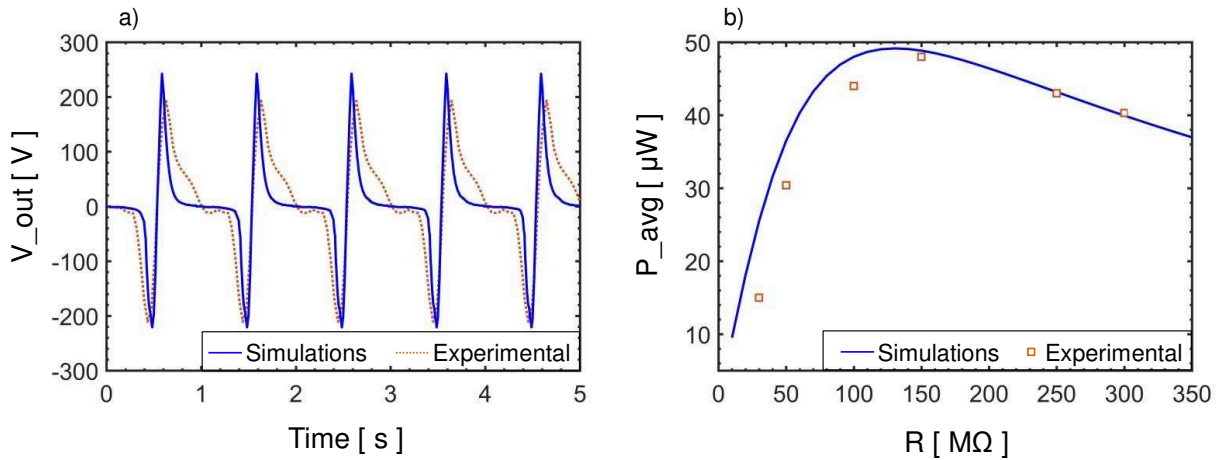


Figure 4.14: Device performance of the ‘rounded’ shaped prototype: experimental and FEM simulations obtained for the output voltage obtained through the optimal resistive load (a) and for the average scavenged power through different  $R$  (b).

The voltage output experimentally measured has quite the same trend as the simulated one, typical of electrostatic devices (Figure 4.14a). The maximal voltage value is similar in the two cases (240 V), while differences can be observed specifically in the release phase of the cycle, when electret goes forward from the dielectric elastomer. In the stretching phase, when electret gets closer to the dielectric, the dynamic of the structure obtained from experimental and simulation data is the same. In the release phase, the dynamic between experiment and simulation differs; an added phenomenon appears in the release phase which is not taken into account in the simulations. The structure does not have the time to perfectly follow the imposed deformation surely due to its low mechanical response time (viscous losses and relaxation). Moreover, one can note that on the entire experiments, the voltage response of the structure is shifted compared to the simulations, probably due to its electric time response (bulk resistive losses in the dielectric and the electret layers and surface resistive losses at electrodes level). An average scavenged power of 49  $\mu\text{W}$  (Figure 4.14b) was found from experimental results on an optimal load of 150  $\text{M}\Omega$  with a final air gap of 100  $\mu\text{m}$ , namely a value 56% lower compared to the theoretical one calculated in the condition of  $g_f=0$  (112  $\mu\text{W}$ ). This corresponds to an increase of  $\sim 48\%$  compared to the basic triangular structure (where 33  $\mu\text{W}$  on 99  $\text{M}\Omega$  was scavenged). A reduction of the von Mises stresses is also obtained from FEM simulations (see paragraph 4.3). The figure of merit (FOM) proposed in [4.5] was calculated for our device with the following equation:

$$FOM = \frac{P_h}{U^2 f S} \quad (4.3)$$

Where  $P_h$  is the output power of the scavenger,  $U$  is the maximal voltage applied on the capacitive transducer ( $\sim 1000\text{V}$ ),  $f$  is the working frequency and  $S$  is the device total surface area. The FOM obtained with our device was equal to  $2 \times 10^{-8} \mu\text{W} \cdot (\text{mm}^2 \cdot \text{Hz} \cdot \text{V}^2)^{-1}$ , which is higher compared to the other electret-based devices analyzed by the authors, as shown in Table 4. 6.

Author [reference]	FOM [ $10^{-8} \mu\text{W} \cdot (\text{mm}^2 \cdot \text{Hz} \cdot \text{V}^2)^{-1}$ ]
Tsutsumino <i>et al.</i> [4.6]	1
Ma <i>et al.</i> [4.7]	0.30
Suzuki <i>et al.</i> [4.8]	$2 \times 10^{-3}$
Vu Cong <i>et al.</i> [4.1]	1.32
This work	1.96

Table 4. 6: FOM of different electret-based energy harvesting devices

Results obtained from this prototype are promising, but further improvements are necessary to reach the targeted value of  $100 \mu\text{W}$  scavenged power. This value may be obtained through substitution of the electret material with fluorinated Parylenes or through prototype design solutions, as proposed in paragraph 4.4. Indeed, section 4.2 underlines that Parylene AF-4 presents a higher charge density and stability than the structure using this electret can scavenge more than a structure using Teflon electret. Parylene AF-4 was deposited onto our ‘rounded’ frame by Comelec Sa and experiments on corona discharge and surface potential stability were done (see section 4.3.3).

As already explained in paragraph 1.2 and shown in Figure 4.15, the complete energy harvesting cycle begins with the application of an external mechanical excitation to the transduction system.

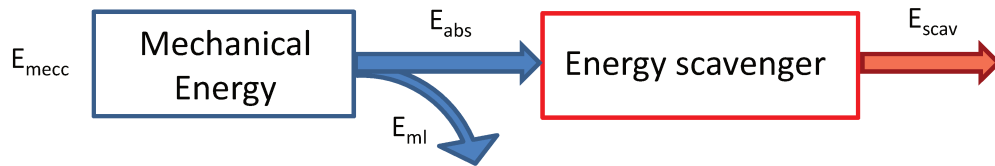


Figure 4.15: Mechanical conversion stage

The global electromechanical conversion efficiency can be expressed through the following equation:

$$\eta_{\text{mecc}} = \frac{E_{\text{scav}}}{E_{\text{mecc}}} \quad (4.4)$$

Where  $E_{\text{scav}}$  stands for the electrical energy output of the scavenger and  $E_{\text{mecc}}$  the mechanical energy applied to the prototype (Figure 4.15). It is important to underline that not all the mechanical energy applied to the prototype will be absorbed ( $E_{\text{abs}}$ ) by the scavenger, but part of this mechanical energy ( $E_{\text{ml}}$ ) will be given back to the environment.

The mechanical force applied by the linear test bench on the prototype to stretch it, is measured with the force sensor (Figure 4.16).

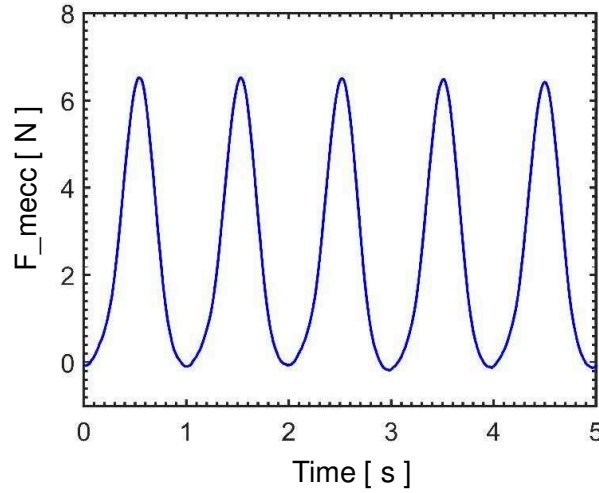


Figure 4.16: Mechanical force applied to the ‘rounded’ prototype

The mechanical force presents the expected sinusoidal trend, following the imposed sinusoidal deformation: the maximal force value, correspondent to the maximal deformation state of the device is equal to 6.8 N. This output force remains low and it is acceptable for applications embedded on human body. The additional energy that a person will spend to deform the prototype during daily activities can be considered negligible [4.9]. Our device electromechanical efficiency, equal to 0.075%, was calculated from equation (4.4). This efficiency is quite low compared to data found on the literature, but most of the works detailed in literature present efficiency calculated between  $E_{\text{abs}}$  and  $E_{\text{scav}}$  or only consider a part of the device for the calculation. Finally, first lifetime tests were done on our structure underlying no performance degradation after 1000 cycles. The scavenged energy after 1000 cycles was the same as the one

scavenged in the first cycles and no mechanical crack or visual deterioration was notified.

### 4.3.3 Ideal macroscopic scavenger prototype

Section 4.2 underlines that Parylene AF-4 or VT-4 are the best choices as electret materials for our scavenger and section 4.3 confirms that ‘rounded’ shape is the best design. Combining Parylene AF-4 or VT-4 and the ‘rounded’ shapes seems the best solutions to increase the output power but also the lifetime of our scavenger.

When integrated on the scavengers, electret materials withstand a mechanical cyclic solicitation that could compromise the charge stability on the material and thus the device performance. To verify this point, the surface potential of the electret deposited on the ‘rounded’ 3D-printed frame was monitored as a function of the number of deformation cycles. The tested structure is thus made of the flexible frame (SemiFlex), a metallic ground electrode deposited on it and an electret material, consisting of 9- $\mu\text{m}$ -thick fluorinated polymers (AF-4 and VT-4). First, the surface potentials of different points on the electret surface at rest were measured, whose results are shown in Figure 4.17.



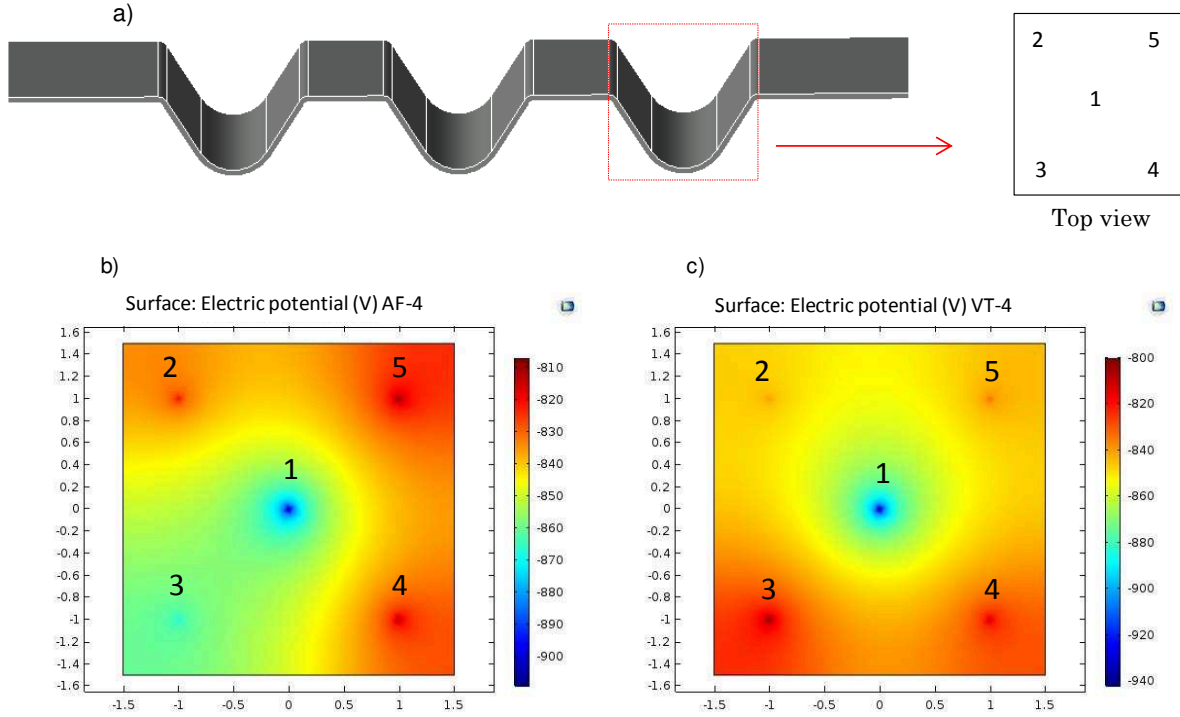


Figure 4.17: Schematic of the sample (a) and surface potential distribution on the electret surface for AF-4 (b) and VT-4 (c) electret materials

At rest, the surface potential distribution on the two tested configurations are not perfectly homogenous (presenting values in the range of  $[-810 \text{ V}; -910 \text{ V}]$  for AF-4 and  $[-800 \text{ V}; -940 \text{ V}]$  for VT-4) surely due to the charging protocol (see 4.3.1). The central part shows higher potentials values, probably because of structure geometry and edge effects. We would like to check if the surface potential distribution remains the same under cyclic deformations or if the charge migrates in the central part where higher potential values exist.

Thus, 1 Hz deformation cycles were applied to the device and the surface potential was measured every 100 deformation cycles applied on the material. Measurements were performed with an electrostatic probe (TREK 347) maintained at 3 mm from the electret surface. The results of the measurements made on the different points (mean value and standard deviations over 4 measurements) as a function of the number of deformation cycles applied to the device are shown in Figure 4.18.

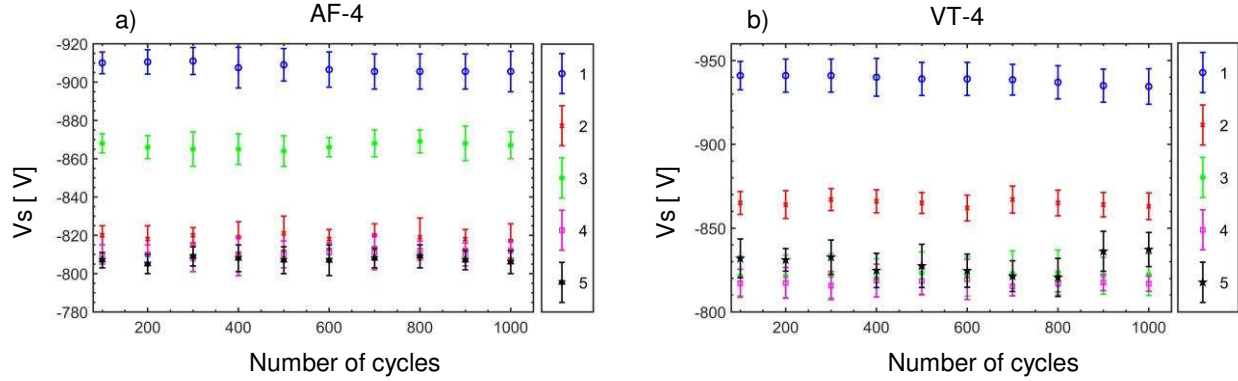


Figure 4. 18: Evolution of the electret surface potential of the control points as a function of the number of cycles applied to the device for Parylene AF-4 (a) and VT-4 (b)

From the above figures one can note that surface potential of all points resulted stable during all the 1000 tested deformation cycles, with surface potential decrease equal to less than  $-0.5\%$ . It can be thus concluded that the mechanical deformation applied on the device does not influence the electret charge stability over time for our ‘rounded’ structure.

#### 4.3.4 Towards an embedded scavenger

To facilitate the integration of the device on humans, the total height must be reduced. Namely, the initial air gap must be in the millimeter scale and not in the centimeter one. The operating principle of our hybrid structure encourages this size reduction, as the useful capacitance variation occurs for low air gap values ( $< 1$  mm). The concept of ‘rounded’ structure is preserved, as it allows obtaining higher device lifetimes (lower von Mises stresses). To improve the energy harvested by the device, one solution may consist in increasing the number of active elements in the scavenger structure, resulting in a higher capacitance variation when passing from the rest to the deformed state. Starting from the design consideration adopted for the first prototype, the total length of 10 cm imposed by the scavenger location and the 3D printer resolution, it can be derived a maximal length for the active part  $L_1$  of 1 cm, namely a number of patterns equals to 10. With 10 patterns, no more ‘inactive’ part exists in the scavenger as in the

previous versions (Figure 4.3 and 4.12); thus, the frame presents only a contact point with the elastomeric membrane. Mechanically, the structure will not sustain the imposed stretch and the elastomeric membrane will probably crack in this area. To avoid those damages, the frame is set tangent to the dielectric elastomer on a small line contact (see Figure 4.19). As for the previous design, the geometrical parameters ( $g_i$ ,  $R_1$  and  $R_2$ ) influence on the energy output was evaluated through Comsol Multiphysics numerical simulations (evaluation of the capacitance variation of the structure). The initial air gap  $g_i$  between the upper DE elastomeric membrane and the lower electret surface is the main control parameter, ranging from 2 to 4 mm, as a millimeter gap is our target for this embedded structure. Moreover, above this limit of 4 mm, the higher  $R_1$  value results in higher stresses at electrode and electret level and in higher  $g_f$  values in the maximal deformation state, which leads to lower power output. The schematics and geometrical parameters for the different prototypes named V2, V3 and V4, are shown in Figure 4.19.

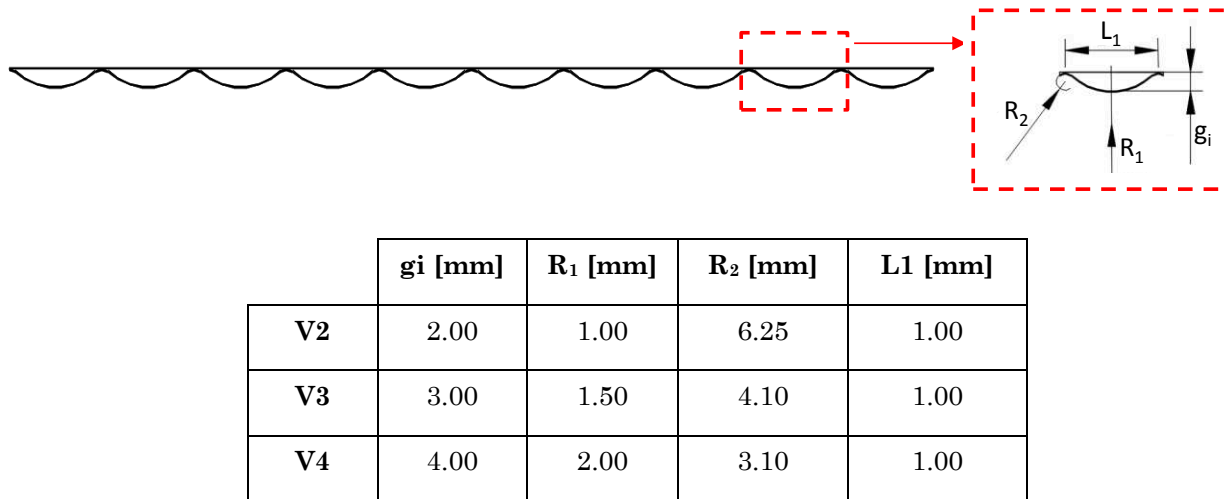


Figure 4. 19: Schematic and geometrical parameters of the devices

While in the previous structures a passive and an active zone were present (to obtain a total deformation of 50%), in this case there is no passive zone. It is thus necessary to find for each case (namely for structures V2, V3 and V4) the maximal deformation value ( $d_{\max}$ ).

This parameter ( $d_{\max}$ ) was determined in order to reach a final air gap between the upper and lower part of the device equal to 100  $\mu\text{m}$ , which was found from experimental prototype realization to be the minimal reachable value (paragraph 4.3). Figure 4.20 shows the evolution of the air gap  $g$  as a function of the deformation imposed to the device.

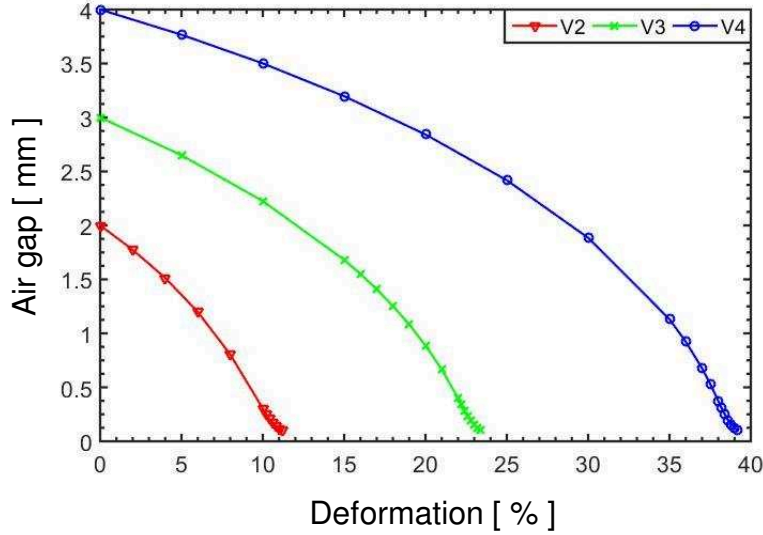


Figure 4.20: Evolution of the air gap as a function of the deformation imposed to the device

One can note that lower initial air gap values result in lower  $d_{\max}$ : this latter is equal to 12% for  $g_i=2$  mm, 23% for  $g_i=3$  mm and 40% for  $g_i=4$  mm. A lower mechanical input force is also necessary to deform the device with lower final deformation.

The capacitance variations of the three prototypes were calculated through the electromechanical module of Comsol Multiphysics by imposing the previously described deformation conditions at 1Hz, while the harvested powers were derived by the implementation of the system of equations (4.2) in Matlab Simulink. The materials employed were the same as the ones described in Table 4. 3 (Sylgard 186 DE and Teflon electret) in order to highlight the reduction size effect alone. Results are shown in Figure 4.21 and in Table 4. 7.

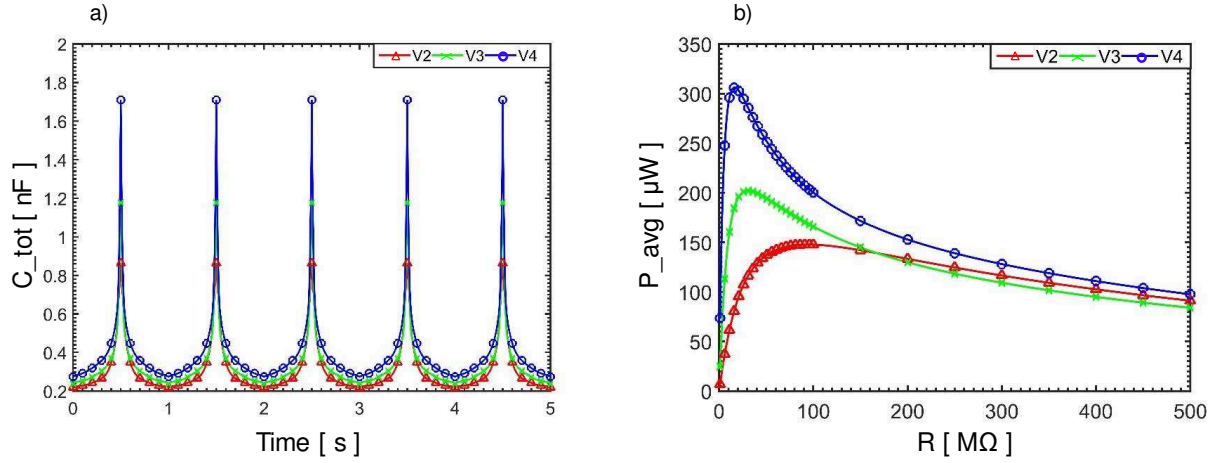


Figure 4.21: FEM simulations on the prototypes performance: variation of the electrical capacitance (a) and average scavenged power (b)

	gi [mm]	$C_{\max}$ [F]	$C_{\min}$ [F]	$C_{\max} / C_{\min}$	$P_{\text{avg}}$ [ $\mu\text{W}$ ]	$R_{\text{opt}}$ [ $\text{M}\Omega$ ]	$\eta$ [%]
<b>V2</b>	2	8.63e-10	2.20e-10	3.93	148	94	0.023
<b>V3</b>	3	1.18e-09	2.37e-10	4.97	201.98	31	0.015
<b>V4</b>	4	1.71e-09	2.74e-10	6.23	305.98	17	0.012

Table 4. 7: Schematic table on the devices performance

Compared to the proof of concept ( $33 \mu\text{W}$  on  $99 \text{ M}\Omega$ ) and to the ‘rounded’ prototype ( $49 \mu\text{W}$  on  $150 \text{ M}\Omega$ ), the three proposed solutions scavenge high level of energy ( $>148 \mu\text{W}$ ) for lower load values ( $<94 \text{ M}\Omega$ ). From the above results, one can note that the prototype allowing scavenging the higher theoretical energy output is the one presenting an initial air gap of 4 mm, namely the one presenting the higher capacitance variation between the rest and maximal deformation state (capacitance ratio equal to 6).

The devices efficiencies were calculated using equation (4.3), resulting in values respectively equals to 0.023, 0.015 and 0.012% for V2, V3 and V4. One can conclude that the better choice in terms of scavenged power is represented by the prototype V4

(306  $\mu\text{W}$ ). Nevertheless, the advantage of V2 consists in presenting a lower deformation value (12%) necessary to reach the final state. This could be advantageous for embedded solution with thin thickness when the prototype is located in zones with low relative displacements imposed by the external source.

To sum up, prototype optimization has been performed with the aim of increasing the output power of the device, reduce the mechanical stresses and reduce the size for an embedded structure. Electret material and harvester structure have been analyzed independently with the aim of evaluating their influence on the output performance. 9- $\mu\text{m}$ -thick Parylene AF-4 resulted the most suitable electret material among the polymers tested, while the structure presenting the higher energy density (equal to 2.2  $\text{mJ.g}^{-1}$ ) consisted of a 10-frame ‘rounded’ shape with initial air gap of 4 mm (V4 in Table 4.7).

## 4.4 Power management unit

In this paragraph, we will consider the power management unit, namely the last stage of the complete energy harvesting cycle. In our prototype, the energy transferred from the variable capacitor through the resistor is alternative and presents high values ( $>100\text{ V}$ ), making it not suitable to supply low-power-consumption devices (constants voltages between 3 V and 5 V). Most of electronic devices require in fact DC input voltages. To this aim, a power management unit is needed to couple the scavenger electric output to the final application input, as shown in Figure 4.22.

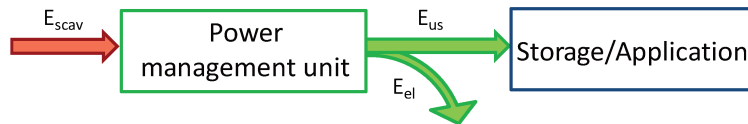


Figure 4.22: Schematic of the energy harvesting cycle electrical conversion efficiency

The first simple solution is to use passive electronic components to realize the rectifying stage: a standard full bridge rectifier is the first basic solution to obtain a rectified signal across the storage capacitance  $C_s$ , as shown in Figure 4.23.

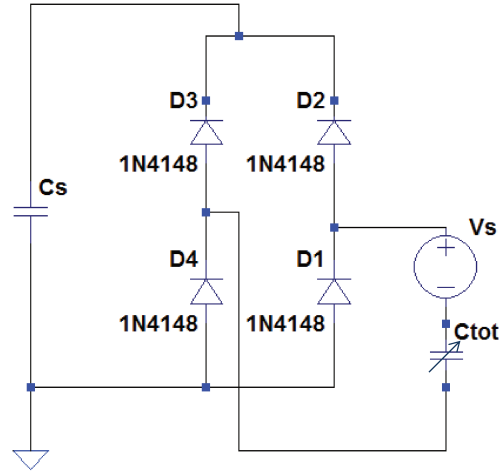


Figure 4.23: Passive power management unit: full bridge rectifier

The main power losses in this type of circuit are mainly related to the diodes: forward voltage drop, leakage current when the diodes are reverse biased and diodes' internal resistance [4.10].

Circuit implementation of this full bridge was performed by using the software LTSPICE, imposing as input sources ( $V_s$  and  $C_{tot}$ ) the results obtained from the numerical simulations (Comsol) on the 'rounded' device presented in paragraph 4.3. Classic high voltage diodes (1N4148 from Vishay) were employed. Simulations results on two different  $C_s$  values (1  $\mu\text{F}$  and 1 nF) are shown in Figure 4.24

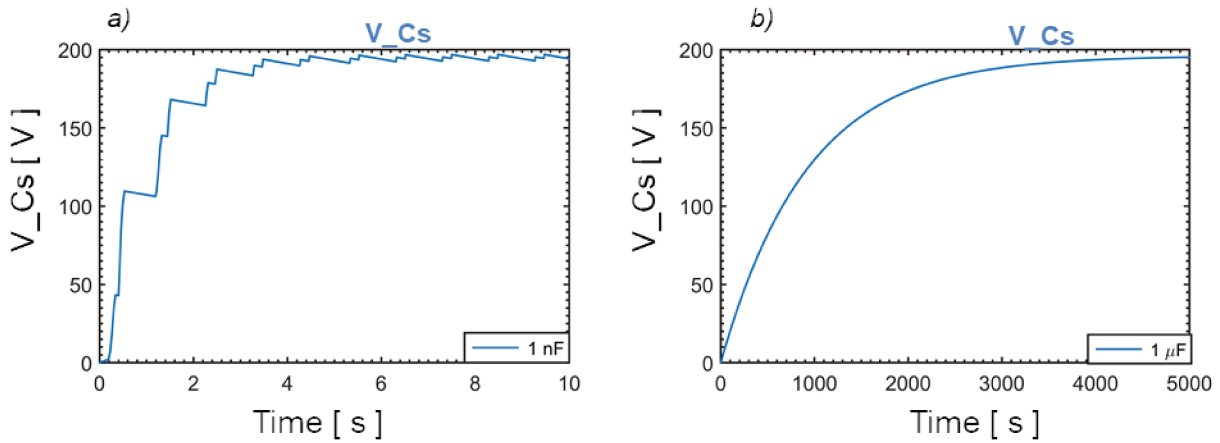


Figure 4.24: Simulations results of passive rectification of the 'rounded' shapes prototype on a 1 nF (a) and 1  $\mu\text{F}$  (b) storage capacitance

One can note that higher storage capacitances results in a higher time to be fully charged. A total time of 4 seconds is necessary to fully charge the storage 1 nF capacitance to the maximal value of 200 V, corresponding to 4 deformations cycles (Figure 4.24a). A total energy equal to 20  $\mu\text{J}$  is scavenged during these 4 cycles. As expected, this value is lower than the one obtained from impedance matching (mean output power of 49 $\mu\text{W}$ ). From Figure 4.24a it can be noticed that tension decrease from the maximal tension value occurs due to ohmic losses at diodes level and Cs level. The voltage value obtained by the scavenger output rectification remains too high to be exploited as power supply source. After the AC-DC conversion stage (realized with diodes bridge rectifier), a further DC-DC conversion may thus be necessary to adapt the transducer voltage level to the load (basically a buck converter to decrease the voltage), as shown in the schematic in Figure 4.25.

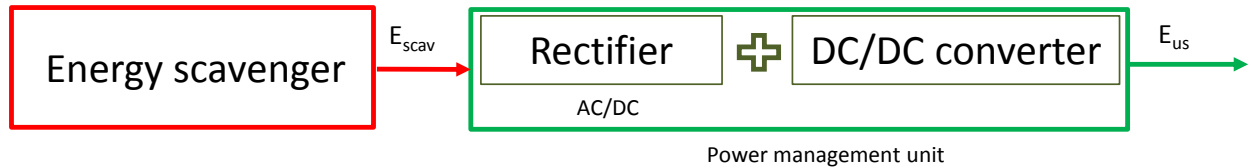


Figure 4.25: Schematic of the complete energy management circuit

A 2-in-1 simple solution may consist in the employment of a commercialized circuit: LTC3588-1 by Linear Technology, which schematic is shown in Figure 4.26:



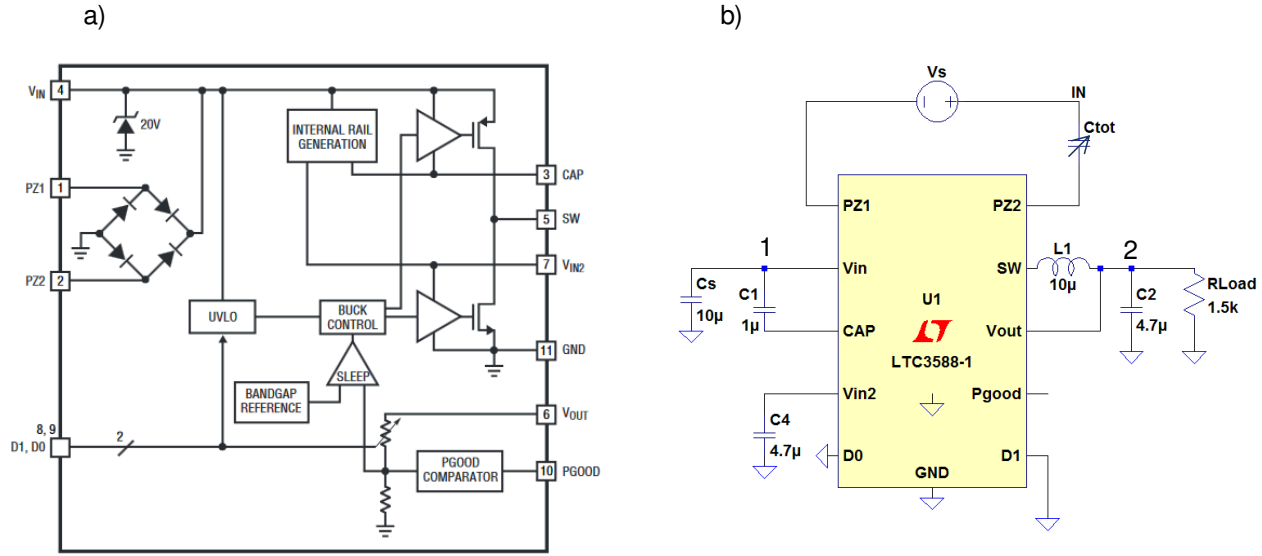


Figure 4.26: Schematic of the LTC3588-1 circuit by Linear Technology (a) and configuration employed for simulations (b) (from the datasheet [4.11])

This circuit presents a full-wave bridge rectifier, followed by a buck converter. An ultralow quiescent current undervoltage lockout (ULVO) mode allows charge to build up in an input capacitor. When  $V_{in}$  reaches the threshold value, an internal buck converter transfers part of the stored energy from the input capacitor to the output. Four output voltages (1.8 V, 2.5 V, 3.3 V and 3.6 V) can be selected through the  $D_0$  and  $D_1$  pins values. The advantage of this circuit consists in the regulation of the output voltage over a capacitor, eliminating the need of an external battery to control the energy transfer. Nevertheless, the conversion efficiency of the device is low and diminishes drastically for low current sources, as shown in Figure 4.27.

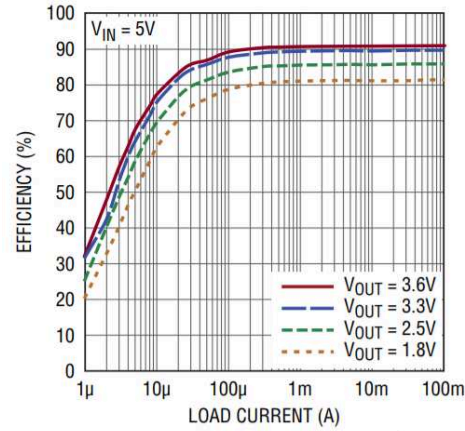


Figure 4.27: LTC3588-1 conversion efficiency (from datasheet)

The LTSPICE implementation was performed using the ‘rounded’ scavenger output voltage obtained in paragraph 4.3 through the circuit implementation shown in Figure 4.26b. The results are shown in Figure 4.28.

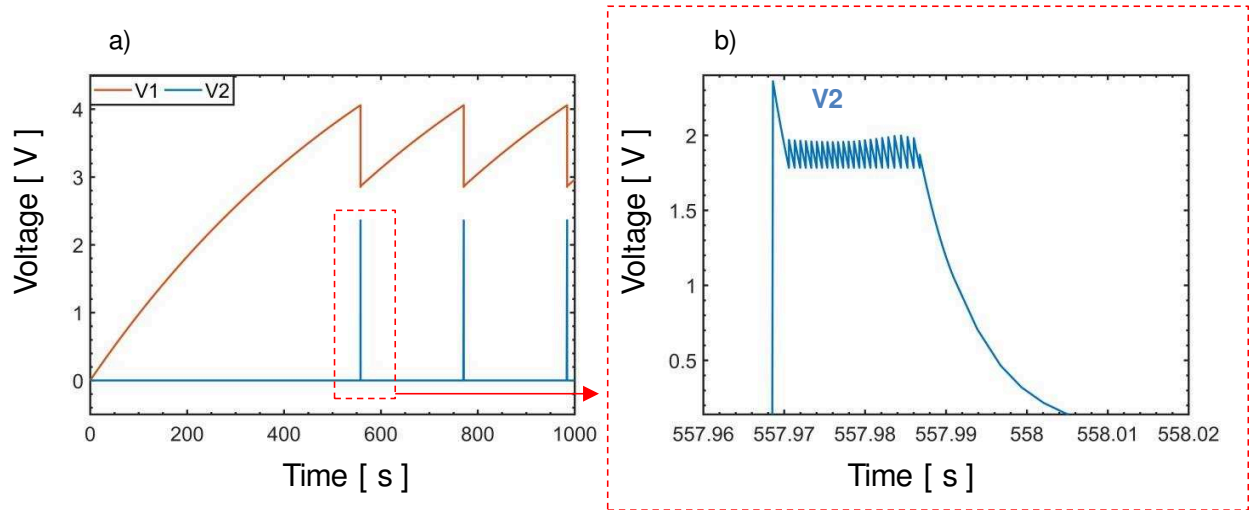


Figure 4.28: Simulated results on the ‘rounded’ shapes prototype for V1 and V2 (see Figure 4.26b)

One can note that a regulated voltage output of 1.8 V can be delivered by the system after 558 seconds of start-up on the resistive load and only during 16 ms. A time interval of 220 seconds is then necessary to reach again the level of 1.8 V. Indeed, the scavenged energy is in fact not enough high to maintain a constant output voltage for long durations. The ripple observed in Figure 4.28 is related to the capacitance value

employed in the circuit. The obtained performance are lower compared to the ones given by the passive circuit, mainly due to the high losses present in the circuit to charge the first capacitor.

In order to obtain high conversion efficiency other power management circuits may be employed. Among them, parallel or series Synchronized Switch Harvesting on Inductor (SSHI), respectively shown in Figure 4.29 a and, b are widely adopted.

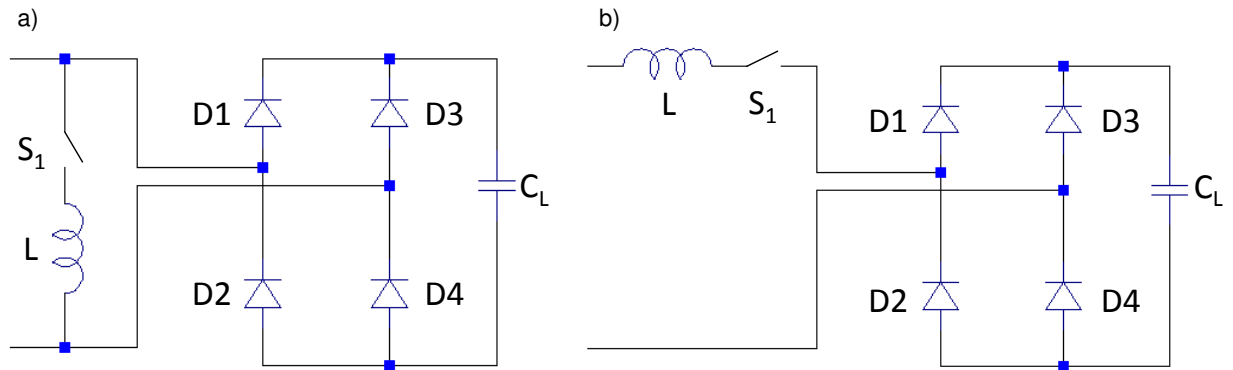


Figure 4.29: Parallel SSHI (a), and Series SSHI (b) implementations

Both the parallel and series SSHI present a voltage inversion through an inductor element which is triggered on the scavenger peaks voltage through the presence of an active switch. The main difference between the two techniques consists in the fact that, while in the P-SSHI the voltage inversion occurs after an energy extraction process, in the s-SSHI the voltage inversion and energy extraction occurs at the same time [4.12]. Basically, in the Parallel SSHI [4.13], [4.14] the switch is open most of the time, except for the instants in which a peak is detected in the rectified voltage output. When this condition occurs, the switch is closed and the current flows through the inductive element. The internal capacitor of the scavenger and the inductance form a resonant circuit and thus the inversion of the scavenger voltage occurs through an oscillating process. In the series SSHI [4.14] instead, the inductive element and the switch are connected in series with the scavenger. The currents flow through the inductor and then the diode bridge occurs only when the switch is closed. At these instants, the

voltage inversion occurs. The power provided by series and parallel SSHI is comparable but the optimal load for the two techniques is different [4.15].

In Figure 4.30 are instead shown two different topologies of Synchronous Electric Charge Extraction (SECE): through a buck-boost or a flyback [4.16].

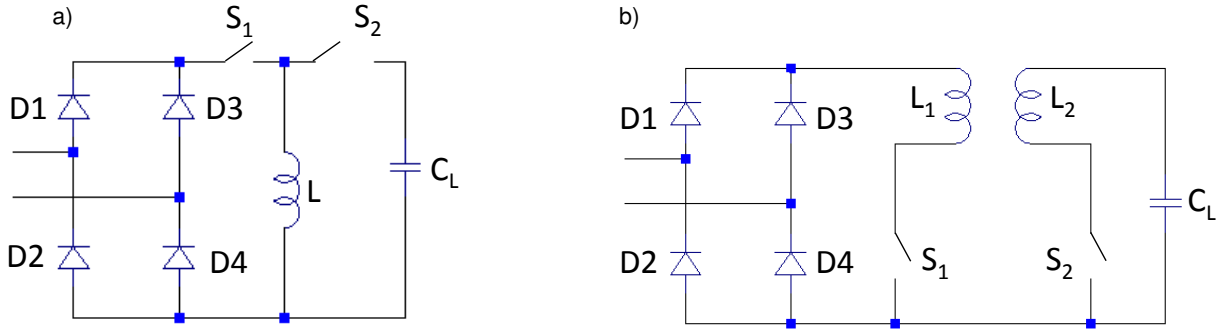


Figure 4.30: Examples of SECE circuit implementations through buck-boost (a) and flyback (b)

Differently from the SSHI techniques, the inductive elements and the switches are connected after the diodes rectifier. This technique consists in discharging the scavenger capacitance when the tension reaches a local maximum. Then, through an inductive system (a flyback or buck-boost), the energy is transferred from the inductance to the storage element  $C_L$ . In this work we chose a SECE flyback topology through the implementation proposed by [4.16] on LTSPICE software. This topology seems in fact more adapted to the high conversion ratio between input and output voltages. The schematic and the results on the total output given by our prototype are shown in Figure 4.31. The circuit components employed are:  $C_s = 1 \mu\text{F}$ ,  $L_1 = 82 \text{ mH}$  and  $L_2 = 100 \mu\text{H}$  to create the appropriate reduction ratio, and ideal switch to reduce losses.

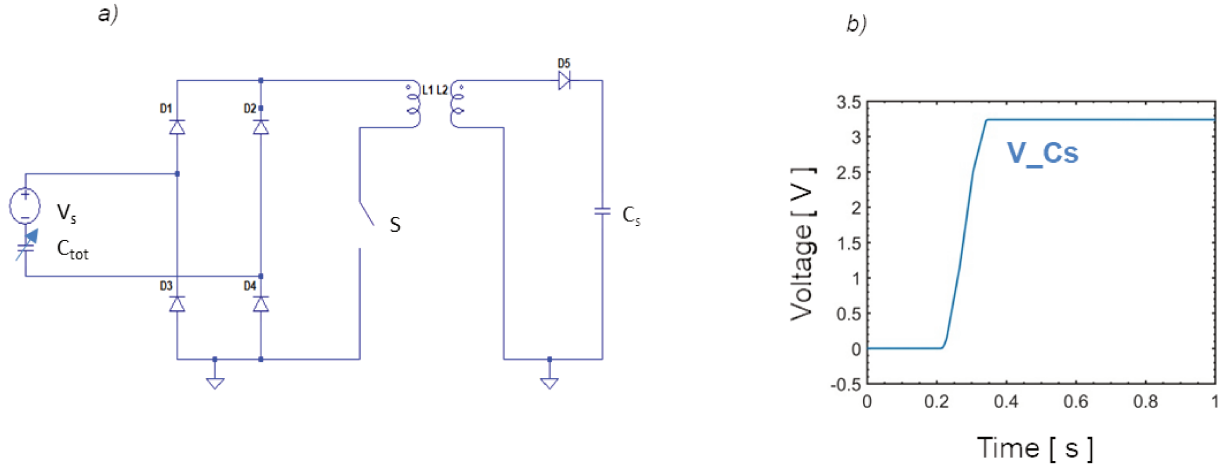


Figure 4.31: Schematic (a) and results (b) on the non-linear power management circuit on the ‘rounded’ prototype described in 4.5

This technique presents the better performance compared to the previously described passive and LTC358-1 cases.

The disadvantage of this solution consists in the presence of the active switch requiring an energy source to commute. Solutions may consist either in the employment of an external battery or, ideally, in the employment of part of the energy output given by the scavenger, as presented in [4.16]. This envisaged solution allows the complete autonomy of the energy harvesting device.

## Conclusion

In this chapter the conception, realization and tests of the first energy scavenging device based on electret material were presented. This device presents a hybrid structure coupling dielectric elastomers with electrets materials, acting as separating dielectric layer and allowing the improvement of the scavenger performance. Influence of the electret materials was evaluated based on the results presented in chapter 2, showing a theoretical power output increase of 40% when 50- $\mu\text{m}$  thick Teflon FEP was substituted with 9- $\mu\text{m}$ -thick Parylene AF-4. In addition, the scavenger shape optimization was performed and an experimental prototype scavenging up to 49  $\mu\text{W}$

was realized, namely 50% more than the first proof of concept and with von Mises stresses on the electret material 2 orders of magnitude lower increasing the lifetime of the structure. Possible solutions for size reduction were presented through FEM simulations, by the conception of structures with maximal deformations values ranging between 12 to 40%. Among them, the optimal structure with initial air gap of 4mm was able to scavenge a maximal energy density of  $2.2\text{mJ.gr}^{-1}$  (over the total structure weight). The results are summarized in Table 4.8.

Shape	Materials			Output power
	Electret	DE	Frame	
Simple triangle	50- $\mu\text{m}$ -thick Teflon FEP	Sylgard 186	Plastic acetate	85 $\mu\text{W}$ (33 $\mu\text{W}$ experimental)
Simple triangle	9- $\mu\text{m}$ -thick Parylene AF-4	Sylgard 186	Plastic acetate	120 $\mu\text{W}$
Rounded triangle	50- $\mu\text{m}$ -thick Teflon FEP	Sylgard 186	Semiflex <sup>TM</sup>	112 $\mu\text{W}$ (49 $\mu\text{W}$ experimental)
10 frames (V4)	50- $\mu\text{m}$ -thick Teflon FEP	Sylgard 186	Semiflex <sup>TM</sup>	305.98 $\mu\text{W}$

Table 4.8: Summary of the results obtained for the first energy harvesting device

Finally, discussion on power management unit solutions was performed to evaluate the complete energy harvesting cycle, to obtain a DC output voltage for autonomous sensors power supply.



# **CHAPTER 5.**

## **DEG-BASED ENERGY HARVESTING DEVICES**





## **Chapter 5.     DEG-based energy harvesting                   devices**

In this chapter, an innovative operating mode of hybrid energy harvesting devices employing dielectric elastomers materials will be presented.

As explained in Chapter 1, dielectric elastomer generators are electrostatic converters based on the voltage boost of a dielectric elastomer membrane sandwiched between two compliant electrodes. Despite their several advantages, these generators are not well developed in the literature due to the need of an external voltage (bias or polarization voltage) to perform the energetic cycle, which compromises their autonomy as energy scavengers.

In order to overcome this drawback and to design a scavenger with a longer lifetime, in this chapter we propose two different solutions to substitute the external bias voltage in DEGs. The first one consists in employing electret material to polarize the DEG: the operating principle, governing equations but also the influence of the geometrical parameters of the scavenger and of the materials properties on the estimated scavenged energy will be presented. The second solution instead aims in fabricating hybrid devices employing piezoelectric materials as DEG polarization source: two different prototypes have been realized and the experimental performance will be presented.

These solutions, compared to the ones proposed in the literature (see 2.2.2.4), present the advantages to be compact, does not need additional electronic element and can guarantee a polarization source to the device at each deformation cycle.

## 5.1 Electret polarization

The first hybrid solution proposed in this chapter consists in coupling the DEG with an electret material: in the literature, few works on this hybrid solution have been proposed.

Using electret materials as polarization source for DEG was firstly presented in [5.1], with theoretical considerations on the device performance. In the next paragraph, the design of a structure working on this principle will be presented and the influence of the geometry and material properties will be investigated with the aim of proposing a fully coupled hybrid device.

### 5.1.1 Device structure and working principle

Our experimental proof of concept for this hybrid structure is shown in Figure 5. 1.

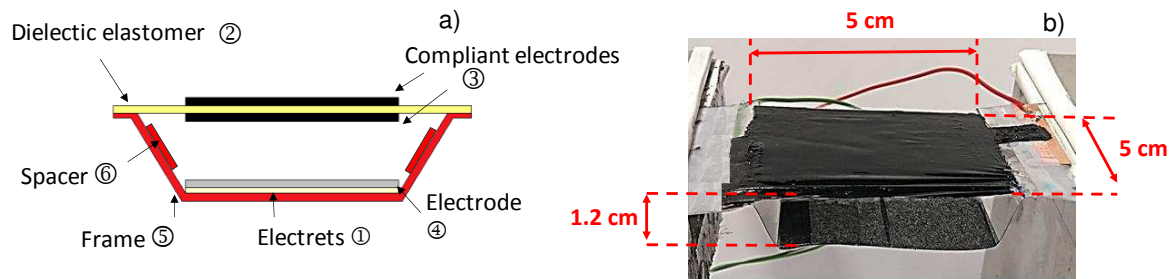


Figure 5. 1: Device schematic (a) and experimental realization (b)

The structure is similar to the one described in the previous chapter: a DE membrane (②) stands in the upper part of the device, coupled through a plastic frame (⑤) with an electret material (①). The difference compared to the previous operating principle ('electret mode') is the presence of a compliant electrode in the lower part of the membrane: the DE is thus sandwiched between two compliant electrodes in order to perform the voltage boost.

The total surface area was set to  $25 \text{ cm}^2$ , as the previous designed hybrid structure in electret mode (chapter 4), in order to be adaptable to wearable applications and make easier comparisons between our various solutions. The width here is larger (5 cm) compared to our previous solutions (2.5 cm). The structure will be deformed under 50% strain at 1Hz, leading to an initial gap of 1.2 cm with the chosen trapezoidal frame. Contrary to our previous hybrid structure, this device is composed of only one pattern. The trapezoidal shape of the frame ensures that the upper part (namely the dielectric ② sandwiched between two compliant electrodes ③) is perfectly parallel to the electret material ① if the electret stands in the lower part of the trapezoidal shape (as shown in Figure 5.1). This parallel configuration is a simple structure to create a high level of coupling between the electret and the dielectric material, leading to a high induced polarization voltage level on the lower electrode of the DEG. Indeed, an electric field appears around the electret, due its surface potential. The main central electric field, which is higher than the edge electric field, is thus used to polarize the dielectric elastomer. In order to avoid contact between the two electroactive elements, which could compromise the electret charge stability over time, two  $50\mu\text{m}$ -thick spacers (⑥) need to be placed on the oblique sides of the structure.

The working principle of the proposed hybrid device is described in Figure 5. 2.

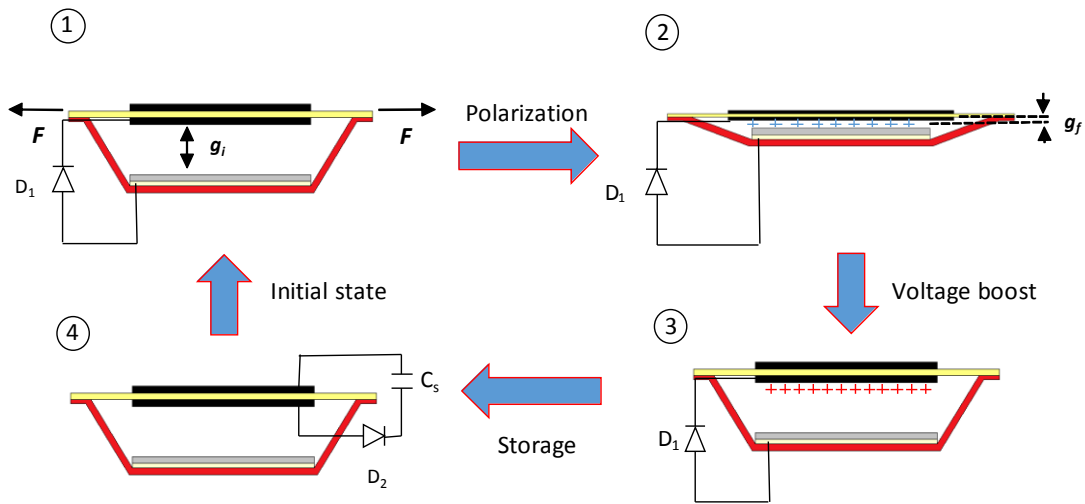


Figure 5. 2: Device working principle schematic

The energetic cycle begins by applying a force  $F$  on the two sides of the device, stretching the elastomeric membrane of a quantity  $\lambda$  on its longitudinal length. Consequently, the frame induces a vertically movement and the electret material moves towards the elastomeric membrane. The air gap between the two materials thus decreases from an initial value  $g_i=1.2$  cm to a final value  $g_f$  (phase 1 to 2). The value of  $g_f$  should be the lowest possible in order to increase the induced polarization voltage on the lower electrode given by the electret material (see 5.1.4) but enough high to avoid the contact between the electret material and the upper electrode. In position 2, the electret material is at the minimal distance from the membrane and the elastomeric membrane is stretched at its maximal value, corresponding to its maximal equivalent electrical capacitance ( $C_{max}$ ). During the polarization state, from position 1 to 2, the floating potential of the lower electrode of the DEG increases from 0 to a polarization voltage value  $V_{min}$ . This value is induced on the lower electrode by the electret material polarization and it is directly linked to the initial electret surface potential and to the final value of the air gap  $g_f$ . The diode  $D_1$  ensures charge flow from the electret toward the dielectric elastomer and avoids flow-back of charges to the electret during the rest of the energetic cycle. Then, the elastomeric membrane is relaxed to its initial length (phase 2 to 3). During this phase, the DEG electrical capacitance decreases from its maximal to its minimal value ( $C_{max} \rightarrow C_{min}$ ) thus inducing a voltage boost across the dielectric elastomer ( $V_{min} \rightarrow V_{max}$ ), as classically realized with electrostatic generators. The voltage across the DEG is then collected through the diode  $D_2$  and storage capacitance  $C_s$  (phase 3 to 4) and the electrostatic generator returns to the initial state (phase 3 to 4) to begin a new cycle.

The full system can be represented by the equivalent electrical circuit shown in Figure 5. 3.

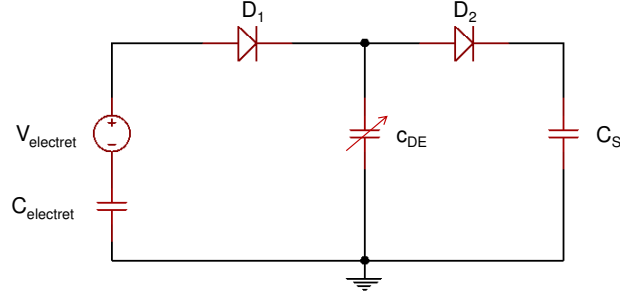


Figure 5. 3: Equivalent electric circuit of the device

The device is made of a DEG (an elastomeric membrane with two compliant electrodes), which can be considered as a variable capacitor ( $C_{DE}$ ) and an electret material, acting as polarization source (modelled with a capacitance  $C_{electret}$  and a voltage source  $V_{electret}$ ). In this configuration, the polarization source is connected in parallel to the elastomeric membrane and the energy transfer in the circuit occurs in only one direction. By assuming a constant charge working mode during the voltage-boost phase (phase 2 to 3 in Figure 5.2), the following relationship occurs:

$$V_{max} = \frac{V_{min} * C_{max}}{C_{min}} \quad (5.1)$$

The total energy scavenged by the device  $E_s$  can be expressed as the difference between the energies stored in the elastomeric membrane, *i.e.* the DEG, in the rest state ( $E_{def\_min}$ ) and in the maximal deformation state ( $E_{def\_max}$ ), namely:

$$E_s = E_{def\_min} - E_{def\_max} = \frac{1}{2} \frac{C_{max}}{C_{min}} V_{min}^2 * (C_{max} - C_{min}) \quad (5.2)$$

The total energy scavenged by the device is thus proportional to the electrical capacitance variation of the DEG and to the square of  $V_{min}$ , which corresponds to the polarization voltage induced by the electret material in the maximal deformation state.

### 5.1.2 Materials selection

While in the previous scavenger design presented in Chapter 3, the elastomeric membrane played the role of dielectric layer separating the electret material from the upper electrode, in this working mode it performs the voltage boost of the polarization

source. In this case, we selected an acrylic material as dielectric elastomeric membrane because of its higher dielectric constant and dielectric strength compared to the silicones (as shown in [5.2]), leading to a theoretical energy density more than 2.5 higher than the one obtained with silicone materials. Figure 5. 4a shows the principal characteristics of the VHB 4910 acrylic material, which was employed as DE in the present work and in Figure 5. 4b its dielectric strength as a function of the radial stretch [5.3].

<b>3M™ 4910 VHB™ Tape</b>	
Young's modulus [kPa]	220
Shear modulus [kPa]	73
Maximal uni-axial reversible deformation [%]	860
Poisson's Ratio	0.49
Dielectric constant@ $\lambda=1$	4.55
Dielectric loss factor @ $\lambda=1$	0.43
Breakdown field @ $\lambda=1$ [ $V \cdot \mu m^{-1}$ ]	10
Thermal Conductivity [ $W \cdot mK^{-1}$ ]	0.16

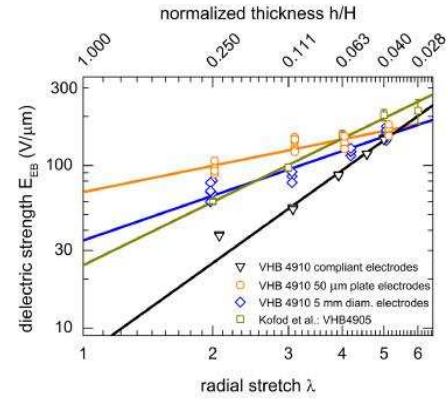


Figure 5. 4: Mechanical and thermal properties of VHB 4910 (a) and variation of the electrical properties as a function of the membrane stretch (b) [5.3], [5.4]

One can note that membrane pre-stretch can ensure a uniform strain distribution in the material and can increase the dielectric strength of the membrane (Figure 5. 4b), thus increasing the scavenged energy. Nevertheless, when the values of  $\lambda$  in the two in-plane directions are higher than 2 (corresponding to a total area pre-stretch  $\lambda_{pre-stretch}=4$ ), an increase of more than 4 times in leakage currents may occur, as shown in [5.5]. Beneath, a decrease of  $\sim 10\%$  in the dielectric constant occurs for radial stretches higher than 3 [5.3], leading to lower scavenged energy. From the above considerations, a bi-axial pre-stretch equal to  $\lambda_p=1.5$  was applied to the material. A pure-shear mode

(see chapter 2 for description) is assumed for the active phase imposed by the 50% external deformation in one plane direction (uniaxial applied force  $F$ , as shown in Figure 5.1). In the next paragraph, the impact of this hypothesis on the capacitance estimation will be discussed. In this way, the pre-stretch and the active stretch applied to the polymer lead to a total asymmetric DE deformation in both in-plane directions (equations 5.3 and 5.4).

$$\lambda_{1,total} = \lambda_{1,pre-stretch} * \lambda_{1,active} = 1.5 \times 2 = 3.375 \quad (5.3)$$

$$\lambda_{2,total} = \lambda_{2,pre-stretch} * \lambda_{2,active} = 1.5 \times 1 = 1.5 \quad (5.4)$$

These values stand in the security margin necessary to limit leakage currents increase and dielectric constant drop. Membrane behavior was modelled using an hyperelastic Moonley Rivlin model, described in paragraph 2.2.2.2 using  $C_1$  and  $C_2$  values respectively equals to 0.0241 MPa and 0.0183 Mpa [5.5],[5.6].

Both compliant electrodes are made with carbon grease (846 MG Chemicals) to ensure good electric and mechanical properties, as described in chapter 2. This grease is classically used to realize proofs of concept, as it is easy and fast to apply.

Electret materials employed in the design correspond to a commercial 50- $\mu$ m-thick Teflon FEP which properties are reported in Table 4.3. This electret is used instead of Parylene AF-4 or VT-4, in order to allow us compare the benefits between the two operating modes with quite the same materials. Finally, thanks to the simple geometry of the hybrid structure, the only key parameter of the electret material is the surface potential level  $V_s$  used for DEG polarization.

### 5.1.3 DE capacitance variation

A “pure shear” deformation mode was considered, with constant membrane length over the second principal direction during deformation ( $L_2$ ). Nevertheless, as the deformations are not perfect, a “necking” phenomenon could appear [5.8], as shown in Figure 5. 5.



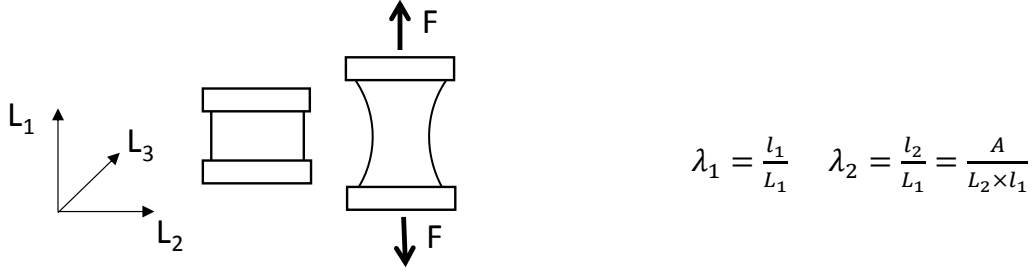


Figure 5. 5: Resulting inhomogeneous deformation in the elastomeric membrane

In order to evaluate the influence of this ‘necking’ phenomenon on the variation of the DE capacitance, FEM simulations of the elastomeric membrane capacitance values (DE alone) were performed using the electromechanics module of the software Comsol Multiphysics. The simulated configuration was the one shown in Figure 5.6: a fixed displacement condition is used to pull the opposite ends of the structure apart, producing a strain in the active zone of the elastomer. A parametric steady-state analysis is lead for an applied strain varying between 0% up to 50% with a step of 10%. The dielectric elastomer is made of VHB4910, whose parameters are listed in Figure 5.5 and which is supposed having constant permittivity while stretching. The electrode was supposed to be ideal, with no mechanical impact on the membrane deformation, explaining the absence of electrodes in these simulations. The capacitance values were deduced from the total internal electrical energy ( $W_e$ ) computed by the software when the capacitance  $C_{eq}$  is charged under a voltage  $V$  ( $W_e = 0.5 \times C_{eq} \times V^2$ ). Experimental validation of the simulation results was performed using a LCR meter (HP 4248A). The capacitance variations were measured in static conditions for different deformation values applied to the DE membrane alone, in the first principal direction, using the mechanical test bench shown in Figure 5. 6. A description of our test-bench can be found in chapter 4.

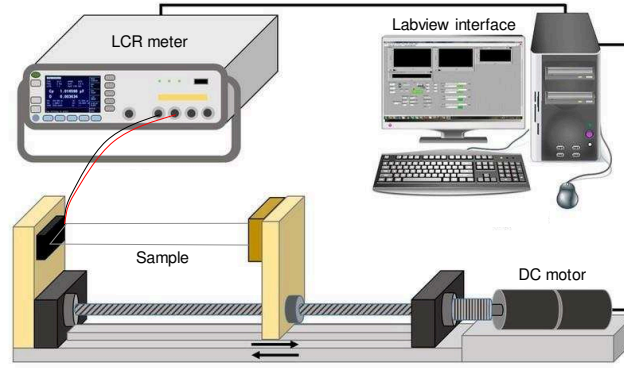


Figure 5. 6: Experimental setup for device capacitance measurement

Figure 5.7a shows the von Mises stresses distribution obtained in the final deformed configuration (50% of strain applied to the membrane). The inhomogeneous deformation clearly appears with clamped effect (high stress near limit conditions of imposed displacement) and ‘necking phenomenon’. The initial shape is also reported on Figure 5.7a. On Figure 5.8b the equivalent capacitance values obtained from numerical simulations in static conditions (named ‘inhomogeneous’ condition in Figure 5.7b), equivalent capacitance from basic expression of a plate capacitance (named ‘pure shear’ in Figure 5.7b) and the experimental validation values are reported.

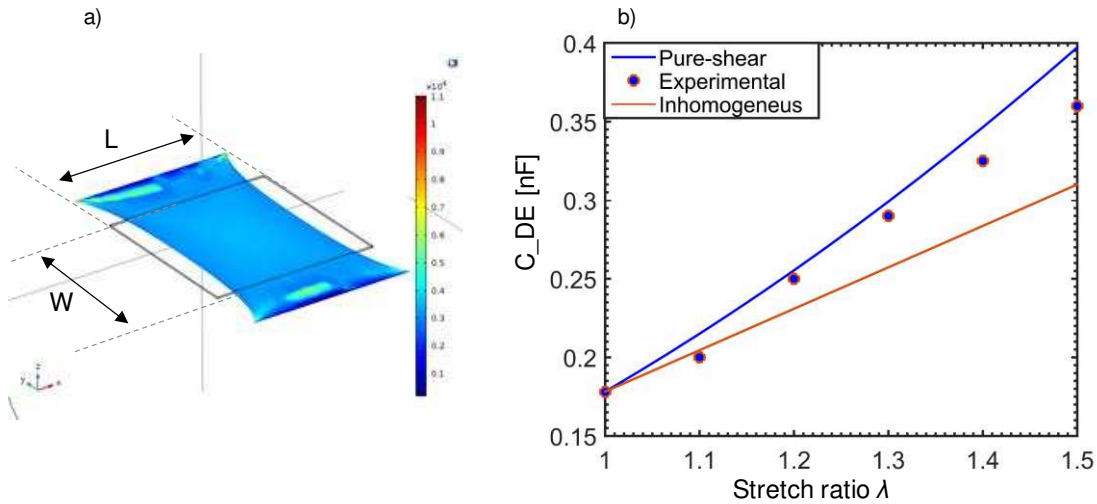


Figure 5. 7: FEM simulation results of the von Mises stresses [Pa] (a) and comparison between the electrical capacitance values obtained from numerical simulations and experimental measurements (b).  $W=L=5\text{cm}$

As shown in Figure 5.7b, the capacitance increases quite linearly with the increase of the strain imposed to the membrane. The maximal capacitance value  $C_{max}$  is obtained when the maximal stretch is imposed to the membrane. The “ideal case” over-estimates the capacitance value while the “inhomogeneous case” under-estimates it, as the capacitance area is lower. For stretching ratios lower than 30% (stress ratio of 1.3), experimental data are close to the pure-shear ideal model. Between 30 and 50% instead, the capacitances values are  $\sim 10\%$  lower than the one obtained in the ideal case. The ‘inhomogeneous case’ presents lower values than experimental data, meaning that the ‘necking phenomenon’ is less influent in our experiments probably due to the mechanical movement imposed to the device by the set-up. Further experiences, especially a video recording of the deformation during active phase, are needed to confirm this hypothesis. Thus, to estimate the potential scavenged energy, the ideal model of a plate capacitance will be used.

#### 5.1.4 Electret polarization voltage

FEM simulations were performed using the electrostatic module of the software Comsol Multiphysics (under the conditions described in 5.1.3) to predict the lower electrode polarization voltage ( $V_{low}$ ) induced by electret polarization during the deformation phase of the device.

The polarization values on the lower electrode of the dielectric elastomer were calculated as a function of the electret surface potential (from  $-200$  V up to  $-2000$  V) and the final air gap  $g_f$  between the lower membrane electrode and the electret material, as shown in Figure 5. 8. The final air gap was varied between  $4.5$  mm and  $0.5$  mm (namely the height of the spacers in the harvester structure). For higher final air gap values, the polarization voltage on the lower electrode is too low and thus not exploitable.

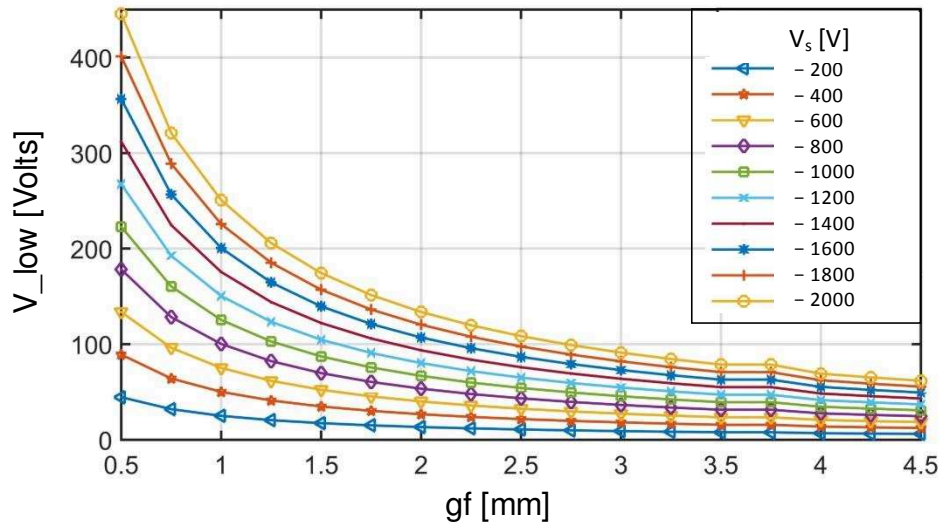


Figure 5. 8: Lower DE electrode polarization voltages as a function of the air gap and the electret surface potentials  $V_s$

As expected, the polarization voltages are proportional to the electret surface potential and to the inverse of the final air gap between the electret and the lower electrode. Indeed, with a small final air gap, the lower electrode is located in an area where the electric field induced by the electret is high, leading to a higher value of the floating potential obtained on this electrode. Moreover, as the surface potential of the electret increases, the induced electric field around the electret increases leading to higher value of the polarization voltage on the lower electrode. Polarization voltages on the lower electrode higher than 100 V were obtained for electret surface potential equal to at least  $-400$  V and final air gap of 0.5 mm.

To validate the possible high polarizations on the lower DE membrane, polarization voltage as a function of the final air gap values was experimentally measured using the test bench described in Figure 5.9. A 50- $\mu\text{m}$ -thick commercial Teflon FEP charged with a surface potential equal to  $-1000$  V is used as electret. The ground electrode is made with a copper conductive tape (3M 1181), insuring a high conductivity. The electret material and the ground electrode were maintained fixed, while another

electrode standing as DEG lower electrode was connected to a moving surface. The horizontal displacement of the movable part was controlled by a linear motor (set-up described in chapter 4) at a frequency of 1Hz, reproducing the movement of the final device. The value of the final air gap  $g_f$  was varied between 0.5 and 4.5 mm using a micro-positioner, allowing pre-positioning the fixed and movable part of the set-up. The value of the final air gap is checked thanks to a thickness sensor. The initial value of the air gap ( $g_i$ ) was fixed at 1.2 cm for each tested configuration, which corresponds to  $g_i$  in the harvester device. As in the final device, a diode  $D_I$  (1N4148) is connected between the ground electrode and the lower electrode. The lower electrode voltage was measured using a TREK347 electrostatic probe on a delocalized contact point having the same potential as the one obtained on the lower electrode.

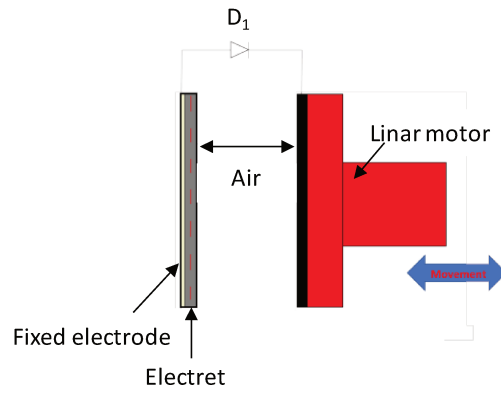


Figure 5. 9: Experimental setup employed for lower electrode electret polarization

Two different types of electrodes, standing as lower DE electrode, were tested: one electrode with a resistivity value equal to  $1.6 \cdot 10^{-10} \Omega \cdot \text{cm}$  (100-nm Cu electrode) and one made of carbon grease MG Chemical (the one used in the proposed device), whose resistivity is  $117 \Omega \cdot \text{cm}$ . The trend of the lower electrode polarization voltage is shown in Figure 5. 10 for both types of electrodes, while Figure 5. 11 represents the maximal lower electrode polarization values as a function of  $g_f$ .

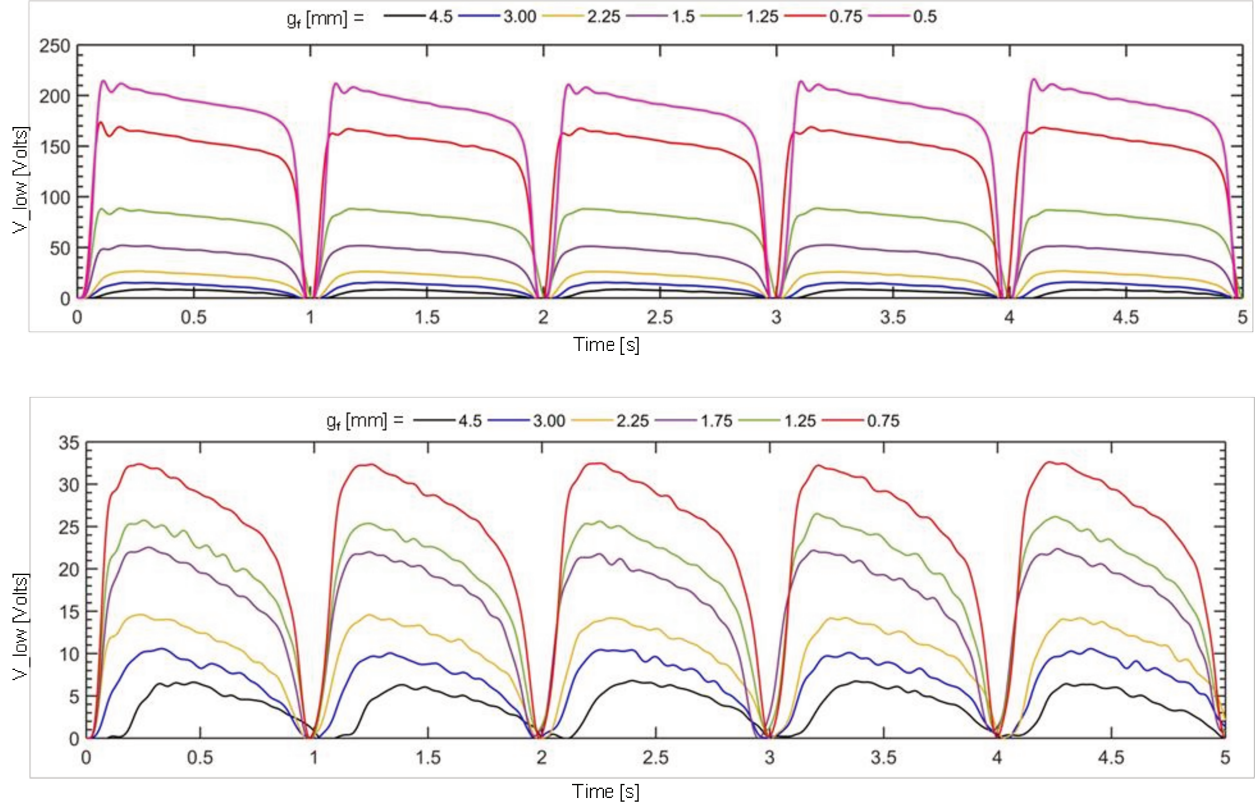


Figure 5. 10: Trend of the lower DE electrode polarization voltages obtained for Cu electrodes (a) and carbon grease electrodes (b)

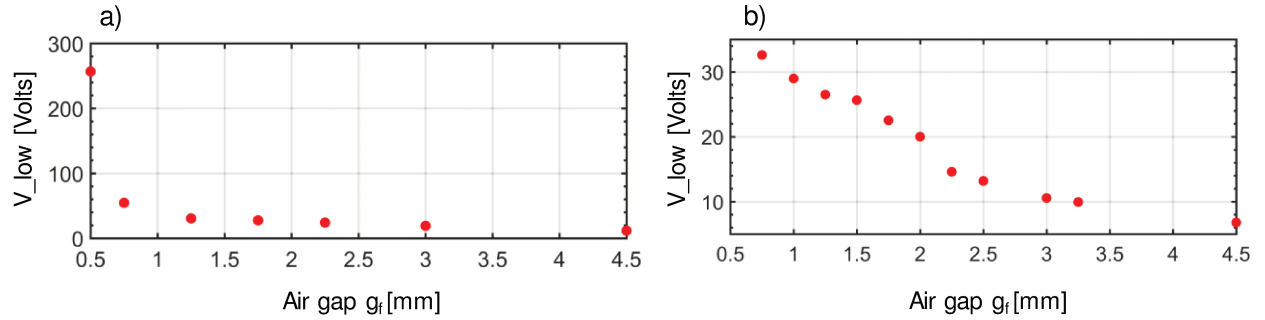


Figure 5. 11: Maximal polarization values obtained on the lower DE electrode as a function of  $g_f$  for Cu electrodes (a) and carbon grease electrodes (b)

The first consideration to be derived from these measurements is that the minimal air gap experimentally reachable with the Cu electrode was 500  $\mu\text{m}$ , while on the carbon grease electrode it was possible to achieve only 750  $\mu\text{m}$  due to manufacturing issues. Indeed, as the carbon grease electrode is applied on the surface by brushing, its

deposition is not perfectly flat and for air gap values lower than 750  $\mu\text{m}$  the moving electrode may touch the electret on some small contact points leading to electret partial discharge and lower polarization voltage values. The maximal floating potential is ensured during the electret movement (go back and approach) due to the use of the diode. The small voltage decrease observed on the maximal polarization value (i.e. from 210 V to 190 V with a final air gap of 0.5 mm) is probably due to losses at electrode and diode  $D_1$  levels. The values obtained on the carbon grease electrode were lower compared to the one on the Cu electrode: this is surely due to the higher resistivity of carbon grease (8 order of magnitude higher than the Cu electrode) which might cause higher losses in the measured value of electric potential. With highly conductive electrodes, an electrode surface potential of 220 V can thus be reached with a final air gap of 0.5 mm, which is close to the one obtained theoretically thanks to our FEM simulations (equal to 218 V) shown in Figure 5. 8 for the  $-1000$  V electret surface potential.

The polarization of the DEG lower electrode is obtained thanks to the use of an electret material. The obtained values are interesting and exploitable if a high conductivity electrode is used. Indeed, with carbon grease electrode, induced polarization voltages on the lower electrode are very low (maximum of 30 V)) thus drastically reducing the potential scavenged energy with DEG. Once the lower electrode is polarized (phase 1 to 2 in the cycle described in Figure 5.2), the classic DEG cycle can be realized and the voltage boost across the electrode will occur (phase 2 to 3 in Figure 5.2).

### 5.1.5 Scavenging phase

Once the polarization phase of the device is completed, voltage boost due to DE electrical capacitance variation occurs (see Figure 5. 2). As previously explained in chapter 2, in case of pure shear deformation, a voltage value proportional to  $\lambda^2$  can be obtained through the elastomeric membrane deformation during the active phase. To verify these values, LTSpice simulations were performed by reproducing the equivalent electrical circuit shown in Figure 5. 3.

As no model of variable capacitor is already implemented in the software, the voltage  $V_{DEG}(t)$  through the DEG was calculated through a controlling voltage  $V_c$  and through the electric charge given by the electret material polarization, as following [5.9]:

$$V_{DEG}(t) = \frac{Q(t)}{C(t)} = \frac{\int_0^T i(t)}{V_c(t)} \quad (5.5)$$

We chose a polarization voltage of 190 V induced on the DEG lower electrode by the electret material, corresponding to a final air gap of 0.5 mm with an electret surface potential of  $-1000$  V (Figure 5.12). The other electrode was set to ground. The capacitances calculated from FEM simulations (Figure 5.7) were employed as  $V_c(t)$  values, while HV 1N4148 diodes were used in the circuit. In Figure 5. 12 the results obtained for the voltage across the DE and the energy stored on a 1 nF capacitance are shown.

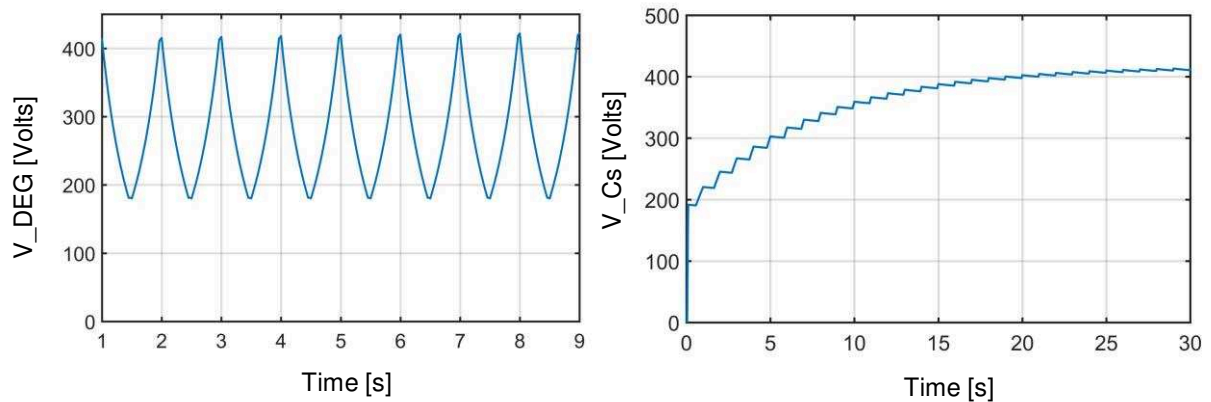


Figure 5. 12: Voltage across the elastomeric membrane (a) and in the storage capacitance (b)



These values were consistent with equation 5.1: the membrane voltage boost simulated across the DEG corresponds to 2.2 times the polarization voltage given by the electret material which is close to the theoretical value of 2.25 (calculation done with ideal plate capacitance). A time of 20 seconds (corresponding to 20 deformation cycles) is necessary to charge the storage capacitance to the maximal voltage value, corresponding to a stored energy of 84  $\mu\text{J}$ . The energy density of our hybrid device is 0.14  $\text{mJ.g}^{-1}$ . Of course, this value remains lower than the one that can be obtained with a pure DEG (up to 0.8  $\text{J.g}^{-1}$ ) but it is enough high to supply a low power consumption system and it an embedded and autonomous solution (no need of high voltage supply).

Despite the high polarization voltages obtainable from the experimental tests on the DE membrane and the estimated scavenged energy of the device, experimental realization of the final prototype presents critical points. Indeed, high polarization voltages are reachable with high conductivity electrode. With carbon grease electrode, a maximum of 30 V is reachable with a final air gap of 750  $\mu\text{m}$ . This final air gap value is chosen to limit the risk of electret discharge due to lower electrode contact. To present high performance in DEG mode, the hybrid structure need highly conductive compliant electrodes that can be deposited easily and whose thickness can be perfectly controlled. Grease electrodes do not represent an appropriate solution but conductive polymers or composite polymers (i.e. carbon charges in silicone matrix) could be employed. Moreover, the presence of a common ground on the electret electrode and on the upper DEG electrode induces problems in the lower electrode polarization. For these reasons, no truthful experimental results were obtained for the DEG phase (phase 2 to 3 in Figure 5.2) with this hybrid structure and different solutions for autonomous DEG devices development were conceived by employing piezoelectric materials as polarization sources for autonomous DEG devices. This constitutes the topic of the next part of this chapter.

## 5.2 Piezoelectric polarization

To overcome the previously described problems found for electret-based scavengers, other solutions to polarize the DEG membrane were conceived, namely the use of piezoelectric materials as polarization sources.

Piezoelectric materials (described in paragraph 2.1) can generate electric charge thanks to the direct piezoelectric effect. In the literature, few works can be found on the coupling of piezoelectric elements with the electrostatic conversion principle: Khbeis *et al.* [5.10] presented the first MEMS hybrid device (with a total volume of  $0.054 \text{ cm}^3$ ) coupling the two principles on a resonator beam structure made of a PZT material and a variable capacitor made of a polymeric dielectric layer. In the paper, the authors focus on the piezoelectric element characterization and the conception of the electronic circuit to perform synchronous electrostatic charge control. Under external 120 Hz solicitation, the beam structure can scavenge a maximal output power of  $145 \text{ }\mu\text{W}$ . Rocha *et al.* [5.11] developed a hybrid device by integrating in the sole of a shoe a PVDF piezoelectric film and an electrostatic generator, which consisted of two metallic plates separated by a flexible dielectric foam. The authors demonstrate that the presence of the electrostatic element can increase the energy scavenged by the piezoelectric material alone. Under foot pressure excitation, the average energy generated in 1 hour by a running person (2 Hz) was equal to 50 mJ. More recently, Cornogolub *et al.* [5.12] investigated the possibility of piezoelectric-electrostatic systems by focusing on the optimization of the electrical energy transfer between the two elements to optimize the scavenged energy. Starting from these promising results, in this chapter two different structures combining the piezoelectric and electrostatic generator hybrid systems will be presented: the first device employs PZT ceramic materials as polarization source for autonomous DEG devices, while in the second one PVDF polymeric materials are used. Our devices work under external longitudinal mechanical excitation (strain at low frequency) representing human movements at joints level. Moreover, the devices must present coupling mechanical structures to

synchronize the deformations acting on the two elements, thus allowing us to employ simple electronic circuit with few components.

### 5.2.1 Working principle

The working principle of these devices is similar to the case of electret polarization: the polarization voltage to the DEG device (which is necessary to perform the energetic cycle) is in this case given by a piezoelectric material: the schematic of this hybrid system operating mode is illustrated in Figure 5. 13.

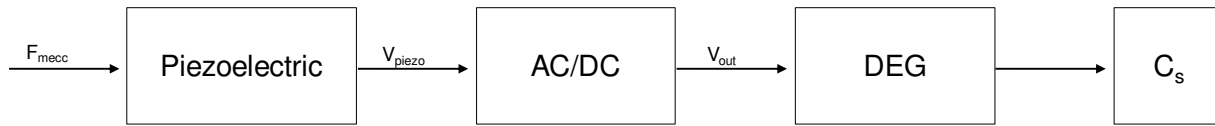


Figure 5. 13: Schematic of the hybrid piezoelectric-electrostatic device working principle

Piezoelectrics, differently from electret materials, presents an intrinsic internal polarization which allows scavenging electrical energy under mechanical excitation. From an electrical point of view these materials can be represented through the equivalent electrical circuit model shown in Figure 5. 14 [5.13].

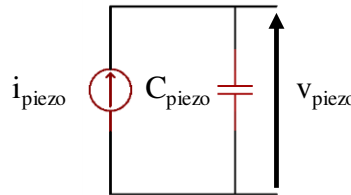


Figure 5. 14: Equivalent electric circuit of a piezoelectric element excited in quasi-static conditions

The electrical equivalent circuit of these systems consists of a capacitor ( $C_{piezo}$ ) connected in parallel with a current source ( $i_{piezo}$ ). This latter represents the total current of the piezoelectric structure generated by an external force solicitation.

Under charge mode, the total charge ( $Q$ ) that can be originated by the application of an external applied force  $\vec{F}$ , can be predicted by the following relationship:

$$D = \frac{Q}{A} = d_{3n}T_n \quad (5.6)$$

Where  $D$  stands for the total developed charge density,  $Q$  represents the resulting charge,  $A$  the total area of the piezoelectric element electrodes,  $d_{3n}$  the piezoelectric coefficient for the axis  $n$  along which the stress or strain is applied and  $T_n$  is the stress applied in the relevant direction.

When considering the coupling with the DEG, many different configurations could be adopted and different charge transfer techniques could be used to polarize the elastomeric materials. Before performing the charge transfer, anyway, a rectifying stage is necessary. To do so, two possible solutions can be considered: two or four diodes rectifier, as shown in Figure 5. 15.

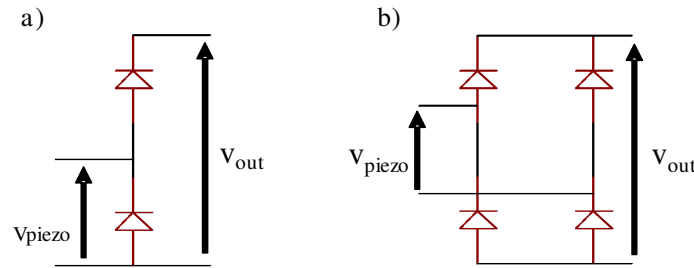


Figure 5. 15: Possible rectifier configurations for the piezoelectric voltage output

The 2 diodes rectifier allows scavenging higher energy output when the excitation periods of the two elements are the same ( $T_{piezo}=T_{DE}$ ). The solution with 4 diodes results more efficient when the polymer excitation is two-times faster than the piezoelectric one ( $T_{piezo}=2 \cdot T_{DE}$ ) [5.12].

Once the rectifying stage is completed, the electric charge needs to be transferred toward the elastomeric material to polarize the DEG element and boost the piezoelectric voltage output. As previously explained, this must occur when the DEG

is at its maximal capacitance value, namely the instant in which the maximal mechanical excitation is applied. Starting from these considerations, different configurations can be adopted. The solution proposed in [5.12] (Figure 5. 16) is interesting when using low voltage source for the DEG polarization.

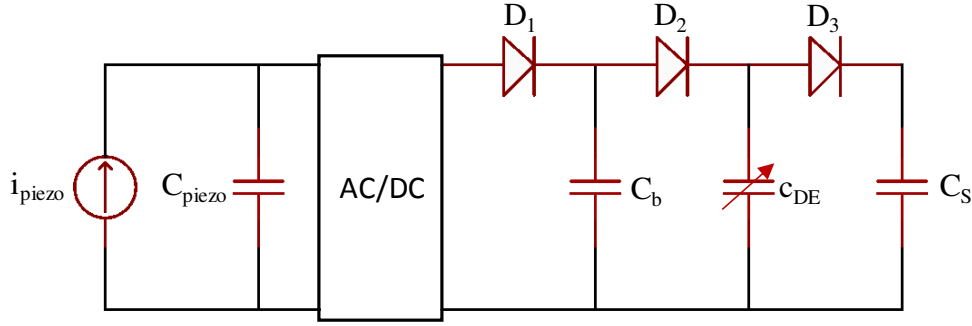


Figure 5. 16: Possible electrical configuration of hybrid system with intermediate capacitor

This schematic is specifically adopted when no synchronization between the maximal piezoelectric output and the DE maximal capacitance value occurs or when the excitation frequencies of the two elements are different. An additional buffer capacitor  $C_b$  is added in parallel to the piezoelectric polarization source, acting as intermediate storage stage between the two elements (and as smoothing capacitor for the polarization voltage).

A different situation occurs when the piezoelectric and DE deformations are synchronized, which means that they are excited at the same mechanical frequency, resulting in a concurrence between the maximal polarization through the piezoelectric element and the maximal DEG capacitance. In this case, no buffer capacitance is needed, and the rectified piezoelectric output voltage is directly used to polarize the DEG to perform the energetic cycle. Only one diode ( $D_2$  instead of  $D_1$  and  $D_2$  on Figure 5.16) is necessary to transfer the charge through the elastomer because the tension through this latter is not alternative. The boosted output tension of the DEG is then stored on a capacitor ( $C_s$ ) using the diode  $D_3$ . The DE is then relaxed and a new scavenging cycle can begin.

### 5.2.2 Materials selection

The piezoelectric materials employed in this hybrid configuration need to generate high voltage output at low working frequencies (1 Hz) and low deformation forces (few Newton) conditions, which are typical of human movements. Under these conditions, two different piezoelectric families were tested in order to compare and evaluate the device performance with these two different polarization sources. Materials tested consisted of a piezoelectric ceramic buzzer (7BB-27-4, Murata) and a PVDF film (DT4, Meas-spec), made of a rectangular piezoelectric film with silver ink screen-printed electrodes encapsulated in a thin urethane coating. Table 5. 1 shows the most relevant properties of the two materials employed in this work.

PZT buzzer properties		PVDF film properties	
Plate diameter [mm]	35.0	Dimensions [cm <sup>2</sup> ]	30
Total Thickness [mm]	0.53	Capacitance [nF]	5.7
Capacitance [nF]	30.0 ±30%	Young's Modulus [Gpa]	3
Plate Material	Brass	Relative permittivity	12
Coupling coefficient $k_{31}$ [CV.Nm <sup>-1</sup> ]	0.44	Coupling coefficient $k_{31}$ [CV.Nm <sup>-1</sup> ]	0.12
Coupling coefficient $k_{33}$ [CV.Nm <sup>-1</sup> ]	0.75	Coupling coefficient $k_{33}$ [CV.Nm <sup>-1</sup> ]	0.14

Table 5. 1: Principal properties of the selected piezoelectric materials

As can be seen from Table 5.1 and explained in paragraph 2.1, PZT present higher piezoelectric performance compared to PVDF, but this latter is characterized by lower Young modulus, lower density and encumbrance that could make it more suitable for wearable applications.

Based on the considerations described in 5.1.2, the dielectric material chosen as DEG was an acrylic membrane (VHB 4910) sandwiched between two compliant electrodes (864 MG Chemical carbon grease).

### 5.2.3 Devices structures

Based on the characteristics of the selected piezoelectric materials, two different structures need to be designed: one coupling DEG with a PZT buzzer and one employing PVDF as polarization source. Both structures need a mechanical coupling element which can transmit the uni-axial deformation (necessary to stretch the elastomeric membrane) to the piezoelectric element and guarantee the concurrence between the maximal DEG capacitance and the maximal piezoelectric polarization voltage.

#### 1. PZT-BASED STRUCTURE

For the PZT ceramic, a non-texturized structure similar to the one presented in paragraph 5.1.4 for electret polarization seemed more adapted due to the hard and undeformable nature of the piezoelectric material. The electromechanical coupling coefficient  $k_{33}$  being higher than the  $k_{31}$  one for the PZT buzzer, implies that the stretching movement imposed to the DE element needs to be converted on a compressive periodic force on the piezoelectric buzzer. Indeed, piezoelectric materials do not work well in quasi-static conditions. Various principles can be used to frequency-up the input mechanical excitation. Among them, mechanical impact solution on the PZT buzzer was chosen: a hitting cubic mass was employed to convert and transmit the mechanical excitation to the PZT material.

Schematic of the harvester structure and operating mode are represented on Figure 5. 17. **The energetic cycle** begins with the application of a strain along the x axis. This induces the structure to get elongated, imposing a stretch to the dielectric elastomer and a lateral displacement to the sides of the trapezoid (phase ① to ②). The arc-shaped structure (connected to the lateral sides of the trapezoidal frame) pushes down the hitting mass, which impacts the PZT buzzer, producing an output voltage due to the direct piezoelectric effect (phase ②). This voltage is conditioned and serves as polarization voltage for the DEG (② to ③). During the scavenging phase (③ to ④), the structure is released and the dielectric elastomer membrane can increase its stored

energy (given by the piezoelectric material polarization) thanks to its capacitance variation. The input electric energy is thus amplified by means of the strain movement and then the device returns to the initial state (④ to ①). The hybrid structure was performed under cyclic release-deformation cycles of 1Hz working frequency.

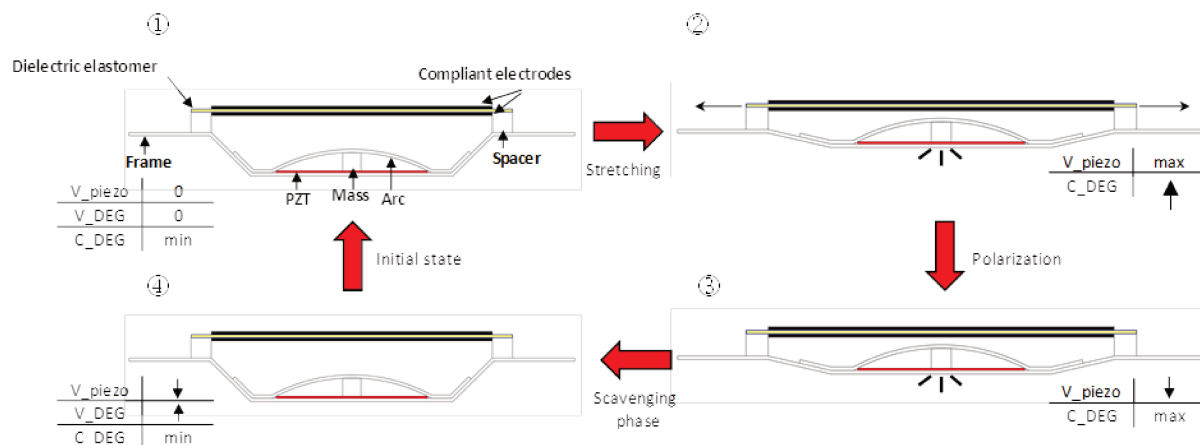


Figure 5. 17: Schematic and working principle of the PZT-based prototype

The experimental prototype is shown on Figure 5. 18, while the geometrical parameters are reported in Table 5. 2.

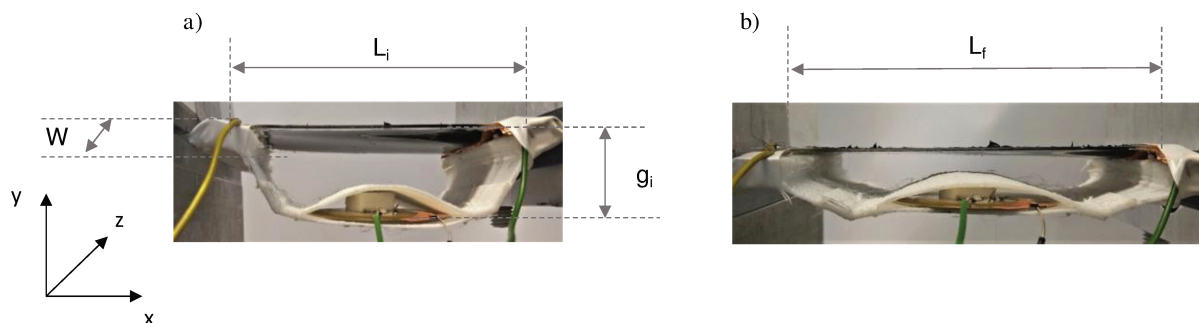


Figure 5. 18: PZT-based experimental prototype in rest (a) and deformed (b) state



Li [cm]	5
Lf [cm]	$L_i \cdot \lambda = 7.5$
W [cm]	5
gi [cm]	1.2
Structure weight [gr]	14

Table 5. 2: PZT-based structure parameters

The frame, the arc-shape and the impact mass were 3-D printed with Semiflex™ by Ninjatek (see Table 4.5 for details), resulting in a light-weight and highly deformable structure. The thickness of the frame and the arc-shape is 0.8 mm.

The piezoelectric material (PZT buzzer) was glued in the middle of the frame, as shown in Figure 5.18. The cubic mass optimal side length was found through experimental tests (maximization of the output voltage for a given input mechanical impact) to be equal to 0.7 cm, with a total weight of 1.2 mg. In order to synchronize the maximal PZT output voltage with the maximal DE capacitance, the mass was glued under an arc-shaped support, which is connected to the lateral sides of the trapezoidal support. The arc was dimensioned in such a way that the mass applies the higher impact force during the maximal deformation state. Finally, the pre-stretched dielectric elastomer was set on the upper part of the device and sandwiched between the two compliant carbon grease electrodes.

## 2. PVDF-BASED PROTOTYPE

The second prototype schematic, characterized by a PVDF polarization element, is shown in Figure 5. 19.

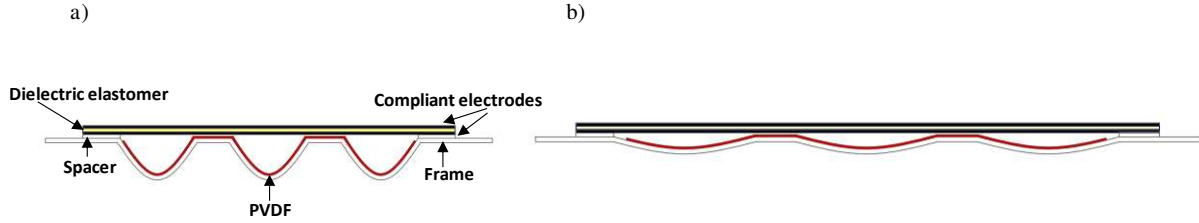


Figure 5. 19: PVDF-based device schematic in the rest (a) and deformed (b) state

In this case, a 3D-printed serpentine-shaped frame made of Semiflex™ was employed: the flexible nature of the PVDF material resulted well adapted to be integrated on a texturized frame in order to convert the high deformations applied into voltage. Moreover, the texturized frame allows limiting the deformation applied to the DEG, which stands in the upper part of the device.

Also in this case, the frame allowed us to synchronize the maximal electrical capacitance of the DEG with the maximal output voltage of the PVDF material: when the device is stretched through an external force, the piezoelectric material is deformed and generates electrical charges. These latter are transferred to the upper DEG (which is in the maximal capacitance state) as polarization source. Then, when the structure is released, the DEG goes back to its minimal capacitance configuration, thus boosting the PVDF polarization voltage.

In this case, the support frame element allows the piezoelectric solicitation in the longitudinal direction and, to further improve the energy conversion, the PVDF element was constrained along its length using tape. This latter, when the frame is at its maximal stretch, guarantees the exertion of a pressure on the polymer length, thus exploiting both the  $k_{33}$  and  $k_{31}$  electromechanical conversion coefficients.

The experimental prototype realization and dimensions are respectively shown in Figure 5. 20 and Table 5. 3.

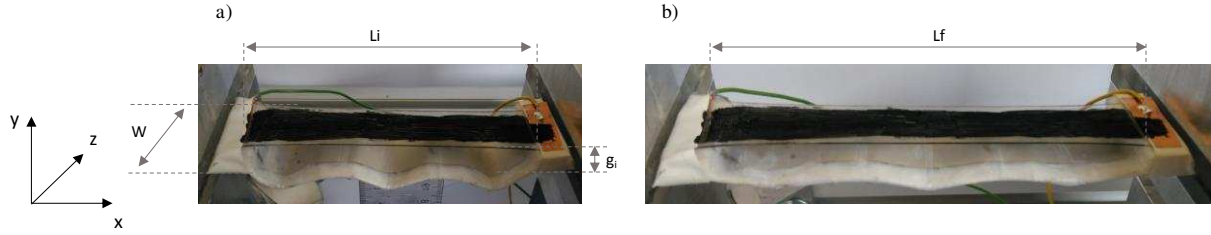


Figure 5. 20: Experimental prototype in the rest (a) and deformed (b) configuration

$L_i$ [cm]	8
$L_f$ [cm]	$L_i \cdot \lambda = 12$
$W$ [cm]	3
$g_i$ [cm]	1
Structure weight [gr]	11.5

Table 5. 3: PVDF-based structure parameters

As shown in Figure 5.20 and Table 5.3, the total height of this prototype is lower than the one of the first presented device, resulting in a lower encumbrance and a higher embeddable structure for wearable applications. Due to the polymeric nature of this piezoelectric material, the total device weight is  $\sim 20\%$  lower than the PZT-based prototype.

#### 5.2.4 Mechanical excitation

Devices tests were performed using the mechanical test bench presented in paragraph 4.3.1 under uni-axial 50% deformation cycles at 1Hz frequency (typical of human limbs). The results on the total mechanical forces measured on the two prototypes to pass from the rest to the maximal deformation state are shown in Figure 5. 21.

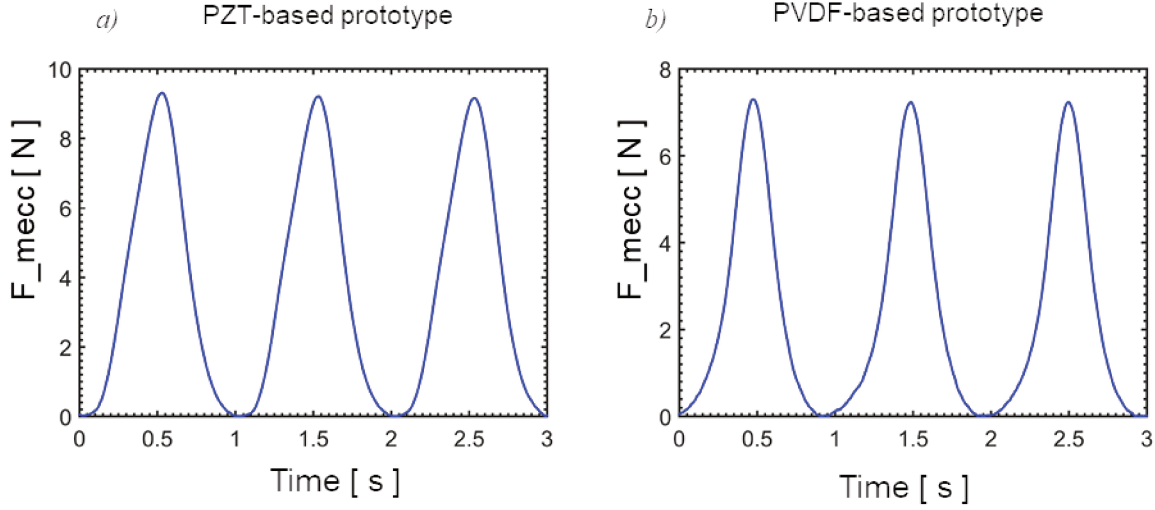


Figure 5. 21: Resulting mechanical forces trends on the two hybrid devices (the measures performed on 2 prototypes resulted highly reproducible)

The mechanical force presents the expected sinusoidal trend with time and its maximum value corresponds to the maximal deformation position (end of the stretch phase). The maximal values obtained on the PZT and PVDF-based devices were respectively equals to 9 and 7 N. These low values will not disturb the user during daily activity and do not require additional efforts (see 4.3.2). By comparing the results obtained for the two prototypes, one can note that the mechanical force needed to deform the PVDF-based prototype is 20% lower. We attribute this difference to the arc-shape support in the PZT-based device, which made the structure more rigid and consequently more difficult to deform. The maximal total mechanical energies inputs for the PZT and PVDF based prototypes are respectively equal to 273 mJ and 261 mJ.

### 5.2.5 DE capacitance variation

The DEG capacitance variations resulting from external stretch were derived from numerical simulations (Comsol Multiphysics as described in 5.1.3) and experimentally measured using the setup described in 4.1.5. Figure 5. 22 shows the results obtained

from the two prototypes (the dimensions of the DEG in the two cases are reported on Table 5. 2 and Table 5. 3).

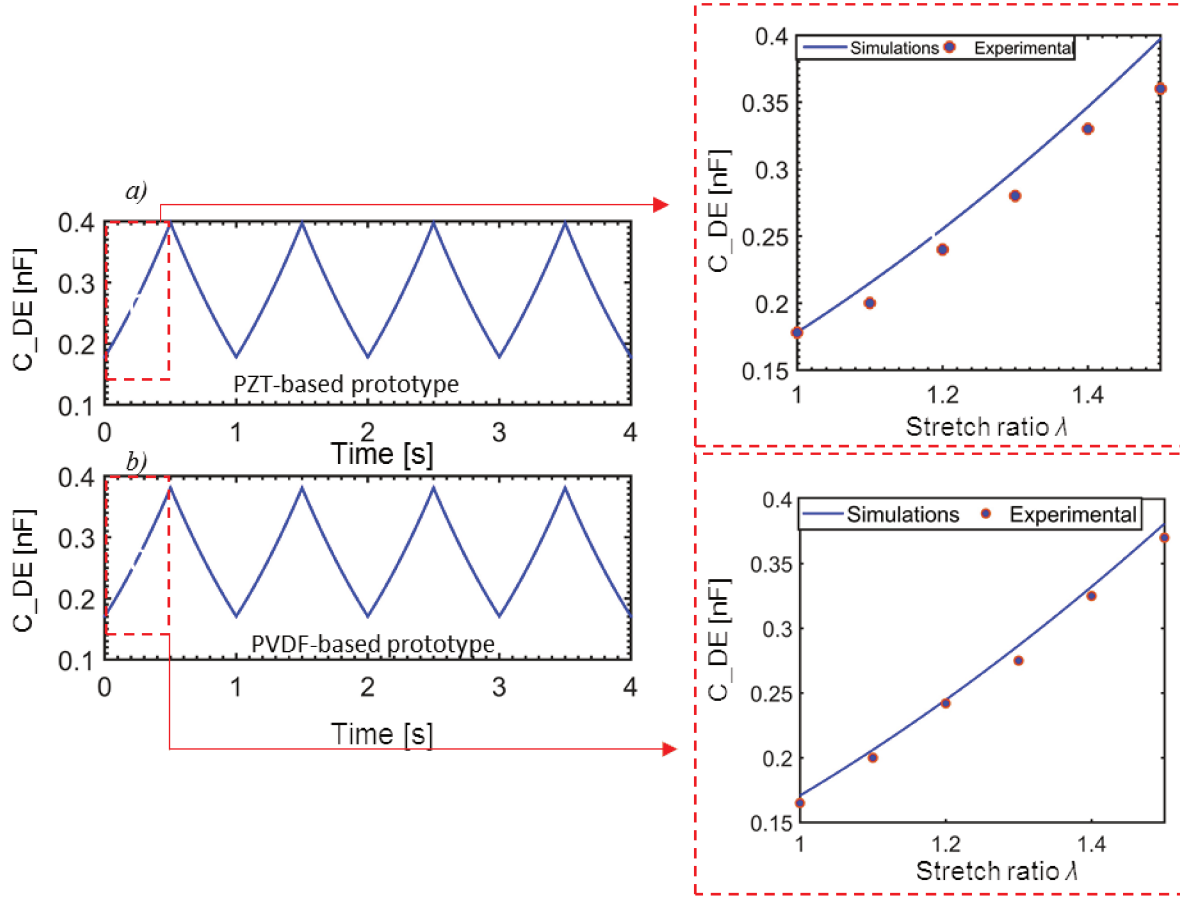


Figure 5. 22: Comparison between the electrical capacitance values obtained from numerical simulations and experimental measurements in the PZT-based (a) and PVDF-based (b) prototypes

The values found for capacitance variation from the simulations and experimental measurements are in good agreement and reflect the trend observed for the electret-based prototype. The PVDF-based device presents slightly lower capacitances values than the PZT-based one, due to geometry configuration (not the same area for the DEG). The manufacturing issues and the experimental tests conditions employed result in a ratio between the maximal and minimal capacitances values respectively equals to 2.2 and 2.15 (instead of 2.25 predicted by analytical ideal model). The values

obtained for capacitance variation are high enough to scavenge energy with electrostatic converters.

### 5.2.6 Experimental setup

Due to the synchronization of the maximal piezoelectric output voltage with the maximal DE capacitance, no intermediated buffer capacitance was needed and passive elements can be used in the circuit. Based on these considerations, the circuits shown in Figure 5. 23 were employed for devices testing.

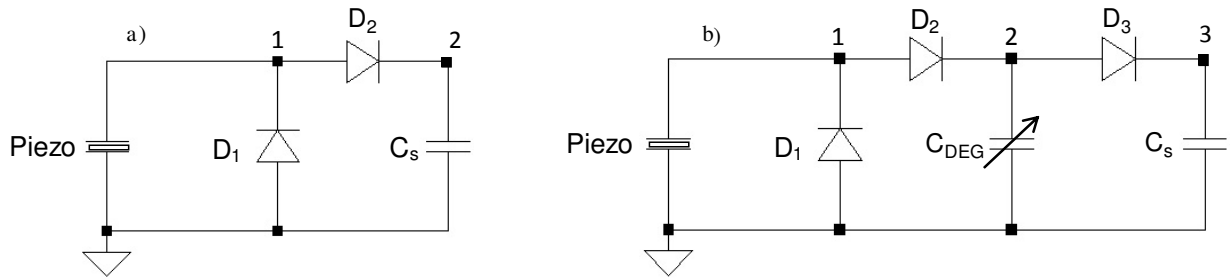


Figure 5. 23: Equivalent circuits models employed for the experimental characterization of the piezoelectric material alone (a) and of the hybrid device (b)

The first circuit (Figure 5. 23a) allowed us to evaluate the energy scavenged by the piezoelectric material. The rectifier circuit was realized using two diodes, based on the considerations described in paragraph 5.2.1. Two different low losses diodes were tested, 1N4148 (Vishay) and BAS45A (Nexperia), the latter resulting in lower losses in the output energy value. For the hybrid system, the circuit shown in Figure 5. 23b was employed. Similarly to the case of electret polarization, the active element (DEG) is connected in parallel with the polarization source and a unidirectional energy transfer occurs thanks to the presence of the diodes. In this way, the rectified piezoelectric output is directly transferred to the DEG element to perform the energetic cycle. The measurements were performed using the setup described in paragraph 4.3.1, under deformation-release external excitation at 1Hz and with acceleration value set to  $8 \text{ m.s}^{-2}$  and 50% deformation. Different values of storage capacitance  $C_s$  were tested,

starting from a value of 1 nF, close to  $C_{\text{DEG}}$ , until a value of 1  $\mu\text{F}$ , namely 3 orders higher.

### 5.2.7 Devices performance

In order to characterize the performance of the proposed devices, the voltage across the rectified voltage output of the piezoelectric device and through the DEG (respectively corresponding to points 1 and 2 in the hybrid circuit of Figure 5. 23b) were registered. The results for the two devices are shown in Figure 5. 24.

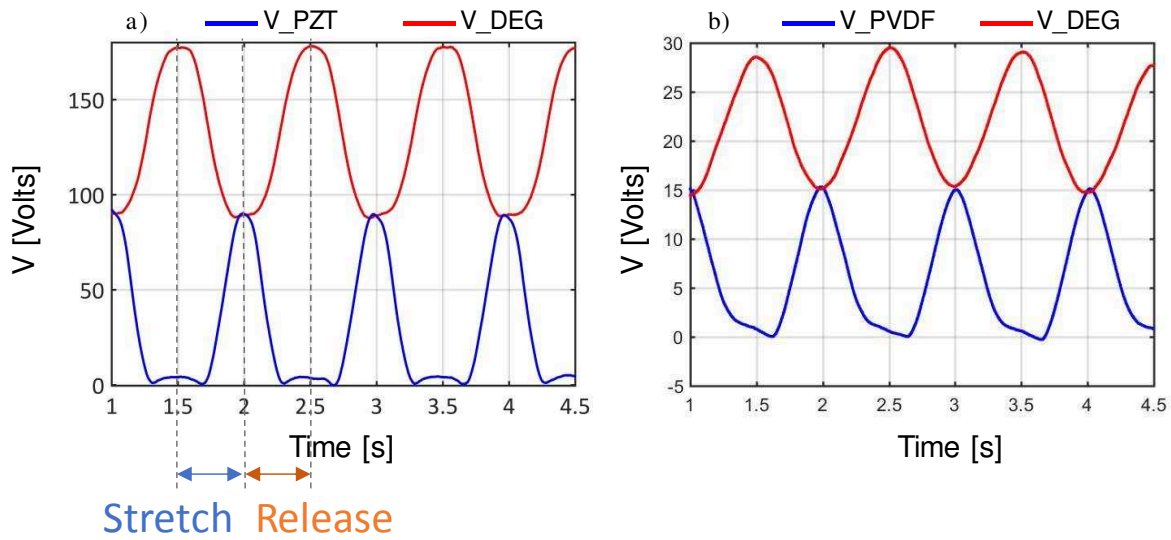


Figure 5. 24: Voltage outputs of the piezoelectric material and through the DE membrane in the PZT-based (a) and PVDF-based (b) prototypes.

From Figure 5. 24, the following consideration can be derived:

- The polarization voltage given by the piezoelectric materials presents the expected sinusoidal trend following the mechanical 1Hz excitation. The PZT element maximal voltage output (which presents a peak value equal to 85 V) is more than 5 times higher than the PVDF material (whose maximal value is equal to 15 V). In addition, it was observed that the PVDF output voltage presented a less constant trend among the different deformation cycles

(variation of the maximal output). This can be attributed to the fact that the PVDF material is glued on the serpentine frame and deformed on all its length, following the deformation given by the support. Due to its low Young modulus and to the soft nature of the material, the deformation it withstands in the different deformation cycles can slightly vary. Consequently, a standard deviation equal to  $\pm 4$  V on the maximal voltage output values was observed. The PZT voltage output presented instead a higher repeatability through the different deformation cycles. This can be associated to the lower degree of freedom of the PZT buzzer (which is fixed on the bottom of the trapezoidal frame) and to the more localized mechanical excitation. The hitting mass impact point is in the centre of the ceramic and exercises quite always the same force on the piezoelectric material, resulting in a lower difference among the different cycles. This mechanical consideration can be also the reason explaining the difference between the curves shapes: while the slope of the PZT voltage output curve is higher,  $V_{PVDF}$  goes back to 0 V with a lower speed. This difference in the dynamic of the two hybrid structures could be attributed to the different solicitation conditions (impact versus longitudinal).

Moreover, it can be noticed that the two structures reach a released state (no output voltage) before the end of the relaxed phase and that their behavior just before reaching the rest position differ. A slightly variation of  $V_{PZT}$  occurs probably due to seismic movement of the structure imposed by the test bench (namely one additional peak). In the  $V_{PVDF}$  curve voltage, electric losses can be observed, mainly associated to the impact of the electronics on the piezoelectric material output.

- Concerning the DE membrane voltage boost ( $V_{max}=C_{max}*V_{min}/V_{max}$ ), it can be observed from the above graphs that theoretical predictions well represented the experimental results. Specifically, the voltage across the DE after the scavenging phase passes from 85 V to 180 V in the PZT-based device, while the polarization voltage given by the PVDF material (15 V) is boosted from DE membrane to a value of 30 V. These latter correspond to respective amplification



of 2.12 and 1.93, which are close to the theoretical value of 2.25 and to the experimental values of 2.2 and 2.15 respectively found from capacitance variation for PZT and PVDF prototypes (see paragraph 5.2.5). The slight differences between the two values may be attributed to leakage current at electrodes or diodes levels or to measurements incertitude.

To characterize the two systems, the energies stored on the storage capacitance  $C_s$  were compared using the piezoelectric element alone (point 1 of the circuit in Figure 5. 23a) and the hybrid systems (point 3 of the circuit in Figure 5. 23b). Results obtained using  $C_s$  equal to 1 nF (close to  $C_{DEG}$  value) are shown in Figure 5. 25.

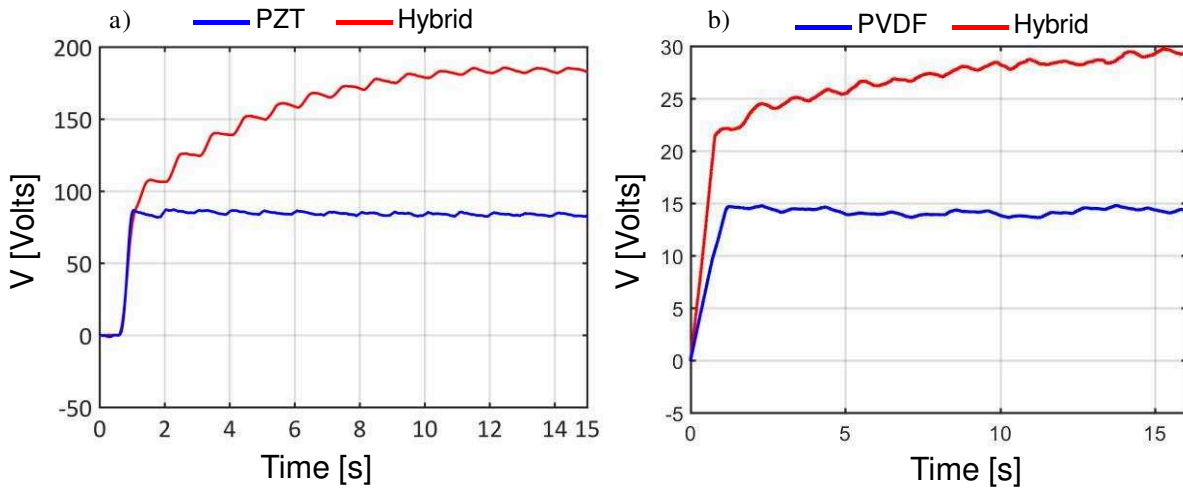


Figure 5. 25: Voltage outputs through 1nF storage capacitor in the PZT-based (a) and PVDF-based (b) prototypes.

For each deformation cycle the storage capacitance is charged (from which derives the ‘steps’ present in the curve) due to charge transfer from the DEG through the diode  $D_3$ . The voltage presents a slight decrease after each cycle due to electric losses in the circuit.

For the first hybrid system, the maximal voltage of 180V was obtained through the storage capacitor after 10 seconds, namely after 10 deformation cycles. 12 deformation cycles were needed in the PVDF-based prototype to reach the maximal voltage of 30 V across the storage capacitance, which is a value significantly lower compared to the

first case. Beneath, the steps observable in Figure 5.25a are less defined in the second prototype. These results are in accordance with the voltage output values presented in Figure 5. 24 and well reflect the previously described considerations.

The storage capacitance charging time is attributed to the difference between  $C_{DE}$  and  $C_s$  values: higher  $C_s$  result in higher stored energy but consequently the time needed to charge them is higher. Compared to the piezoelectric element alone, the values obtained with the hybrid system reflect the voltage boost given by the DE membrane. The total stored energies are respectively equals to 17.13  $\mu\text{J}$  and 0.45  $\mu\text{J}$  for the PZT and PVDF hybrid devices, which correspond to energy density of 16.1  $\mu\text{J.gr}^{-1}$  and 0.6  $\mu\text{J.gr}^{-1}$  of active material.

Even if the values obtained in this section are lower compared to the previously described electret prototypes, they represent a proof of concept of the piezoelectric-electrostatic conversion principle with a complete in-one structure (namely the two electroactive materials are deposited onto one structure and not on two different host structures).

Further improvements of these quantities are possible and different factors can contribute to increase the energy output of the device, as described in the next paragraph.

### 5.2.8 Performance optimization

Evaluations on the devices performance optimization was performed though the implementation of the equivalent circuit of the system (Figure 5. 23b) on LTSPICE software, as previously described in 5.1.5. Three parameters have been considered with this aim: the influence of the number of dielectric layers forming the DEG, the polarization voltage (piezoelectric voltage output) on the DEG and the working frequency of the device. In the last two cases, the maximal voltage output of the piezoelectric materials was verified though experimental tests.

### - Effect of the dielectric layers stack

The first simple solution to increase the performance of the presented prototypes is to employ a stack of  $N$  dielectric layers as DEG. This solution, frequently employed in the literature [5.12], [5.14], can allow us to increase the equivalent capacitance of the DEG. Results of voltages through the storage capacitor obtained for the two prototypes are shown in Figure 5. 26.

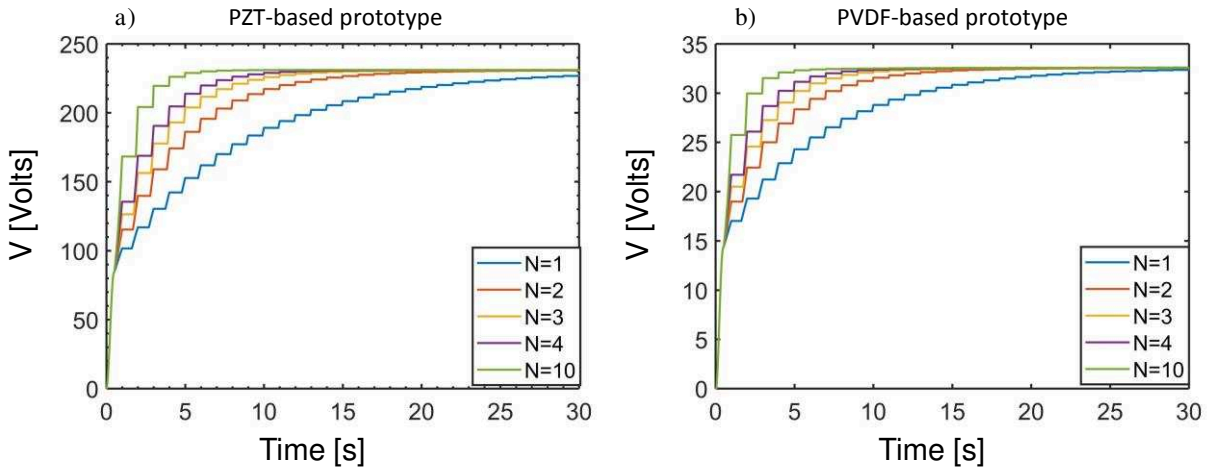


Figure 5. 26: Voltage through the storage capacitor for stack configurations with different number of dielectric layers ( $N$ )

One can note that the increase of the dielectric layers numbers ( $N$ ) decreases the storage capacitor charging time. A difference of  $\sim 25$  seconds is registered among the single-stack structure and the one made of the stack of 10 dielectric layers. This is due to the resulting lower difference between the DEG capacitance and the storage one, which leads to a higher energy transferred to  $C_s$  during the discharge phase of the energy cycle. In fact, for each deformation cycle, the height of each step in the storage capacitance voltage is higher with increasing number of DE layers.

-Effect of the polarization voltage

DEG polarization voltage increase leads to higher device scavenged energy (see 5.1.1). In order to evaluate this possibility, different polarization voltages were considered for the DEG device. For the PZT-based prototype, voltages values equal to 100V and 125V were compared. Indeed, we experimentally verified that these values were reachable through higher impact mass volumes and for higher mechanical deformations accelerations. In case of PVDF-based prototype, instead, due to the lower encumbrance and softness of this piezoelectric material, higher polarization voltages were reachable by stacking different PVDF on the structure. Through the stack of 4 PVDF layers, voltages output up to 4-times the single layer can be obtained. The integration and synchronization between each PVDF layer is in fact easy to obtain for the conceived geometry. Figure 5. 27 shows the simulation results obtained on the voltage stored through  $C_s$  for the two prototypes.

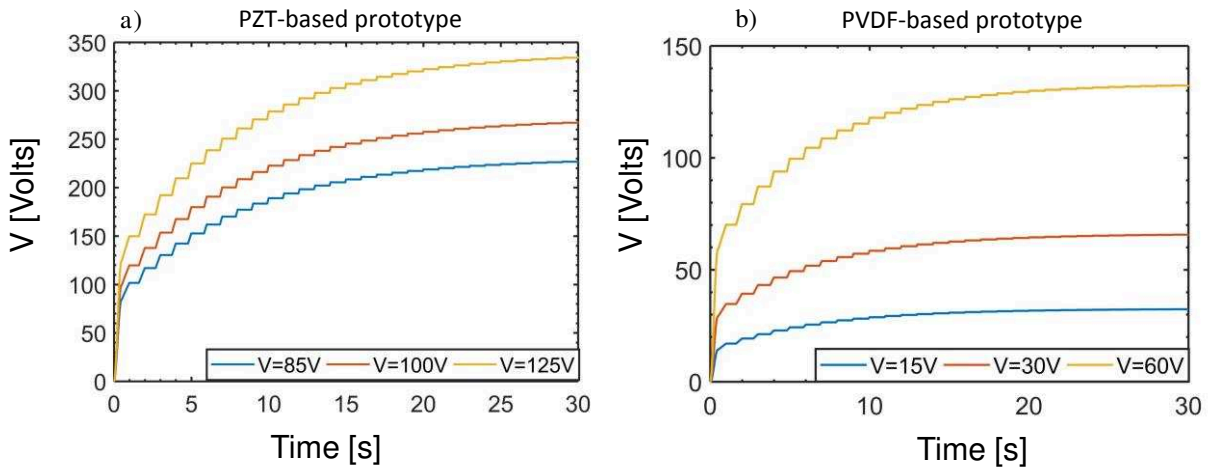


Figure 5. 27: Voltage through the storage capacitor for different piezoelectric voltage output polarization

As expected, higher polarization voltages lead to higher stored energy. The theoretical  $\lambda^2$ -proportionally between input and output DEG voltages was verified for both prototypes. Maximal stored energies of  $58 \mu J$  and  $9.2 \mu J$  can be respectively obtained for the PZT and PVDF-based devices with this technique.

### - Effect of the working frequency

Another parameter considered in this study was the working frequency of the device. In fact, so far, a mechanical deformation of 1Hz (correspondent to the walking frequency) was employed. Nevertheless, higher frequency (close to 2 Hz) can be registered on human body movements while running. The influence of the working frequency on the charging time of the storage capacitor is shown on Figure 5. 28.

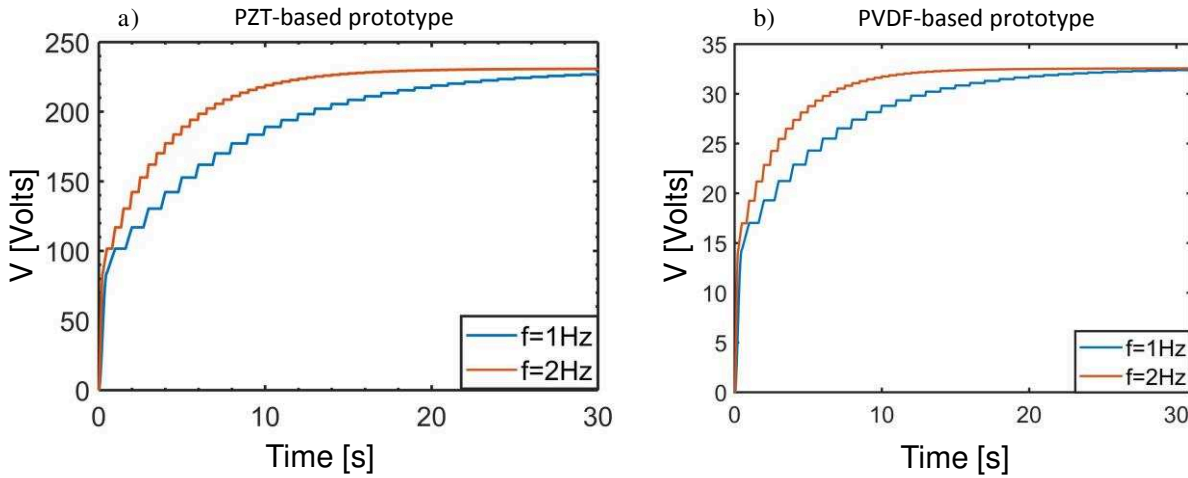


Figure 5. 28: Influence of the working frequency on the voltage through the storage capacitor

In this case, while the energy transferred for each cycle is the same in the two tested conditions (as seen from the same step height in the voltage curves) the maximal stored energy is reached ~20 seconds before for the higher frequency case. This is associated to the higher power output obtained from the piezoelectric materials in our configuration when working at 2 Hz frequency.

## Conclusion

In this chapter, two different solutions for DEG-based device polarization have been proposed. In the first one, the DEG is coupled with an electret material, while in the

second one piezoelectric elements are employed as polarization source. Results are summarized in Table 5.6.

	<b>Polarization material</b>	<b>Polarization voltage</b>	<b>Total dimensions</b>	<b>Energy density</b>
Prototype 1	Electret	190 V	L5×W5×H1.2 cm <sup>3</sup>	0.14 mJ.g <sup>-1</sup>
Prototype 2	PZT	85 V	L5×W5×H1.2 cm <sup>3</sup>	16.1 μJ.g <sup>-1</sup>
Prototype 2	PVDF	15 V	L8×W3×H1 cm <sup>3</sup>	0.6 μJ.g <sup>-1</sup>

Table 5.6: Results obtained for the second operating mode energy harvesting devices

In the first case we showed that an energy output of 84 μJ can be obtained after 20 seconds on a 1-nF storage capacitor when polarized with an electret material charged at −1000 V.

For piezoelectric polarization, the conception and experimental testing of two different prototypes was performed. The first one is made of a trapezoidal shape coupling DEG with a ceramic PZT: this structure, under 1Hz mechanical deformation (typical of human body) can develop a maximal polarization voltage of 85 V, resulting in a total energy scavenged of 17.13 μJ. The second one, employing PVDF as active materials, is lighter and more embeddable compared to the first one, but its performance are lower: a maximal polarization voltage of 15V, corresponding to a total 0.45 μJ scavenged energy was obtained.

Even if these values are lower compared to the electret-based solution, we showed that the employment of DE layers stack, increase of piezoelectric voltage output and increase of the device working frequency can improve the performance of these harvesters. This new proposed solution is in fact interesting for further development. Contrary to electrets materials, piezoelectric materials are less influenced by external environmental conditions and can thus be considered as a promising alternative for DEG based hybrid devices, especially for wearable applications.



# Conclusions and perspectives

The work carried out during this PhD project aims to fabricate soft wearable energy harvesting devices to scavenge the kinetic energy at human knee level to supply low-power consumption sensors.

In this context, we fulfilled the following **principal objectives**:

1. Study and characterization of conformant polymeric electret materials employed as polarization source for electrostatic energy harvesting devices with evaluation of their performance in harsh environments, targeting wearable applications.
2. Optimization of the performance of the first generation of hybrid devices developed by our research group based on the coupling between dielectric elastomers and electret materials.
3. Conception and realization of new hybrid solutions and designs of dielectric elastomers generators devices.

To fulfill these objectives, we have first reviewed the most employed technologies in the literature for kinetic energy harvesting applications. From the comparison of these technologies, we have concluded that dielectric elastomers generators present the most suitable characteristics for satisfying the requirement of our applications, namely high-energy density, low working frequency (1 to 2Hz, typical of human movements), low-weight and softness. Nevertheless, further studies need to be performed to overcome the principal drawback of these structures, namely the need of an external polarization source to perform the energetic cycle. To overcome this limitation without introducing in the system additional electronics or bulky systems, we have identified that hybrid devices made by the coupling with piezoelectric or electret materials may respond to the need of external polarization elimination in



DEGs. An extensive state-of-the-art research on these two technologies was thus performed, especially by focusing on the examples of wearable applications found in the literature.

Starting from these considerations, the first part of the work was focused on electret materials, whose stability along the time was shown to be the most important parameter for electret-based devices performance. Highly conformant electret materials with long-term charge stability were envisaged for our applications. The chemical structure and properties of poly(p-xylylene) polymers (i.e. Parylenes) seemed adapted to reach these objectives. Three variants of Parylene materials (C, AF-4 and VT-4) were thus fabricated and tested through long-term surface potential monitoring of corona discharge electrets. In fact, while in the literature Parylene C is widely employed among other commonly used electrets (i.e. Teflon families or CYTOP), fluorinated Parylenes AF-4 and VT-4 are less or no used as electret materials. Nevertheless, the presence of fluorinated atoms in their chain was expected to guarantee a longer lifetime than the C variant. The results obtained from the measurements made on different samples thicknesses and with different charging parameters confirmed our hypothesis: charge densities equal  $1.7 \text{ mC.m}^{-2}$  and  $1.8 \text{ mC.m}^{-2}$  were respectively found after 100 days for AF-4 and VT-4 polymers, which are comparable with the best result found in the literature on corona discharge polymer electrets. Beneath, we showed that Parylene AF-4 presents good stability both for positive and negative charge over long time (300 days), making it advantageous over other reviewed materials. Both fluorinated polymers present good stability in harsh environments (temperatures up to  $80^{\circ}\text{C}$  and relative humidity reaching 60%), indicating their suitability for wearable applications.

The second part of the work was focused on the development of hybrid energy scavengers coupling electroactive materials.

An optimization study was carried out to increase the performance obtained on the first generation of hybrid DE-electret devices. These structures can scavenge energy

through the principle of charge recombination between the electrodes of a variable capacitor. We showed that substituting 50- $\mu\text{m}$ -thick Teflon FEP (employed in the first proof of concepts) with 9-  $\mu\text{m}$ -thick Parylene AF-4 can enhance the device output power of 40%, while shape optimization leads to 49% performance increase, confirmed by the tests realized on experimental prototypes. Possible solutions for more embeddable structures designs were proposed, the optimal one resulting in an initial air gap of 4 mm and a scavenged energy density of  $2.2 \text{ mJ.gr}^{-1}$ .

Other operating modes for electrostatic transducers were also investigated, through the conception of innovative hybrid devices solutions working as autonomous DEGs. Electrets materials were first tested in this new coupling concept, showing that their permanent electric polarization can be employed for HV source replacement. While in the first operating mode the device works under electret charge recombination following capacitance variation, in this case the electret material is employed for DEG polarization. We correlated the obtained polarization voltages on the DEGs to the geometrical parameters of the device through FEM simulations and experimental measurements, experimentally showing polarization values of 200 V on the DEG electrode. This high polarization voltage can allow scavenging over the complete energy harvesting cycle, a stored energy equal to  $84 \mu\text{J}$  in 20 seconds, through a simple rectifier circuit.

New hybrid structures were also realized coupling DEGs with piezoelectric materials. Specifically, we presented two different devices allowing the synchronization between the maximal piezoelectric material output and the maximal DEG capacitance. The first one is based on the solicitation of a piezoelectric ceramic under impact mode, while the second one operates under longitudinal solicitation of a PVDF material. The two structures, aimed as proof-of-concepts of this innovative hybrid solution, showed the feasibility of this new polarization source. The first structure can scavenge a total energy of  $17.13 \mu\text{J}$  over 10 seconds under 1 Hz-mechanical stretching, while the one made of PVDF, even if lighter and less encumbering, presented lower performance ( $0.45\mu\text{J}$  over 12 seconds). The energy values experimentally obtained from these

prototypes are lower than in case of electret polarization. Nevertheless, this new solution may represent a promising alternative to electret materials, as the polarization given by piezoelectric materials derives from their internal structure and is thus not sensitive to discharge upon contact or external environmental conditions (in the range considered by our applications). Indeed, through simulations, we showed that several parameters can improve the global performance of the structure, namely, the number of elastomers layers, the working frequency, and the piezoelectric output voltage. The latter can be obtained through stacking structures, or through scavenger geometrical parameters optimization.

From a global point of view, one more stepping stone has been posed towards the development of wearable energy harvesting devices. In fact, even if the energy obtained with our prototypes are lower compared to classical DEGs, our solution is completely embeddable. It requires few electronics components and no external polarization source is needed, thanks to the coupling between electroactive materials.

Based on these promising results, **new perspectives** for the development of this work can be envisaged:

1. Dielectric elastomer and electrodes improvement

Improvement of the elastomeric membrane employed as active material in this work can be envisaged to increase the device performance. Specifically, on the bibliographic review (chapter 2) we have found that composite materials embedding fillers in the polymeric matrix can enhance the dielectric constant of the material. When overcoming the main issue associated with this technique (increase of the losses and decrease of the breakdown field), this can lead to an increase in the energy output scavenged by our devices. Incorporation of these high-performance composite elastomers in our scavengers is thus envisaged in future works.

Moreover, our experiments indicate that the lower conductivity of carbon grease electrodes limits the maximal polarization that can be obtained with our

structures in DEG mode. The employment of more performant electrodes could thus boost the performance of our devices.

## 2. Development of an embedded structure

The optimization study performed on the first operating mode has led to the fabrication of a second generation of more performant prototype. New more embeddable structures have been designed and simulation results underline energy scavenging boost up to 3 times. Further studies could consist in the realization and testing of an operational prototype to experimentally verify these possible higher values. Moreover, the integration of the proposed structures on a wearable band to test its performance on a real application is envisaged, towards the supply of a low-power consumption sensor.

## 3. Improvement of the hybrid DEG-piezoelectric structure

Two proof-of-concept structures coupling DEGs with piezoelectric materials were experimentally realized, demonstrating the feasibility of this new working mode for autonomous devices. As showed in numerical simulations, different parameters can be varied to increase the performance of the structure. In the optic of these results, experimental realization of optimized structures is envisaged to further push ahead the comparison between the two presented DEGs polarization sources in this work: piezoelectric vs electret materials.



# Résumé

Ce manuscrit présente mes travaux de thèse sur le développement de dispositifs de récupération d'énergie cinétique à partir de mouvements du corps humain pour produire de l'électricité. Cette solution est une alternative prometteuse pour l'alimentation de dispositifs à faible consommation d'énergie. Les textiles électroniques pour la surveillance médicale déportée ou les implants biomédicaux sont quelques-unes des applications possibles pour lesquelles un système d'auto-alimentation serait bénéfique.

Dans ce contexte, en 2013, un premier prototype de récupérateur d'énergie souple a été développé par notre groupe de recherche à travers une collaboration entre les laboratoires LaMCoS et G2Elab. Ce générateur électrostatique est basé sur la technologie des générateurs à élastomères diélectriques (*Dielectric Elastomer Generators* DEGs), qui fonctionnent sur la déformation mécanique d'une couche fine de matériau diélectrique (acrylique ou silicone) entre deux électrodes déformables et un matériau électret (i.e. isolant constituant un réservoir de charges stockées).

Les objectifs de ce travail de thèse se sont focalisés sur l'optimisation du premier prototype pour réaliser un dispositif de deuxième génération plus performant, moins encombrant et avec une durée de vie plus longue. De nouvelles alternatives de récupérateurs hybrides basées sur d'autres principes de fonctionnement mais aussi diverses associations de matériaux actifs ont aussi été proposées et ont constitué une autre partie importante de ce travail de thèse.

Le manuscrit a été organisé en cinq chapitres. Le premier chapitre introductif vise à donner une vue d'ensemble du principe de fonctionnement et des principales technologies de récupération de l'énergie ambiante afin d'aider le lecteur à comprendre

les motivations du choix technologique adopté dans le présent travail pour récupérer l'énergie cinétique humaine au niveau du genou.

Dans le deuxième chapitre, un état de l'art sur les générateurs piézoélectriques et électrostatiques est présenté. Ce chapitre décrit le principe de fonctionnement et les équations régissant ces technologies, les performances et les conditions de travail optimales pour ces systèmes. Des exemples issus de la littérature ont été décrits avec des applications centrées sur la récupération de l'énergie cinétique humaine. À partir de cet aperçu, des choix technologiques se sont dégagés pour développer nos DEGs.

Le troisième chapitre est consacré à la caractérisation de différentes variantes de Parylène en tant que matériau électret pour des applications de récupération d'énergie. Le principe physique des matériaux électrets et les techniques expérimentales utilisées dans ce travail pour la caractérisation des électrets sont présentés. Ensuite, les résultats obtenus sur l'applicabilité des différentes variantes de Parylène pour nos applications sont décrits pour diverses conditions de tests prenant en compte des paramètres environnementaux.

Dans le quatrième chapitre, le premier dispositif de récupérateur d'énergie est exposé en se focalisant principalement sur l'optimisation du design, l'influence des matériaux utilisés sur les performances des structures et la réduction de la taille. Les résultats obtenus sur la réalisation expérimentale d'un prototype opérationnel sont fournis et différentes solutions pour le circuit de gestion d'énergie sont considérées.

Le dernier chapitre présente le deuxième mode opérationnel de récupération d'énergie, employant des élastomères diélectriques comme transducteurs actifs pour la conversion d'énergie. Deux solutions de polarisation couplant des générateurs à élastomères diélectriques avec des matériaux actifs (électret et piézoélectrique) sont proposées, en se concentrant sur la réalisation expérimentale et les performances du dispositif. Les résultats obtenus sur trois prototypes opérationnels sont décrits. Des pistes d'amélioration de leurs performances sont finalement discutées ouvrant de nouvelles perspectives pour de futurs travaux.

Un bilan global clôture enfin cette thèse, avec un résumé des points les plus pertinents de ce travail. Des perspectives basées sur des dispositifs hybrides sont proposées dans le but de disposer d'une structure complète finale incorporable sur le corps humain.

## **Chapitre 1 : Objectif et contexte**

Le terme récupération d'énergie désigne le processus consistant à convertir l'énergie environnementale ambiante en énergie électrique pour un faible niveau de puissance ( $<1\text{W}$ ). Pour un niveau de puissance électrique plus élevé, le terme « production d'énergie » désigne généralement des structures bien connues telles que les éoliennes ou les panneaux photovoltaïques. Durant ces dernières années, des récupérateurs d'énergie à petite échelle ont été développés pour l'alimentation des dispositifs électroniques embarqués à faible consommation d'énergie, avec l'objectif de remplacer les batteries dans des systèmes de capteurs. Grâce aux développements de systèmes électroniques à ultra-basse consommation, la consommation d'énergie et la taille des dispositifs et composants électroniques ont considérablement diminué. Les niveaux de consommation d'énergie des dispositifs à petite échelle sont généralement compris entre quelques microwatts pour les capteurs et les actionneurs des systèmes microélectromécaniques (MEMS), jusqu'à quelques centaines de milliwatts pour les lecteurs GPS (Global Positioning System) et MP3. L'une des technologies les plus matures et les plus développées pour la transduction d'énergie concerne les cellules photovoltaïques, qui convertissent la lumière en énergie électrique. Les générateurs thermiques sont eux utilisés pour produire de l'électricité à partir d'un gradient de température en exploitant l'effet Seebeck. Néanmoins, lorsqu'il n'y a pas de gradients de lumière ou de température dans l'environnement, d'autres sources d'énergie doivent être envisagées. Parmi celles-ci, les sources d'énergie mécanique représentent l'une des sources les plus prometteuses, en particulier à petite échelle, en raison de leur omniprésence, leur densité énergétique élevée et leur polyvalence. Diverses sources d'énergie mécanique (vibration, pression ou déformation) peuvent être trouvées dans l'environnement quotidien, comme les phénomènes naturels (vent, vagues,



mouvements sismiques ...), les machines et équipements industriels, les appareils électroménagers (ventilateurs, frigos ...) et les véhicules (voitures, avions, trains...). De plus, les mouvements humains peuvent être utilisés comme source d'énergie cinétique de haute amplitude / basse fréquence, comme présenté dans ce travail de thèse.

Les niveaux d'énergie produite dans les différentes parties du corps humain ont été discutés dans le §1.3 et les principales stratégies de récupération d'énergie pour dispositifs embarqués (électromagnétiques, piézoélectriques et électrostatiques) ont été énumérées. La comparaison entre les différentes technologies a été faite pour permettre au lecteur de comprendre l'emplacement et le choix technologique des dispositifs de récupération d'énergie développés dans ce travail.

Considérant la déformation résultante induite par le mouvement des jambes, les fréquences normales de marche / course (1-3 Hz) et l'encombrement maximal du système (surface de  $10 \times 5 \text{ cm}^2$ , faible épaisseur), les convertisseurs électrostatiques basés sur les élastomères diélectriques (DE pour *Dielectric Elastomer*) ont été sélectionnés comme technologie pour la récupération d'énergie dans ce travail. En effet, par rapport aux matériaux piézoélectriques, les DE peuvent supporter un haut niveau de déformations, développer une densité énergétique élevée et sont des matériaux très souples, intéressant pour les capteurs embarqués (masse additionnelle modérée, haute conformabilité et pas de gêne pour l'utilisateur). Le principal inconvénient de la technologie DE étant la source de polarisation externe, des structures hybrides garantissant le remplacement de cette tension extérieure doivent être conçues. Les solutions proposées dans ce travail consistent à coupler des DEG avec des matériaux électret et des matériaux piézoélectriques.

## **Chapitre 2 : État de l'art : technologies piézoélectriques et électrostatiques**

L'objectif de ce chapitre est de passer en revue les deux technologies utilisées dans ce travail pour la conception et le développement des dispositifs de récupération d'énergie, à savoir les dispositifs piézoélectriques et électrostatiques.

Pour ces deux technologies, les principes de base et les équations décrivant les modes de fonctionnement sont reportés et les matériaux utilisés pour la fabrication des dispositifs sont décrits.

La piézo-électricité provient de matériaux présentant une forte asymétrie cristalline. Au repos, le système est à l'équilibre électrique mais, lorsqu'une sollicitation mécanique est appliquée, les charges sont décalées par rapport à leur barycentre. En conséquence, un dipôle électrique est formé dans la cellule unitaire du cristal. La somme des dipôles individuels conduit à une polarisation qui induit un potentiel électrique sur des faces d'électrodes opposées (effet piézoélectrique direct). Inversement, l'application d'un champ électrique à travers le matériau induit une modification de la structure mécanique (effet piézoélectrique inverse). Le principe de base et les équations de l'effet piézoélectrique ont été décrits ainsi que les différents modes de fonctionnement. Parmi les différents matériaux piézoélectriques, l'attention s'est particulièrement portée sur deux catégories : les céramiques et les matériaux polymères. Les performances du titanate de zirconate de plomb (PZT) et du fluorure de polyvinylidène (PVDF) ont été discutées car ces matériaux piézoélectriques ont été incorporés dans nos dispositifs. Les coefficients de déformation et les coefficients électromécaniques des matériaux céramiques sont significativement plus élevés que ceux du PVDF, ce qui entraîne des tensions de sortie plus élevées. Néanmoins, en raison de leur rigidité et de leur grande fragilité, les matériaux PVDF sont préférés pour les applications à haute conformabilité et à faible impédance mécanique.

Le §2.2 décrit les générateurs électrostatiques, qui sont des condensateurs électriques variables, dont la valeur est modifiée par l'application d'un déplacement mécanique externe. Après avoir décrit les équations et les modes de fonctionnement de ces générateurs, nous décrivons deux technologies de transducteurs électrostatiques : les récupérateurs à énergie vibratoire (VEH) et les générateurs à élastomères diélectriques (DEGs).

Le premier groupe consiste en deux plaques électriquement isolées dont la position varie soit dans la direction principale de leur plan, soit dans la direction normale. La plupart des dispositifs électrostatiques VEH développés dans la littérature sont à l'échelle centimétrique et fonctionnent sous des fréquences de résonance comprises entre 2 Hz et 2 kHz, lorsqu'une accélération externe comprise entre 0,25 g et 14,2 g est appliquée aux systèmes.

Les générateurs à élastomères diélectriques (DEG) sont des dispositifs électrostatiques souples constitués d'une membrane élastomère déformable prise en sandwich entre deux électrodes modelables. Les principaux avantages de ces systèmes résident dans leur faible coût, leur facilité de fabrication, leur résistance aux contraintes élevées (dépassement de 100% de la longueur initiale), leur capacité à travailler dans une large gamme de fréquences et leur forte densité énergétique. Cette technologie étant celle développée dans ce travail, une description détaillée des principes de base, des équations, des matériaux et des modes de fonctionnement des dispositifs existant a été développée dans ce chapitre. Le dernier paragraphe décrit une solution employée dans la littérature pour surmonter le besoin d'une source de polarisation externe pour effectuer le cycle énergétique dans les dispositifs électrostatiques. A savoir, l'intégration dans ces dispositifs d'une couche de matériau diélectrique avec des charges électriques incorporées (électret) pour assurer la polarisation électrique permanente du condensateur variable, éliminant le besoin d'une source de tension externe. Le principe de fonctionnement et les principaux dispositifs à base d'électret trouvés dans la littérature ont été reportés en y incluant un premier prototype développé par notre groupe de recherche en 2013. Ce générateur hybride, adapté aux

mouvements humains, couple les DEGs avec des matériaux électret et peut récupérer jusqu'à  $33\mu\text{W}$  à 1Hz.

### **Chapitre 3. Matériaux électrets**

Ce chapitre est axé sur les matériaux électrets, dont la stabilité dans le temps constitue un paramètre fondamental pour la performance des dispositifs incorporant ces matériaux. Des électrets hautement conformes avec une stabilité de charge à long terme ont été envisagés pour nos applications. La structure chimique et les propriétés des polymères de type poly(p-xylylène) (connus sous le nom de Parylène) semblaient adaptées pour atteindre ces objectifs. Nous avons ainsi mené des études sur trois variantes de Parylène (C, AF-4 et VT-4).

Tout d'abord, un aperçu des principales définitions et principes physiques des matériaux électret a été fourni pour aider le lecteur à bien appréhender les résultats. Ensuite, les techniques de fabrication et les tests de caractérisation utilisés dans ce travail sont décrits. Plus précisément, la méthode de dépôt chimique en phase vapeur (CVD) a été utilisée pour le dépôt du Parylène. Alors que les échantillons de Parylène C ont été déposés en utilisant les installations de l'Institut Néel au CNRS de Grenoble, les variantes fluorées ont été déposées par la société Comelec SA basée en Suisse. Pour former des électrets, ces films de Parylène de quelques microns d'épaisseur ont été soumis à une décharge corona. La stabilité des charges implantées a été enregistrée à partir de mesures de décroissance de potentiel de surface (SPD) en utilisant une sonde électrostatique sans contact couplé à un voltmètre spécifique (TREK 347). Nos résultats ont été comparés avec les travaux de la littérature concernant les électrets à base notamment de téflon et considérés comme étant parmi les plus performants (mais non utilisables pour nos dispositifs car non conformant). En fait, alors que dans la littérature le Parylène C est employé parmi d'autres électrets couramment utilisés (familles des Téflon ou CYTOP), les Parylènes fluorés AF-4 et VT-4 sont plus exotiques

et leur utilisation en tant qu'électret est discrète et apparait ainsi comme une originalité dans ce travail de thèse.

L'intérêt de Parylènes fluorés réside dans la présence d'atomes fluorés dans leur chaîne garantissant une durée de vie plus longue que celle de la variante C (qui de plus est polaire). Les résultats obtenus à partir des mesures effectuées sur différentes épaisseurs d'échantillons et avec différents paramètres de charge ont confirmé cette hypothèse : des densités de charge de l'ordre de  $1.8 \text{ mC.m}^{-2}$  pour les polymères AF-4 et VT-4 ont été trouvées cent jours après la décourage corona. Ces résultats sont comparables au meilleur résultat trouvé dans la littérature sur les électrets chargés par décharge corona. Par ailleurs, nous avons montré que le Parylène AF-4 présente une bonne stabilité à la fois pour les charges positives et négatives sur une longue période (300 jours), ce qui le rend attractif. Des mesures de décharge thermiquement stimulée (*Thermally Stimulated Discharge* : TSD) ont complété ces mesures et en particulier une meilleure stabilité des échantillons de Parylène AF-4 de  $9 \text{ }\mu\text{m}$  d'épaisseur par rapport aux échantillons plus minces. Enfin dans le contexte de ces travaux, les deux polymères fluorés présentent une bonne stabilité dans des environnements hostiles (températures allant jusqu'à  $80^\circ\text{C}$  et humidité relative atteignant 60%), ce qui les rend aptes aux applications embarquées sur le corps humain. Le Parylène AF-4 a montré une stabilité en température allant jusqu'à  $100^\circ\text{C}$  pour toutes les épaisseurs testées et une rétention de charge plus élevée que le Parylène VT-4 lorsqu'il était maintenu pendant 24 heures à  $80^\circ\text{C}$ .

En conclusion, le Parylène AF-4 de  $9 \text{ }\mu\text{m}$  d'épaisseur est ressorti comme étant l'électret le plus approprié pour le développement de dispositifs de récupération d'énergie électrostatiques à base d'électrets.

## **Chapitre 4. Dispositifs de récupération d'énergie à base d'électrets**

Ce chapitre commence par la description du principe de fonctionnement et la performance du premier dispositif de récupération d'énergie hybride précédemment développé par notre équipe. Ce dernier était constitué d'un support triangulaire texturé constitué de trois motifs et capable de récupérer une énergie théorique de 85  $\mu\text{W}$  et expérimentale de 33  $\mu\text{W}$  lorsqu'une déformation active de 50% à 1 Hz était appliquée au dispositif.

Ici, nous avons analysé à la fois l'influence de la performance des matériaux électrets étudiés dans le chapitre 3 et la géométrie des récupérateurs, avec pour but l'augmentation de la puissance de sortie du dispositif et la réduction de l'encombrement total de la structure. Nous avons montré à travers des simulations que le remplacement du Teflon FEP de 50  $\mu\text{m}$  (utilisé dans le prototype disponible avant le démarrage de cette thèse) par du Parylène AF-4 de 9  $\mu\text{m}$  d'épaisseur permettait d'augmenter la puissance de sortie du dispositif de 40%, tandis que l'optimisation de la géométrie permettait de gagner pratiquement 50%. Ces résultats ont ensuite été confirmés par des tests réalisés sur des prototypes expérimentaux. De plus, les premiers résultats de la durée de vie du dispositif ont été présentés, montrant que le potentiel de surface du matériau électret était stable pendant au moins 1000 cycles de déformation (tests stoppés ensuite par manque de temps).

Des solutions possibles pour la conception de structures plus intégrables ont également été proposées (§4.3.4) la solution optimale se traduisant par un entrefer initial de 4 mm et une densité d'énergie récupérée de 2,2  $\text{mJ.gr}^{-1}$ .

Pour finir, des solutions ont été suggérés pour la réalisation du circuit de gestion d'énergie : un circuit simple de redressement à 4 diodes, un circuit commercialisé LTC3588-1 par Linear Technology et un circuit de gestion d'énergie non linéaire basé

sur la technologie d'extraction synchrone de charge électrique (SECE) en topologie flyback.

## **Chapitre 5. Dispositifs de récupération d'énergie à base de DEGs**

Dans ce chapitre, d'autres modes de fonctionnement de générateurs électrostatiques ont été étudiés, à travers la conception de solutions innovantes de dispositifs hybrides fonctionnant comme des DEG autonomes.

Les matériaux à électrets ont d'abord été testés dans ce nouveau concept de fonctionnement, montrant que leur polarisation électrique permanente peut être utilisée pour le remplacement de la source haute-tension dans les DEGs. Alors que dans le premier mode de fonctionnement (chapitre 4), le dispositif fonctionne sous la recombinaison de charges d'électret suivant la variation de capacité, dans le cas présent le matériau électret est utilisé pour la polarisation du DEG. Les tensions de polarisation obtenues sur les DEG ont été corrélés aux paramètres géométriques du dispositif par des simulations FEM et par des mesures expérimentales, montrant expérimentalement des valeurs de polarisation de 200 V sur l'électrode du DEG. Cette tension de polarisation élevée permet de stocker, sur tout le cycle de récupération d'énergie, une énergie égale à 84  $\mu\text{J}$  en 20 secondes, à travers un simple circuit redresseur.

De nouvelles structures hybrides ont également été réalisées en couplant des DEG avec des matériaux piézoélectriques. Plus précisément, nous avons présenté deux dispositifs différents permettant la synchronisation entre la sortie en tension maximale du matériau piézoélectrique et la capacité maximale du DEG. Le premier prototype est basé sur la sollicitation d'une céramique piézoélectrique (PZT) en mode choc, tandis que le second fonctionne sous sollicitation longitudinale d'un matériau PVDF. Ces deux structures, ayant pour vocation de valider le concept de cette solution hybride innovante, ont démontré leur faisabilité comme nouvelle source de polarisation. La

première structure peut récupérer une énergie totale de 17  $\mu\text{J}$  en 10 secondes sous un étirement mécanique à 1 Hz, alors que celle en PVDF, même si elle est plus légère et moins encombrante, présente une performance inférieure (3,8  $\mu\text{J}$  en 12 secondes). Les valeurs d'énergie obtenues expérimentalement à partir de ces prototypes sont plus faibles qu'en cas de polarisation d'électret. Néanmoins, cette nouvelle solution peut représenter une alternative prometteuse aux matériaux électret, car la polarisation donnée par les matériaux piézoélectriques dérive de leur structure interne et n'est donc pas sensible à la décharge, aux contacts ou aux conditions environnementales externes (dans la gamme considérée par nos applications). Enfin, grâce à des simulations, nous avons montré que plusieurs paramètres permettent d'améliorer la performance globale de la structure, à savoir le nombre de couches d'élastomères, la fréquence de travail et la tension de sortie piézoélectrique.

Pour conclure sur l'ensemble de ce travail de thèse, nous avons proposé une structure optimisée de DEG à partir d'électrets originaux à base de Parylènes fluorés ainsi que de nouvelles structures alliant des céramiques et des élastomères. Même si l'énergie obtenue avec nos prototypes est inférieure à celle des DEG classiques, notre solution est complètement autonome et intégrable et ouvre de nouvelles voies prospectives. Notre approche est d'autant plus attractive qu'elle nécessite peu de composants électroniques et aucune source de polarisation externe n'est nécessaire, grâce au couplage entre matériaux électroactifs.

Sur la base de ces résultats prometteurs, de nouvelles perspectives peuvent être envisagées comme l'optimisation des matériaux élastomères diélectriques et des électrodes utilisées dans ce travail. La réalisation de structures plus complexes, dont les briques ont été énoncées lors de simulations dans ce travail, permettront d'atteindre des énergies produites comparables aux DEG conventionnels.





## REFERENCES

### Chapter 1 references

- [1.1] A. Nordrum, "Popular Internet of Things Forecast of 50 Billion Devices by 2020 Is Outdated," *IEEE Spectrum: Technology, Engineering, and Science News*, 18-Aug-2016. [Online]. Available: <https://spectrum.ieee.org/tech-talk/telecom/internet/popular-internet-of-things-forecast-of-50-billion-devices-by-2020-is-outdated>. [Accessed: 11-Oct-2017].
- [1.2] D. Briand, E. Yeatman, and S. Roundy, *Micro Energy Harvesting*. John Wiley & Sons, 2015.
- [1.3] "Energy Harvester Uses RF Waves to Power Air Pollution Sensors - Tech Briefs :: Tech Briefs." [Online]. Available: <https://www.techbriefs.com/component/content/article/tb/features/application-briefs/23996>. [Accessed: 14-Nov-2017].
- [1.4] E. M. Yeatman, "Advances in Power Sources for Wireless Sensor Nodes," in *Proc. of BSN 2004*, 2004, pp. 6–7.
- [1.5] T. TORFS, "Pulse oximeter fully powered by human body heat," *Sens. Transducers J*, vol. 80, no. 6, pp. 1230–1238, 2007.
- [1.6] P. Spies, M. Pollak, and L. Mateu, *Handbook of Energy Harvesting Power Supplies and Applications*. Pan Stanford, 2015.
- [1.7] S. Beeby and N. White, *Energy Harvesting for Autonomous Systems*. Artech House, 2010.
- [1.8] R. Riemer and A. Shapiro, "Biomechanical energy harvesting from human motion: theory, state of the art, design guidelines, and future directions," *J. NeuroEngineering Rehabil.*, vol. 8, p. 22, Apr. 2011.
- [1.9] Y.-M. Choi, M. G. Lee, and Y. Jeon, "Wearable Biomechanical Energy Harvesting Technologies," *Energies*, vol. 10, no. 10, p. 1483, Sep. 2017.
- [1.10] S. Wang, X. Mu, X. Wang, A. Y. Gu, Z. L. Wang, and Y. Yang, "Elasto-Aerodynamics-Driven Triboelectric Nanogenerator for Scavenging Air-Flow Energy," *ACS Nano*, vol. 9, no. 10, pp. 9554–9563, Oct. 2015.
- [1.11] C. Sun, J. Shi, D. J. Bayerl, and X. Wang, "PVDF microbelts for harvesting energy from respiration," *Energy Environ. Sci.*, vol. 4, no. 11, pp. 4508–4512, Oct. 2011.
- [1.12] J.-J. Wang, H.-J. Su, C.-I. Hsu, and Y.-C. Su, "Composite Piezoelectric Rubber Band for Energy Harvesting from Breathing and Limb Motion," *J. Phys. Conf. Ser.*, vol. 557, no. 1, p. 012022, 2014.
- [1.13] T. S. J.A. Paradiso, "Human-Generated Power for Mobile Electronics," in *Low-Power Electronics Design*, 2004, pp. 1–35.
- [1.14] M. Deterre, E. Lefevre, Y. Zhu, M. Woytasik, B. Boutaud, and R. D. Molin, "Micro Blood Pressure Energy Harvester for Intracardiac Pacemaker," *J. Microelectromechanical Syst.*, vol. 23, no. 3, pp. 651–660, Jun. 2014.
- [1.15] A. Nanda and M. A. Karami, "Energy harvesting from arterial blood pressure for powering embedded micro sensors in human brain," *J. Appl. Phys.*, vol. 121, no. 12, p. 124506, Mar. 2017.
- [1.16] H. Vocca and F. Cottone, "Kinetic energy harvesting," in *ICT - Energy - Concepts Towards Zero - Power Information and Communication Technology*, InTech, 2014.
- [1.17] J. M. Gilbert and F. Balouchi, "Comparison of energy harvesting systems for wireless sensor networks," *Int. J. Autom. Comput.*, vol. 5, no. 4, pp. 334–347, Oct. 2008.
- [1.18] C. Jean-Mistral, S. Basrour, and J.-J. Chaillout, "Comparison of electroactive polymers for energy scavenging applications," *Smart Mater. Struct.*, vol. 19, no. 8, p. 085012, 2010.
- [1.19] R. Pelrine *et al.*, "Dielectric elastomers: generator mode fundamentals and applications," presented at the Smart Structures and Materials 2001: Electroactive Polymer Actuators and Devices, 2001, vol. 4329, pp. 148–157.
- [1.20] X. Yuan, S. Changgeng, G. Yan, and Z. Zhenghong, "Application review of dielectric electroactive polymers (DEAPs) and piezoelectric materials for vibration energy harvesting," *J. Phys. Conf. Ser.*, vol. 744, no. 1, p. 012077, 2016.

- [1.21] C. Jean-Mistral, “Récupération d’énergie mécanique par polymères électroactifs pour microsystèmes autonomes communicants,” phdthesis, Université Joseph-Fourier - Grenoble I, 2008.
- [1.22] T. Vu-Cong, C. Jean-Mistral, and A. Sylvestre, “Electrets substituting external bias voltage in dielectric elastomer generators: application to human motion,” *Smart Mater. Struct.*, vol. 22, no. 2, p. 025012, 2013.

## Chapter 2 references

- [2.1] “Enhancing Science Learning Through Electronic Library.” [Online]. Available: [http://resources.edb.hkedcity.net/physics/articleIE/smartmaterials/SmartMaterials\\_e.htm](http://resources.edb.hkedcity.net/physics/articleIE/smartmaterials/SmartMaterials_e.htm). [Accessed: 04-Oct-2017].
- [2.2] T. Hehn and Y. Manoli, *CMOS Circuits for Piezoelectric Energy Harvesters - Efficient* | Thorsten Hehn | Springer. 2015.
- [2.3] A. L. Kholkin, N. A. Pertsev, and A. V. Goltsev, “Piezoelectricity and Crystal Symmetry,” in *Piezoelectric and Acoustic Materials for Transducer Applications*, Springer, Boston, MA, 2008, pp. 17–38.
- [2.4] “Fundamentals of Piezoelectricity,” in *Piezoelectric Transducers for Vibration Control and Damping*, Springer, London, 2006, pp. 9–35.
- [2.5] K. Hyunuk, Y. Tadesse, and S. Priya, “Piezoelectric Energy Harvesting,” in *Energy Harvesting Technologies*, Springer US, 2009, pp. 3–39.
- [2.6] C. Hwu, “Piezoelectric Materials,” in *Anisotropic Elastic Plates*, Springer, Boston, MA, 2010, pp. 369–410.
- [2.7] S. Pramanik, B. Pingguan-Murphy, and N. A. Osman, “Developments of immobilized surface modified piezoelectric crystal biosensors for advanced applications,” *Int J Electrochem Sci*, vol. 8, pp. 8863–8892, 2013.
- [2.8] H. Kawai, “The Piezoelectricity of Poly (vinylidene Fluoride),” *Jpn. J. Appl. Phys.*, vol. 8, no. 7, p. 975, Jul. 1969.
- [2.9] J. S. Harrison and Z. Ounaies, “Piezoelectric Polymers,” in *Encyclopedia of Polymer Science and Technology*, John Wiley & Sons, Inc., 2002.
- [2.10] S. Roundy, P. K. Wright, and J. M. Rabaey, *Energy Scavenging for Wireless Sensor Networks: With Special Focus on Vibrations*. Norwell, MA, USA: Kluwer Academic Publishers, 2004.
- [2.11] P. Dineva, D. Gross, R. Müller, and T. Rangelov, *Dynamic Fracture of Piezoelectric Materials: Solution of Time-Harmonic Problems via BIEM*, 1st ed. Springer Publishing Company, Incorporated, 2016.
- [2.12] H. Li, C. Tian, and Z. D. Deng, “Energy harvesting from low frequency applications using piezoelectric materials,” *Appl. Phys. Rev.*, vol. 1, no. 4, p. 041301, Nov. 2014.
- [2.13] Y. Kuang, A. Daniels, and M. Zhu, “A sandwiched piezoelectric transducer with flex end-caps for energy harvesting in large force environments,” *J. Phys. Appl. Phys.*, vol. 50, no. 34, p. 345501, 2017.
- [2.14] K. Tang, J. Kan, T. Peng, Z. Yang, and G. Cheng, “Power performance of circular piezoelectric diaphragm generators,” *Front. Mech. Eng. China*, vol. 3, no. 4, pp. 434–440, Dec. 2008.
- [2.15] C. Mo, L. J. Radziemski, and W. W. Clark, “Experimental validation of energy harvesting performance for pressure-loaded piezoelectric circular diaphragms,” *Smart Mater. Struct.*, vol. 19, no. 7, p. 075010, 2010.
- [2.16] S. Pobering and N. Schwesinger, “A Novel Hydropower Harvesting Device,” in *2004 International Conference on MEMS, NANO and Smart Systems, 2004. ICMENS 2004. Proceedings*, 2004, pp. 480–485.
- [2.17] A. Massaro *et al.*, “Freestanding piezoelectric rings for high efficiency energy harvesting at low frequency,” *Appl. Phys. Lett.*, vol. 98, no. 5, p. 053502, Jan. 2011.

- [2.18] J. F. Antaki *et al.*, “A gait-powered autologous battery charging system for artificial organs,” *ASAIO J. Am. Soc. Artif. Intern. Organs* 1992, vol. 41, no. 3, pp. M588-595, Sep. 1995.
- [2.19] J. Kyrmis, C. Kendall, J. Paradiso, and N. Gershenfeld, “Parasitic power harvesting in shoes,” in *Digest of Papers. Second International Symposium on Wearable Computers (Cat. No.98EX215)*, 1998, pp. 132–139.
- [2.20] N. S. Shenck and J. A. Paradiso, “Energy Scavenging with Shoe-Mounted Piezoelectrics,” *IEEE Micro*, vol. 21, no. 3, pp. 30–42, May 2001.
- [2.21] T. Nishi, T. Ito, H. Hida, and I. Kanno, “Shoe-mounted vibration energy harvester of PZT piezoelectric thin films on metal foils,” *J. Phys. Conf. Ser.*, vol. 773, no. 1, p. 012062, 2016.
- [2.22] A. Khaligh, P. Zeng, and C. Zheng, “Kinetic Energy Harvesting Using Piezoelectric and Electromagnetic Technologies #x2014;State of the Art,” *IEEE Trans. Ind. Electron.*, vol. 57, no. 3, pp. 850–860, Mar. 2010.
- [2.23] B. Yang and K.-S. Yun, “Piezoelectric shell structures as wearable energy harvesters for effective power generation at low-frequency movement,” *Sens. Actuators Phys.*, vol. 188, no. Supplement C, pp. 427–433, Dec. 2012.
- [2.24] M. Renaud, T. Sterken, P. Fiorini, R. Puer, K. Baert, and C. van Hoof, “Scavenging energy from human body: design of a piezoelectric transducer,” in *The 13th International Conference on Solid-State Sensors, Actuators and Microsystems, 2005. Digest of Technical Papers. TRANSDUCERS '05.*, 2005, vol. 1, p. 784–787 Vol. 1.
- [2.25] M. Pozzi and M. Zhu, “Characterization of a rotary piezoelectric energy harvester based on plucking excitation for knee-joint wearable applications,” *Smart Mater. Struct.*, vol. 21, no. 5, p. 055004, 2012.
- [2.26] “Design and characterisation of a piezoelectric knee-joint energy harvester with frequency up-conversion through magnetic plucking - IOPscience.” [Online]. Available: <http://iopscience.iop.org/article/10.1088/0964-1726/25/8/085029>. [Accessed: 05-Nov-2017].
- [2.27] P. Pillatsch, E. M. Yeatman, and A. S. Holmes, “A piezoelectric frequency up-converting energy harvester with rotating proof mass for human body applications,” *Sens. Actuators Phys.*, vol. 206, no. Supplement C, pp. 178–185, Feb. 2014.
- [2.28] J. Feenstra, J. Granstrom, and H. Sodano, “Energy harvesting through a backpack employing a mechanically amplified piezoelectric stack,” *Mech. Syst. Signal Process.*, vol. 22, no. 3, pp. 721–734, Apr. 2008.
- [2.29] Y. Cha, J. Hong, J. Lee, J.-M. Park, and K. Kim, “Flexible Piezoelectric Energy Harvesting from Mouse Click Motions,” *Sensors*, vol. 16, no. 7, p. 1045, Jul. 2016.
- [2.30] M. Colin, S. BASROUR, and L. Rufer, “Very low frequency piezoelectric energy harvester designed for heart beat vibration scavenging,” in *Proceedings of SPIE - The International Society for Optical Engineering*, 2013, vol. 8763, p. 87631P–87631P.
- [2.31] D.-H. Choi, C.-H. Han, H.-D. Kim, and J.-B. Yoon, “Liquid-based electrostatic energy harvester with high sensitivity to human physical motion,” *Smart Mater. Struct.*, vol. 20, no. 12, p. 125012, 2011.
- [2.32] “Wiley: Electrostatic Kinetic Energy Harvesting - Philippe Basset, Elena Blokhina, Dimitri Galayko.” [Online]. Available: <http://eu.wiley.com/WileyCDA/WileyTitle/productCd-1848217161.html>. [Accessed: 05-Nov-2017].
- [2.33] K. Tao, J. Wu, A. G. P. Kottapalli, S. W. Lye, and J. Miao, “MEMS/NEMS-Enabled Vibrational Energy Harvesting for Self-Powered and Wearable Electronics,” in *Outlook and Challenges of Nano Devices, Sensors, and MEMS*, Springer, Cham, 2017, pp. 271–297.
- [2.34] F. U. Khan and M. U. Qadir, “State-of-the-art in vibration-based electrostatic energy harvesting,” *J. Micromechanics Microengineering*, vol. 26, no. 10, p. 103001, 2016.
- [2.35] M. Deterre, S. Risquez, B. Bouthaud, R. D. Molin, M. Woytasik, and E. Lefeuvre, “Multilayer out-of-plane overlap electrostatic energy harvesting structure actuated by blood pressure for powering intra-cardiac implants,” *J. Phys. Conf. Ser.*, vol. 476, no. 1, p. 012039, 2013.
- [2.36] P. Mitcheson, A. Holmes, E. Yeatman, T. Green, and P. Miao, “Micro-Machined Variable Capacitors for Power Generation,” in *Electrostatics 2003*, 0 vols., Taylor & Francis, 2004, pp. 53–58.

- [2.37] P. D. Mitcheson, P. Miao, B. H. Stark, E. M. Yeatman, A. S. Holmes, and T. C. Green, “MEMS electrostatic micropower generator for low frequency operation,” *Sens. Actuators Phys.*, vol. 115, no. 2, pp. 523–529, Sep. 2004.
- [2.38] B. Yang, C. Lee, R. K. Kotlanka, J. Xie, and S. P. Lim, “A MEMS rotary comb mechanism for harvesting the kinetic energy of planar vibrations,” *J. Micromechanics Microengineering*, vol. 20, no. 6, p. 065017, 2010.
- [2.39] F. Cottone, P. Basset, F. Marty, D. Galayko, L. Gammaitoni, and T. Bourouina, “Electrostatic generator with free micro-ball and elastic stoppers for low-frequency vibration harvesting,” in *2014 IEEE 27th International Conference on Micro Electro Mechanical Systems (MEMS)*, 2014, pp. 385–388.
- [2.40] T. Galchev, R. Raz, and O. Paul, “An electrostatic springless inertial harvester for converting multi-dimensional low-frequency motion,” in *2013 IEEE 26th International Conference on Micro Electro Mechanical Systems (MEMS)*, 2013, pp. 102–105.
- [2.41] M. E. Kiziroglou, C. He, and E. M. Yeatman, “Flexible substrate electrostatic energy harvester,” *Electron. Lett.*, vol. 46, no. 2, pp. 166–167, Jan. 2010.
- [2.42] S. J. A. Koh, X. Zhao, and Z. Suo, “Maximal energy that can be converted by a dielectric elastomer generator,” *Appl. Phys. Lett.*, vol. 94, no. 26, p. 262902, Jun. 2009.
- [2.43] C. T. Vu, *Contribution à la conception de générateurs électroactifs souples*. Grenoble, 2013.
- [2.44] R. D. Kornbluh *et al.*, “From boots to buoys: promises and challenges of dielectric elastomer energy harvesting,” presented at the Electroactive Polymer Actuators and Devices (EAPAD) 2011, 2011, vol. 7976, p. 797605.
- [2.45] R. Kornbluh and R. Pelrine, “High-performance acrylic and silicone elastomers,” in *Dielectric elastomers and Electromechanical Transducers*, Elsevier, 2011.
- [2.46] F. B. Madsen, A. E. Dugaard, S. Hvilsted, and A. L. Skov, “The Current State of Silicone-Based Dielectric Elastomer Transducers,” *Macromol. Rapid Commun.*, vol. 37, no. 5, pp. 378–413, Mar. 2016.
- [2.47] L. J. Romasanta, M. A. Lopez-Manchado, and R. Verdejo, “Increasing the performance of dielectric elastomer actuators: A review from the materials perspective,” *Prog. Polym. Sci.*, vol. 51, no. Supplement C, pp. 188–211, Dec. 2015.
- [2.48] R. Pelrine *et al.*, “Dielectric elastomers: generator mode fundamentals and applications,” 2001, p. 148.
- [2.49] C. Jean-Mistral, S. Basrour, and J.-J. Chaillout, “Comparison of electroactive polymers for energy scavenging applications,” *Smart Mater. Struct.*, vol. 19, no. 8, p. 085012, 2010.
- [2.50] J.-D. Nam, H. R. Choi, J. C. Koo, Y. K. Lee, and K. J. Kim, “Dielectric Elastomers for Artificial Muscles,” in *Electroactive Polymers for Robotic Applications*, Springer, London, 2007, pp. 37–48.
- [2.51] X. Yuan, S. Changgeng, G. Yan, and Z. Zhenghong, “Application review of dielectric electroactive polymers (DEAPs) and piezoelectric materials for vibration energy harvesting,” *J. Phys. Conf. Ser.*, vol. 744, no. 1, p. 012077, 2016.
- [2.52] L. J. Romasanta, M. Hernández, M. A. López-Manchado, and R. Verdejo, “Functionalised graphene sheets as effective high dielectric constant fillers,” *Nanoscale Res. Lett.*, vol. 6, p. 508, Aug. 2011.
- [2.53] R. Kaltseis *et al.*, “Natural rubber for sustainable high-power electrical energy generation,” *RSC Adv.*, vol. 4, no. 53, pp. 27905–27913, 2014.
- [2.54] L. Yu and A. L. Skov, “Silicone rubbers for dielectric elastomers with improved dielectric and mechanical properties as a result of substituting silica with titanium dioxide,” *Int. J. Smart Nano Mater.*, vol. 6, no. 4, pp. 268–289, Oct. 2015.
- [2.55] Z. Wang *et al.*, “Effect of high aspect ratio filler on dielectric properties of polymer composites: a study on barium titanate fibers and graphene platelets,” *IEEE Trans. Dielectr. Electr. Insul.*, vol. 19, no. 3, pp. 960–967, Jun. 2012.
- [2.56] F. Carpi, G. Gallone, F. Galantini, and D. De Rossi, “Silicone–Poly(hexylthiophene) Blends as Elastomers with Enhanced Electromechanical Transduction Properties,” *Adv. Funct. Mater.*, vol. 18, no. 2, pp. 235–241, Jan. 2008.

- [2.57] J. Vilčáková *et al.*, “Effect of surfactants and manufacturing methods on the electrical and thermal conductivity of carbon nanotube/silicone composites,” *Mol. Basel Switz.*, vol. 17, no. 11, pp. 13157–13174, Nov. 2012.
- [2.58] T. D. Nguyen *et al.*, “Highly stretchable dielectric elastomer material based on acrylonitrile butadiene rubber,” *Macromol. Res.*, vol. 22, no. 11, pp. 1170–1177, Nov. 2014.
- [2.59] D. M. Opris, M. Molberg, C. Walder, Y. S. Ko, B. Fischer, and F. A. Nüesch, “New Silicone Composites for Dielectric Elastomer Actuator Applications In Competition with Acrylic Foil,” *Adv. Funct. Mater.*, vol. 21, no. 18, pp. 3531–3539, Sep. 2011.
- [2.60] F. Galantini, S. Bianchi, V. Castelvetro, and G. Gallone, “Functionalized carbon nanotubes as a filler for dielectric elastomer composites with improved actuation performance,” *Smart Mater. Struct.*, vol. 22, no. 5, p. 055025, 2013.
- [2.61] M. Molberg *et al.*, “High Breakdown Field Dielectric Elastomer Actuators Using Encapsulated Polyaniline as High Dielectric Constant Filler,” *Adv. Funct. Mater.*, vol. 20, no. 19, pp. 3280–3291, Oct. 2010.
- [2.62] T. Wissler, “Modeling dielectric elastomer actuators,” Doctoral Thesis, ETH Zurich, 2007.
- [2.63] *Electroactivity in Polymeric Materials | Lenore Rasmussen | Springer.*
- [2.64] S. Rosset and H. R. Shea, “Flexible and stretchable electrodes for dielectric elastomer actuators,” *Appl. Phys. A*, vol. 110, no. 2, pp. 281–307, Feb. 2013.
- [2.65] A. Pimpin, Y. Suzuki, and N. Kasagi, “Microelectrostrictive Actuator With Large Out-of-Plane Deformation for Flow-Control Application,” *J. Microelectromechanical Syst.*, vol. 16, no. 3, pp. 753–764, Jun. 2007.
- [2.66] M. Benslimane, P. Gravesen, and P. Sommer-Larsen, “Mechanical properties of dielectric elastomer actuators with smart metallic compliant electrodes,” presented at the Smart Structures and Materials 2002: Electroactive Polymer Actuators and Devices (EAPAD), 2002, vol. 4695, pp. 150–158.
- [2.67] S. Rosset, M. Niklaus, P. Dubois, and H. R. Shea, “Mechanical characterization of a dielectric elastomer microactuator with ion-implanted electrodes,” *Sens. Actuators Phys.*, vol. 144, no. 1, pp. 185–193, May 2008.
- [2.68] S. Yun, X. Niu, Z. Yu, W. Hu, P. Brochu, and Q. Pei, “Compliant Silver Nanowire-Polymer Composite Electrodes for Bistable Large Strain Actuation,” *Adv. Mater.*, vol. 24, no. 10, pp. 1321–1327, Mar. 2012.
- [2.69] U. Kim *et al.*, “A transparent and stretchable graphene-based actuator for tactile display,” *Nanotechnology*, vol. 24, no. 14, p. 145501, 2013.
- [2.70] StretchSense, “Download the Energy Harvesting Kit Information Sheet.” [Online]. Available: <http://info.stretchsense.com/download-energy-harvesting-kit-information-sheet>. [Accessed: 05-Nov-2017].
- [2.71] S. CHIBA, R. PERLINE, R. Kornbluh, H. PRAHLAD, S. STANFORD, and J. Eckerle, “New Opportunities in Electric Generation Using Electroactive Polymer Artificial Muscle (EPAM),” *J. Jpn. Inst. Energy*, vol. 86, pp. 743–747, Sep. 2007.
- [2.72] S. Chiba, M. Waki, R. Kornbluh, and R. Pelrine, “Current status and future prospects of power generators using dielectric elastomers,” *Smart Mater. Struct.*, vol. 20, no. 12, p. 124006, 2011.
- [2.73] J. Slade, “Bio-kinetic energy harvesting using electroactive polymers,” presented at the Head-and Helmet-Mounted Displays XVII; and Display Technologies and Applications for Defense, Security, and Avionics VI, 2012, vol. 8383, p. 83830R.
- [2.74] C. Jean-Mistral, “Récupération d’énergie mécanique par polymères électroactifs pour microsystèmes autonomes communicants,” phdthesis, Université Joseph-Fourier - Grenoble I, 2008.
- [2.75] T. McKay, B. O’Brien, E. Calius, and I. Anderson, “An integrated, self-priming dielectric elastomer generator,” *Appl. Phys. Lett.*, vol. 97, no. 6, p. 062911, Aug. 2010.
- [2.76] T. G. McKay, S. Rosset, I. A. Anderson, and H. Shea, “Dielectric elastomer generators that stack up,” *Smart Mater. Struct.*, vol. 24, no. 1, p. 015014, 2015.
- [2.77] S. Chiba, M. Waki, R. Kornbluh, and R. Pelrine, “Extending applications of dielectric elastomer artificial muscle,” presented at the Electroactive Polymer Actuators and Devices (EAPAD) 2007, 2007, vol. 6524, p. 652424.

- [2.78] T. Tsutsumino, Y. Suzuki, N. Kasagi, and Y. Sakane, “Seismic Power Generator Using High-Performance Polymer Electret,” in *19th IEEE International Conference on Micro Electro Mechanical Systems*, Istanbul, Turkey, 2006, pp. 98–101.
- [2.79] Z. Yang, J. Wang, and J. Zhang, “A high-performance micro electret power generator based on microball bearings,” *J. Micromechanics Microengineering*, vol. 21, no. 6, p. 065001, 2011.
- [2.80] Y. Zhang *et al.*, “Electrostatic energy harvesting device with dual resonant structure for wideband random vibration sources at low frequency,” *Rev. Sci. Instrum.*, vol. 87, no. 12, p. 125001, Dec. 2016.
- [2.81] T. Vu-Cong, C. Jean-Mistral, and A. Sylvestre, “Electrets substituting external bias voltage in dielectric elastomer generators: application to human motion,” *Smart Mater. Struct.*, vol. 22.
- [2.82] Y. Naruse, N. Matsubara, K. Mabuchi, M. Izumi, and S. Suzuki, “Electrostatic micro power generation from low-frequency vibration such as human motion,” *J. Micromechanics Microengineering*, vol. 19, no. 9, p. 094002, 2009.
- [2.83] M. Edamoto *et al.*, “Low-Resonant-Frequency Micro Electret Generator for Energy Harvesting Application,” in *2009 IEEE 22nd International Conference on Micro Electro Mechanical Systems*, 2009, pp. 1059–1062.
- [2.84] Y. Sakane, Y. Suzuki, and N. Kasagi, “The development of a high-performance perfluorinated polymer electret and its application to micro power generation,” *J. Micromechanics Microengineering*, vol. 18, no. 10, p. 104011, 2008.
- [2.85] P. Spies, M. Pollak, and L. Mateu, *Handbook of Energy Harvesting Power Supplies and Applications*. Pan Stanford, 2015.

## Chapter 3 references

- [3.1] A. Thyssen, *Charge distribution and stability in electret materials*. DTU Nanotech, 2016.
- [3.2] V. Kestelman, L. Pinchuk, and V. Goldade, “Electret Effect and Electric Technologies,” in *Electrets in engineering*, Kluwer Academic Publishers, 2000.
- [3.3] G. M. Sessler, Ed., *Electrets*, vol. 33. Berlin, Heidelberg: Springer Berlin Heidelberg, 1987.
- [3.4] D. A. Seanor, *Electrical Properties of Polymers*. Elsevier, 2013.
- [3.5] A. Crisci, B. Gosse, J.-P. Gosse, and V. Ollier-Duréault, “Surface-potential decay due to surface conduction,” *Eur. Phys. J. Appl. Phys.*, vol. 4, no. 1, pp. 107–116, Oct. 1998.
- [3.6] S. Boisseau, “Récupération d’énergie vibratoire à électrets,” phdthesis, Université de Grenoble, 2011.
- [3.7] D. Rychkov and R. A. P. Altafim, “Polymer Electrets and Ferroelectrets as EAPs: Models,” in *Electromechanically Active Polymers*, F. Carpi, Ed. Springer International Publishing, 2016, pp. 645–659.
- [3.8] “Electrets In Engineering - Fundamentals and | Vladimir N. Kestelman | Springer.” [Online]. Available: <http://www.springer.com/la/book/9780792377542>. [Accessed: 18-Aug-2017].
- [3.9] J. A. Giacometti, S. Fedosov, and M. M. Costa, “Corona charging of polymers: recent advances on constant current charging,” *Braz. J. Phys.*, vol. 29, no. 2, pp. 269–279, Jun. 1999.
- [3.10] “TREK Product - Model 347 Electrostatic Voltmeter.” [Online]. Available: <http://www.trekinc.com/products/347.asp>. [Accessed: 06-Sep-2017].
- [3.11] T. Vu-Cong, C. Jean-Mistral, and A. Sylvestre, “Electrets substituting external bias voltage in dielectric elastomer generators: application to human motion,” *Smart Mater. Struct.*, vol. 22.
- [3.12] G. Chen, “A new model for surface potential decay of corona-charged polymers,” *J. Phys. Appl. Phys.*, vol. 43, no. 5, p. 055405, 2010.
- [3.13] D. Rychkov, A. Kuznetsov, and A. Rychkov, “Electret properties of polyethylene and polytetrafluoroethylene films with chemically modified surface,” *IEEE Trans. Dielectr. Electr. Insul.*, vol. 18, no. 1, pp. 8–14, Feb. 2011.

- [3.14] M. Raposo, P. A. Ribeiro, and J. N. M. Mendes, "Possible protonic conduction in Teflon FEP under humid atmospheres," in *Proceedings of 8th International Symposium on Electrets (ISE 8)*, 1994, pp. 405–410.
- [3.15] J. Kindersberger and C. Lederle, "Surface charge decay on insulators in air and sulfurhexafluorid - part I: simulation," *IEEE Trans. Dielectr. Electr. Insul.*, vol. 15, no. 4, pp. 941–948, Aug. 2008.
- [3.16] H. von Berlepsch, "Interpretation of surface potential kinetics in HDPE by a trapping model," *J. Phys. Appl. Phys.*, vol. 18, no. 6, p. 1155, 1985.
- [3.17] Z. Chen, Z. Lv, and J. Zhang, "PECVD SiO<sub>2</sub>/Si<sub>3</sub>N<sub>4</sub> double layers electrets on glass substrate," *IEEE Trans. Dielectr. Electr. Insul.*, vol. 15, no. 4, pp. 915–919, Aug. 2008.
- [3.18] M. Perez, S. Boisseau, P. Gasnier, J. Willemin, and J. L. Reboud, "An electret-based aeroelastic flutter energy harvester," *Smart Mater. Struct.*, vol. 24, no. 3, p. 035004, 2015.
- [3.19] Y. Sakane, Y. Suzuki, and N. Kasagi, "The development of a high-performance perfluorinated polymer electret and its application to micro power generation," *J. Micromechanics Microengineering*, vol. 18, no. 10, p. 104011, 2008.
- [3.20] J. Boland, Y.-H. Chao, Y. Suzuki, and Y. C. Tai, "Micro electret power generator," in *The Sixteenth Annual International Conference on Micro Electro Mechanical Systems, 2003*, Kyoto, Japan, 2003, pp. 538–541.
- [3.21] S. Boisseau, G. Despesse, and B. A. Seddik, *Electrostatic Conversion for Vibration Energy Harvesting*. 2012.
- [3.22] Y. Feng, X. Zhang, Y. Han, Z. Yu, and W. Lou, "Airflow-driven rotary electret energy harvester," in *2017 IEEE 12th International Conference on Nano/Micro Engineered and Molecular Systems (NEMS)*, 2017, pp. 260–263.
- [3.23] M. Mrlík, S. M. Leadenham, M. Al-Ali Al-Maadeed, and A. Erturk, *Figure of merit comparison of PP-based electret and PVDF-based piezoelectric polymer energy harvesters*. International Society for Optical Engineering (SPIE), 2016.
- [3.24] K. Tao, S. W. Liu, J. M. Miao, and S. W. Lye, "A three-dimensional electrostatic/electret micro power generator for low acceleration and low frequency vibration energy harvesting," in *2014 IEEE 27th International Conference on Micro Electro Mechanical Systems (MEMS)*, 2014, pp. 366–369.
- [3.25] S. Genter and O. Paul, "Parylene-C as an electret material for micro energy harvesting," in *The 12th International Workshop on Micro and Nanotechnology for Power Generation and Energy Conversion Applications EMS 2012*, Atlanta, Georgia, USA, 2012, pp. 129–132.
- [3.26] Y. Chiu, M. H. Lee, and S.-H. Wu, "PDMS-based flexible energy harvester with Parylene electret and copper mesh electrodes," *J. Micromechanics Microengineering*, vol. 25, no. 10, p. 104007, 2015.
- [3.27] H. Lo and Y.-C. Tai, "Parylene-based electret power generators," *J. Micromechanics Microengineering*, vol. 18, no. 10, p. 104006, 2008.
- [3.28] Y. Wada, Y. Hamate, S. Nagasawa, and H. Kuwano, "Aging characteristics of electret used in a vibration-based electrostatic induction energy harvester," in *16th International Solid-State Sensors, Actuators and Microsystems Conference*, Beijing, China, 2011, pp. 2626–2629.
- [3.29] A. Kahouli, "Étude des propriétés physico-chimiques et (di)-électriques du parylène C en couche mince," phd thesis, Université de Grenoble, 2011.
- [3.30] S. Diahm, M. Bechara, M.-L. Locatelli, R. Khazaka, C. Tenailleau, and R. Kumar, "Dielectric strength of parylene HT," *J. Appl. Phys.*, vol. 115, no. 5, p. 054102, Feb. 2014.
- [3.31] "What is Parylene?" [Online]. Available: <http://www.globaladvtech.com/properties-conformal-coatings/parylene-coating/> [Accessed: 19-Dec-2017].
- [3.32] "The properties of parylene." [Online]. Available: <https://www.plasma.com/en/plasmatechnik/parylene-beta-version/the-properties-of-parylene/> [Accessed: 19-Dec-2017].
- [3.33] A. Kachroudi, C. Lagomarsini, and A. Sylvestre, "Post-annealing effect on the parylene C electret thermal stability," presented at the 16th International Symposium on Electrets (ISE16), Louvain, Belgium, 2017.



- [3.34] C. R. Raschke and T. E. Nowlin, "Polyparaxylylene electrets usable at high temperatures," *J. Appl. Polym. Sci.*, vol. 25, no. 8, pp. 1639–1644, Aug. 1980.
- [3.35] J. Li, F. Zhou, D. Min, S. Li, and R. Xia, "The energy distribution of trapped charges in polymers based on isothermal surface potential decay model," *IEEE Trans. Dielectr. Electr. Insul.*, vol. 22, no. 3, pp. 1723–1732, Jun. 2015.
- [3.36] Z. Xu, L. Zhang, and G. Chen, "Decay of electric charge on corona charged polyethylene," *J. Phys. Appl. Phys.*, vol. 40, no. 22, p. 7085, 2007.
- [3.37] K. Tao, J. Wu, L. Tang, L. Hu, S. W. Lye, and J. Miao, "Enhanced electrostatic vibrational energy harvesting using integrated opposite-charged electrets," *J. Micromechanics Microengineering*, vol. 27, no. 4, p. 044002, 2017.
- [3.38] D. Rychkov and R. Gerhard, "Stabilization of positive charge on polytetrafluoroethylene electret films treated with titanium-tetrachloride vapor," *Appl. Phys. Lett.*, vol. 98, no. 12, p. 122901, Mar. 2011.
- [3.39] D. Rychkov, A. Rychkov, N. Efimov, A. Malygin, and R. Gerhard, "Higher stabilities of positive and negative charge on tetrafluoroethylene–hexafluoropropylene copolymer (FEP) electrets treated with titanium-tetrachloride vapor," *Appl. Phys. A*, vol. 112, no. 2, pp. 283–287, Aug. 2013.
- [3.40] A. Kahouli *et al.*, "Dielectric properties of parylene AF4 as low-k material for microelectronic applications," *Thin Solid Films*, vol. 520, no. 7, pp. 2493–2497, Jan. 2012.
- [3.41] J. J. Senkevich *et al.*, "Stability of fluorinated parylenes to oxygen reactive-ion etching under aluminum, aluminum oxide, and tantalum nitride overlayers," *J. Electron. Mater.*, vol. 32, no. 9, pp. 925–931, Sep. 2003.
- [3.42] J. M. Masterton, *Humidex: A Method of Quantifying Human Discomfort Due to Excessive Heat and Humidity*, by J.M. Masterton and F.A. Richardson. Ministere de l'Environnement, 1979.
- [3.43] "Canadian Humidex Calculator." [Online]. Available: <http://www.csgnetwork.com/canhumidexcalc.html>. [Accessed: 06-Sep-2017].
- [3.44] T. Tsutsumino, Y. Suzuki, N. Kasagi, and Y. Tsurumi, "High-Performance Polymer Electret for Micro Seismic Generator," presented at the The Fifth International Workshop on Micro and Nanotechnology for Power Generation and Energy Conversion Applications PowerMEMS2005, Tokyo, Japan, 2005.

## Chapter 4 references

- [4.1] T. Vu-Cong, C. Jean-Mistral, and A. Sylvestre, "Electrets substituting external bias voltage in dielectric elastomer generators: application to human motion," *Smart Mater. Struct.*, vol. 22.
- [4.2] C. Lagomarsini, A. Sylvestre, C. Jean-Mistral, and S. Monfray, "Coupling of electro-active polymers for energy harvesting applications," in *2016 IEEE International Conference on Dielectrics (ICD)*, 2016, vol. 1, pp. 443–446.
- [4.3] E. J. van der Zanden, "Experimental-numerical analysis of copperrubber interfaces in stretchable electronics," Eindhoven University of Technology.
- [4.4] M. Niklaus and H. R. Shea, "Electrical conductivity and Young's modulus of flexible nanocomposites made by metal-ion implantation of polydimethylsiloxane: The relationship between nanostructure and macroscopic properties," *Acta Mater.*, vol. 59, no. 2, pp. 830–840, Jan. 2011.
- [4.5] P. Basset, D. Galayko, A. M. Paracha, F. Marty, A. Dudka, and T. Bourouina, "A batch-fabricated and electret-free silicon electrostatic vibration energy harvester," *J. Micromechanics Microengineering*, vol. 19, no. 11, p. 115025, 2009.
- [4.6] T. Tsutsumino, Y. Suzuki, N. Kasagi, and Y. Sakane, "Seismic Power Generator Using High-Performance Polymer Electret," in *19th IEEE International Conference on Micro Electro Mechanical Systems*, Istanbul, Turkey, 2006, pp. 98–101.

- [4.7] W. Ma, R. Zhu, L. Rufer, Y. Zohar, and M. Wong, "An Integrated Floating-Electrode Electric Microgenerator," *J. Microelectromechanical Syst.*, vol. 16, no. 1, pp. 29–37, Feb. 2007.
- [4.8] Y. Suzuki *et al.*, "Micro Electret Energy Harvesting Device with Analogue Impedance Conversion Circuit," Jan. 2008.
- [4.9] B. Abernethy, V. Kippers, S. Hanrahan, M. Pandy, A. McManus, and L. Mackinnon, *Biophysical Foundations of Human Movement 3rd Edition*. Human Kinetics.
- [4.10] N. Elvin and A. Erturk, *Advances in Energy Harvesting Methods*. Springer Science & Business Media, 2013.
- [4.11] "LTC3588-1 - Nanopower Energy Harvesting Power Supply - Linear Technology." [Online]. Available: <http://www.linear.com/product/LTC3588-1>. [Accessed: 08-Nov-2017].
- [4.12] D. Guyomar and M. Lallart, "Recent Progress in Piezoelectric Conversion and Energy Harvesting Using Nonlinear Electronic Interfaces and Issues in Small Scale Implementation," *Micromachines*, vol. 2, no. 2, pp. 274–294, Jun. 2011.
- [4.13] D. Guyomar, C. Magnet, E. Lefeuvre, and C. Richard, "Nonlinear processing of the output voltage a piezoelectric transformer," *IEEE Trans. Ultrason. Ferroelectr. Freq. Control*, vol. 53, no. 7, pp. 1362–1375, Jul. 2006.
- [14] E. Lefeuvre, A. Badel, C. Richard, L. Petit, and D. Guyomar, "A comparison between several vibration-powered piezoelectric generators for standalone systems," *Sens. Actuators Phys.*, vol. 126, no. 2, pp. 405–416, Feb. 2006.
- [4.15] E. Sazonov and M. Neuman, *Wearable Sensors - 1st Edition*. Academic Press, 2014.
- [4.16] P. Gasnier, "Circuit de récupération d'énergie mécanique pour l'alimentation de capteurs communicants sans fil," phd thesis, Université de Grenoble, 2014.

## Chapter 5 references

- [5.1] C. Jean-Mistral, T. Vu Cong, and A. Sylvestre, "Advances for dielectric elastomer generators: Replacement of high voltage supply by electret," *Appl. Phys. Lett.*, vol. 101, no. 16, p. 162901, Oct. 2012.
- [5.2] R. Pelrine *et al.*, "Dielectric elastomers: generator mode fundamentals and applications," presented at the Smart Structures and Materials 2001: Electroactive Polymer Actuators and Devices, 2001, vol. 4329, pp. 148–157.
- [5.3] A. Tröls *et al.*, "Stretch dependence of the electrical breakdown strength and dielectric constant of dielectric elastomers," *Smart Mater. Struct.*, vol. 22, no. 10, p. 104012, Oct. 2013.
- [5.4] T. Vu-Cong, C. Jean-Mistral, and A. Sylvestre, "Impact of the nature of the compliant electrodes on the dielectric constant of acrylic and silicone electroactive polymers," *Smart Mater. Struct.*, vol. 21, no. 10, p. 105036, 2012.
- [5.5] S. Hammami, C. Jean-Mistral, F. Jomni, and A. Sylvestre, "Pre-stretch induced leakage current in VHB electroactive polymers," presented at the Electroactive Polymer Actuators and Devices (EAPAD) 2016, 2016, vol. 9798, p. 97980Y.
- [5.6] C. Jean-Mistral, "Récupération d'énergie mécanique par polymères électroactifs pour microsystemes autonomes communicants," phd thesis, Université Joseph-Fourier - Grenoble I, 2008.
- [5.7] C. T. Vu, "Contribution à la conception de générateurs électroactifs souple", phd thesis, Grenoble, 2013.
- [5.8] P. Loew, G. Rizzello, D. Naso, and S. Seelecke, "Analytical and finite element modeling of a dielectric elastomer strip membrane undergoing inhomogeneous large deformations," presented at the EuroEAP 2017 7th international conference on Electromechanically Active Polymer (EAP) transducers & artificial muscles Cartagena, Spain, 06/06/2017 - 07/06/2017, Cartagena, Spain, 2017.

## REFERENCES

- [5.9] K. Minami, T. Fujita, K. Sonoda, N. Miwatani, K. Kanda, and K. Maenaka, “An Equivalent Circuit Model for Electrostatic Energy Harvester utilized Energy Harvesting System,” *J. Phys. Conf. Ser.*, vol. 557, no. 1, p. 012040, 2014.
- [5.10] M. Khbeis, J. McGee, and R. Ghodssi, “Development of a simplified hybrid ambient low frequency, low intensity vibration energy scavenger system,” in *TRANSDUCERS 2009 - 2009 International Solid-State Sensors, Actuators and Microsystems Conference*, 2009, pp. 525–528.
- [5.11] J. G. Rocha, L. M. Goncalves, P. F. Rocha, M. P. Silva, and S. Lanceros-Mendez, “Energy Harvesting From Piezoelectric Materials Fully Integrated in Footwear,” *IEEE Trans. Ind. Electron.*, vol. 57, no. 3, pp. 813–819, Mar. 2010.
- [5.12] A. Cornogolub, P.-J. Cottinet, and L. Petit, “Hybrid energy harvesting systems, using piezoelectric elements and dielectric polymers,” *Smart Mater. Struct.*, vol. 25, no. 9, p. 095048, 2016.
- [5.13] A. Phipps and T. Nishida, “System Modeling of Piezoelectric Energy Harvesters,” *IEEE Trans. Power Electron.*, vol. 27, no. 2, pp. 790–802, Feb. 2012.
- [5.14] T. G. McKay, S. Rosset, I. A. Anderson, and H. Shea, “Dielectric elastomer generators that stack up,” *Smart Mater. Struct.*, vol. 24, no. 1, p. 015014, 2015.



# APPENDIX A

## CHEMICAL VAPOR DEPOSITION (CVD)

Chemical vapor deposition is a material-processing technology allowing depositing high quality and purity film on substrates. There are several types of CVD processes, from low pressure to atmospheric pressure to plasma enhanced deposition. In this work, low-pressure CVD was employed to deposit Parylene-C materials to metallic substrates to test their suitability for electrets in energy harvesting applications. CVD process can be divided in the following principal phases:

### 1- SUBLIMATION

This phase, which is carried out at a temperature ranging between 100 to 170°C at a pressure of 1 Torr, allows the sublimation of the initial dimer (dichloro-di-para-xylylene), which is transformed in the gaseous phase. This is possible thanks to the combined action of vacuum and temperature and it is strictly dependent on the vapor pressure, the mass of the dimer and the substrate temperature.

### 2- PYROLYSIS

The gaseous molecules obtained from the sublimation process is then pulled, under vacuum, into the pyrolysis furnace, which presents a temperature ranging between 640°C and 690°C and a pressure of 0.5 Torr. The gaseous dimer is thus split into gaseous monomer (mono-chloro-p-xylylene) thanks to the thermal cleavage of methylene-methylene bonds.

### 3- POLYMERIZATION

The monomer gas is then drawn by vacuum into the deposition chamber, which was maintained in this work at ambient temperature. During this last phase (which occurs close to 1 Torr pressure), the gaseous monomers deriving from the pyrolysis process are deposited on the metal substrate. To enhance the adhesion of the monomers onto the substrates, we employed in this work the adhesion promoter silane A174 in liquid phase.

Excess non-polymerized gas is removed by a cold trap, standing in the side of the deposition chamber, presenting a temperature lower than  $-70^{\circ}\text{C}$ .

The different phases are summarized in Figure A.1:

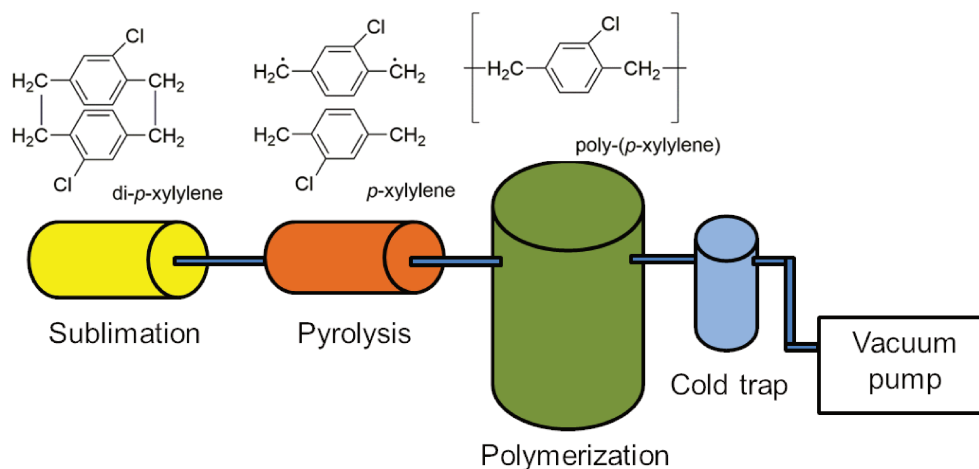


Figure A.1: Different phases of the CVD process

The deposition total duration and the film thickness are controlled by the initial mass of the dimer and by the sublimation temperature. Higher dimer mass leads to higher film thicknesses and thus lengthens the deposition time. Higher sublimation temperatures increase the sublimation speed and thus shorten the deposition

duration. Nevertheless, when the sublimation speed is higher, higher percentages of molecules evacuate to the cold trap (and thus not polymerize on the substrate, reducing the film thickness), due to their higher kinetic energy.

Effect of dimer mass and sublimation temperature on the deposition are shown in Figure A.2, from [1.A]

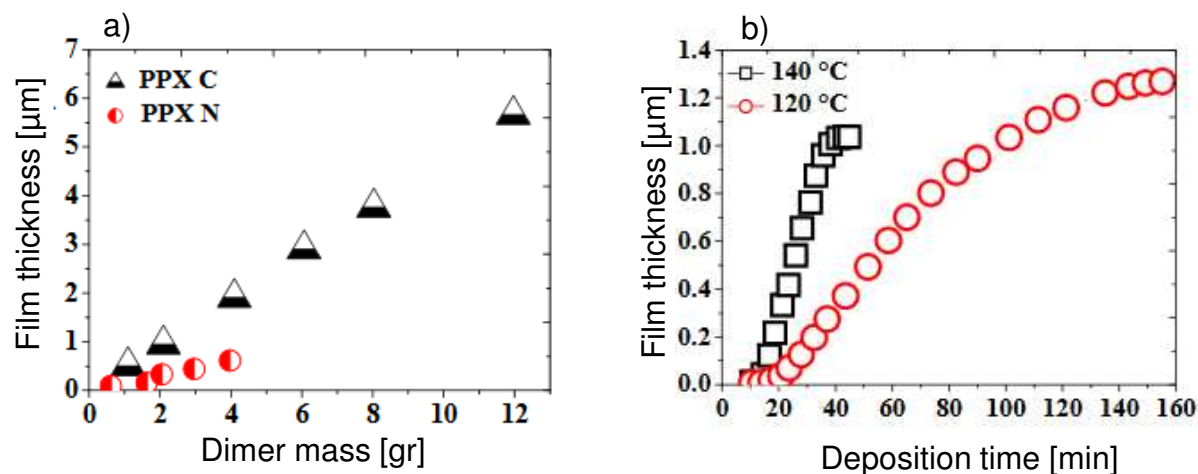


Figure A.2: Effect of the dimer mass on the Parylene C (PPX C) film thickness, compared to the basic variant Parylene N (PPX N) (a) and influence of sublimation temperature on the deposition time (b) (modified from [A.1])

Fluorinated polymers are deposited through the same process, but with different deposition conditions. In this work, the CVD parameters for VT-4 and AF-4 are not reported as these samples were deposited by Comelec Sa. On figure A.3, the chemical transformations in the different phases of the process for Parylene VT-4 and AF-4 are given.

## APPENDIX A

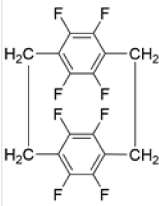
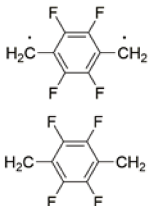
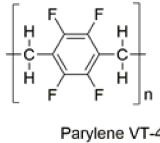
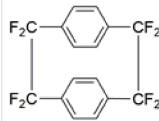
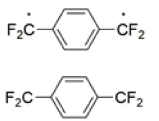
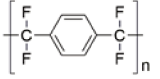
SUBLIMATION	PYROLYSIS	POLYMERIZATION
		 <p style="text-align: center;">Parylene VT-4</p>
		 <p style="text-align: center;">Parylene AF-4</p>

Figure A.3: Fluorinated Parylenes chemical transformations during the different CVD phases



# APPENDIX B

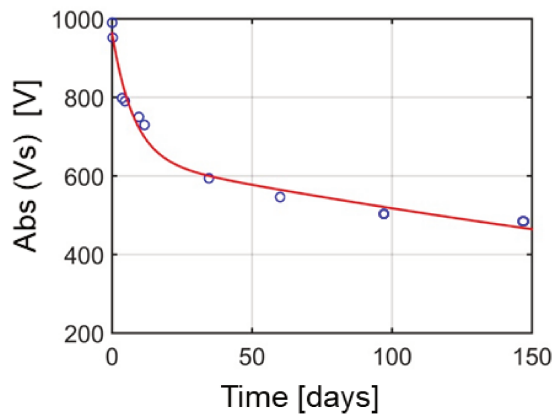
## SPD CURVES FITTING

The surface potential decay curves obtained from electret charging and surface potential measuring (through TREK 347 electrostatic probe, see 3.1.6), were fitted using the Curve Fitting tool in Matlab, to derive the decay parameters.

The function that better described the trend of the SPD curves was the double exponential:

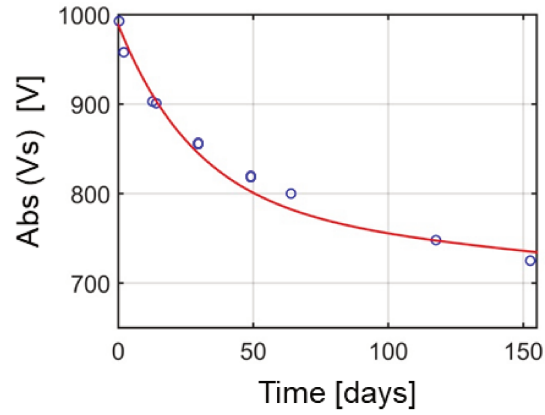
$$V(t) = a_1 e^{-t/\tau_1} + a_2 e^{-t/\tau_2}$$

We will report in this section the fitted curves and fitting parameters of selected fluorinated Parylene samples, whose results have been discussed in paragraph 3.2.2 of this manuscript.

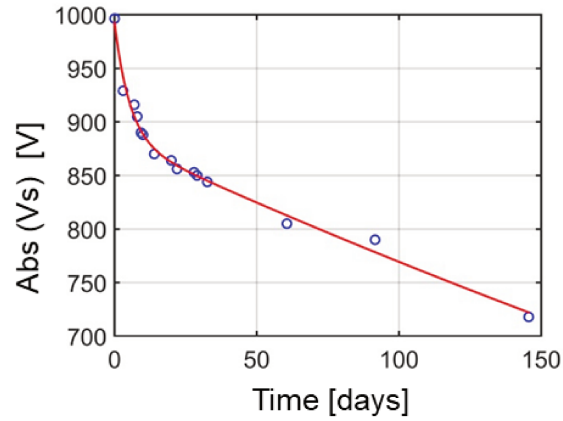


6-μm thick Parylene AF-4					
$V_0$ [V]	$a_1$ [V]	$\tau_1$ [d]	$a_2$ [V]	$\tau_2$ [d]	R-square
-1000	-376.8	7.7	-579.3	460.8	0.98
-1500	-709.3	0.7	-702.9	220.1	0.93
-2000	-2175	0.2	-935.6	191.0	0.96

Figure A.4: 6-μm-thick Parylene AF-4 fitting curve (for  $V_s = -1000$  V) and parameters



9-μm thick Parylene AF-4					
$V_0$ [V]	$a_1$ [V]	$\tau_1$ [d]	$a_2$ [V]	$\tau_2$ [d]	R-square
-1000	-210.7	14.6	-777.9	833.4	0.99
-1500	-354.7	4.7	-854.2	817.7	0.92
-2000	-795.7	4.2	-935.6	351.4	0.96

Figure A.5: 9-μm-thick Parylene AF-4 fitting curve (for  $V_s = -1000$  V) and parameters

9-μm thick Parylene VT-4					
$V_0$ [V]	$a_1$ [V]	$\tau_1$ [d]	$a_2$ [V]	$\tau_2$ [d]	R-square
-1000	-73.3	8.5	-879.6	744.6	0.95
-1500	-460.4	4.1	-1008.0	438.2	0.99
-2000	-461.9	1.0	-1060.0	322.8	0.94

Figure A.6: 9-μm-thick Parylene VT-4 fitting curve (for  $V_s = -1000$  V) and parameters

